



Max-Planck-Institut für Polymerforschung

Max Planck Institute for Polymer Research



Surface Modification of Nanodiamonds for Bioapplication

Dissertation

Zur Erlangung des Grades

„Doktor der Naturwissenschaften“

im Promotionsfach Chemie

am Fachbereichs Chemie, Pharmazie, Geographie und Geowissenschaften

der Johannes Gutenberg-Universität Mainz

Yingke Wu

Geboren in Tianmen (V. R. China)

Mainz, Mai. 2021

JOHANNES GUTENBERG
UNIVERSITÄT MAINZ



Tag der mündlichen Prüfung: 08.07.2021

Die vorliegende Arbeit wurde in der Zeit von September 2017 bis Mai 2021 am Max-Planck-Institut für Polymerforschung in der Arbeitsgruppe von Prof. Dr. Tanja Weil angefertigt.

Hiermit versichere ich gemäß § 10 Abs. 3d der Promotionsordnung vom 24.07.2007

Ich habe die jetzt als Dissertation vorgelegte Arbeit selbst angefertigt und alle benutzten Hilfsmittel (Literatur, Apparaturen, Material) in der Arbeit angegeben. Ich habe oder hatte die jetzt als Dissertation vorgelegte Arbeit nicht als Prüfungsarbeit für eine staatliche oder andere wissenschaftliche Prüfung eingereicht. Ich hatte weder die jetzt als Dissertation vorgelegte Arbeit noch Teile davon bei einer anderen Fakultät bzw. einem anderen Fachbereich als Dissertation eingereicht.

Mainz, Mai 2021

Yingke Wu

Abstract

Cancer is one of the major serious health problems and burdens in both developed and developing countries. To alleviate the situation, it is essential to develop sensitive detectors for early diagnosis and more advanced methods to monitor and treat patients. nanodiamonds (NDs) are a unique carbon-based nanomaterial due to its outstanding optical and magnetic properties as well as excellent biocompatibility. It has attracted a lot of attention from scientists. The optically active atom defects in NDs, for example, the Nitrogen Vacancy (NV) center, endow stable fluorescence without photoblinking and photobleaching. It resulted in NDs have been widely applied in bioimaging and real-time reporters for drug delivery. In addition, NDs containing negatively charged NV (NV⁻) centers can serve as single-spin sensors to detect critical physical parameters in a biological microenvironment, such as temperature, magnetic fields, electron spins, and mechanical strain.

For most of these applications, stable and appropriate functionalized nanodiamonds (NDs) are required. As the colloidal stability of unmodified NDs is very poor in solution, the aggregation of NDs becomes dramatically amplified when the size of the diamond decreases to the nanoscale. In addition, surface functionalization improves the surface flatness, which is often the starting point for further attachment of other motifs such as drug molecules, dyes, targeting groups or antibodies. Importantly, a uniform particle surface increases the amount of binding sites and reproducibility. Furthermore, surface coating is very valuable in vivo to avoid foreign body interactions toward the particles and help the nanoparticles to accumulate and remain at the target sites for a prolonged time period.

In this thesis, two novel nature-inspired coating materials are explored to optimize the surface properties of NDs firstly. The first coating material is poly(L-DOPA), which is obtained by the self-polymerization of the neurotransmitter L-3,4-dihydroxyphenylalanine (L-DOPA) inspired from “protein glue” of mussel foot proteins. The polymerization of L-DOPA provides a highly crosslinked polymer with reactive surface functional groups including amines, carboxylic acids, alcohols, and conjugated Michael acceptors. Herein, L-DOPA is polymerized on NDs with a high

control over the shell thickness. Subsequently, conjugation of transferrin to provide efficient receptor specific cellular transport, improves the colloidal stability and cellular uptake of the poly(L-DOPA)-coated NDs. The loading of the FDA-approved photothermal drug indocyanine green (ICG) yields an integrated biohybrid nanomaterial exhibiting an amplified photothermal effect in cells at very low energy intake ($\sim 90 \text{ mW/cm}^2$).

Viruses are evolutionary optimized carrier systems and have been applied for cell invasion. They have gained great interest in recent years as tools to boost the cell uptake. The second coating material is a capsid protein (CP) from *Cowpea chlorotic mottle virus* (CCMV). CP was first isolated from the CCMV, which is subsequently used to prepare highly stable virus capsid protein encapsulated NDs (ND-CP). A thin layer of protein coating is obtained surrounding the NDs, imparting reactive groups as well as high colloidal stability. It doesn't affect the physical properties of NDs. In addition, the ND-CP shows good cellular uptake and excellent biocompatibility both *in vitro* and *in vivo*. Furthermore, the long-term intracellular trafficking has been investigated by the ND-CP owing to the high photostability. The excellent optical properties will owe them great potential in life science applications.

In studying the above two systems, we have found, First, the small molecules or protein were adsorbed on the surface of NDs, and then the adsorbed coating was "crosslinked" either by polymerization or by stabilizing protein-protein interaction. Consequently, the ND was enclosed in cage. To avoid a few limitations above two coatings. The poly(L-DOPA) lost when being chemically modified. Moreover, the huge amount of aromatic groups quenched the fluorescence of NDs. The virus capsid can de-assemble under different ions strength and pH, it is concern the shell would remain stable in body fluids over longer time periods. Therefore the third approach called adsorption-crosslinking strategy was developed, it caged the NDs and endow the potential of the coating to NDs. In detail, Hyperbranched polyethyleneimine (PEI), a highly branched, cationic, aliphatic polymer with multiple primary/secondary amino groups, was selected to precoat the NDs where 4-armed polyethyleneglycol cross-linkers reacted with PEI to

form a stable and covalent nanogel shell. The nanodiamond-nanogel system has demonstrated the ability to provide good stability and photodynamic therapy after conjugation with ruthenium complexes. Moreover, it was combined with indocyanine green (ICG), and the ND-NG-ICG system to demonstrate the ability to report temperature in the photothermal therapeutic process at the intracellular level.

In summary, two special coatings inspired by nature were developed, i.e., poly(L-DOPA) by self-polymerization of L-DOPA inspired by mussel foot proteins and capsid protein from *Cowpea chlorotic mottle virus* (CCMV). In addition, a general coating strategy called adsorption-crosslinking was explored to surround the nanodiamond with a nanogel network. Potential applications in life science were proven, such as photothermal effects, intracellular tracking, photodynamic therapy, and intracellular temperature sensing. This new approach offers the potential to enhance our understanding of local parameters in cancer cells and tissue and it could be of benefit in cancer research, especially early stage diagnosis and treatment.

Zusammenfassung

Die Krebserkrankung ist eine der größten gesundheitlichen Herausforderungen und betrifft Entwicklungs- sowie Industrieländer. Um die Situation zu verbessern, ist es daher essenziell sensitive Detektoren zur frühen Diagnose sowie fortschrittlichere Methoden zur Überwachung und Behandlung von Patienten zu entwickeln. Nanodiamanten (NDs) sind ein einzigartiges Nanomaterial basierend auf Kohlenstoff, aufgrund ihrer hervorragenden optischen und magnetischen Eigenschaften sowie ihrer ausgezeichneten Biokompatibilität. Daher haben sie die Aufmerksamkeit vieler Wissenschaftler*innen auf sich gezogen. Die optisch-aktiven Fehlstellen im Gitter der NDs, wie z.B. das Stickstoff-Fehlstellen-Zentrum (englisch: Nitrogen Vacancy (NV) center), sorgen für eine stabile Fluoreszenz, die keinerlei Photoblinken noch Photobleichen zeigt. Dies führte dazu, dass NDs weithin in der biologischen Bildgebung und als Echtzeit-Reporter bei der Medikamentenverabreichung eingesetzt wurden. Zudem können NDs, die negativ geladene NV (NV^-) Zentren enthalten, als Single-Spin-Sensoren dienen, um wichtige physikalische Parameter in einer biologischen Mikroumgebung zu erkennen, wie z. B. Temperatur, Magnetfelder, Elektronenspins und mechanische Belastungen.

Für die meisten dieser Anwendungen werden stabile und funktionalisierte Nanodiamanten (NDs) benötigt. Da die kolloidale Stabilität von unbehandelten NDs in Lösung sehr schlecht ist, verstärkt sich die Aggregation von ND drastisch, wenn die Größe des Diamanten in den Nanometerbereich sinkt. Darüber hinaus verbessert die Oberflächenfunktionalisierung die Einheitlichkeit der Oberfläche, die oft der Ausgangspunkt für die weitere Funktionalisierung von anderen Motiven, wie Medikamentenmoleküle, Farbstoffe, Targeting-Gruppen oder Antikörper, ist. Eine einheitliche Partikeloberfläche erhöht die Anzahl der Bindungsstellen und die Reproduzierbarkeit. Darüber hinaus ist die Oberflächenbeschichtung für in vivo Anwendungen wichtig, um körpereigene Reaktionen gegenüber den Partikeln zu vermeiden und den Nanopartikeln zu helfen, sich anzureichern und über einen längeren Zeitraum an den Zielstellen zu verbleiben.

In dieser Arbeit werden zwei neue, von der Natur inspirierte Beschichtungsmaterialien

untersucht, um die Oberflächeneigenschaften von NDs zu optimieren. Das erste Beschichtungsmaterial ist Poly(L-DOPA), welches während der Selbstpolymerisation des Neurotransmitters L-3,4-Dihydroxyphenylalanin (L-DOPA) gebildet wird und seine Inspiration in dem "Proteinkleber" der Muschelfußproteine fand. Die Polymerisation von L-DOPA liefert ein hochvernetztes Polymer mit reaktiven, funktionalen Gruppen auf der Oberfläche, darunter Amine, Carbonsäuren, Alkohole und konjugierte Michael-Akzeptoren. L-DOPA polymerisiert auf NDs mit einer hohen Kontrolle über die Dicke der Beschichtung. Die anschließende Konjugation von Transferrin, die einen effizienten rezeptorspezifischen zellulären Transport ermöglicht, verbessert die kolloidale Stabilität und die zelluläre Aufnahme der Poly(L-DOPA)-beschichteten NDs. Die Beladung mit dem FDA-zugelassenen photothermischen Wirkstoff Indocyaningrün (ICG) ergibt ein integriertes biohybrides Nanomaterial, das einen verstärkten photothermischen Effekt in Zellen, bei sehr geringer Energieaufnahme ($\sim 90 \text{ mW/cm}^2$), aufweist.

Viren sind, durch die Evolution, optimierte Trägersysteme und wurden bereits zur Zellinvasion eingesetzt. Sie haben in den letzten Jahren großes Interesse als Instrumente zur Steigerung der Zellaufnahme erfahren. Das zweite Beschichtungsmaterial ist ein Kapsidprotein (englisch: capsid protein (CP)) aus dem *Cowpea chlorotic mottle virus* (CCMV). CPs wurde zunächst aus dem CCMV isoliert, das anschließend zur Herstellung von hochstabilen, mit Viruskapsidprotein verkapselten NDs (ND-CP) verwendet wird. Es entsteht eine dünne Proteinschicht, die die NDs umgibt und reaktive Gruppen besitzt, sowie den NDs eine hohe kolloidale Stabilität verleiht. Die Proteinschicht beeinträchtigt die physikalischen Eigenschaften der NDs nicht. ND-CP zeigt eine gute zelluläre Aufnahme und eine ausgezeichnete Biokompatibilität sowohl *in vitro* als auch *in vivo*. Darüber hinaus wird das langfristige intrazelluläre Trafficking der ND-CP untersucht, das der hohen Photostabilität zu verdanken ist. Die exzellenten optischen Eigenschaften werden ihnen ein großes Potential in Life Science ermöglichen. Bei der Untersuchung der beiden oben genannten Systeme haben wir festgestellt, dass zunächst die kleinen Moleküle oder Proteine an der Oberfläche der NDs adsorbiert

wurden und dann die adsorbierte Beschichtung entweder durch Polymerisation oder durch stabilisierende Protein-Protein-Wechselwirkung "vernetzt" wurde. Folglich waren die NDs in einer Hülle eingeschlossen. Es zeigten sich einige Limitationen: Das Poly(L-DOPA) ging bei der chemischen Modifikation verloren. Außerdem verringerte die große Menge an aromatischen Gruppen die Fluoreszenz der NDs. Das Viruskapsid kann sich bei verschiedenen Ionenstärken und pH-Werten disassemblieren und es ist zu befürchten, dass die Hülle in Körperflüssigkeiten über längere Zeiträume nicht stabil bleibt. Daher wurde der dritte Ansatz, die Adsorptions-Vernetzungs-Strategie entwickelt, die die NDs in einen Käfige einsperrt und den NDs das Potenzial der Beschichtung verleiht. Im Detail wurde hyperverzweigtes Polyethylenimin (PEI), ein hochverzweigtes, kationisches, aliphatisches Polymer mit mehreren primären/sekundären Aminogruppen, für die Vorbeschichtung der NDs ausgewählt, wobei 4-armige Polyethylenglykol-Vernetzer mit PEI reagierten, um eine stabile und kovalente Nanogel-Schale zu bilden. Das Nanodiamond-Nanogel-System hat gezeigt, dass es nach Konjugation mit Ruthenium-Komplexen eine gute Stabilität und photodynamische Therapie ermöglicht. Darüber hinaus wurde es mit Indocyaningrün (ICG) kombiniert, und das ND-NG-ICG-System demonstrierte die Fähigkeit, die Temperatur im photothermischen therapeutischen Prozess auf intrazellulärer Ebene zu messen.

Zusammenfassend wurden zwei spezielle, von der Natur inspirierte Beschichtungen entwickelt, Poly(L-DOPA), durch Selbstpolymerisation von L-DOPA und inspiriert von Muschelfußproteinen und das Kapsidprotein aus dem *Cowpea chlorotic mottle virus* (CCMV). Außerdem wurde eine Beschichtungsstrategie mit dem Namen Adsorptions-Vernetzung erforscht, um die Nanodiamanten mit einem Nanogel-Netzwerk zu umhüllen. Potenzielle Anwendungen in den Biowissenschaften wurden nachgewiesen, wie z. B. ein photothermischer Effekt, intrazelluläres Tracking, photodynamische Therapie und intrazelluläre Temperaturmessung. Dieser neue Ansatz bietet das Potenzial, unser Verständnis lokaler Parameter in Krebszellen und -gewebe zu verbessern und könnte in der Krebsforschung, insbesondere in frühen Stadien der

Diagnose und Behandlung, von Nutzen sein.

Contents

1. Introduction	1
1.1 Background	1
1.2 Properties of nanodiamonds	3
1.2.1 Fundamental properties	3
1.3 Preparation of nanodiamonds	11
1.3.1 “Bottom-up” detonation method	11
1.3.2 “Top-down” HPHT method	13
1.3.3 Laser ablation method	16
1.4 Biological applications of nanodiamonds	19
1.4.1 Drug delivery	23
1.4.2 Imaging	25
1.4.3 Nanoscale sensing	33
1.5 Functionalization of nanodiamonds	40
1.5.1 Non-covalent modification	40
1.5.2 Covalent modification	43
1.5.3 Other approaches	48
1.6 References	52
2. Motivation and conceptual design	59
3. Transferrin-Coated Nanodiamond–Drug Conjugates for Milliwatt Photothermal Applications	63
3.1 Introduction	65
3.2 Results and Discussion	67
3.3 Conclusion	75
3.4 Acknowledgements	76
3.5 Supporting information	77
3.6 References	88
4. Highly Stable Fluorescent Nanodiamond Encapsulated by Virus Capsid Protein for Intracellular 3D-Trajectory Analysis	91
4.1 Introduction	93
4.2 Results and Discussion	94
4.3 conclusion	105
4.4 Acknowledgements	106
4.5 Supporting information	106

4.6 References	114
5. Fluorescent Nanodiamond–Nanogels for Nanoscale Sensing and Photodynamic Applications	117
5.1 Introduction	120
5.2 Results and Discussion	122
5.3 Conclusion	132
5.4 Acknowledgements	133
5.5 Supporting information	133
5.6 References	149
6. A Nanodiamond-Based Theranostic Agent for Light-Controlled Intracellular Heating and Nanoscale Temperature Sensing	153
6.1 Introduction	156
6.2 Results and Discussion	158
6.3 Conclusion	167
6.4 Acknowledgements	168
6.5 Supporting information	168
6.6 References	178
7. Summary and Outlook	181
Acknowledgement	193
Appendix	194

1. Introduction

1.1 Background

According to World Cancer Report of World Health Organization (WHO), cancer is one of the major disease causes of morbidity and mortality in the world. The incidence of various new cancer cases are still on the rise and expected to increase by at least 60% in the next 20 years.¹ The cases for cancer in Europe are the same as in all other parts of the world. The latest report on cancer in the 40 European countries estimates 3.91 million new cases (excluding non-melanoma skin cancer) and 1.93 million deaths in 2018.² Despite the extraordinary advances in the diagnosis and treatment of cancer, saving the lives of cancer patients is currently still a great challenge. The main challenges are diagnosis in the early stages and more effective treatments. Common magnetic resonance imaging (MRI) contrast agents used for cancer diagnosis have high toxicity and are hardly excreted from the body.^{3, 4} Many conventional anticancer drugs are water-insoluble, unable to differentiate between diseased and healthy cells, and are hardly able to reach their target sites.^{5, 6} There is an urgent need to develop novel materials with diagnosis and treatment capabilities. Nanomaterials could be potential candidate due to their unique properties that stem from their small sizes.

Nanotechnology, defined by National Nanotechnology Initiative (NNI) as “the manipulation of matter with at least one dimension sized at the nanoscale, which is about 1 to 100 nanometers,” has developed in a broad field of science and engineering including chemistry, physics, biology, materials science, and many other interdisciplinary fields. Many nanomaterials have been created, such as Au nanoparticles, Fe₃O₄ nanoparticles, CdS nanoparticles, SiO₂ nanoparticles, polymeric nanoparticle, and carbon nanomaterials, and used in physics⁷⁻⁹, optics¹⁰⁻¹², electronics¹³⁻¹⁵, and life science¹⁶⁻¹⁸ due to their unique properties. In the field of biomedicine, especially in cancer diagnosis and treatment, nanoparticles have higher loading capacity of diagnostic and therapeutic agents than the traditional small molecular agents. They are able to bypass biological clearance through the mononuclear phagocytic system (MPS), formerly known as the reticuloendothelial system (RES)^{19, 20}, and

improve concentration of the agents at the target sites by enhanced permeability and retention (EPR) effect²¹. This results in enhanced diagnostic and therapeutic efficacy. However, there are still major challenges that need to be solved for the design of safe, non-toxic, highly sensitive and multifunctional nanoparticle systems with providing a therapeutic effect in combination with detecting ability.

Among nanomaterials, carbon-based nanomaterials, including fullerenes, nanodiamonds (NDs), carbon dots, carbon nanotubes, graphene, and its derivatives, have attracted great interest in bioapplications due to their unique structural dimensions, and outstanding mechanical, thermal, electrical, optical, and chemical properties (Figure 1.1).²² Compared to the other three allotropes, Nanodiamond (ND) is unique in that its constituent carbon atoms are all present in sp^3 electron configuration resulting in NDs being chemically inert, potentially less toxic, and biocompatible. In addition, many structural lattice defects, such as nitrogen-vacancy (NV) center, can be introduced into NDs, which provide many distinctive properties, such as highly stable fluorescence and sensitivity even towards tiny magnetic fields at ambient conditions. These properties make these ND-NVs a potential candidate particularly in bioimaging and nanoscale sensing.

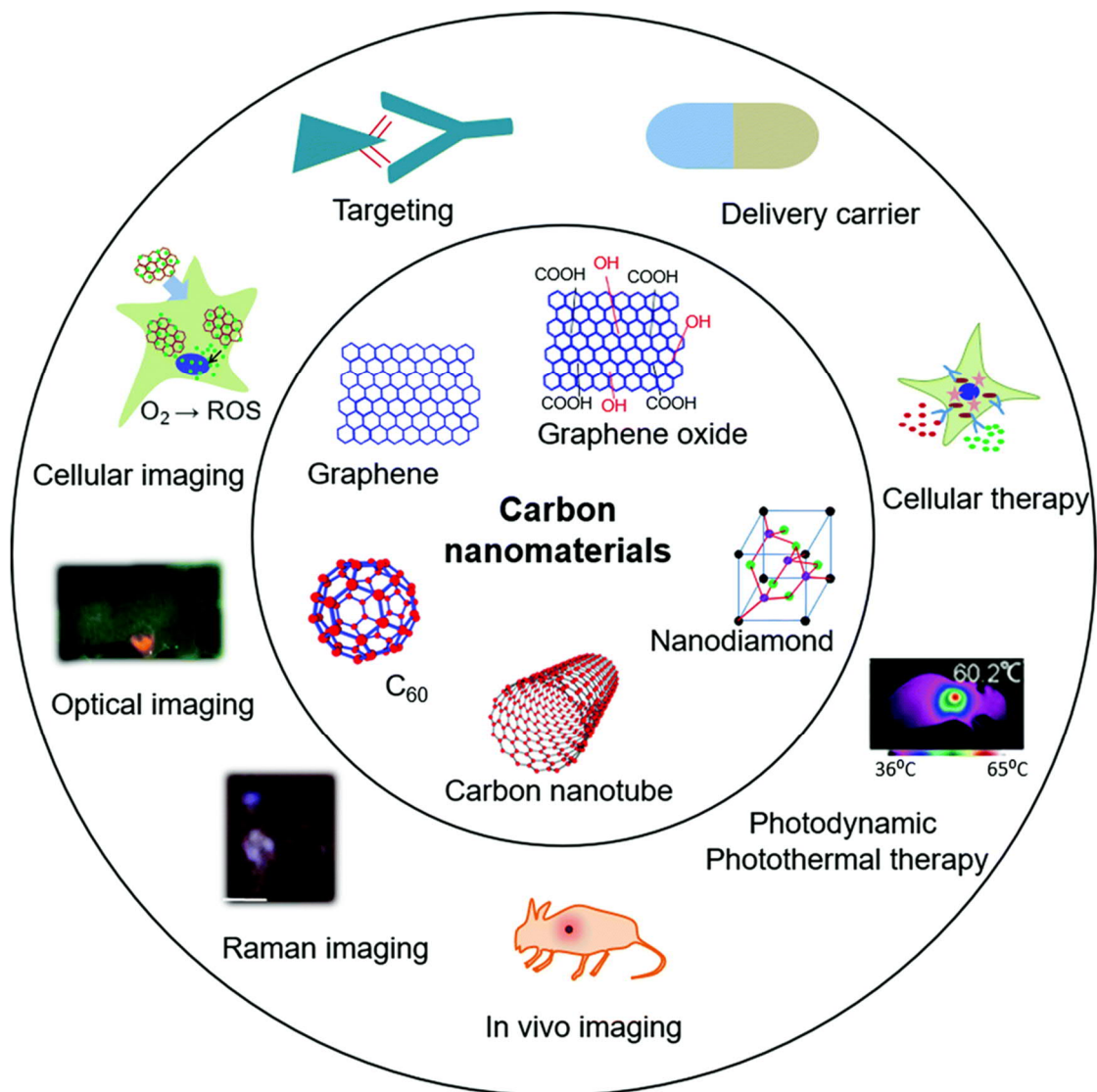


Figure 1.1 Carbon-based nanomaterials and their diverse bioapplications.²²

1.2 Properties of nanodiamonds

1.2.1 Fundamental properties

Nanodiamond (ND) still has the physical properties of diamond if the influence of ND surface does not taken account, which is given by the same molecular structure, i.e., its symmetrical in all three dimensions (3D) crystal structure, known as the diamond cubic lattice, which is also found in silicon, geranium, and some others. Figure 1.2 shows a typical unit cell of the diamond's face-centered cubic Bravais lattice, where each carbon atom is represented by a sphere in a 3D matrix that can be repeated infinitely to fill the entire space. The typical properties of diamond are list in Table 1.1

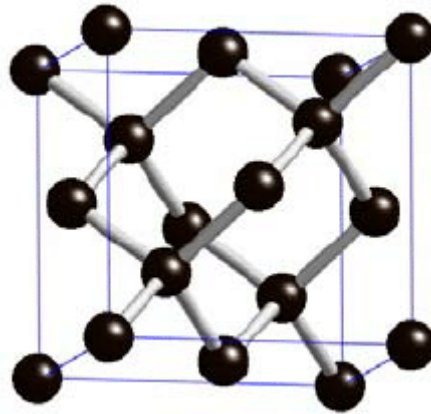


Figure 1.2 Unit cell of the diamond's cubic crystal structure with a lattice constant of 3.57 Å. Carbon atoms are presented in black spheres, adapted with permission from Vermeeren, Veronique, et al.²³ with copyright 2009 Multidisciplinary Digital Publishing Institute.

Table 1.1 Typical physical properties of diamond, adapted with permission from Chang, Huan-Cheng, et al.²⁴ with copyright 2018 WILEY-VCH Verlag GmbH & Co. KGaA, Weinheim.

Property	Value	Unit
Hardness	10 000	kg mm ⁻²
Strength, tensile	>1.2	GPa
Strength, compressive	>110	GPa
Density	3.52	g cm ⁻³
Young's modulus	1220	GPa
Thermal expansion coefficient	0.0000011	K ⁻¹
Thermal conductivity	20.0	W cm ⁻¹ K ⁻¹
Debye temperature	2200	K
Optical index of refraction (at 591 nm)	2.41	Dimensionless
Bandgap	5.45	eV

A pure and structurally perfect diamond is colorless and transparent, like a droplet of

pure water, with its transmittance ranging from 225 to 2000 nm.²⁵ Colors are caused by the presence of chemical impurities and/or structural defects in the diamond lattice. The chemical impurities and/or structural defects are extremely attractive to scientists due to their exciting physical properties, which are suitable for applications in electronics, optics, and biomedicine. Nitrogen atoms (N) and vacancy centers (V) are the most common impurities and structural defects in the crystal lattice of diamond. Figure 1.3 shows the typical structure of vacancy-related color centers. Vacancies in diamond are static at room temperature after being produced by irradiation damage, and start to migrate when heated above 500 °C. Some of them are annihilated at the surface; the majority of them can form stable nitrogen-vacancy (NV) centers with nitrogen atoms.

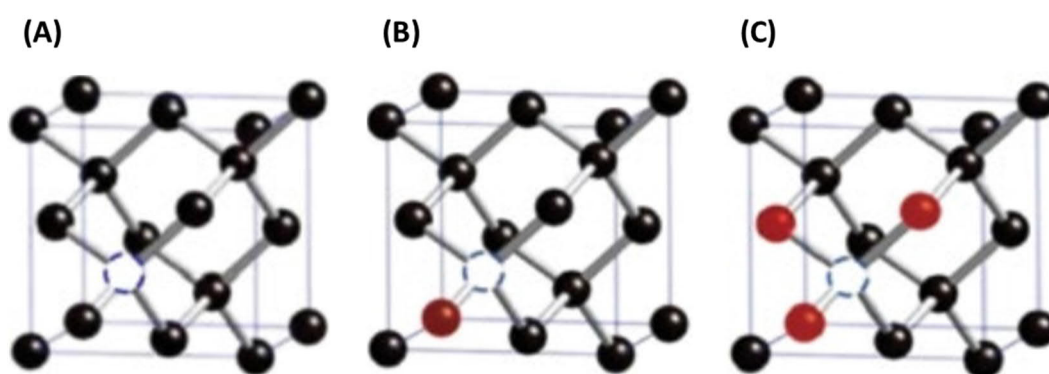


Figure 1.3 Structures of vacancy-related color centers in diamond: (A) V⁰, (B) NV, (C) N₃. The carbon atoms, nitrogen atoms, and vacancies are denoted by black spheres, dark red spheres, and blue dashed circles, respectively, adapted with permission from Hui, Yuen Yung, et al.²⁶ with copyright 2014 WILEY-VCH Verlag GmbH & Co. KGaA, Weinheim.

The NV center is a atom defect comprising of a nitrogen atom adjacent to a vacancy.²⁷ A nitrogen atom has five valence electrons, three of them are covalently bonded to the carbon atoms and two of them remain non-bonded and are referred to as lone pair. The vacancy has three unpaired electrons, two of which make a quasi-covalent bond and one of which remains unpaired, and is presented in a C_{3v} point group symmetry (Figure

1.3B).²⁶ The NV center has two charge states, neutral NV^0 and negative NV^- . The neutral form NV^0 contains five electrons, spin quantum number $S = 1/2$, and is paramagnetic. It can obtain an electron from the lattice and transform into NV^- by changing the Fermi level position. In the negatively charged NV^- , an extra electron is positioned at the vacancy site and form a spin $S = 1$ pair with the one electron in the vacancy. The neutral form NV^0 has a sharp zero-phonon line (ZPL) at 575 nm (or 2.156 eV)²⁸ that is distinctively different from the ZPL at 637 nm (or 1.945 eV) of the negative form NV^- .²⁹ The corresponding emission spectra are shown in Figure 1.4, the associated lifetimes of NV^0 and NV^- are 11.6 ns³⁰ and 19 ns,³¹ respectively. Compared to NV^- , NV^0 is significantly lower in concentration due to the transfer of electrons from N^0 to NV^0 during annealing.³²

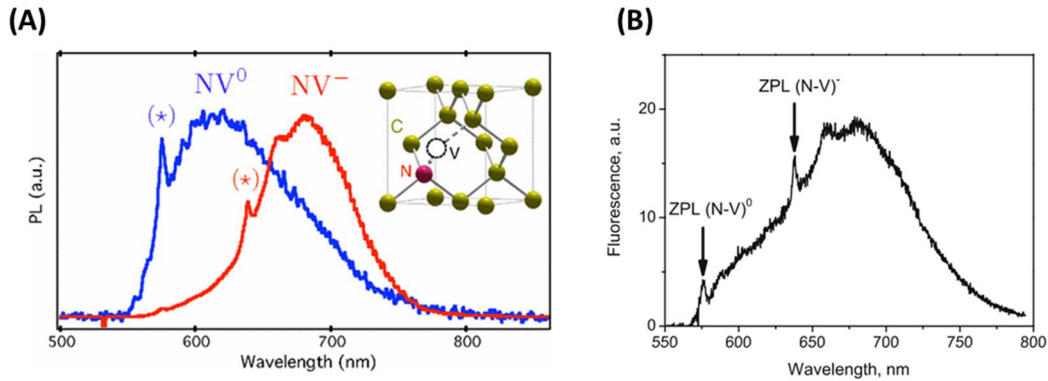
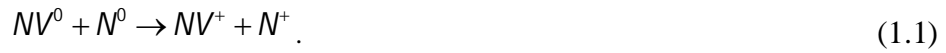


Figure 1.4 (A) PL spectra of single NV^0 (blue) and NV^- (red) color centers in NDs, the zero-phonon line (\star symbols) of NV^0 and NV^- emission are located at 575 nm and 637 nm, respectively, adapted with permission from Rondin, L. et al.³³ with 2010 copyright American Physical Society. (B) Fluorescence spectra of a single fluorescence spot from the confocal image; it shows two ZPLs due to the presence of NV^0 and NV^- , adapted with permission from Gaebel, T. et al.³⁴ with copyright 2006 Springer Nature Publishing Group.

Electromagnetic radiation can induce the charge transfer reaction between NV^0 and

NV^- . It is known as photochromism, which terms a reversible transformation of a chemical species between two forms after absorbing the electromagnetic radiation, where the NV^0 and NV^- have different absorption spectra.³⁵ For the NV centers, the relative ratio of the two different forms, NV^0 and NV^- , can be changed by a shift of the Fermi level using neutron irradiation³⁶ or laser illumination³⁷.

Figure 1.5 presents a schematic representation of the photoinduced ionization and recombination of NV^- and NV^0 . The photoionization of the NV^- occurs in two steps, which involve a two-photon absorption ruled by an Auger process. Simultaneously absorbing two photons promotes one electron in the band gap to the conduction band by the e level in the gap exciting an electron to the e orbital; a continuous excitation can occur promoting an electron from the conduction band into the vacated a_1 orbital in the band gap. NV^- recovering divides into two steps: firstly, an electron is excited from the a_1 to the e orbital and then, an additional electron is transferred from the a_1 orbital in the valance band to the vacant place on the a_1 orbital in the band gap. The left hole moves away from the NV center and keep it in the negative charge state. The position of the defect levels changes with different occupation of states shown schematically for both processes. At the steady state, the NV^- content is close to 75% under continuous laser excitation in the 450–610 nm wavelength range.³⁸ Recently, it was reported that the ratio of NV^- to NV^0 can be controlled by electric field, laser, and surface modification.^{33, 39, 40}

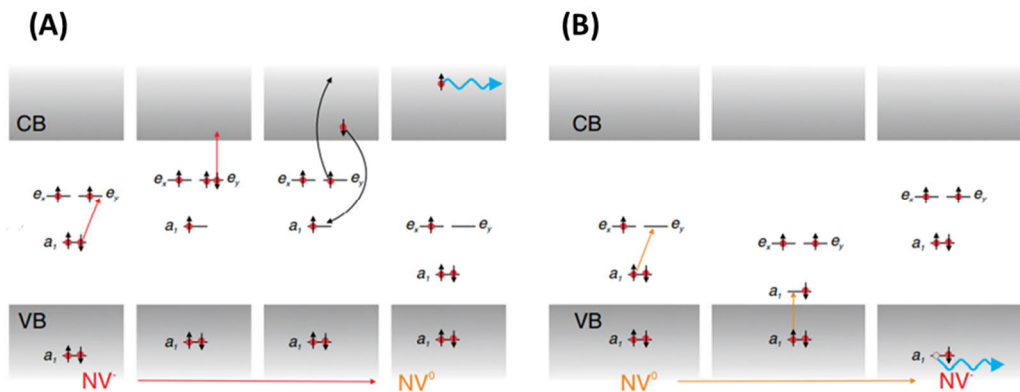


Figure 1.5 Schematic representation of the charge conversion process for negative and

neutral states of the NV defect (A) NV^- to NV^0 conversion, (B) NV^- recovering, adapted with permission from Siyushev, P., et al.⁴¹ with copyright 2013 American Physical Society.

A simple energy-level diagram of the NV^- center is shown in Figure 1.6, it owns a three electronic levels structure, comprising a ground state $|g\rangle$ of 3A_2 symmetry, an excited state $|e\rangle$ of 3E symmetry, and a metastable singlet state $|s\rangle$ containing two levels with symmetries 1A and 1E . The main ground state and excited state transition has a resonant wavelength of 637 nm (638 nm) (zero phonon line, 1.945 eV) and it can be efficiently excited by most of laser with wavelengths below 640 nm. Most emission appears in its side bands between 630 and 800 nm due to vibration (Figure 1.4B), and only a small number of photons are emitted into the zero phonon line.

The ground and excited states are spin triplet, and they further split into three spin sublevels, $m_s = 0$ and ± 1 , where the two $m_s = \pm 1$ states are degenerated and have higher energy than $m_s = 0$ state. In the ground state, the energy gap between $m_s = 0$ and ± 1 is $D = 2.87$ GHz, and the energy gap is $D = 1.42$ GHz in the excited state, where D is called zero-field splitting⁴². The magnetic fields can split degeneracy between $m_s = 0$ and ± 1 , resulting in the $m_s = \pm 1$ levels to split in opposite directions (Figure 1.6B). It is the fundamental mechanism for all of the magnetic sensing applications. Optical transitions are strongly spin preserving e.g. the spin state does not change when cycling between ground state and excited state; the electronic transition can be described as ${}^3A_2 \rightarrow {}^3E$; the photoluminescence of the transition has a lifetime of 11.6 ns with a quantum yield close to 1,⁴³ and the fluorescence is exceptionally stable in an inert and highly thermally conductive matrix, which allows facile detection of individual NV^- center by fluorescence imaging.

The magneto-optical properties allows the use of optically detected magnetic resonance (ODMR) technology⁴⁴, which provides a method to study interactions of the single electron spin at room temperature. The simplest experiment is to record the emission spectrum of the NV^- center by slowly sweeping an auxiliary microwave field. When

the microwave frequency (2.87GHz) is resonant with the transitions between spin sublevels, excitation occurs from $m_s = 0$ to $m_s = \pm 1$ and results in a decrease of fluorescence intensity of about 30% after several cycles of excitation as populations in the $m_s = \pm 1$ sublevels of the excited state return to the ground state by non-radiative decay. In detail, the intersystem crossing (ISC) from the excited triplet state $|e\rangle$ to the metastable singlet state $|s\rangle$ possibly occurs as a function of the excited state sublevel. It was found that the ISC rate from the $m_s = \pm 1$ sublevel of the excited state to the excited singlet state 1E of the metastable state is significantly higher than that from the $m_s = 0$ sublevel due to nonradiative energy transfer processes. The excited singlet state 1E makes a transition to the ground singlet state 1A , which emits infrared wavelength of 1042 nm (1.190 eV). Then the 1A singlet state non-radiatively decays to the $m_s = 0$ sublevel in the ground state. As a consequence, the optically pumping will preferentially occupy the NV^- center in the $m_s = 0$ sublevel in the ground state, which is known as optically induced spin polarization. In other words, the spin information at the ground states can be readout optically.

As shown in Figure 1.6A and B, a magnetic field is applied, two resonance peaks appear in the ODMR spectrum due to the $m_s = \pm 1$ levels is split. The frequency separation between the two resonances is given by $2\gamma B$, where $\gamma = 2\pi \times 28$ GHz/T is the electron gyromagnetic ratio and B is the magnetic field parallel to the NV axis. Thus, the ODMR frequency measurements can immediately report the absolute value of the magnetic field. Furthermore, applications of the technique to several other physical quantities have also been proposed or demonstrated, including magnetic moments (electron spins, nuclear spins)⁴⁵⁻⁴⁷, electric fields^{48, 49}, orientation^{50, 51}, temperature⁵²⁻⁵⁴, pressure⁵⁵, and more physical quantities can be envisioned.

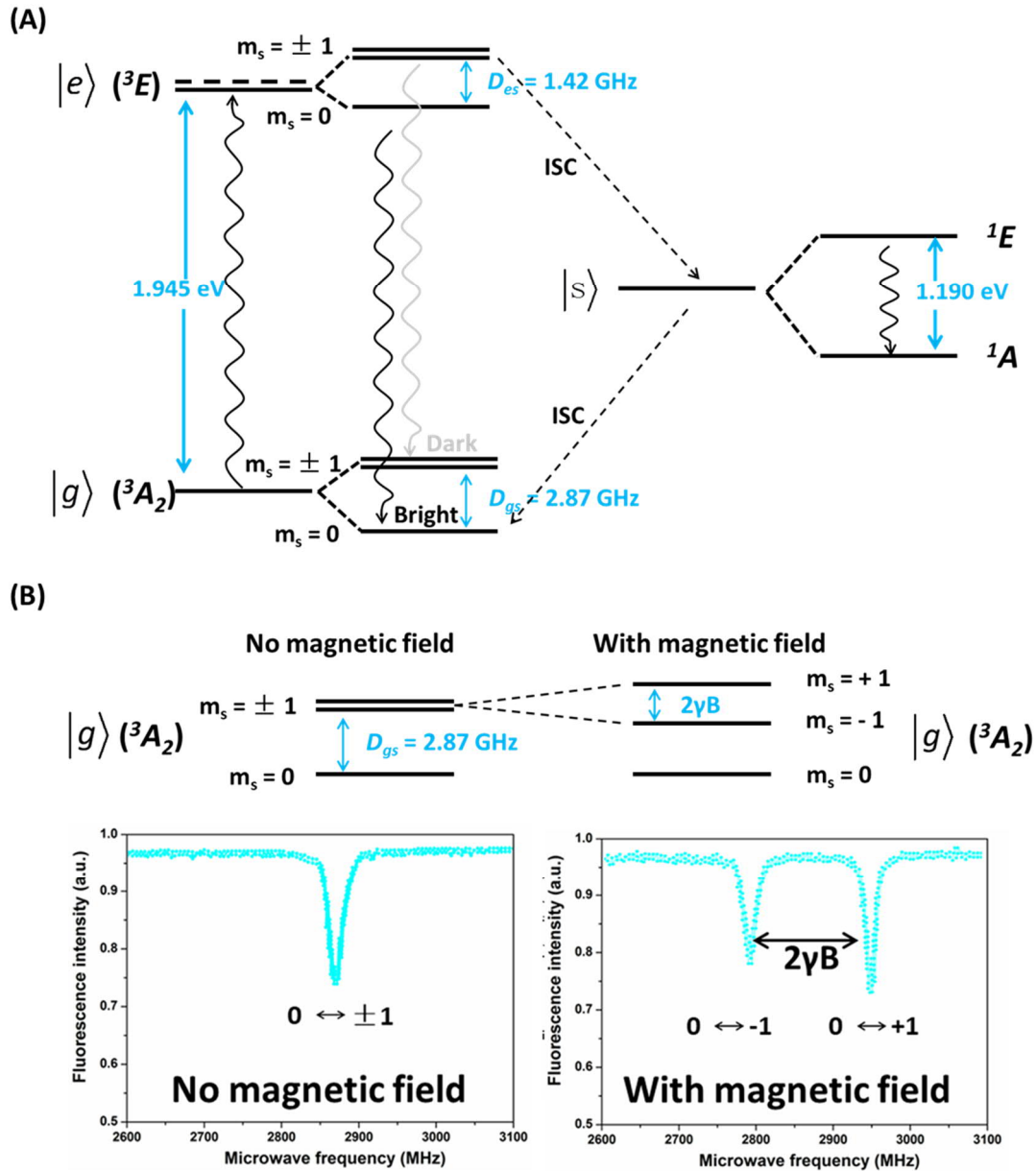


Figure 1.6 (A) Simple energy-level diagram of the NV^- center, $|g\rangle$ (3A_2) denotes the electronic ground state of 3A_2 symmetry, $|e\rangle$ (3E) denotes the excited state of 3E symmetry, $|s\rangle$ denotes metastable singlet state with an electronic ground state of 1A symmetry and an electronic excited state of 1E symmetry. Black wiggly arrows indicate the strong radiative transition, gray wiggly arrows indicate the weak radiative transition, and black dash arrows indicate the strong weak nonradiative decay via the singlet state. (B) Optically detected magnetic resonance (ODMR) spectrum of a single NV^- at zero and non-zero magnetic field. The three spin sublevels with $m_s = 0$ and $m_s = \pm 1$ at zero and non-zero magnetic field B . D is the zero-field splitting and $2\gamma B$ is the Zeeman

splitting, where γ is the electron gyromagnetic ratio. By convention, the lower energy transition is associated with $m_s = -1$.

1.3 Preparation of nanodiamonds

Over the past decades, many different strategies for the preparation of nanodiamonds (NDs) have been developed and categorized such as detonation technique⁵⁶, plasma-enhanced chemical vapor deposition (PECVD)⁵⁷, ultrasound cavitation⁵⁸, high-pressure high-temperature (HPHT) synthesis⁵⁹, chlorination of carbides⁶⁰, cold-compression synthesis⁶¹, electron irradiation of carbon ‘onions’⁶², ion irradiation of graphite⁶³, femtosecond laser irradiation of ethanol⁶⁴, and laser ablation⁶⁵. Among these diverse preparation techniques, commercial production of NDs usually relies on the “bottom-up” detonation method and “top-down” HPHT method as it is at the moment easier to get large scale products with them. In addition, compared with the other new methods, the laser ablation may be a potentially-scalable and cost-effective approach in the foreseeable future. The three methods to produce commercially available NDs are illustrated individually in the following.

1.3.1 “Bottom-up” detonation method

Detonation process is the most common method for large-scale production of NDs.⁶⁶
⁶⁷ Detonation nanodiamonds (DNDs) prepared during detonation of a mixture of explosives, e.g. trinitrotoluene (TNT) and hexogen (RDX) in a sealed metal chamber where supersaturated carbon vapor from the explosives condenses into liquid droplets, and then crystallize to form 3–5 nm nanodiamond particles as temperature and pressure drop (Figure 1.7). The obtained diamonds collected from the wall and the bottom of the chamber are diamond soot containing approximately 75 wt% NDs and 25 wt% other carbon allotropes or impurities, resulting in an effective size of 50–500 nm. Transmission electron microscopy (TEM) reveals the structure DNDs agglomeration, as shown in Figure 1.7D. For most applications, it is necessary to isolate and obtain graphite-free NDs, since the graphite layers greatly weaken sensitivity. Post-processing, deagglomeration and purification, are usually performed to break the covalent bond

between the disordered (sp and sp^2) carbon atoms on the surfaces of NDs. An established method⁶⁸ is wet ball milling with ZrO_2 microbeads and the resulting DND particles have a fairly discrete size distribution with a mean diameter of 3–5 nm. The detonation technique offers a carbon yield of 4–10% of the explosive weight, depending on the cooling media⁶⁹, and they are available in kilogram quantities in different forms such as colloidal sols, gels, and assemblies, and are suitable for different types of applications.

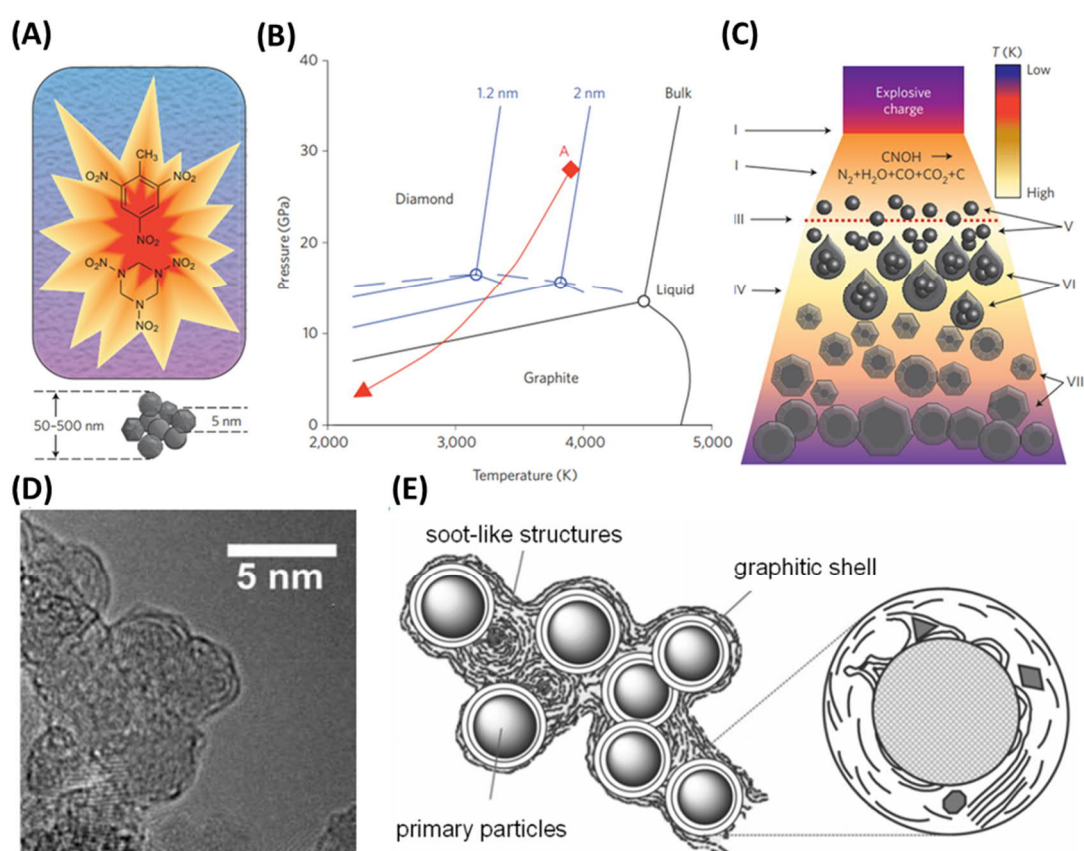


Figure 1.7 (A) Detonation of the explosive material (TNT mixed with hexogen). (B) Phase diagram showing the two best stable states of carbon (i.e., graphite (at low pressure) and diamond (at high pressure)). (C) Schematic representation of detonation wave propagation: (I) production of shock waves due to explosion, (II) decomposition of explosive material, (III) rise in pressure and temperature in the chamber up to the Chapman-Jouguet point, (IV) detonation products in an expanding state, (V) formation

of carbon nanoclusters, (VI) formation of liquid nanodroplets from the coagulation of carbon nanoclusters, (VII) crystal growth and agglomeration of NDs, (A), (B) and (C) are adapted with permission from Mochalin, Vadym N., et al.⁷⁰ with copyright 2011 Springer Nature Publishing Group. (D) TEM image of DNDs, the particles are surrounded by graphitic and soot-like materials. (E) Structure model of the DND agglomerates are adapted with permission from Krueger, A., et al.⁷¹ with copyright 2007 WILEY-VCH Verlag GmbH & Co. KGaA, Weinheim.

1.3.2 “Top-down” HPHT method

High-pressure high-temperature (HPHT) method is the most commonly used method to prepare stable and bright fluorescent NDs. HPHT NDs are obtained by crushing microdiamonds produced by static synthesis, which are formed under high pressure (7–11 GPa) and high temperature (1500–2200 °C) in a hydraulic press in the presence of metal catalysts (Fe, Ni, or/and Co). In more detail, in the HPHT reactor, first N₂ is dissolved in the solvent metal and then introduced into the diamond during subsequent crystal growth. In the formed diamond lattice, the N atoms remain isolated and are bound to four other C atoms for thermokinetics reasons. To obtain the NV centers, the HPHT micron- diamonds are irradiated with high-energy particles (photons, neutrons, electrons, or ions), which remove C atoms from their normal lattice positions by collision and create vacancies (V) in the diamond lattice⁷². Then, they are typically annealed at 800 °C under vacuum, causing the migration of vacancies toward N atoms and the formation of NV centers⁷³. After that, the micro-diamonds containing NV centers are crushed using jet milling and bead milling, and fractionated by ultracentrifugation in a series of sizes. For HPHT NDs, colloidal suspensions with the smallest average particle size around 10–20 nm are commercially available now from Adámas Nanotechnologies. The typical process of preparation of fluorescent NDs by HPHT method is illustrated in Figure 1.8. Compared to the detonation method, the diamond crystals formed by HPHT method owns high quality and do not have non-diamond carbon structures such as diamond-like carbon, graphite, and amorphous

carbon).⁷⁴ A major drawback of HPHT method to produce fluorescent NDs is that the nitrogen atoms are distributed heterogeneously; incorporation of nitrogen into the crystal depends on the crystallographic orientation of the growth surface, where (100) diamond facets are nitrogen-depletion. Furthermore, the nitrogen concentration in the diamond crystals declines with increasing radius of the diamond crystal owing to the nitrogen depletes over time in the metallic catalyst melt. As a consequence, the HPHT NDs exhibit a heterogeneous nitrogen spatial distribution in each ND, which results in non-uniform photoluminescence.⁷⁵

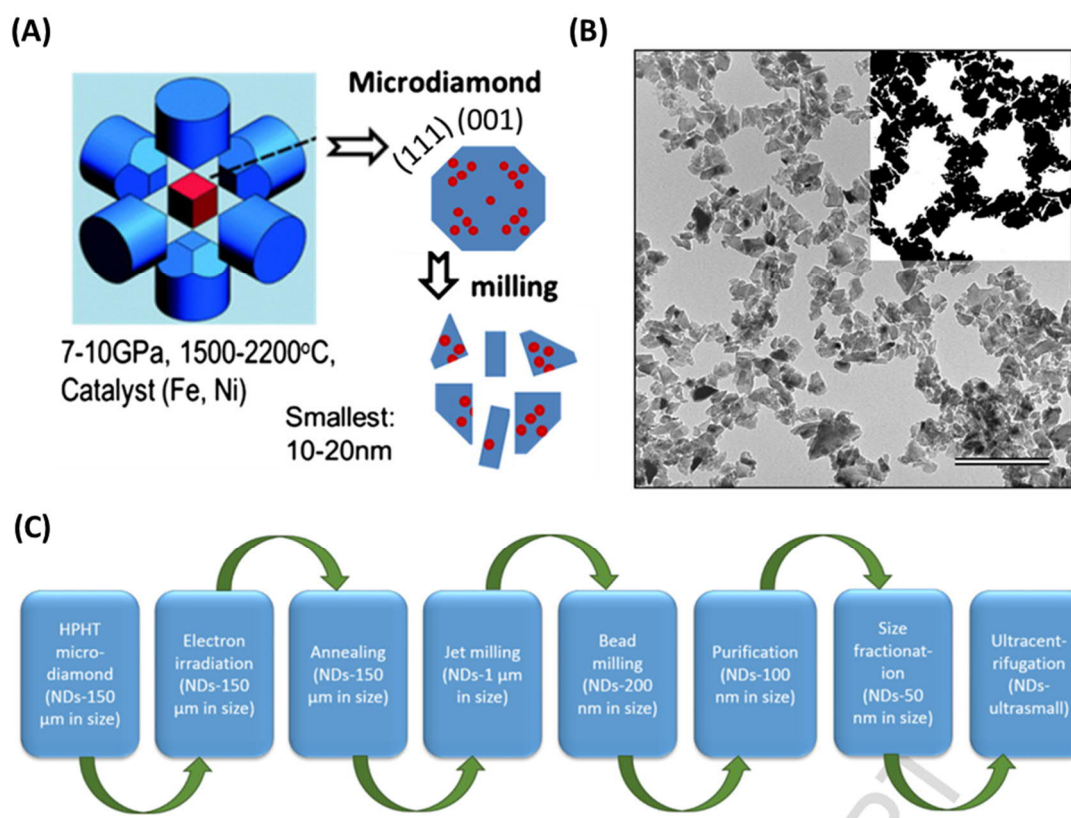


Figure 1.8 (A) Schematic representation of the production of HPHT NDs by grinding microdiamond powders produced by the HPHT method, adapted with permission from Kumar, S., et al.⁷⁴ with copyright 2018 Elsevier Ltd. (B) TEM image of HPHT NDs (scale bar = 200 nm), adapted with permission from Rehor, Ivan, et al.⁷⁶ with copyright 2014 Elsevier Ltd. (C) Typical process of preparation of HPHT NDs from microdiamonds, adapted with permission from Nunn, N., et al.⁷⁷ with copyright 2017 Elsevier

Ltd.

To overcome the challenge of the traditional HPHT method, nowadays a bottom-up variant of HPHT has been developed to synthesize fluorescent NDs with controlled nitrogen (and other dopants) content from nontraditional carbon precursors⁷⁸⁻⁸¹. However, it is still at an exploratory stage. The possibility of nanodiamond synthesis was demonstrated using its molecular analog, adamantane, with a carbon backbone of the molecule that mimics the structure of the diamond lattice. The chemical structure of adamantane makes it ideal for the synthesis of NDs, where it is expected that the existing “building blocks” can participate in the formation of the diamond lattice. The ability to easily “seat” a dopant atom on the molecule, potentially expands the possibilities for the synthesis of doped NDs. A recent report is shown in Figure 1.9. In this work⁸², the authors report on the use of diamondoids (diamond-like, saturated hydrocarbons) as precursors for laser-induced HPHT synthesis. The lowest pressure and temperature (P-T) conditions they used to produce diamond were 12 GPa (at ~2000 K) and 900 K (at ~20 GPa). NDs are produced at thermodynamically stable conditions that are the most favorable for obtaining perfect diamond structures without metal impurities, it is usually existed in traditional HPHT synthesis where metallic media are used.

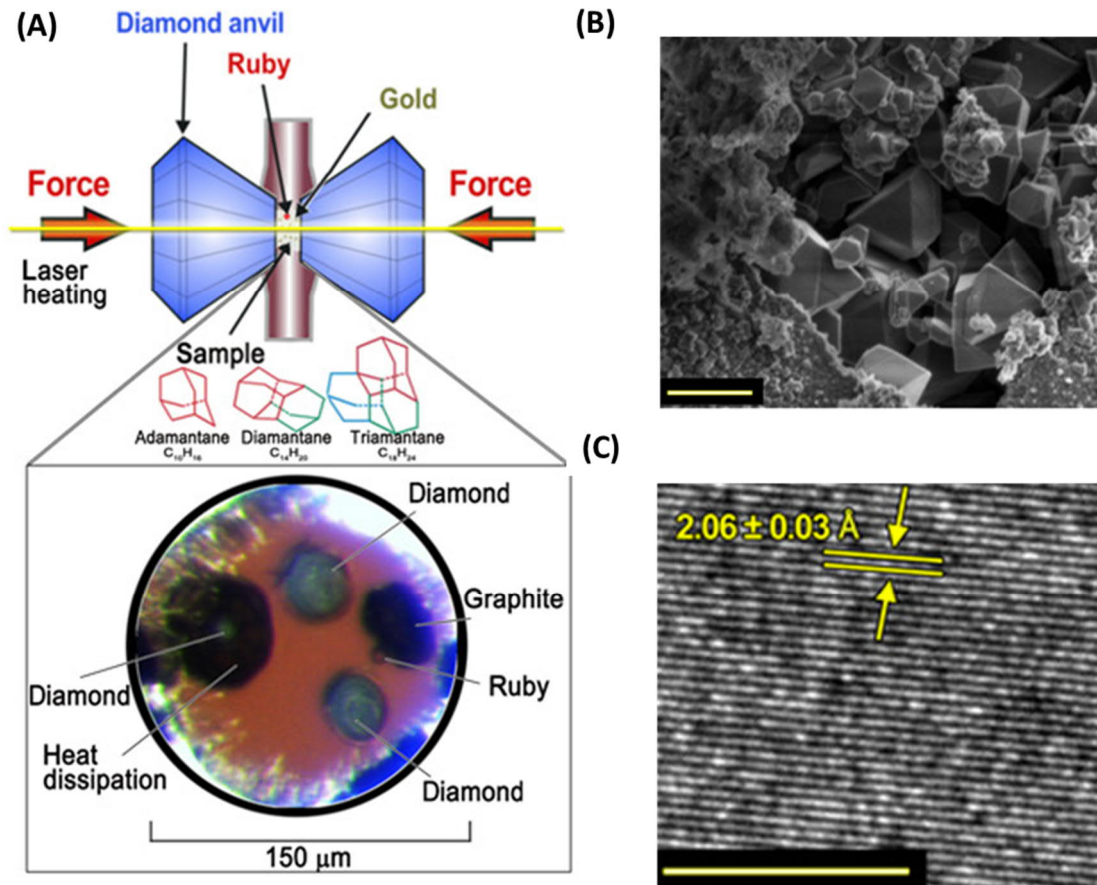


Figure 1.9 (A) Top: Schematic illustration of laser-heated DAC and sample. Bottom: Transmitted light optical image of a sample (inside a DAC) after laser heating. (B) Scanning electron microscope (SEM) image of diamond formed from triamantane at 20 GPa and ~2000 K. Well-formed diamond grains are embedded in smaller crystalline diamond grains. Scale bars, 1 μm . (C) HRTEM image showing the d-spacing of diamond (111) plane corresponding to $2.06 \pm 0.03 \text{ \AA}$. Scale bar, 5 nm, (A), (B), and (C) are adapted with permission from Park, S., et al.⁸² with copyright 2020 American Association for the Advancement of Science.

1.3.3 Laser ablation method

The laser ablation method for NDs production is controllable, environmentally friendly and non-hazardous. The pulsed laser ablation in liquids (PLAL) method includes laser ablation onto a target (a small piece of material or a pressed powder) immersed in a liquid medium (water, ethanol, ether, acetone, and mixtures of them). A high-intensity

laser beam is projected onto the surface of a target material that is in a liquid medium, resulting in ejection and evaporation of the target material in the form of an ablation plume. The atoms of the target material and liquid medium interact under the high pressure and high temperature condition, consequently forming NDs in suspension (Figure 1.10). The PLAL method combines the advantages of standard pulse laser deposition and soft chemical routes, such as the possibility to control the size, morphology, and shape of the obtained NDs by tuning the parameters of the laser radiation, liquid, and the target. In this method, NDs are produced in the formation of stable colloidal suspensions⁸³. These advantages have facilitated it to become one of the most attractive methods to study the purely physical growth of NDs in liquid-solid interface⁸⁴, liquids⁸⁵, or solids using carbon powder⁸⁶. A detailed analysis of nanodiamond nucleation and growth in liquid medium using laser ablation was reported⁸⁷. The synthesis of nanodiamond takes place in following steps (Figure 1.10D): (I) Formation of plasma plume of carbon atoms with 15 GPa peak pressure and 5000 K peak temperature. (II) Steady nucleation of carbon clusters due to condensation of plasma as temperature and pressure fall down from the peak values. This nucleation process lasts until reach the critical nucleation size of diamond. (III) As the steady nucleation, diamond nuclei are formed followed by the synthesis of diamond crystals. Later, the growth of nanodiamond stops due to a further decline of temperature and pressure. After growth of the diamond crystals, the formation of individual nanocrystals and twin structures (Figure 1.10C). The synthesis of nanodiamonds by this method was previously considered e economically impractical⁸⁸ but is now available on the market (Ray Techniques Ltd).

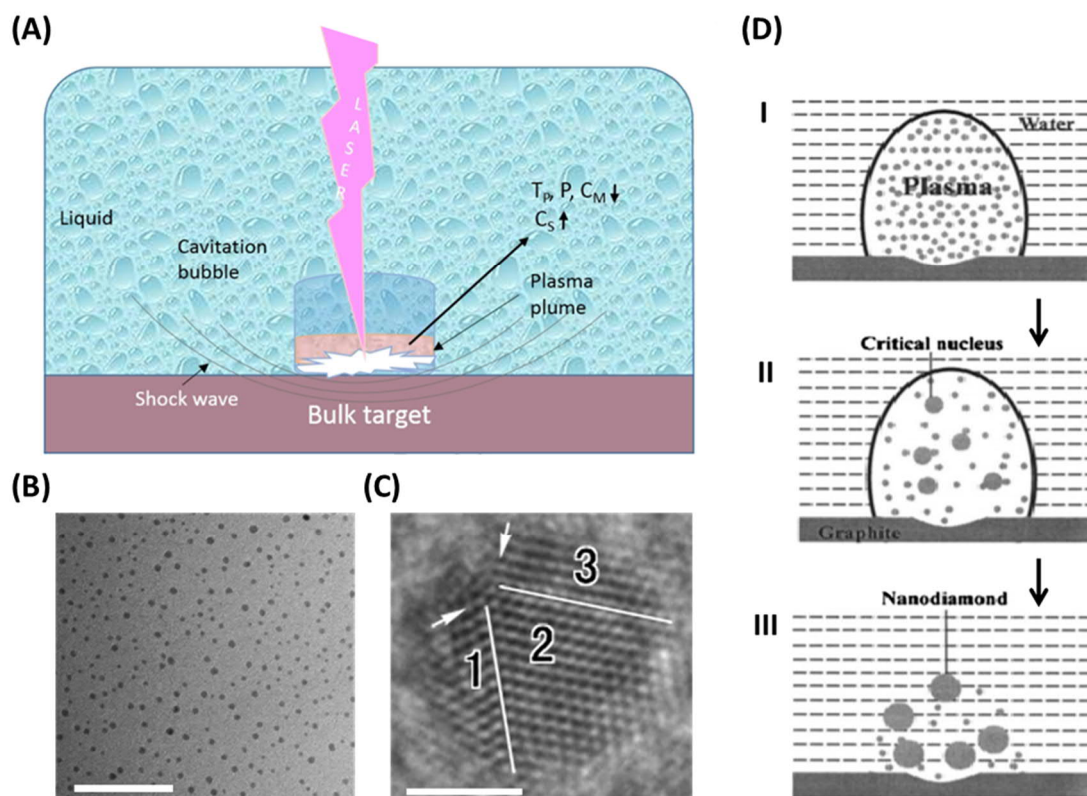


Figure 1.10 (A) Schematic presentation of the different stages in PLAL. The arrows indicate that, as the distance from the laser spot increases, a decrease is observed in the temperature (T), pressure (P), and concentration of the ablated material (C_M), while the concentration of the solution species increases, adapted with permission from Kumar, S., et al.⁷⁴ with copyright 2019 Elsevier Ltd. (B) TEM image of NDs produced by laser ablation, adapted with permission from Hu, S., et al.⁸⁹ with copyright 2008 Elsevier Ltd. (C) HRTEM image of a diamond particle with a triple twinning structure, adapted with permission from Hu, S., et al.⁸⁹ with copyright 2008 Elsevier Ltd. (D) Schematic diagram of the formation of nanodiamond by laser ablation in liquid medium: (I) Formation of the high-temperature, high-pressure, and high-density plasma; (II) Formation of diamond nuclei; (III) Formation of nanodiamonds, after about double the pulse duration, nanodiamonds stop to grow due to dropping down of the pressure and temperature, adapted with permission from Wang, C., et al.⁸⁷ with copyright 2005 American Institute of Physics Publishing.

1.4 Biological applications of nanodiamonds

ND, as a diamond, is physically and chemically highly stable under ambient conditions, and it is considered both chemically inert and biologically compatible because it consists of pure sp^3 -hybridized carbon atoms except for its surface. Its biocompatibility was evaluated at the cellular (cyto) or animal levels by many research groups⁹⁰⁻⁹⁴. The cytotoxicity of surface-oxidized HPHT NDs (around 100 nm in size) was first examined in immortal cell lines where they were avidly taken up by human embryonic kidney cells under serum-free conditions, and no obvious toxicity was observed at the concentration up to 100 $\mu\text{g}/\text{mL}$.⁹⁵ Subsequently cell viability studies of HeLa cells (a cervical cancer cell line), cell proliferation and genotoxicity of human fibroblasts were carried out; the results indicated that NDs have good cell viability, do not impair cell growth, and do not cause DNA damage^{96, 97}. Recently, a thorough and systematic investigation on the biocompatibility of HPHT NDs *in vitro* was carried out. The cytotoxicity and genotoxicity of two types of carboxylated NDs with nominal diameters of 20 and 100 nm were performed in six human cell lines as representatives of potential target organs: HepG2 and Hep3B (liver), Caki-1 and HEK293 (kidney), HT29 (intestine), and A549 (lung). The cytotoxicity was evaluated by impedance sensing for cell proliferation and flow cytometric analysis for dead cells. The genotoxicity was assessed according to the distribution of the number of γ -H2AX foci per nucleus, another highly sensitive technique for the study of DNA double strands break and the results displayed that NDs could effectively enter the cells but neither cause any significant cytotoxic nor genotoxic effects on the six cell lines even at the concentration as high as 250 $\mu\text{g}/\text{mL}$ ⁹³. The typical data is shown in Figure 1.11.

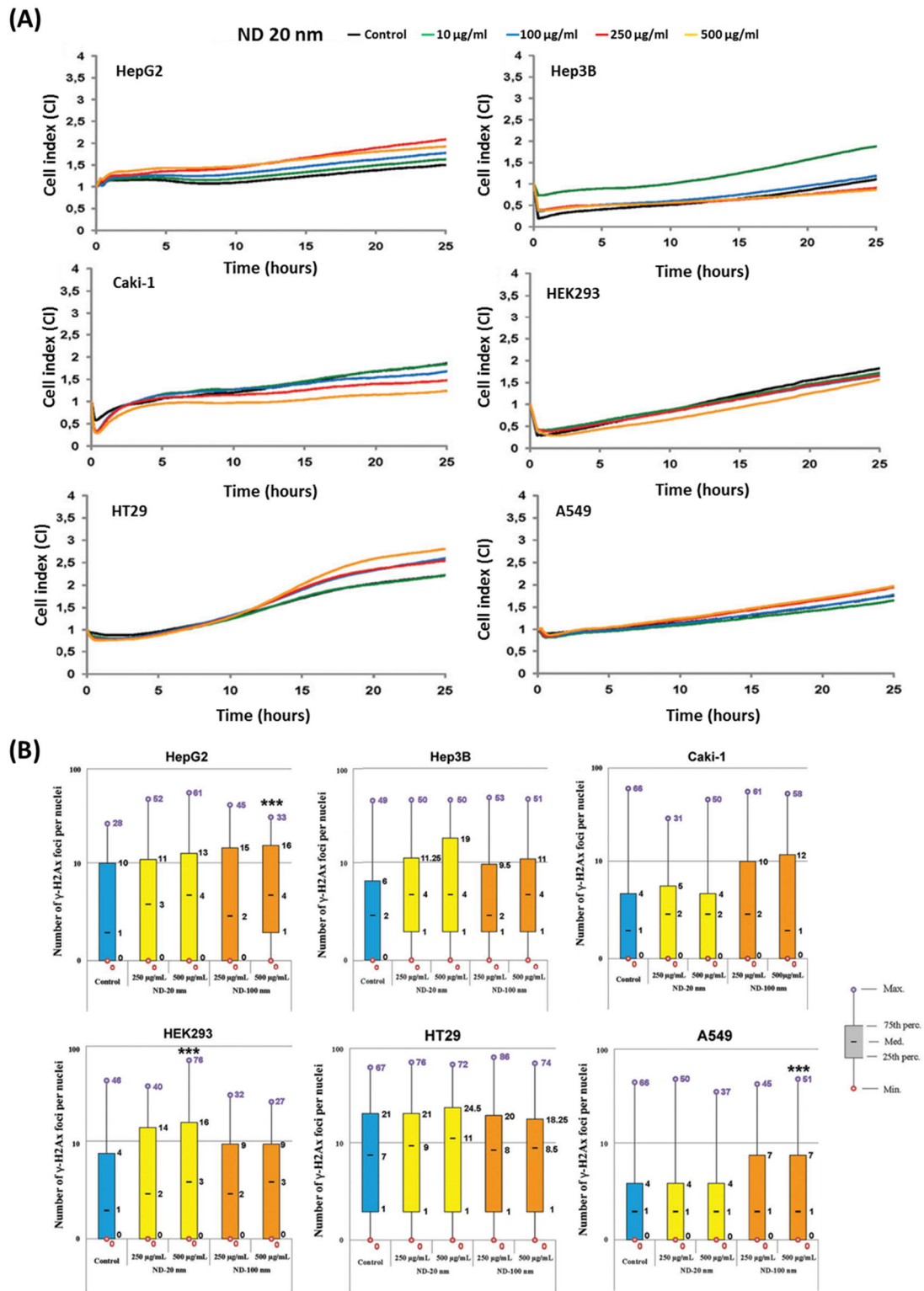


Figure 1.11 (A) Cell index real-time monitoring and viability of HepG2, Hep3B, Caki-1, HEK293, HT, and A549 cells exposed to ND with size of 20 nm, impedance measurements (one representative experiment among three independent experiments)

were carried out for 24 h and cell indices were normalized at time 0 to ensure there was no inter-well variability prior to the addition of nanoparticles. Control cells were not exposed to NDs, adapted with permission from Chang, H., et al.⁹³ with copyright 2018 WILEY-VCH Verlag GmbH & Co. KGaA, Weinheim. (B) Genotoxicity of NDs measured by γ -H2AX foci counts. Counts were performed on at least 200 cells per condition and results are depicted as box plot distribution values [minimum (min), maximum (max), median, 25th and 75th percentiles (25th and 75th perc.)] of the number of foci obtained in each tested condition. A Wilcoxon rank test (comparisons versus control cells not exposed to NDs) was performed (*p < 0.05; **p < 0.01; ***p < 0.001), adapted with permission from Chang, H., et al.⁹³ with copyright 2018 WILEY-VCH Verlag GmbH & Co. KGaA, Weinheim.

The biocompatibility of NDs *in vivo* was also confirmed by a series of model organisms, such as *Caenorhabditis elegans* (*C. elegans*)⁹⁸, zebrafish embryos⁹⁹, *Xenopus* embryos¹⁰⁰, mice^{101, 102}, rats^{94, 103}, rabbits¹⁰³, and so on. A wide range of species were covered, from the nematode to the primate, and both feeding and microinjection methods were used to introduce NDs into the living organisms. A long-term stability and biocompatibility of fluorescent NDs was studied in rat model (Figure 1.12). The researchers injected NDs to the intraperitoneal of rat with a total quantity of up to 75 mg/kg body weight over 3 months; there was no significant difference in fodder consumption, body weight, and organ index between the control and NDs treated animals. The injected NDs were surrounded by macrophages but there were no observable inflammation, necrosis, or tissue reaction surrounding these carbon-laden macrophages.⁹⁴ Clinical trials to validate nanodiamond-embedded biomaterial devices for wound healing and the prevention of re-infection are also ongoing, where the NDs are used to enhance mechanical properties.^{104, 105}

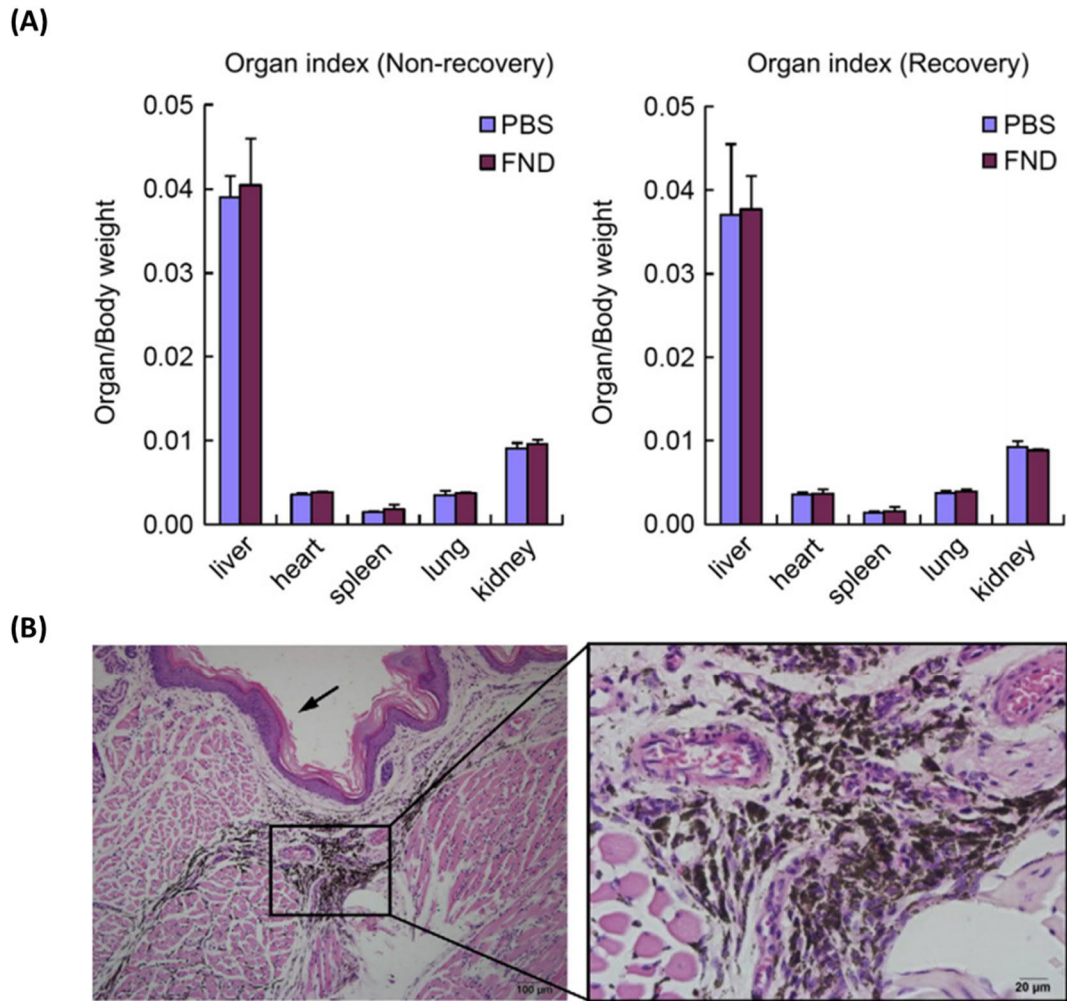


Figure 1.12 (A) Comparison of the organ indices of PBS-injected (control) and ND-injected SD into rats (with a dose of 5 mg/kg b.w. per week) after 12 weeks of treatment for the non-recovery and recovery groups ($n = 3$ each), adapted with permission from Vaijyanthimala, V., et al.⁹⁴ with copyright 2012 Elsevier Ltd. (B) Histological examination of the skin of an ND-treated mouse by H&E staining. The black arrow indicates the epidermis (magnification 100). Macrophages, appearing as dark brownish carbon-laden cells, are found to cluster in the dermis of the right paw, where BSA-coated FNDs were injected. No inflammation, necrosis, or tissue damage occurred in the surrounding cells, adapted with permission from Vaijyanthimala, V., et al.⁹⁴ with copyright 2012 Elsevier Ltd.

As a result, NDs do not induce significant cytotoxicity in a variety of cell types, do not

have side-effect on long-term exocytosis and cell proliferation, do not interfere with the gene or protein expressions and do not have toxicity in organs. Thus, NDs could be considered as a a very promising nanomaterial for biomedical research. In addition, NDs have high surface-to-volume ratios, which is an important feature of nanocarriers for drug delivery. Moreover, the NDs with color centers have stable fluorescence, which make them very suitable for long-term bioimaging. The special magneto-optical physical properties of NDs containing color centers enable them to detect biological signals such as radicals and temperature change.

1.4.1 Drug delivery

Drug delivery is one of the earliest bio-medical applications of NDs due to their large surface area and promising biocompatibility. Early studies on the use of nanodiamonds as drug delivery vehicles were reported by the group of Ho.^{106, 107} Their studies showed that the chemotherapeutic agent doxorubicin (DOX) could be passively absorbed onto the surface of NDs to create nanodiamond-drug complexes (NDX), then delivered into cancer cells with preserved efficacy, and released slowly and sustainably. Similarly, absorption and delivery of other drugs have been reported including, tamoxifen (TAM)¹⁰⁸, cisplatin¹⁰⁹, 4-hydroxytamoxifen (4-OHT)¹¹⁰, insulin¹¹¹, and so on. A representative study is shown in Figure 1.13: The NDX complex could inhibit tumor growth in both murine liver tumor and mammary tumor without affecting normal tissues and also significantly decreased the patient mortality. The potential of NDs as direct drug carrier has been demonstrated, but fundamental mechanisms, thermodynamics and kinetics of drug adsorption on NDs are still poorly understood. Important factors include purity, surface chemistry, dispersion quality, temperature and ionic composition are still needed to be explored further.

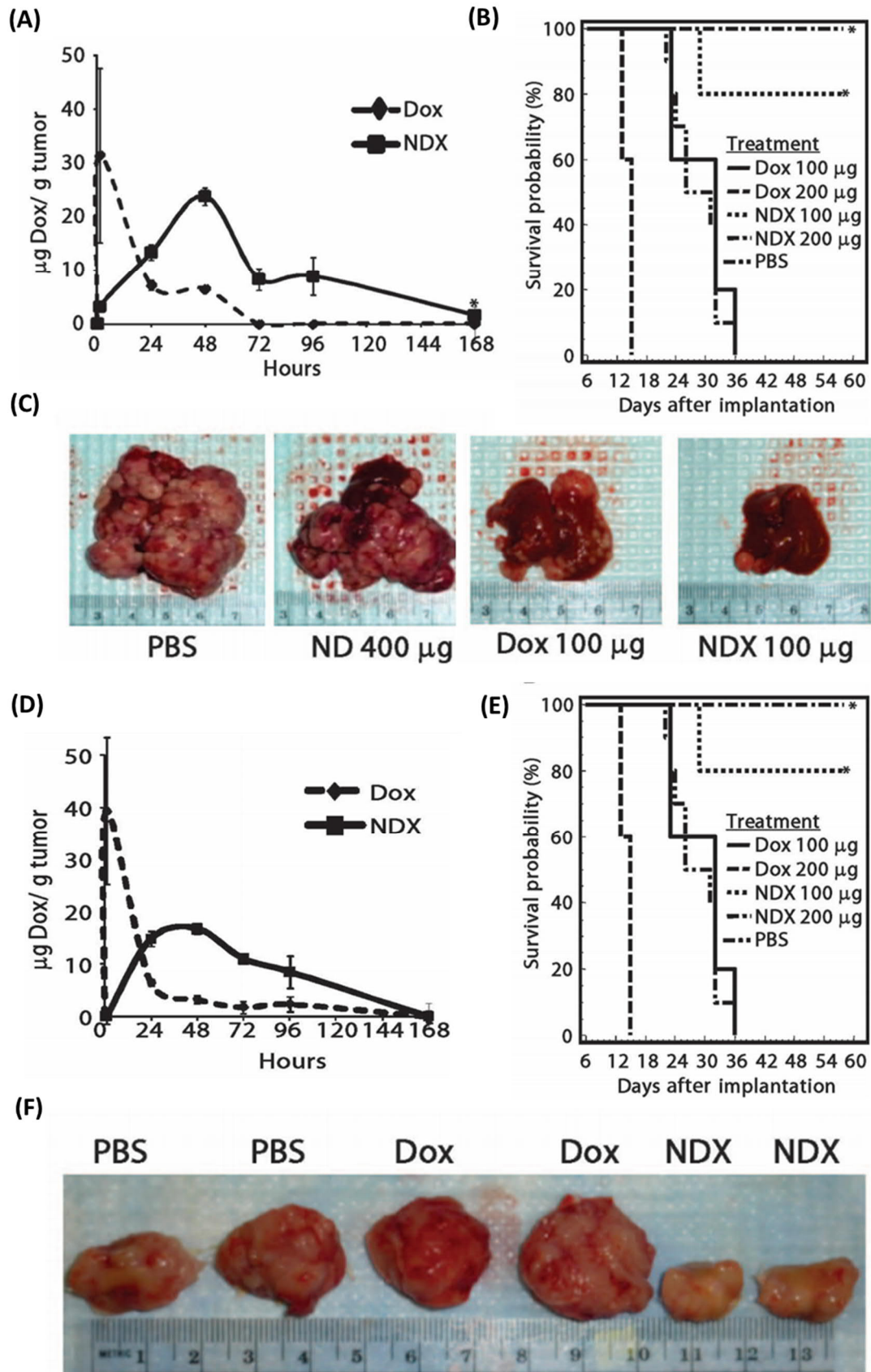


Figure 1.13 NDs delivery of Dox inhibits tumor growth in murine liver tumor models. (A) to (D) are adapted with permission from Chow, E. K., et al.¹⁰⁷ with copyright 2011 American Association for the Advancement of Science. (A) Tumor retention analysis of LT2-Myc mice treated with Dox (200 mg) (n = 4) or NDX (200 mg of Dox equivalent) (n = 4) by tail vein injection. Data are represented as means \pm SD. *P < 0.002. (B) Kaplan-Meier survival plot for LT2-Myc mice treated with PBS (n = 5), Dox (100 mg) (n = 8), or NDX (100 mg of Dox equivalent) (n = 7) by tail vein injection every 7 days. *P < 0.03; **P < 0.06. (C) Images of livers/tumors from treated mice. NDs delivery of Dox inhibits tumor growth in a murine mammary carcinoma model. (D) Tumor retention analysis of 4T1 mice treated with Dox (200 mg) (n = 4) or NDX (200 mg of Dox equivalent) (n = 4) by tail vein injection. Data are represented as means \pm SD. (E) Kaplan-Meier survival plot for 4T1 mice treated with PBS (n = 7), Dox (100 mg) (n = 10), NDX (100 mg of Dox equivalent) (n = 10), Dox (200 mg) (n = 5), or NDX (200 mg of Dox equivalent) (n = 5) by tail vein injection every 6 days. *P < 0.003. (F) Representative images of excised tumors from treated mice.

1.4.2 Imaging

NDs containing NV centers possess many unique optical features, including high photostability (no photobleaching and photoblinking), extended far-red emission, long lifetime and high quantum efficiency. Thus, it has drawn much attention as an attractive fluorophore for optical imaging.

In biological imaging, the signal to background (auto-fluorescence) ratio and photostability are essential. These were studied in detail and summarized in Figure 1.14A and B, which compares signal-to-background (autofluorescence) ratio (SBR) of NDs with organic dyes and QDs and showed photostability for the same fluorescent emitters to illustrate the tradeoff in brightness versus bleaching rate. Alexa 647 and beads display a single exponential decrease over time. Carbon dots and Au NCs can be showed two exponential decrease over time, whereas NDs and nanorubies show fair photostability (over hours and days). The fluorescence of QDs rises over time for

several minutes before starting to bleach. Since most photobleaching traces do not display simple exponential decrease over time, the half-life time τ at which the fluorescence intensity falls to half of initial value are is taken as a photostability metric. While half-life time for Alexa 647, Au NCs, beads, carbon dots, and QDs are 8 s, 27 s, 85 s, 2.5 min, and 25 min.¹¹²

Due to their very high photostability without photobleaching and blinking, NDs are promising candidates for stimulated emission depletion (STED) microscopy¹¹³, one of the superresolution fluorescence imaging techniques, developed by Stefan W. Hell, who was awarded the Nobel Prize in Chemistry in 2014. In this technique, two laser beams with different wavelengths and shapes are used. While measuring, the first laser beam (a Gaussian beam) is responsible for exciting the fluorophore of interest to its excited state. The second laser beam owing doughnut shape at the focus of the objective lens, depletes all of the excited molecules under doughnut, resulting in a nanometer-sized volume (Figure 1.14C)¹¹⁴. Consequently, the final “fluorescent volume” becomes actually smaller than the diffraction limit first Gaussian laser beam. Theoretically, the smaller the fluorescent volume is, the higher the image resolution is. However, very high laser power is required to get “fluorescent volume”, it strictly limits the application of STED in bioimaging because molecular fluorophores (such as fluorescein and fluorescent proteins) are usually photobleaching rapidly under intense laser illumination. Probing NDs in fixed HeLa cells by STED was carried out (Figure 1.14D); bovine serum albumin (BSA) coated NDs were delivered to the cell cytoplasm by endocytosis. They attained a spatial resolution of approximately 40 nm.¹¹⁵ A later study showed that individual NVs can be resolved within single NDs with a resolution of 10 nm, which is even smaller than the size of the NDs used (average size 40 - 250 nm)¹¹⁶.

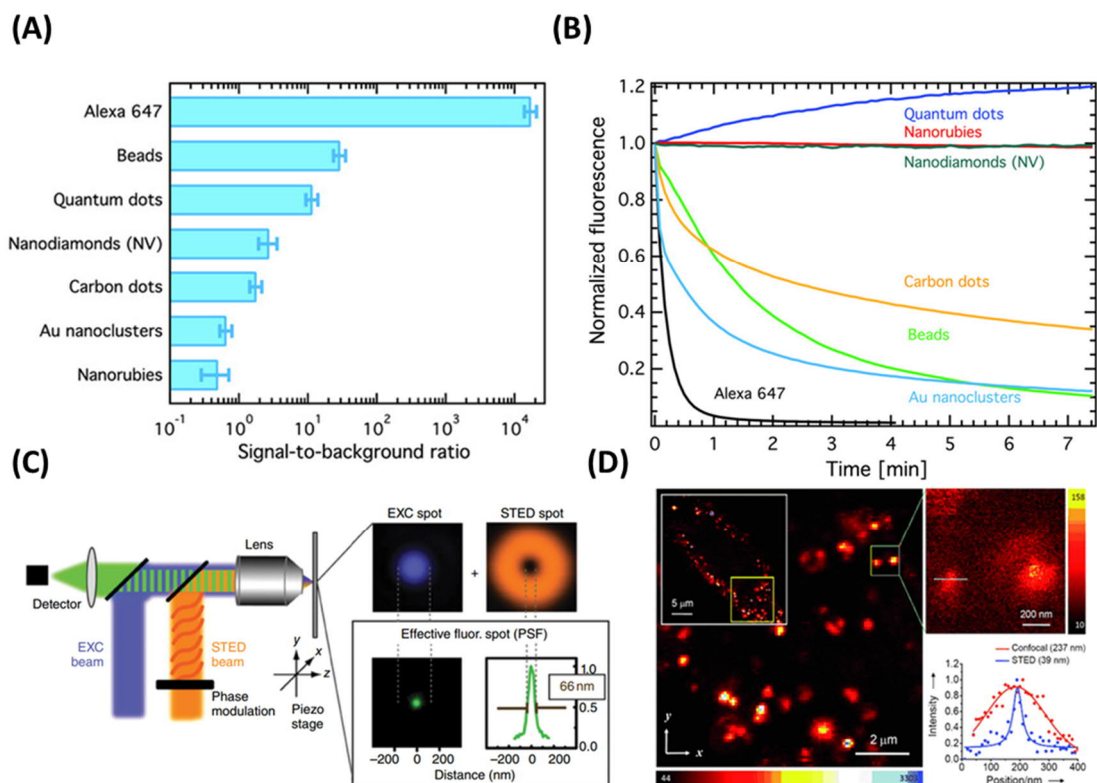


Figure 1.14 (A) Comparison of the Signal-to-noise ratio of different fluorescent materials performed on a commercial microscope, adapted with permission from Reineck, P., et al.¹¹² with copyright 2016 WILEY-VCH Verlag GmbH & Co. KGaA, Weinheim. (B) Normalized fluorescence emission intensity as a function of time for different fluorescent probes under continuous excitation, adapted with permission from Reineck, P., et al.¹¹² with copyright 2016 WILEY-VCH Verlag GmbH & Co. KGaA, Weinheim. (C) Principle of STED microscopy. A blue excitation (EXC) beam is focused to a diffraction-limited excitation spot, shown in the adjacent panel in blue, while the orange STED beam de-excites molecules. The STED beam is phase-modulated to form the focal doughnut shown in the top right panel. Superimposition of the two focal spots confines the area in which emission is only possible in the doughnut center, yielding the effective fluorescent spot of subdiffraction size shown in green in the lower panel, adapted with permission from Willig, K. I., et al.¹¹⁴ with copyright 2006 Springer Nature Publishing Group. (D) Confocal and STED imaging of HeLa cells labeled with BSA conjugated FNDs by endocytosis. The fluorescence image of

the entire cell is shown in the white box, STED image of single BSA-FND particles are enclosed within the green box. Solid curves are best fits to one-dimensional Gaussian (confocal) or Lorentzian (STED) functions. The corresponding full widths at half-maximum are given in parentheses, adapted with permission from Tzeng, Y. K., et al.¹¹⁵ with copyright 2011 WILEY-VCH Verlag GmbH & Co. KGaA, Weinheim.

As presented in Figure 1.15A, the NDs have a worse signal-to-background (autofluorescence) ratio than Alexa 647. To improve the sensitivity of detecting NDs in a noisy background, the time-gating techniques, including fluorescence lifetime imaging microscopy (FLIM), can be utilized considering the long lifetime of NDs of 20 ns. The lifetime of Alexa 647 is only 1.0 ns and most of the endogenous and exogenous fluorophores commonly used in bioimaging are 0.3–6.8 ns. This prompts researchers to improve the image contrast by isolating the emission of NDs from the autofluorescence backgrounds in cells and tissues based on various time-gating techniques.¹¹⁷ FLIM is a time-resolved imaging technique, which uses the differences in average fluorescence lifetimes of molecules or particles to generate high-contrast images. It was applied to detect the NDs in HeLa cells. Significant improvement of the image contrast was achieved by using a picosecond pulsed laser (532 nm) as the excitation source and detecting emitted photons at 15–53 ns after the laser pulses¹¹⁸, and the signal to noise increased by an order of magnitude. A representative result is shown in Figure 1.15.

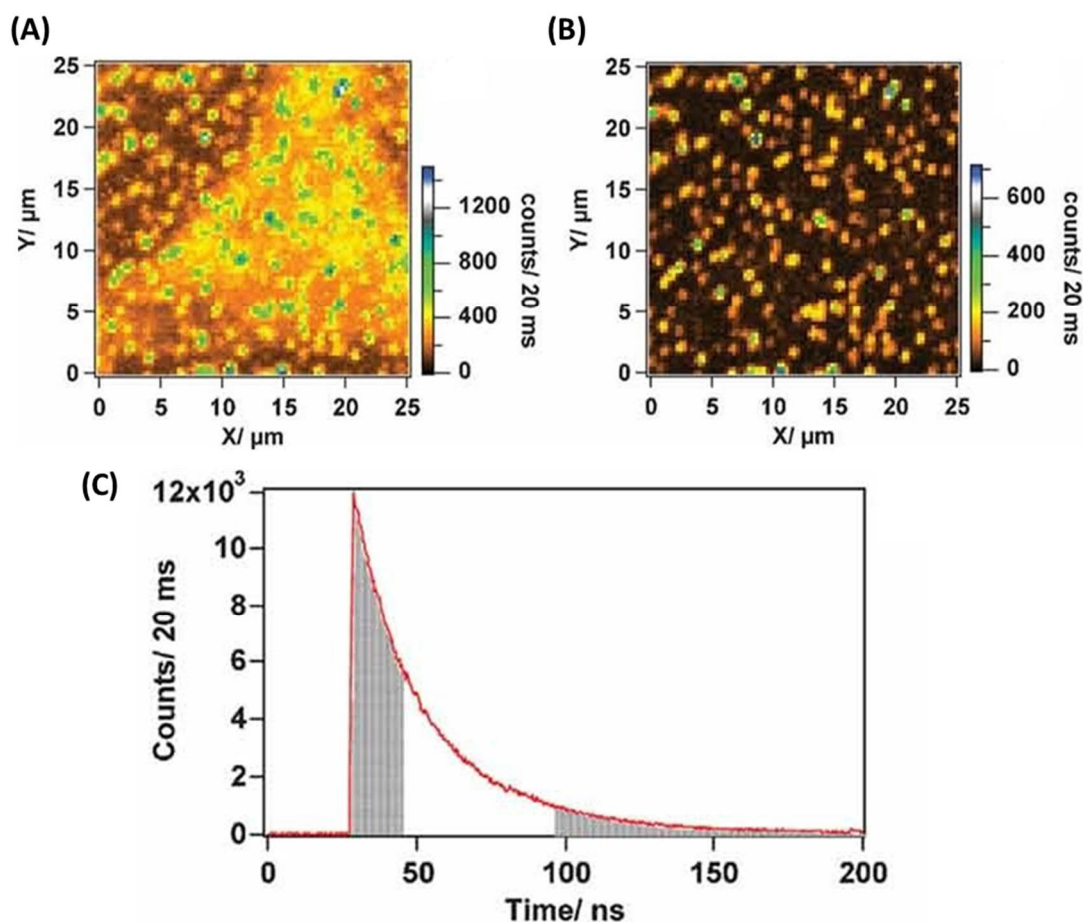


Figure 1.15 (A) Raster scan of a fixed HeLa cell containing NDs obtained from all detected photons, displaying NDs together with autofluorescence from the cell. (B) Time-gated raster scan of a fixed HeLa cell containing NDs constructed from photons detected between 15 and 53 ns after the laser excitation pulse. Scan area is $25 \times 25 \mu\text{m}$. (C) Fluorescence time decay from one of the NDs, adapted with permission from Faklaris, O., et al.¹¹⁸ with copyright 2008 WILEY-VCH Verlag GmbH & Co. KGaA, Weinheim.

NDs are considered as promising candidates for real-time tracking probe due to their photostable and bright color centers and extraordinary biocompatibility. The application of fluorescent probes in real-time tracking, including organic dyes and QDs, is often limited by photostability, cytotoxicity, and low quantum efficiency.¹¹⁹ The long-term labeling and tracking capabilities of the ND-based platform for cell division, proliferation, and differentiation was investigated over eight days;¹²⁰ the results showed

that NDs were predominantly entrapped in lysosomes, and surprisingly, no significant exocytosis of the lysosomal FNDs was found during cell proliferation. The fluorescence intensity of each cell decreases exponentially with time due to cell proliferation (Figure 1.16A and B). The transport of substance in bEnd.3 (a mouse brain cell line) via actin bridges was revealed by long-term tracking (Figure 1.16C). The potential of long-term tracking of NDs in vivo was also proven in different animal models.^{103, 121, 122}

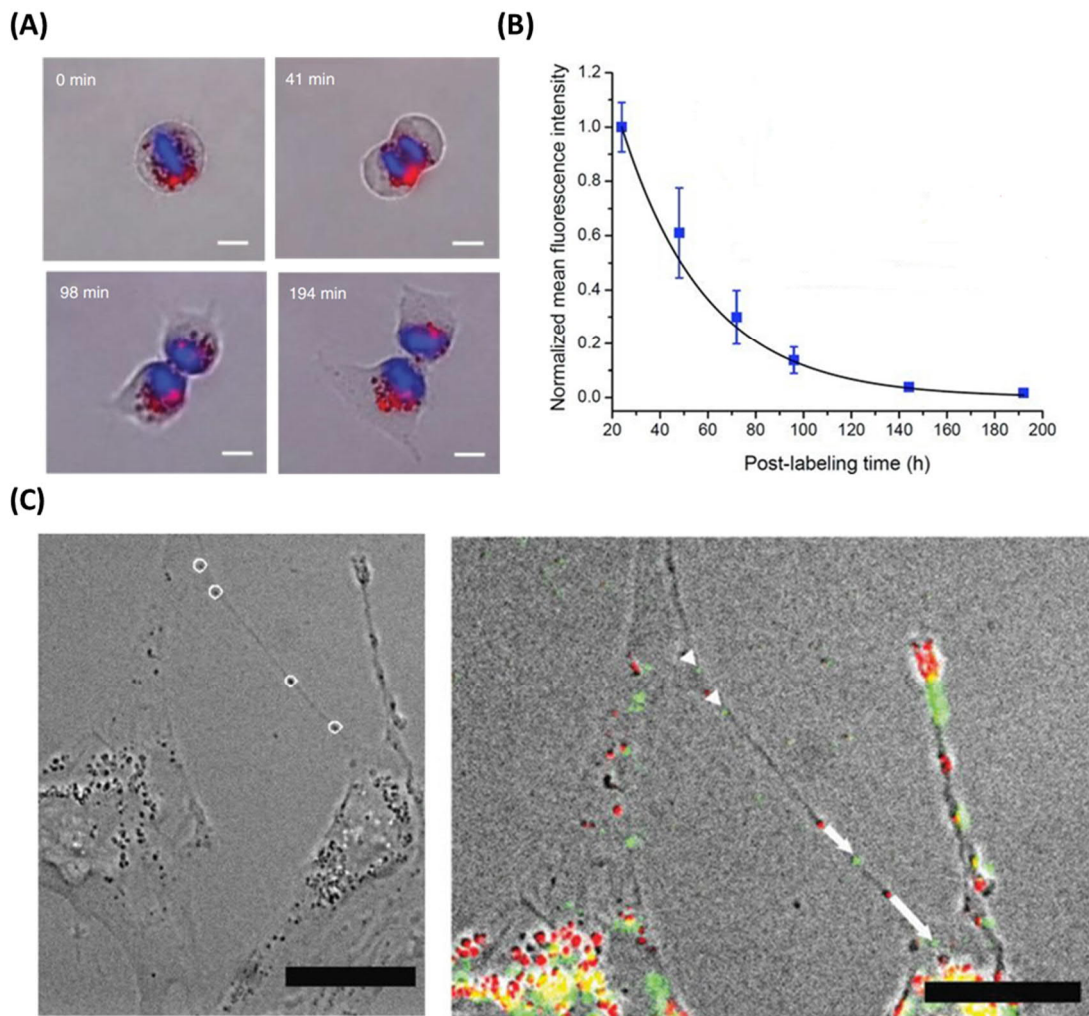


Figure 1.16 (A) Time-lapse images of a ND-labeled HeLa cell undergoing division, adapted with permission from Fang, C. Y., et al.¹²⁰ with copyright 2011 WILEY-VCH Verlag GmbH & Co. KGaA, Weinheim. (B) Long-term tracking of ND-labeled HeLa cells over eight days by flow cytometry adapted with permission from Fang, C. Y., et al.¹²⁰ with copyright 2011 WILEY-VCH Verlag GmbH & Co. KGaA, Weinheim. (C)

Time-lapse tracking of NDs movements along actin bridges in bEnd.3 cells, merging BF picture with those of fluorescence at 0 min (red) and 45 min (green). White circles indicate the tracked NDs; white arrows indicate length and direction of NDs migration (scale bar: 20 μm), adapted with permission from Moscariello, P., et al.¹²³ with copyright 2019 WILEY-VCH Verlag GmbH & Co. KGaA, Weinheim.

NDs are also an excellent marker in correlative light-electron microscopy (CLEM). CLEM is a method developed to investigate the same sample with both light microscopy (LM) and electron microscopy (EM). It combines the advantages of the multicolor versatility of LM with the high-resolution power of EM. However, it has a stringent requirement for the fluorescent marker. In the process of sample preparation for EM imaging, the samples must be fixed by high-pressure freezing to avoid damage of the markers, stained with heavy metal reagents, such as OsO₄ and uranyl acetate, which often results in fluorescence quenching. NDs are excellent candidate due to its high stable fluorescence, which can hardly be quenched by the environmental changes, and its highly dense carbon core, which can be visualized by EM. An application of CLEM to image and localize the positions of antigens on cell surface was first reported by the group of Chang¹²⁴ where they used biotinylated lipid-coated NDs to target the surface antigen CD44 on HeLa cells by sandwich immunostaining. The result are shown in Figure 1.17A. It has opened the door to locate the positions of antigens on cell surface with unprecedented precision and accuracy. Recently, the amount of NDs in cells was quantitatively analyzed down to single particle level using CLEM, which made it possible to obtain quantitative information on nanoparticle trafficking and their various interactions with cells, membranes, and organelles (Figure 1.17B).¹²⁵

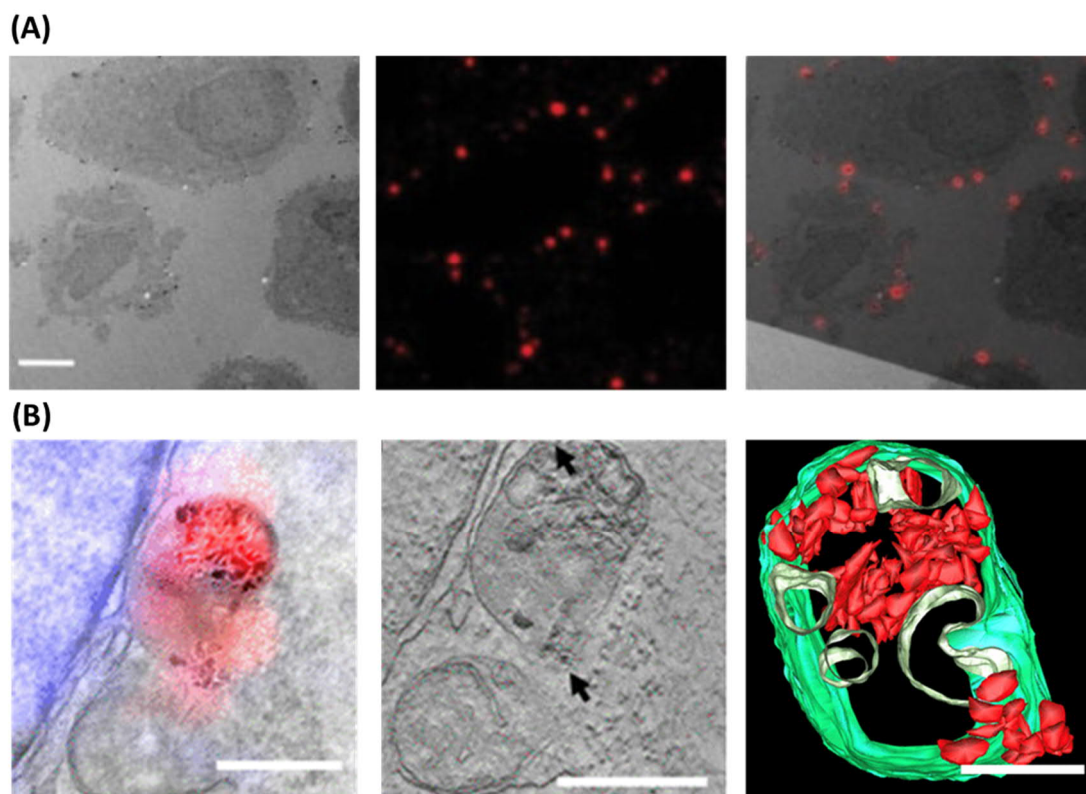


Figure 1.17 (A) TEM images of suspended HeLa cells labeled with biotinylated lipid-coated ND, fluorescence images of HeLa cells labeled with biotinylated lipid-coated ND and CLEM images of HeLa cells labeled with biotinylated lipid-coated ND (from left to right), scale bar is 5 μm , adapted with permission from Hsieh, F. J., et al.¹²⁴ with copyright 2017 American Chemical Society. (B) CLEM micrograph, tomogram section and the 3D model of fNDs clusters inside the endosomal vesicle (from left to right), scale bar are 500 nm in left and middle diagrams, and 250 nm in right diagram, adapted with permission from Han, S., et al.¹²⁵ with copyright 2020 American Chemical Society.

Nanodiamonds can also be used for other types of imaging such as magnetic resonance imaging (MRI). The paramagnetic impurities on the surface of NDs can be polarized and the spin polarization can be transferred to surrounding H^1 spins of the water molecules due to the nuclear Overhauser effect (NOE). NDs can provide partially polarized electron spins in the form of paramagnetic impurities, including NV centers, substitutional nitrogen (P1) centers, and unpaired electrons on the surface. By applying

a radiofrequency, the spin transfer can be induced to create MRI contrast on-demand. This was showed by the Rosen group as a proof of principle.¹²⁶ In addition, another possibility is hyperpolarization of ^{13}C spins in NDs to polarize liquid solutions by spin diffusion, which was proved in bulk diamond. The electron spins of NV^- centers can be hyperpolarized and transferred to the nuclear spins of surrounding ^{13}C atoms in the diamond lattice. However, in NDs, the orientation of the NV^- centers in NDs constantly change due to the Brownian motion. An orientation-independent method is under investigation.¹²⁷

1.4.3 Nanoscale sensing

Based on the remarkable magneto-optical property of NV centers (NV^-) in NDs discussed in section 1.2, it is possible to develop many different quantum sensors with very high sensitivity in the nanoscale at room temperature. The quantum nature of NV^- allows us to detect parameters in the surrounding in cell biology applications. Furthermore, the NV^- can even detect the single spin. Nevertheless, the highest resolution is not achieved due to the complex biological application and the large size of the NDs (more than 10 nm). The sensitivity can be greatly improved by collecting signals from many NV centers simultaneously, however at the expense of losing the partial exquisite resolution provided by a single NV defect. The typical example is magnetic relaxometry for probing spin-active intracellular species using NV centers.

In a so-called spin-lattice relaxation measurement (T_1 measurement) (Figure 1.18A), the equilibrium of the magnetic states is first changed using a laser (initialization) and then restored over a certain time (T_1) without laser illumination via the process of spin-lattice relaxation. T_1 relaxation depends on the number of spins in the surroundings, which provides a measure of the number of spins. In the case of using NV with its magneto-optical properties, the relaxation time can be conveniently readout by observing a decrease in photoluminescence intensity. Using this approach, Tetienne et al. even achieved a detection limit of 14 external spins originated from Gd^{3+} ions¹²⁸. Ermakova et al. demonstrated the detection of a few ferritin molecules attached on a

single ND particle containing NV^- centers (Figure 1.18B). Ferritin is an iron storage protein capable of transporting about 4500 atoms of iron with a magnetic moment of $300 \mu_B$. The researchers first attached ferritin to the surface of a 35 nm NDs by unspecific adsorption to form ferritin-ND complexes. The T_1 relaxation times were measured and compared with free NDs and ferritin-ND complexes for more than 30 particles in each group. A significant decrease of T_1 time (from 41.8 μs of free FNDs to 5.7 μs of the ferritin-ND complexes) was found due to the protein conjugation¹²⁹. Compared to existing magnetic force microscopy techniques, it does not require cryogenic temperature or vacuum, which is a major improvement in a practical sense. In a proof-of-principle experiment for biological sensing with the relaxometry, Kaufmann et al.¹³⁰ applied NDs containing NV^- centers to detect spin labels (Gd^{3+}) in an artificial cell membrane under ambient conditions. The Gd^{3+} ion has a spin of 7/2, it is widely used magnetic resonance imaging contrast agent. It can attach to the negatively charged head of the lipid molecule in a supported lipid bilayer by electrostatic interaction. The Gd^{3+} labeled lipids can thus produce considerable magnetic fluctuations in the artificial cell membrane. The researchers found that the T_1 relaxation times of the membrane-bound NDs were significantly shortened after the artificial membrane was labeled with 10% Gd spin-labeled lipids, which means a sensitivity of roughly 5 Gd spins $Hz^{-1/2}$. The ability of detecting such a tiny amount of spins in a model biological setting enables in situ nanoscale investigating dynamical processes in a single living cell.

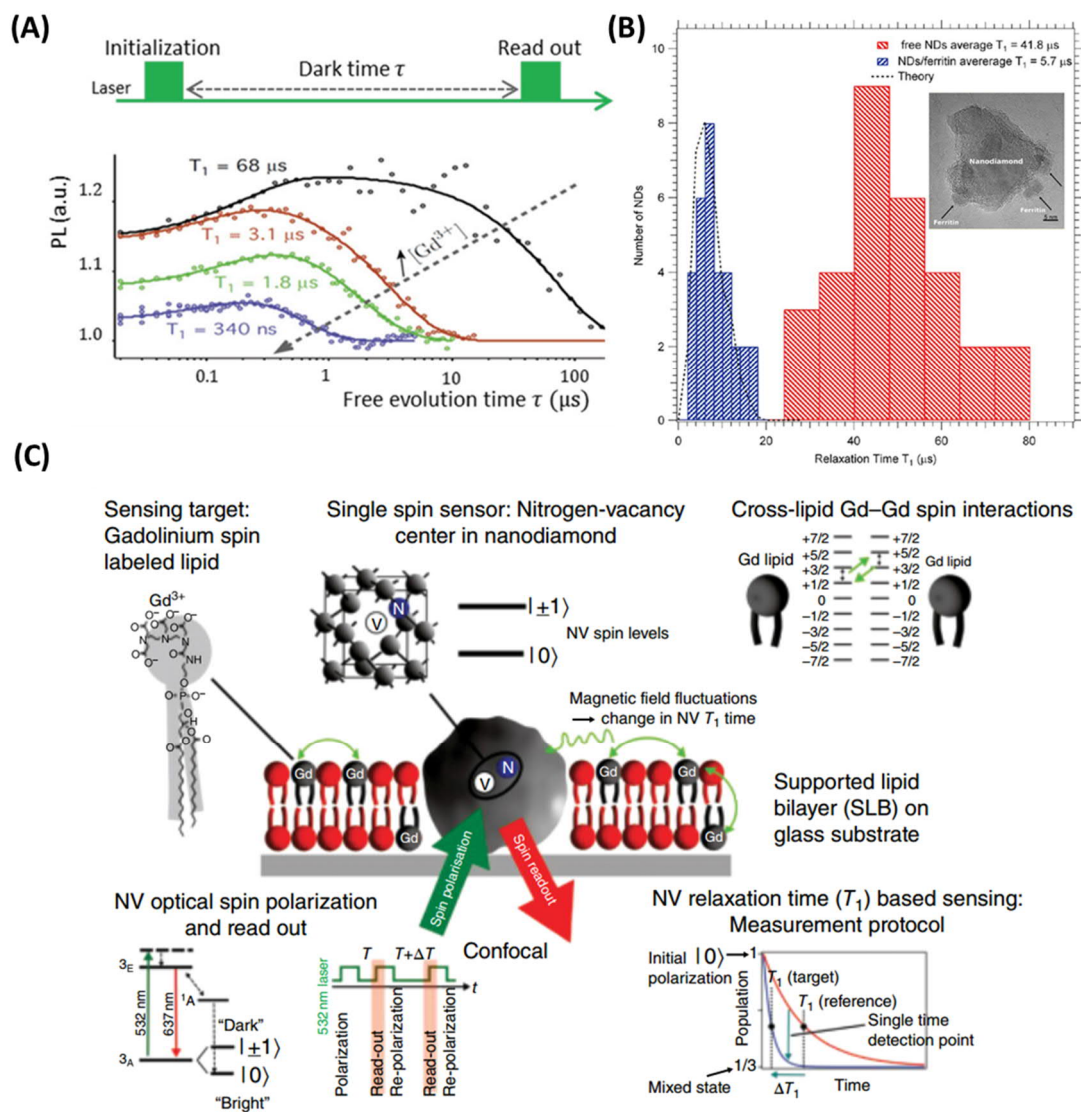


Figure 1.18 (A) T_1 measurement, varying the time τ before reading out the spin states results in the curves shown. If the NV center is still unperturbed in $m_s = 0$, it will give a higher photoluminescence than when it has already interacted with the surrounding. As a result, a decrease in Gd^{3+} (or other substances with a nonzero spin) shifts the curve to the left. The decrease can be described as an exponential function with a characteristic time constant T_1 , adapted with permission from Tetienne, J. P., et al.¹²⁸ with copyright 2013 American Physical Society. (B) Statistical distribution of the T_1 for free nanodiamonds and for ferritin coated nanodiamonds. The black dotted curve is a theoretical model using the fluctuation dynamics of the iron ions, adapted with permission from Ermakova, A., et al.¹²⁹ with copyright 2013 American Chemical

Society. (C) Schematic representation of the nanoscopic detection of spin labels in an artificial cell membrane using a single spin ND sensor, adapted with permission from Kaufmann, S., et al.¹³⁰ with copyright 2012 US National Academy of Sciences.

The magnetic resonance frequencies within the NV quantum system are also sensitive to temperature. This provides fascinating prospects for nanoscale thermometry based on the temperature dependence of the zero-field splitting.⁵² The increase of temperature results in a shift of magnetic resonance to lower frequency and an increase of their linewidth at ODMR spectrum (Figure 1.19A)¹³¹. A nanoscale thermometer supporting precise local temperature measurements in living systems would be a powerful tool in temperature-related biological research.¹³²⁻¹³⁴ The plot in Figure 1.19B compares sensor sizes and temperature accuracies between the NV⁻ based quantum thermometer and other techniques reported in the literature⁵⁴. It clearly shows that NDs performs better than other nanothermometers (such as quantum dots and green fluorescent proteins) in terms of its precision in the temperature measurement. However, it is still far from ideal. In a proof-of-principle experiment to measure temperature in human embryonic fibroblast cells (Figure 1.19C)⁵⁴, a gold nanoparticle was associated with nanodiamonds and heated by infrared laser illumination providing a means for local temperature changes. A sensitivity of 44 ± 10 mK with a resolution of 100 nm was achieved. The temperature changes of a ND particle was monitored while locally heating a nearby gold nanoparticle by a separate laser. At an infrared laser power of 12 μ W, a temperature increase of 0.5 K was found at the ND location, corresponding to a change of approximately 10 K at the location of the gold nanoparticle without affecting the viability of the cell. However, cell death occurred when the laser power was increased to 120 μ W, which caused a temperature change of 3.9 K at the ND location and 80 K at the gold nanoparticle position. The results revealed that it enables to investigate the efficiency of photothermal therapy and cell viability at the single-cell or subcellular level. By using a different method for temperature measurement in cells based on changes of the of the zero phonon line position, temperature accuracy of 1.8 ± 0.3 mK

in human embryonic kidney cells was achieved¹³⁵. In addition, the intracellular temperature map in primary cortical neurons cells was obtained based on the magneto-optical properties of NDs.¹³⁶

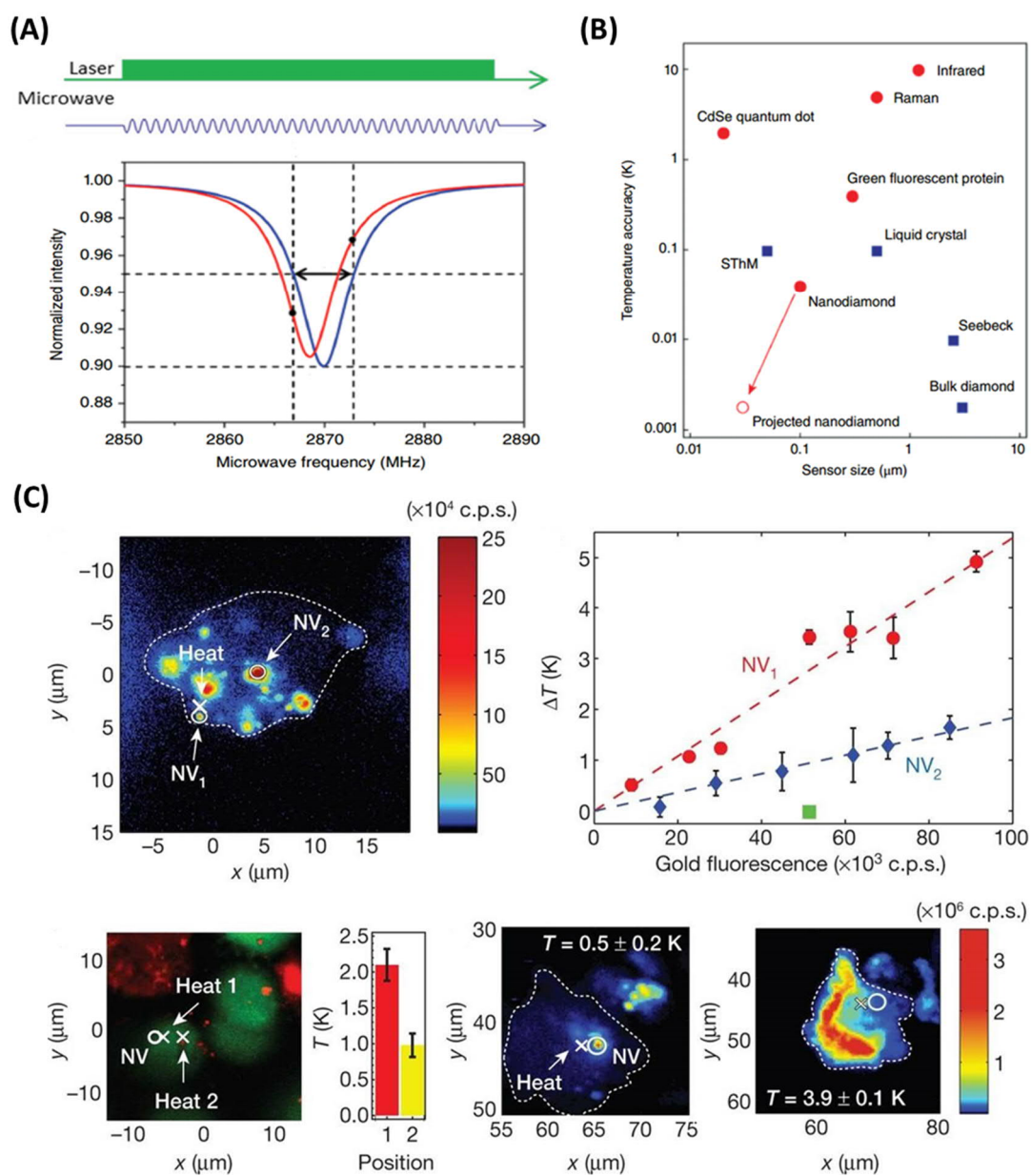


Figure 1.19 (A) Temperature measurement by ODMR spectroscopy of NV⁻. The temperature increase results in a shift of magnetic resonance to lower frequency and an increase of their linewidth, adapted with permission from Tzeng, Y. K., et al.¹³¹ with copyright 2015 American Chemical Society. (B) Comparison of sensor sizes and

temperature accuracies for the NV^- based quantum thermometer and other reported techniques. Biocompatible methods are labeled in red. The open red circle indicates the ultimate expected accuracy for NDs. SthM, scanning thermal microscopy, adapted with permission from Kucsko, G., et al.⁵⁴ with copyright 2013 Springer Nature Publishing Group. (C) Confocal scan of a single cell under laser excitation at a wavelength of 532 nm, with collection at wavelengths greater than 638 nm. The cross marks the position of the gold nanoparticle used for heating, and circles represent the location of the NDs (NV1 and NV2) used for thermometry. The dotted line provides a guide to the eye and outlines the cell membrane, adapted with permission from Kucsko, G., et al.⁵⁴ with copyright 2013 Springer Nature Publishing Group.

The NV quantum system is found to be also sensitive to pH. Based on the switching between the negatively charged (NV^-) and neutral states of NV centers (NV^0), a ND pH sensor was developed¹³⁷ (Figure 1.19A). Poly(diallyldimethylammonium) cation is used to coat the NDs and it is able to reversibly switch between positively charged and neutral states resulting in the change of rate of NV^- and NV^0 . Furthermore, a new pH nanosensor using electronic spins in NDs is proven (Figure 1.20B, 1.20C and 1.20D).¹³⁸ It is found that the longitudinal relaxation time T_1 of the electron spins in the NV centers inside a nanodiamond modified by carboxyl groups on the particle surface depends on ambient pH between pH 3 and pH 7. When the NDs are coated by a cationic polycysteine layer, a pH dependence between pH 7 and pH 11 is obtained.

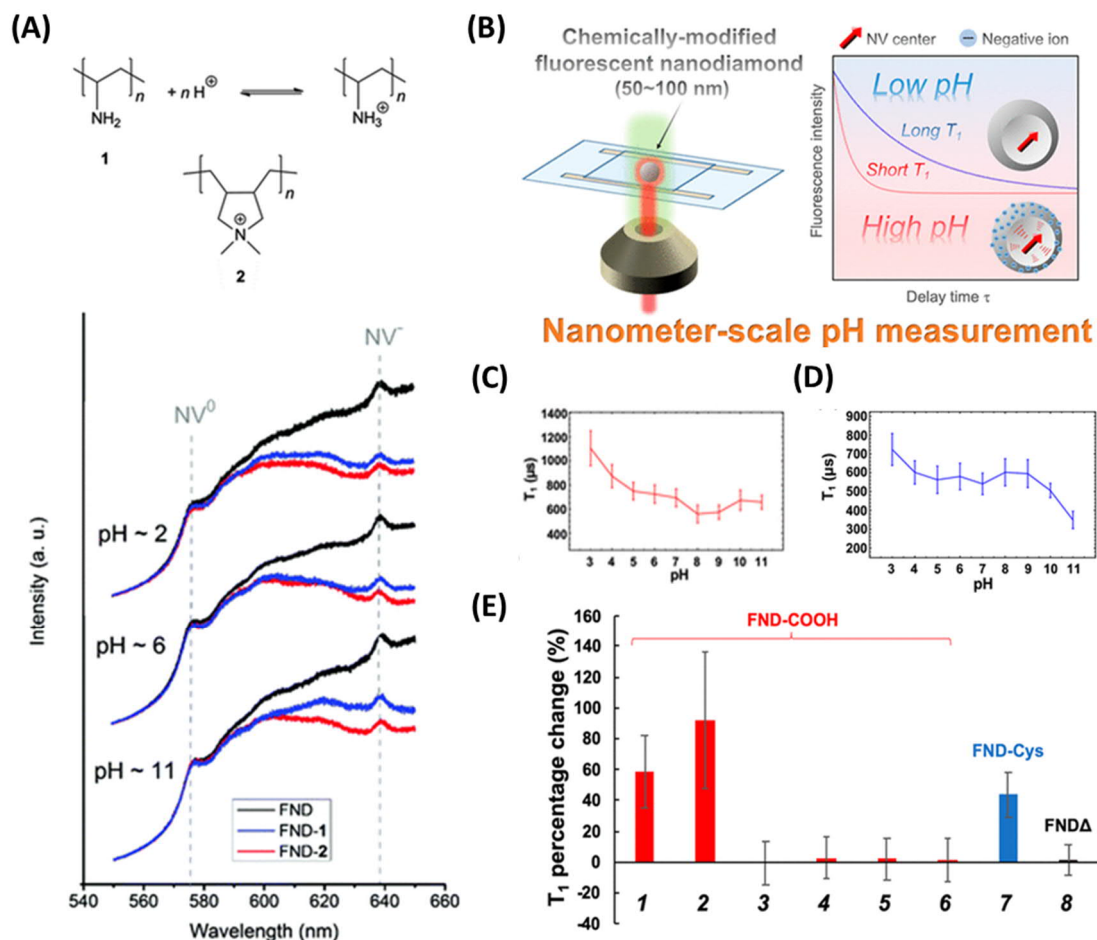


Figure 1.20 (A) Section of fluorescence spectra involving ZPL of the NV^0 and NV^- states for FND and FND-1 and FND-2 complexes measured at $pH \approx 2, 6,$ and 11 . The spectra for each pH are normalized to the NV^0 ZPL. The triads of FND, FND-1 and FND-2 spectra are shifted for clarity, adapted with permission from Petrakova, V., et al.¹³⁷ with copyright 2015 The Royal Society of Chemistry. (B) schematic of the nanodiamond pH sensor. (C) Typical result of the pH dependence of the T_1 of FND-COOH. (D) Typical result of the pH dependence of T_1 of FND-Cys. (E) Mean \pm standard deviation T_1 percentage changes of FND-COOH (red bars), FND-Cys (blue bar), and untreated FND (FND Δ) between different solutions, (B) and (C) are adapted with permission from Fujisaku, T., et al.¹³⁸ with copyright 2019 American Chemical Society.

In summary, the energy levels of NV^- in NDs can also be perturbed by a number of other physical quantities¹³⁹ including electric field, strain, orientation and pressure. This

could be helpful in understanding certain activities in the biological field.

1.5 Functionalization of nanodiamonds

As discussed before, NDs have promising biocompatibility as well as unique magneto-optical properties. It is extremely suitable for bioapplications. However, NDs must be modified or functionalized so that the targeting molecules can be connected. In addition, an appropriate surface modification and/or functionalization for NDs can help to enhance the colloidal stability in physiological buffer systems and prevent the aggregation or precipitation of NDs.

NDs produced either by the detonation method or the HPHT method are always contaminated with residual chemical compounds from the manufacturing processes, leaving sp^2 or graphitic carbon atoms on the surface. To remove these components, the most common method is surface oxidation. The NDs were treated in a strong oxidative atmosphere such as concentrated $H_2SO_4/HNO_3/HClO_4$ mixtures¹⁴⁰, ozone¹⁴¹, at elevated temperatures. As a consequence, these NDs are derivatized with a variety of oxygen-containing functional group, e.g. $-COOH$, $-C=O$, $-OH$, $-O-$ etc. Subsequently it is further modified and/or functionalized for different application. The modification method can be mainly categorized in two types: non-covalent modification and covalent modification. They are described in the following.

1.5.1 Non-covalent modification

Non-covalent modification is a very flexible and comparatively simple way to introduce the required functional groups on the surface of nanoparticles. This concept is also applicable to NDs. As mentioned above, the typical NDs after surface oxidation occupies a hydrophilic surface and large number of different oxygen-containing groups. They enable the formation of numerous hydrogen bonds with suitable polar compounds. The larger biomolecules are suitable for immobilization because several or even large number of non-covalent bonds can be formed by one attached molecule, which makes the interaction between NDs and biomolecule much stronger. Besides, the attached

biomolecules are able to provide numerous additional functional groups. Many proteins have been adsorbed on the surface of NDs, including insulin¹¹¹, cytochrome c¹⁴², lysozyme^{143, 144}, apoobelin,¹⁴⁵ and serum albumin^{146, 147}. A research¹⁴⁸ was carried out to illustrate the loading capacity of different proteins (containing cytochrome c, myoglobin, and serum albumin) on a ND particle (see Figure 1.21A). The results revealed that the protein loading capacity varied from 60 to 150 mg/g, relying on the sizes and molecular weights (12–66 kDa) of the adsorbed proteins. For a 100 nm ND, it showed more than 1000 protein molecules are adsorbed to the surface. It is important to confirm whether their functionalities are conserved when proteins are attached to NDs. This concern was addressed by Nguyen et al.¹⁴⁴. Lysozyme was adsorbed on the surface of NDs. They found their activity was significantly lower than that of free lysozymes in aqueous solution, because the spreading of proteins on the surface results in the loss of protein conformation. The activity, however, could be boosted by blocking the ND surface with additional proteins such as cytochrome c to create a more moderate environment that would decrease the loss of lysozyme conformation (see Figure 1.21B). Especially, adsorbed BSA can work as a good stabilizing agent to prevent NDs agglomeration of NDs under physiological conditions (in phosphate buffer saline (PBS) and cell culture media) and also boost the cellular uptake of NDs.^{115, 149}

A large variety of polymers can be also immobilized on the surface of NDs by non-covalent interactions. These conjugates can either be used for the direct application as a composite or to present a certain functional group on the outer surface of the coated NDs. Chang et al.⁹⁶ have used poly-L-lysine to produce an ND conjugate with a high amount of primary amino groups. They can then be easily functionalized such as amide formation. Other composites are formed by the non-covalent conjugation of NDs and PANI (polyaniline)¹⁵⁰, NDs and polyethyleneimine,¹⁵¹ or NDs and poly(lactic acid) (PLLA)¹⁵². Unfolded HSA polypeptide is a precisely defined sequence. It was stabilized with PEG and applied to modify NDs by non-covalent interactions (see Figure 1.21C). It increased the colloidal stability of NDs and reduce plasma protein binding. This conjugate showed exceptional stability even when loaded with hydrophobic DOX. It

was stable in 1 M NaCl solution over long periods of time and across a broad pH range.¹⁵³

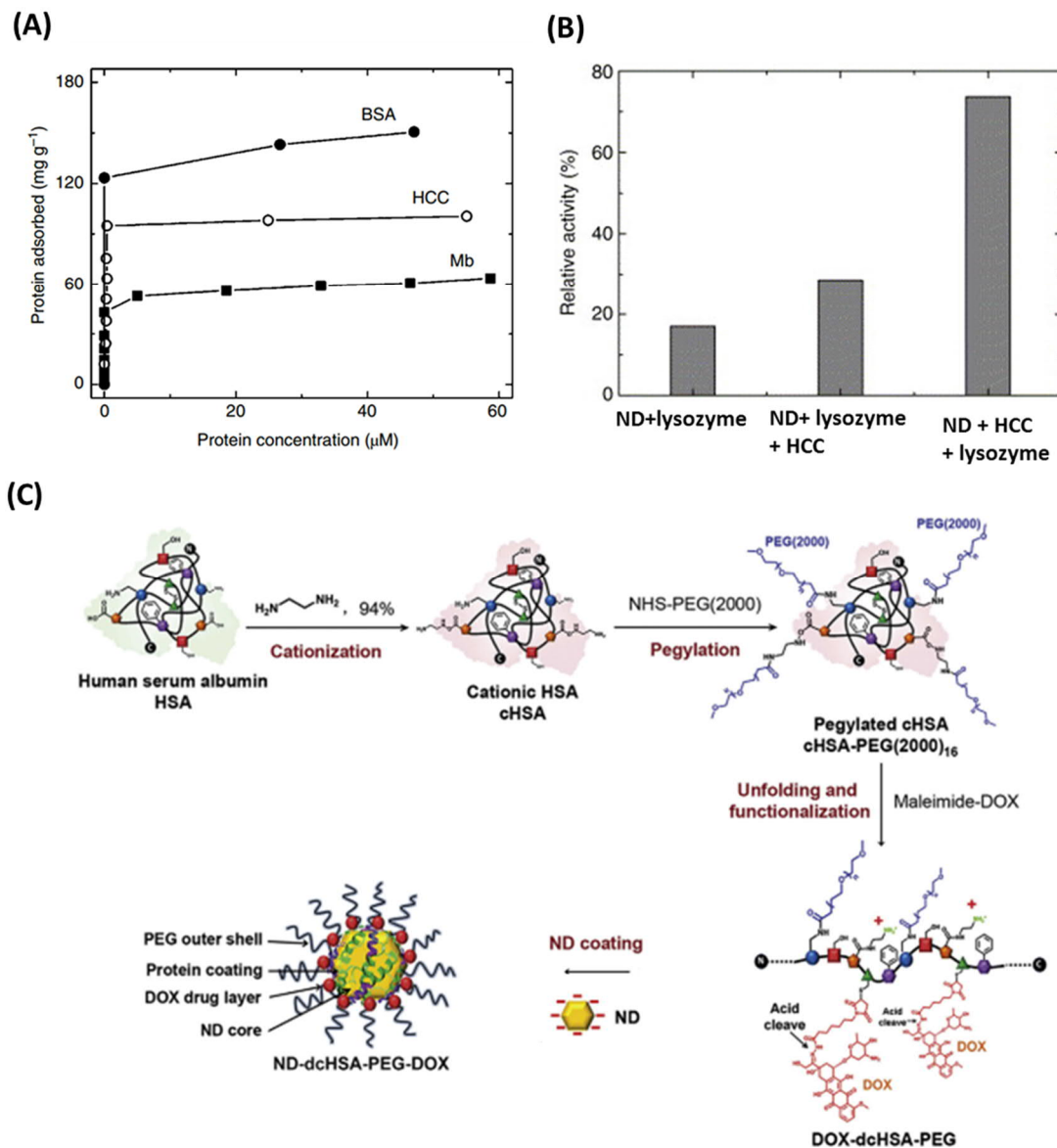


Figure 1.21 (A) Adsorption isotherms of horse heart cytochrome c (HCC), horse heart myoglobin (Mb), and bovine serum albumin (BSA) on 100 nm NDs at pH 10.5, 6.9, and 4.7, adapted with permission from Kong, X., et al.¹⁴⁸ with copyright 2005 American Chemical Society. (B) Hydrolytic activities of ND + lysozyme, ND + lysozyme + HCC and ND + HCC + lysozyme, adapted with permission from Nguyen, T. T. B., et al.¹⁴⁴ with copyright 2007 Elsevier Ltd. (C) Schematic preparation of NDs coated with an

inner protein and outer polymeric shell. The drug doxorubicin (DOX) is conjugated onto the biopolymer, adapted with permission from Wu, Y., et al.¹⁵³ with copyright 2015 WILEY-VCH Verlag GmbH & Co. KGaA, Weinheim.

1.5.2 Covalent modification

In spite of the facile and straightforward approach that unspecific adsorption may provide, the long-term stability of NDs in physiological condition is mainly concerns. Covalent modification is a more appropriate method. An overview of strategies for the surface modifications of NDs is shown in Figure 1.22.⁷⁰ It illustrates how the functional groups are achieved on the surface of NDs by wet chemistry and high-temperature gas treatments. High temperatures hydrogen plasma treatment can reduce $-C=O$ to $-C-OH$ and then $-C-H$ groups. NH_3 treatment at high temperatures gives a variety of nitrogen-containing groups such as $-NH_2$, $-CN$. Cl_2 or F_2 treatment at high temperatures can produce acylchlorides or $-C-F$. Treatment with $LiAlH_4$ can reduce all kinds of $-C=O$ related functional groups to $-OH$ groups. Reaction with $SOCl_2$ can convert $-COOH$ to highly activated $-COCl$. After termination, modified NDs undergo further functionalization more easily.

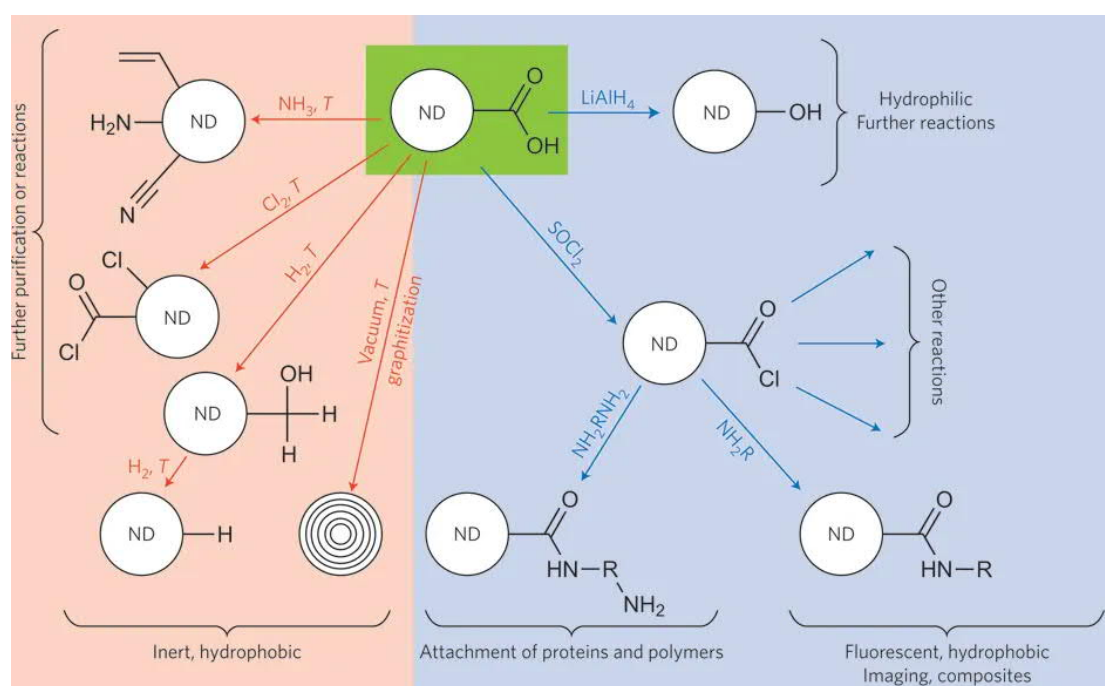


Figure 1.22 Overview of the commonly used methods for chemical modification and functionalization of ND surfaces, adapted with permission from Mochalin, V. N., et al.⁷⁰ with copyright 2012 Springer Nature Publishing Group.

Esterification, is a very convenient approach to introduce larger molecules. For the most common COOH-terminated NDs, to improve the reaction efficiency with alcohols, they are firstly transformed into acid chloride group or activated esters. Coupling agents which form the reactive moieties are widely used, including *N,N'*-dicyclohexylcarbodiimide (DCC), EDC (1-ethyl-3-(3-dimethylaminopropyl)carbodiimide) and DIC (*N,N'*-diisopropylcarbodiimide). However, the obtained NDs usually have poor stability against cleavage and agglomeration in water. A study was reported by Zhang et al.¹⁵⁴ where an oxidized nanodiamond reacted with thionyl chloride first to form the reactive acid chloride and then polyethylene glycol chains were immobilized in the presence of trimethylamine (to capture the released HCl) by ester formation with the surface (Figure 1.23A). PEGylation of the carboxylated diamond surface made it more hydrophilic and water-dispersible, but the aggregation was still serious. For these direct modifications, high steric hindrance of the reactions is severe. Another possibility was presented by Zhao et al.¹⁵⁵ They used nanodiamonds with both OH and COOH groups to react with glycidol in a “grafting from” ring-opening polymerization, forming branched polyglycerol on the nanodiamond surface (Figure 1.23B). The hydrophilicity of NDs are significantly improved due to the higher number of OH groups and obtained fully water-dispersible nanodiamond conjugates. Due to the high solubility, they can be purified by chromatographic approach characterized with solution phase NMR methods. Later, such conjugates were used for many bioapplications after further modifications.¹⁵⁶⁻¹⁵⁹ This polyglycerol coating is promising for the future, however, there are still concerns regarding yield and complex separation.

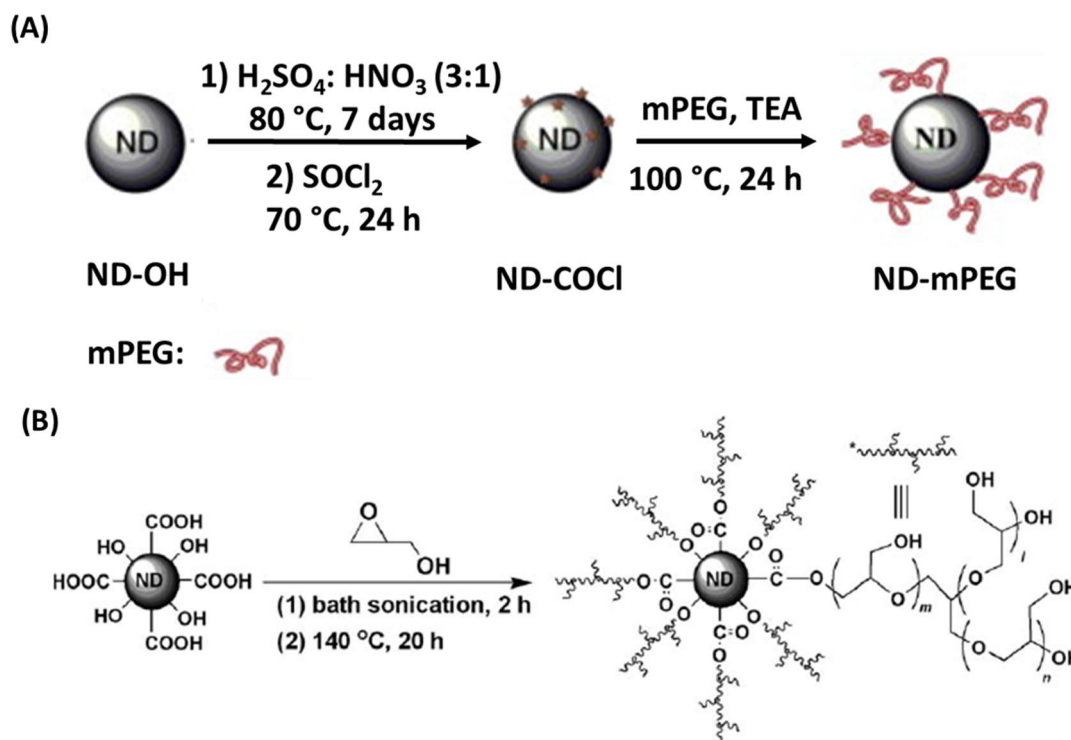


Figure 1.23 (A) Preparation of mPEG coated NDs by “grafting to” method, adapted with permission from Zhang, X., et al.¹⁵⁴ with copyright 2012 Elsevier Ltd. (B) Synthesis of NDs functionalized with hyperbranched polyglycerol through the ring-opening polymerization of glycidol, adapted with permission from Zhao, L., et al.¹⁵⁶ with copyright 2014 Beilstein-Institut.

Amidation, the formation of amide bonds, is the other versatile approach to modify the COOH-terminated NDs. It is more stable compared to ester bonds and also more applicable for the immobilization of functional molecules such as proteins, dyes, polymer chains, etc., on the surface of NDs.¹⁶⁰ As mentioned in the previous section on the high steric hindrance, the steric constraints can be reduced and the bioactivities can be retained by inserting some spacers between NDs and aimed biomolecules. It is particularly important for proteins to avoid their active sites hindering. Furthermore, the non-specific absorption and the influence on the protein conformation can be minimized. Polyethylene glycol (PEG) is most widely used spacer due to its high biocompatibility and lower nonspecific interactions with other molecules. Many kinds of PEG derivations are commercially available, such as amine terminal, which can be

covalently conjugated with carboxylated NDs via the amino groups on their termini by carbodiimide chemistry as shown in Figure 1.24

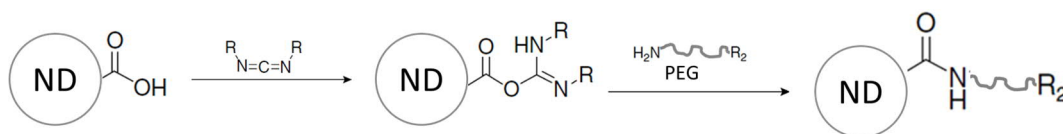


Figure 1.24 Schematic preparation of PEG modified NDs.

Many other chemical reactions can also be used to covalently modify and post-functionalize the NDs with different terminal groups, which are summarized in Figure 1.25. However, these methods could not completely solve the problems of aggregation of NDs in physiological condition.

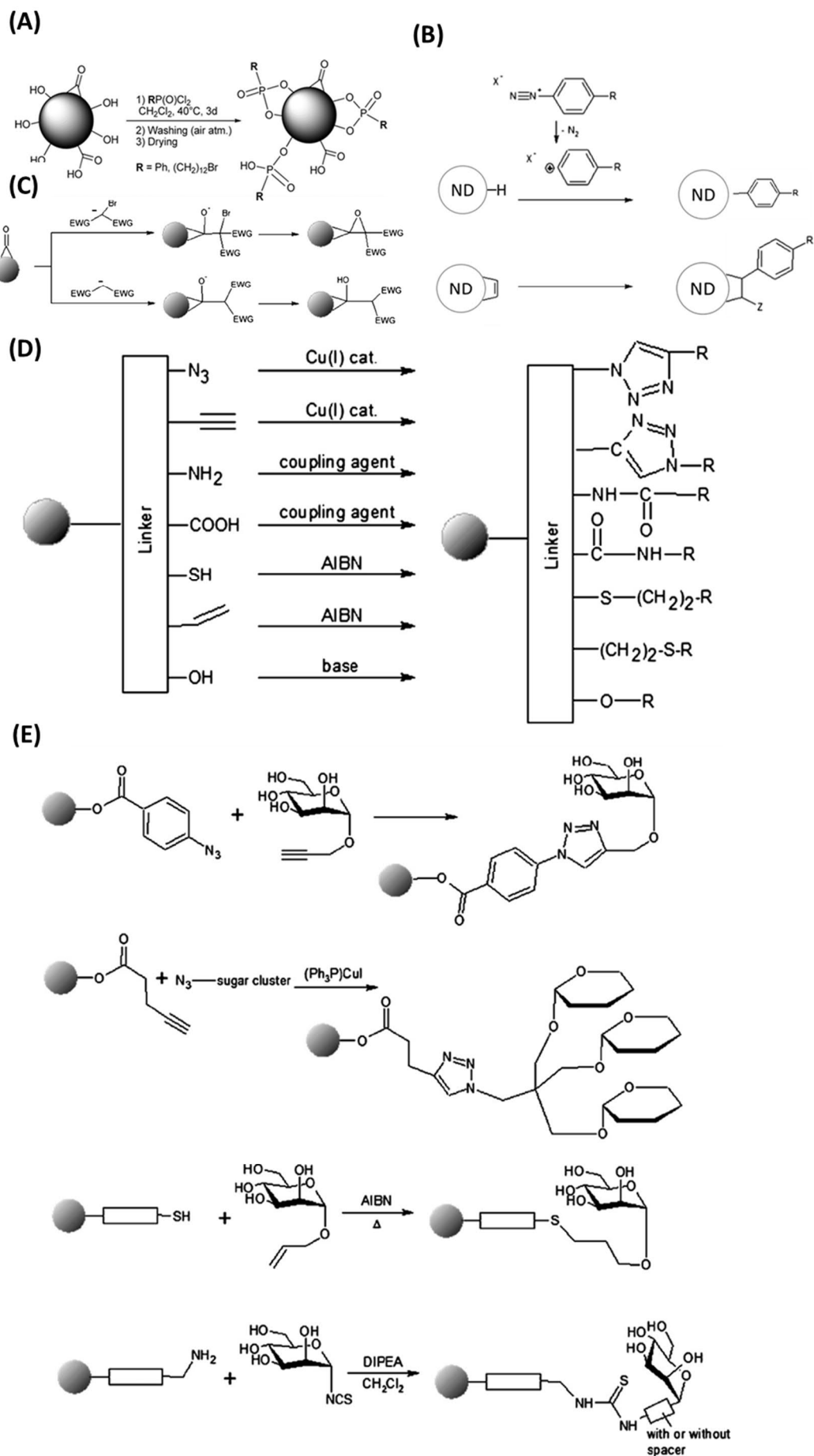


Figure 1.25 (A) Reaction of nanodiamond surfaces with phosphorylating agents, adapted with permission from Presti, C., et al.¹⁶¹ with copyright 2014 American Chemical Society. (B) Arylation of nanodiamond with different surface terminations using diazonium salts, adapted with permission from Yeap, W. S., et al.¹⁶² with copyright 2009 American Chemical Society, Girard, H., et al.¹⁶³ with copyright 2010 Elsevier Ltd. (C) The epoxide resulting from the reaction of a bromomalonate with a surface carbonyl group opens during aqueous workup to the corresponding diol, adapted with permission from Betz, P., et al.¹⁶⁴ with copyright 2012 WILEY-VCH Verlag GmbH & Co. KGaA, Weinheim. (D) Methods for subsequent grafting of more complex moieties onto prefunctionalized nanodiamond, adapted with permission from Krueger, A., et al.¹⁶⁵ with copyright 2017 Elsevier Ltd. (E) Covalent grafting of peptides onto nanodiamond using artificial anchor groups and thereby increasing the site selectivity of the grafting, adapted with permission from Krueger, A., et al.¹⁶⁵ with copyright 2017 Elsevier Ltd.

1.5.3 Other approaches

In functionalization of nanomaterials, enclosing the nanoparticle with a shell and form core-shell structure is useful and universal strategy. The shell can be formed covalently and/or non-covalently and made of organic materials, inorganic materials or mixtures of them. In the coating process, crosslinking between the atoms or molecules are used to for stable network and stabilize them for further use. The typical material has been successfully applied to prepare well-dispersed NDs is silica.

Researchers have enclosed NDs in silica shells in many works¹⁶⁶⁻¹⁶⁹, which provides a platform for subsequent chemical functionalization based on the well-investigated silica chemistry. Silica coating can assist in maintaining the stability of ND suspensions over a range of pH or electrolyte concentrations. Moreover, the silanol groups render the surface lyophilic. Furthermore, the silica coating is optically transparent¹⁷⁰, allowing efficient transmission of excitation and emission light. Figure 1.26A shows, the process of synthesis and post-functionalization of silica-coated NDs and the

transmission electron microscopy (TEM) images of NDs before and after silica coating, respectively.¹⁶⁷ The thickness of silica shell can be tuned down to 10 nm.¹⁷¹ Noticeably, the irregular shape of the prickly NDs became egg-like spheroids. Another exciting work synthesized ND-silica core-shell structure with the assistance of liposome and the liposome was easily removed by washing with sodium dodecyl sulfate (SDS). With this combined approach, it is possible to selectively attach bioactive ligands to NDs of various sizes and concurrently improve the colloidal stability of these nanoparticles in biological buffers.¹⁶⁹

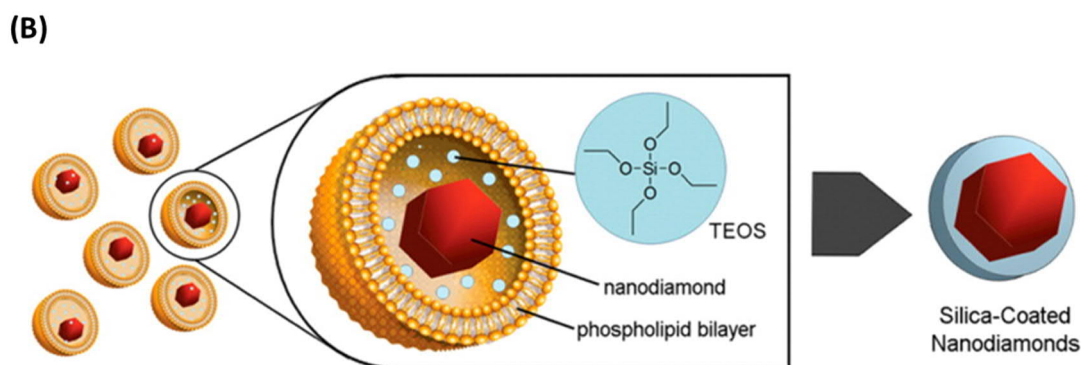
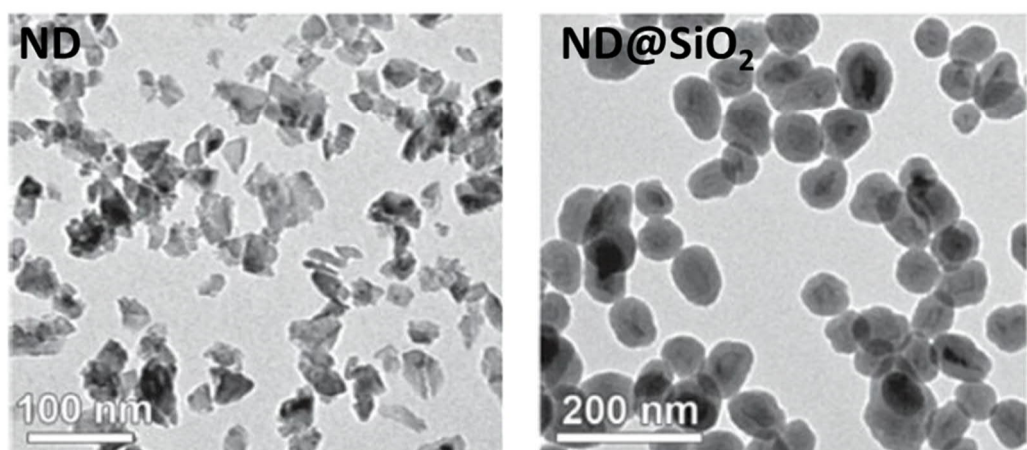
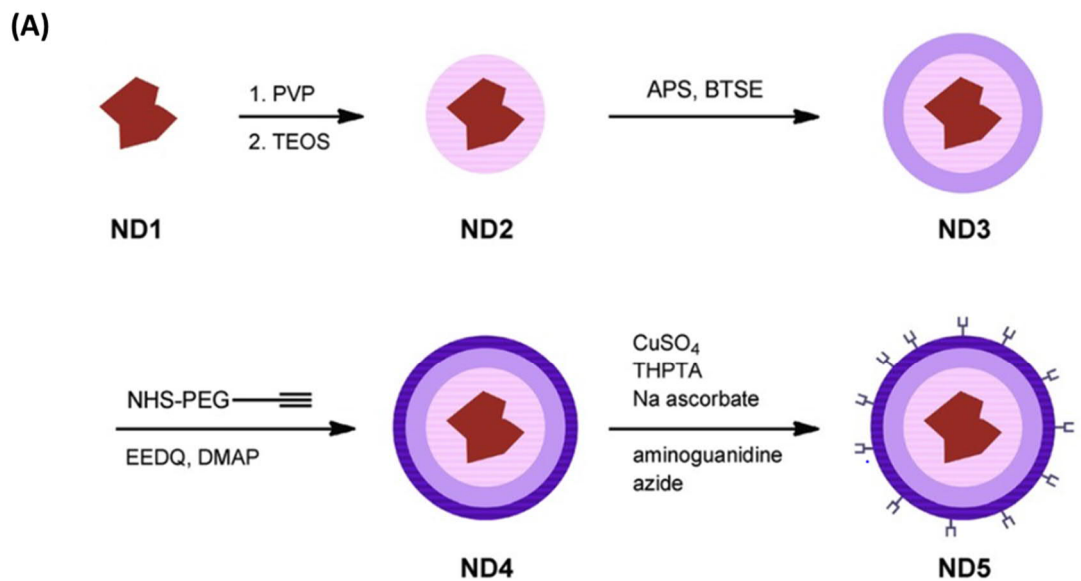


Figure 1.26 (A) Synthesis and post-functionalization of silica-coated NDs (top) and the TEM images of uncoated NDs and silica-coated NDs (bottom), adapted with permission from Rehor, I., et al.¹⁶⁷ with copyright 2014 WILEY-VCH Verlag GmbH & Co. KGaA, Weinheim. (B) Synthesis of silica-coated NDs by liposome-based

encapsulation, adapted with permission from Bumb, A., et al.¹⁶⁹ with copyright 2013 American Chemical Society.

However, after purification, free silanes are removed from silanized NDs dispersion, the polycondensation reaction proceeds reversely, resulting in the hydrolysis of the silica shell and increase of ionic strength due to the dissolution amorphous silica shell.^{172, 173} Notably, weakly crosslinked functionalized silanes are even more prefer to hydrolyzing original silica.

In summary, NDs are promising candidates for drug delivery, bioimaging, and nanoscale sensing due to their excellent biocompatibility and outstanding magneto-optical physical properties. For drug delivery, the loading capacity is usually limited by the surface property of NDs. Hereby, the drugs are adsorbed/conjugated to the surface of NDs. In the field of bioimaging, it is essential to introduce the targeting moieties to the surface of NDs. For nanoscale sensing, the shell thickness is very important, e.g. for the magnetic field sensing, the magnetic signal decrease as the cube of the shell thickness. All of these biological applications rely on surface modification. Many typical surface modification techniques of NDs have been introduced. Nevertheless, they still have different drawbacks, e.g. the loaded molecules may be released unexpectedly due to the nonspecific adsorption and are highly dependent on the environmental conditions. The directly covalent modifications of NDs usually cause aggregation of NDs and lower the efficiency because only a few functional groups are available on the NDs surface. Thick shell results in the sensitivity decrease. Therefore, it is necessary to develop thin and universal coatings or coating strategy in the future.

1.6 References

1. W. H. Organization, 2020.
2. C. P. Wild, C. Espina, L. Bauld, B. Bonanni, H. Brenner, K. Brown, J. Dillner, D. Forman, E. Kampman and M. Nilbert, *Mol. Oncol.*, 2019, 13, 528-534.
3. F. G. Shellock and E. Kanal, *J Magn Reson Imaging.*, 1999, 10, 477-484.
4. K. M. Hasebroock and N. J. Serkova, *Expert Opin. Drug Metab. Toxicol.*, 2009, 5, 403-416.
5. I. Ali, M. Nadeem Lone, M. Suhail, S. Danish Mukhtar and L. Asnin, *Curr. Med. Chem.*, 2016, 23, 2159-2187.
6. S. Marchal, A. El Hor, M. Millard, V. Gillon and L. Bezdetrnaya, *Drugs*, 2015, 75, 1601-1611.
7. A. W. Hübler and O. Osuagwu, *Complexity*, 2010, 15, 48-55.
8. C. Stephenson and A. Hubler, *Sci. Rep.*, 2015, 5, 15044.
9. D. Lyon and A. Hubler, *IEEE Trans. Dielectr. Electr. Insul.*, 2013, 20, 1467-1471.
10. Y.-x. Zhang and Y.-h. Wang, *RSC Adv.* 2017, 7, 45129-45144.
11. M. R. Vaziri, A. Omidvar, B. Jaleh and N. P. Shabestari, *Opt. Mater.*, 2017, 64, 413-420.
12. A. Omidvar, M. RashidianVaziri and B. Jaleh, *Physica E Low Dimens. Syst. Nanostruct.*, 2018, 103, 239-245.
13. K. T. Nguyen and Y. Zhao, *Nanoscale*, 2014, 6, 6245-6266.
14. L. Nayak, S. Mohanty, S. K. Nayak and A. Ramadoss, *J. Mater. Chem. C*, 2019, 7, 8771-8795.
15. T. Chen and Y. Liu, *Semiconductor Nanocrystals and Metal Nanoparticles: Physical Properties and Device Applications*, CRC Press, 2016.
16. W. C. Chan, *Bio-applications of Nanoparticles*, Springer Science & Business Media, 2009.
17. J. M. Chan, P. M. Valencia, L. Zhang, R. Langer and O. C. Farokhzad, in *Cancer Nanotechnology*, Springer, 2010, pp. 163-175.
18. L. Gong, Y. Wang and J. Liu, *Biomater. Sci.*, 2017, 5, 1393-1406.
19. S.-D. Li and L. Huang, *Biochim. Biophys. Acta, Biomembr.*, 2009, 1788, 2259-2266.
20. S. Guo and L. Huang, *J. Nanomater.*, 2011, 2011.
21. J. W. Nichols and Y. H. Bae, *J. Controlled Release*, 2014, 190, 451-464.
22. K. D. Patel, R. K. Singh and H.-W. Kim, *Materials Horizons*, 2019, 6, 434-469.
23. V. Vermeeren, S. Wenmackers, P. Wagner and L. Michiels, *Sensors*, 2009, 9, 5600-5636.
24. H.-C. Chang, W. W.-W. Hsiao and M.-C. Su, *Fluorescent Nanodiamonds*, John Wiley & Sons, 2018.
25. J. I. PANKOVE and C. Qiu, *Synthetic Diamond*, 1994, 401-418.
26. Y. Y. Hui and H. C. Chang, *J. Chin. Chem. Soc. (Taipei, Taiwan)*, 2014, 61, 67-76.
27. A. Haque and S. Sumaiya, *J. manuf. mater.*, 2017, 1, 6.
28. G. Davies, *J Phys C Solid State Phys*, 1979, 12, 2551.
29. G. Davies and M. Hamer, *Proc. Math. Phys. Eng. Sci.*, 1976, 348, 285-298.
30. A. Collins, M. Thomaz and M. I. B. Jorge, *J Phys C Solid State Phys*, 1983, 16, 2177.
31. G. Liaugaudas, G. Davies, K. Suhling, R. Khan and D. Evans, *J. Phys.: Condens. Matter*, 2012, 24, 435503.
32. A. T. Collins, A. Connor, C.-H. Ly, A. Shareef and P. M. Spear, *J. Appl. Phys.*, 2005, 97, 083517.
33. L. Rondin, G. Dantelle, A. Slablab, F. Grosshans, F. Treussart, P. Bergonzo, S. Perruchas, T. Gacoin, M. Chaigneau and H.-C. Chang, *Phys. Rev. B: Condens. Matter Mater. Phys.*, 2010, 82, 115449.
34. T. Gaebel, M. Domhan, C. Wittmann, I. Popa, F. Jelezko, J. Rabeau, A. Greentree, S. Prawer, E.

- Trajkov and P. R. Hemmer, *Appl. Phys. B: Lasers Opt.*, 2006, 82, 243-246.
35. M. Irie, *Chem. Rev.*, 2000, 100, 1683-1684.
 36. Y. Mita, *Phys. Rev. B: Condens. Matter Mater. Phys.*, 1996, 53, 11360.
 37. K. Iakoubovskii, G. Adriaenssens and M. Nesladek, *J. Phys.: Condens. Matter*, 2000, 12, 189.
 38. N. Aslam, G. Waldherr, P. Neumann, F. Jelezko and J. Wrachtrup, *New J. Phys.* 2013, 15, 013064.
 39. Y. Doi, T. Makino, H. Kato, D. Takeuchi, M. Ogura, H. Okushi, H. Morishita, T. Tashima, S. Miwa and S. Yamasaki, *Phys. Rev. X*, 2014, 4, 011057.
 40. K.-M. Fu, C. Santori, P. Barclay and R. Beausoleil, *Appl. Phys. Lett.*, 2010, 96, 121907.
 41. P. Siyushev, H. Pinto, M. Vörös, A. Gali, F. Jelezko and J. Wrachtrup, *Phys. Rev. Lett.*, 2013, 110, 167402.
 42. M. W. Doherty, N. B. Manson, P. Delaney, F. Jelezko, J. Wrachtrup and L. C. Hollenberg, *Phys. Rep.*, 2013, 528, 1-45.
 43. I. Gordon Davies, *INSPEC publication, Institution of Electrical Engineers*, 1994.
 44. A. Gruber, A. Dräbenstedt, C. Tietz, L. Fleury, J. Wrachtrup and C. Von Borczyskowski, *Science*, 1997, 276, 2012-2014.
 45. K. Ohashi, T. Rosskopf, H. Watanabe, M. Loretz, Y. Tao, R. Hauert, S. Tomizawa, T. Ishikawa, J. Ishi-Hayase and S. Shikata, *Nano Lett.*, 2013, 13, 4733-4738.
 46. M. S. Grinolds, S. Hong, P. Maletinsky, L. Luan, M. D. Lukin, R. L. Walsworth and A. Yacoby, *Nat. Phys.*, 2013, 9, 215-219.
 47. T. Staudacher, F. Shi, S. Pezzagna, J. Meijer, J. Du, C. A. Meriles, F. Reinhard and J. Wrachtrup, *Science*, 2013, 339, 561-563.
 48. E. Van Oort and M. Glasbeek, *Chem. Phys. Lett.*, 1990, 168, 529-532.
 49. F. Dolde, H. Fedder, M. W. Doherty, T. Nöbauer, F. Rempp, G. Balasubramanian, T. Wolf, F. Reinhard, L. C. Hollenberg and F. Jelezko, *Nat. Phys.*, 2011, 7, 459-463.
 50. L. P. McGuinness, Y. Yan, A. Stacey, D. A. Simpson, L. T. Hall, D. Maclaurin, S. Prawer, P. Mulvaney, J. Wrachtrup and F. Caruso, *Nat. Nanotechnol.*, 2011, 6, 358-363.
 51. R. Epstein, F. Mendoza, Y. Kato and D. Awschalom, *Nat. Phys.*, 2005, 1, 94-98.
 52. V. M. Acosta, E. Bauch, M. P. Ledbetter, A. Waxman, L.-S. Bouchard and D. Budker, *Phys. Rev. Lett.*, 2010, 104, 070801.
 53. D. M. Toyli, F. Charles, D. J. Christle, V. V. Dobrovitski and D. D. Awschalom, *Proc. Natl. Acad. Sci. U. S. A.*, 2013, 110, 8417-8421.
 54. G. Kucsko, P. C. Maurer, N. Y. Yao, M. Kubo, H. J. Noh, P. K. Lo, H. Park and M. D. Lukin, *Nature*, 2013, 500, 54-58.
 55. M. W. Doherty, V. V. Struzhkin, D. A. Simpson, L. P. McGuinness, Y. Meng, A. Stacey, T. J. Karle, R. J. Hemley, N. B. Manson and L. C. Hollenberg, *Phys. Rev. Lett.*, 2014, 112, 047601.
 56. N. R. Greiner, D. Phillips, J. Johnson and F. Volk, *Nature*, 1988, 333, 440-442.
 57. J. Rabeau, A. Stacey, A. Rabeau, S. Prawer, F. Jelezko, I. Mirza and J. Wrachtrup, *Nano Lett.*, 2007, 7, 3433-3437.
 58. A. K. Khachatryan, S. Aloyan, P. May, R. Sargsyan, V. Khachatryan and V. Baghdasaryan, *Diamond Relat. Mater.*, 2008, 17, 931-936.
 59. J.-P. Boudou, P. A. Curmi, F. Jelezko, J. Wrachtrup, P. Aubert, M. Sennour, G. Balasubramanian, R. Reuter, A. Thorel and E. Gaffet, *Nanotechnology*, 2009, 20, 235602.
 60. S. Osswald, J. Chmiola and Y. Gogotsi, *Carbon*, 2012, 50, 4880-4886.
 61. M. Amsler, J. A. Flores-Livas, L. Lehtovaara, F. Balima, S. A. Ghasemi, D. Machon, S. Pailhes, A.

- Willand, D. Caliste and S. Botti, *Phys. Rev. Lett.*, 2012, 108, 065501.
62. J. Xiao, G. Ouyang, P. Liu, C. Wang and G. Yang, *Nano Lett.*, 2014, 14, 3645-3652.
 63. F. Gorrini, M. Cazzanelli, N. Bazzanella, R. Edla, M. Gemmi, V. Cappello, J. David, C. Dorigoni, A. Bifone and A. Miotello, *Sci. Rep.*, 2016, 6, 1-9.
 64. C.-H. Nee, S.-L. Yap, T.-Y. Tou, H.-C. Chang and S.-S. Yap, *Sci. Rep.*, 2016, 6, 33966.
 65. D. Amans, M. Diouf, J. Lam, G. Ledoux and C. Dujardin, *J. Colloid Interface Sci.*, 2017, 489, 114-125.
 66. O. Shenderova, *Detonation nanodiamonds: science and applications*, CRC Press, 2014.
 67. V. Y. Dolmatov, *Russ. Chem. Rev.*, 2007, 76, 339.
 68. E. Ōsawa, *Pure Appl. Chem.*, 2008, 80, 1365-1379.
 69. V. Y. Dolmatov, *Russ. Chem. Rev.*, 2001, 70, 607-626.
 70. V. N. Mochalin, O. Shenderova, D. Ho and Y. Gogotsi, *Nat. Nanotechnol.*, 2012, 7, 11-23.
 71. A. Krueger, M. Ozawa, G. Jarre, Y. Liang, J. Stegk and L. Lu, *Phys. Status Solidi*, 2007, 204, 2881-2887.
 72. A. Beveratos, R. Brouri, T. Gacoin, J.-P. Poizat and P. Grangier, *Phys. Rev. A*, 2001, 64, 061802.
 73. K. Iakoubovskii, I. Kiflawi, K. Johnston, A. Collins, G. Davies and A. Stesmans, *Physica B: Condensed Matter*, 2003, 340, 67-75.
 74. S. Kumar, M. Nehra, D. Kedia, N. Dilbaghi, K. Tankeshwar and K.-H. Kim, *Carbon*, 2019, 143, 678-699.
 75. O. A. Shenderova, A. I. Shames, N. A. Nunn, M. D. Torelli, I. Vlasov and A. Zaitsev, *J. Vac. Sci. Technol.*, 2019, 37, 030802.
 76. I. Rehor and P. Cigler, *Diamond Relat. Mater.*, 2014, 46, 21-24.
 77. N. Nunn, M. Torelli, G. McGuire and O. Shenderova, *Curr. Opin. Solid State Mater. Sci.*, 2017, 21, 1-9.
 78. M. H. Alkahtani, F. Alghannam, L. Jiang, A. A. Rampersaud, R. Brick, C. L. Gomes, M. O. Scully and P. R. Hemmer, *Opt. Lett.*, 2018, 43, 3317-3320.
 79. V. A. Davydov, A. Rakhmanina, S. Lyapin, I. Ilichev, K. N. Boldyrev, A. Shiryaev and V. N. Agafonov, *JETP letters*, 2014, 99, 585-589.
 80. E. A. Ekimov, O. S. Kudryavtsev, A. A. Khomich, O. I. Lebedev, T. A. Dolenko and I. I. Vlasov, *Adv. Mater.*, 2015, 27, 5518-5522.
 81. E. A. Ekimov, O. S. Kudryavtsev, N. E. Mordvinova, O. I. Lebedev and I. I. Vlasov, *ChemNanoMat*, 2018, 4, 269-273.
 82. S. Park, I. I. Abate, J. Liu, C. Wang, J. E. Dahl, R. M. Carlson, L. Yang, V. B. Prakapenka, E. Greenberg and T. P. Devereaux, *Sci. Adv.*, 2020, 6, eaay9405.
 83. H. Zeng, X. W. Du, S. C. Singh, S. A. Kulinich, S. Yang, J. He and W. Cai, *Adv. Funct. Mater.*, 2012, 22, 1333-1353.
 84. J. Wang, C. Zhang, X. Zhong and G. Yang, *Chem. Phys. Lett.*, 2002, 361, 86-90.
 85. G. Yang, *Progress in Materials Science*, 2007, 52, 648-698.
 86. M. Baidakova, Y. A. Kukushkina, A. Sitnikova, M. Yagovkina, D. Kirilenko, V. Sokolov, M. Shestakov, A. Y. Vul, B. Zousman and O. Levinson, *Phys. Solid State*, 2013, 55, 1747-1753.
 87. C. Wang, P. Liu, H. Cui and G. Yang, *Appl. Phys. Lett.*, 2005, 87, 201913.
 88. B. Zousman and O. Levinson, in *Nanodiamond*, Royal Society of Chemistry, 2014, pp. 112-127.
 89. S. Hu, J. Sun, X. Du, F. Tian and L. Jiang, *Diamond Relat. Mater.*, 2008, 17, 142-146.
 90. E. Kozlova, A. Chernysh, V. Moroz, O. Gudkova, V. Sergunova and A. Kuzovlev, *Sci. Rep.*, 2014, 4,

6033.

91. K. Adach, M. Fijalkowski, G. Gajek, J. Skolimowski, R. Kontek and A. Blaszczyk, *Chem.-Biol. Interact.*, 2016, 254, 156-166.
92. M. Ibrahim, Y. Xue, M. Ostermann, A. Sauter, D. Steinmueller - Nethl, S. Schweetberg, A. Krueger, M. R. Cimpan and K. Mustafa, *J. Biomed. Mater. Res. A*, 2018, 106, 1697-1707.
93. V. Paget, J. Sergent, R. Grall, S. Altmeyer-Morel, H. Girard, T. Petit, C. Gesset, M. Mermoux, P. Bergonzo and J.-C. Arnault, *Nanotoxicology*, 2014, 8, 46-56.
94. V. Vijayanthimala, P.-Y. Cheng, S.-H. Yeh, K.-K. Liu, C.-H. Hsiao, J.-I. Chao and H.-C. Chang, *Biomaterials*, 2012, 33, 7794-7802.
95. S.-J. Yu, M.-W. Kang, H.-C. Chang, K.-M. Chen and Y.-C. Yu, *J. Am. Chem. Soc.*, 2005, 127, 17604-17605.
96. V. Vijayanthimala, Y.-K. Tzeng, H.-C. Chang and C.-L. Li, *Nanotechnology*, 2009, 20, 425103.
97. H. H. Lin, H. W. Lee, R. J. Lin, C. W. Huang, Y. C. Liao, Y. T. Chen, J. M. Fang, T. C. Lee, A. L. Yu and H. C. Chang, *Small*, 2015, 11, 4394-4402.
98. N. Mohan, C.-S. Chen, H.-H. Hsieh, Y.-C. Wu and H.-C. Chang, *Nano Lett.*, 2010, 10, 3692-3699.
99. C.-C. Chang, B. Zhang, C.-Y. Li, C.-C. Hsieh, G. Duclos, F. Treussart and H.-C. Chang, 2012.
100. L. Marcon, F. Riquet, D. Vicogne, S. Szunerits, J.-F. Bodart and R. Boukherroub, *J. Mater. Chem.*, 2010, 20, 8064-8069.
101. Y. Yuan, Y. Chen, J.-H. Liu, H. Wang and Y. Liu, *Diamond Relat. Mater.*, 2009, 18, 95-100.
102. X. Zhang, J. Yin, C. Kang, J. Li, Y. Zhu, W. Li, Q. Huang and Z. Zhu, *Toxicol. Lett.*, 2010, 198, 237-243.
103. L. Moore, J. Yang, T. T. H. Lan, E. Osawa, D.-K. Lee, W. D. Johnson, J. Xi, E. K.-H. Chow and D. Ho, *ACS Nano*, 2016, 10, 7385-7400.
104. D.-K. Lee, T. Kee, Z. Liang, D. Hsiou, D. Miya, B. Wu, E. Osawa, E. K.-H. Chow, E. C. Sung and M. K. Kang, *Proc. Nat. Acad. Sci. U.S.A.*, 2017, 114, E9445-E9454.
105. C. Hong, D. Song, D.-K. Lee, L. Lin, H. C. Pan, D. Lee, P. Deng, Z. Liu, D. Hadaya and H.-L. Lee, *Proc. Nat. Acad. Sci. U.S.A.*, 2017, 114, E7218-E7225.
106. H. Huang, E. Pierstorff, E. Osawa and D. Ho, *Nano Lett.*, 2007, 7, 3305-3314.
107. E. K. Chow, X.-Q. Zhang, M. Chen, R. Lam, E. Robinson, H. Huang, D. Schaffer, E. Osawa, A. Goga and D. Ho, *Sci. Transl. Med.*, 2011, 3, 73ra21-73ra21.
108. L.-L. Landeros-Martínez, D. Chavez-Flores, E. Orrantia-Borunda and N. Flores-Holguin, *Journal of Nanomaterials*, 2016, 2016.
109. B. Guan, F. Zou and J. Zhi, *Small*, 2010, 6, 1514-1519.
110. M. Chen, E. D. Pierstorff, R. Lam, S.-Y. Li, H. Huang, E. Osawa and D. Ho, *ACS Nano*, 2009, 3, 2016-2022.
111. R. A. Shimkunas, E. Robinson, R. Lam, S. Lu, X. Xu, X.-Q. Zhang, H. Huang, E. Osawa and D. Ho, *Biomaterials*, 2009, 30, 5720-5728.
112. P. Reineck, A. Francis, A. Orth, D. W. M. Lau, R. D. V. Nixon - Luke, I. D. Rastogi, W. A. W. Razali, N. M. Cordina, L. M. Parker and V. K. A. Sreenivasan, *Advanced Optical Materials*, 2016, 4, 1549-1557.
113. S. W. Hell and J. Wichmann, *Opt. Lett.*, 1994, 19, 780-782.
114. K. I. Willig, S. O. Rizzoli, V. Westphal, R. Jahn and S. W. Hell, *Nature*, 2006, 440, 935-939.
115. Y. K. Tzeng, O. Faklaris, B. M. Chang, Y. Kuo, J. H. Hsu and H. C. Chang, *Angew. Chem. Int. Ed.*, 2011, 50, 2262-2265.

116. S. Arroyo-Camejo, M.-P. Adam, M. Besbes, J.-P. Hugonin, V. Jacques, J.-J. Greffet, J.-F. Roch, S. W. Hell and F. Treussart, *ACS Nano*, 2013, 7, 10912-10919.
117. C. W. Chang, D. Sud and M. A. Mycek, *Methods Cell Biol.*, 2007, 81, 495-524.
118. O. Faklaris, D. Garrot, V. Joshi, F. Druon, J. P. Boudou, T. Sauvage, P. Georges, P. A. Curmi and F. Treussart, *Small*, 2008, 4, 2236-2239.
119. M. H. Alkahtani, F. Alghannam, L. Jiang, A. Almethen, A. A. Rampersaud, R. Brick, C. L. Gomes, M. O. Scully and P. R. Hemmer, *Nanophotonics*, 2018, 7, 1423-1453.
120. C. Y. Fang, V. Vaijayanthimala, C. A. Cheng, S. H. Yeh, C. F. Chang, C. L. Li and H. C. Chang, *Small*, 2011, 7, 3363-3370.
121. T.-J. Wu, Y.-K. Tzeng, W.-W. Chang, C.-A. Cheng, Y. Kuo, C.-H. Chien, H.-C. Chang and J. Yu, *Nat. Nanotechnol.*, 2013, 8, 682-689.
122. L.-J. Su, M.-S. Wu, Y. Y. Hui, B.-M. Chang, L. Pan, P.-C. Hsu, Y.-T. Chen, H.-N. Ho, Y.-H. Huang and T.-Y. Ling, *Sci. Rep.*, 2017, 7, 45607.
123. P. Moscariello, M. Raabe, W. Liu, S. Bernhardt, H. Qi, U. Kaiser, Y. Wu, T. Weil, H. J. Luhmann and J. Hedrich, *Small*, 2019, 15, 1902992.
124. F.-J. Hsieh, Y.-W. Chen, Y.-K. Huang, H.-M. Lee, C.-H. Lin and H.-C. Chang, *Anal. Chem.*, 2018, 90, 1566-1571.
125. S. Han, M. Raabe, L. Hodgson, J. Mantell, P. Verkade, T. Lasser, K. Landfester, T. Weil and I. Lieberwirth, *Nano Lett.*, 2019, 19, 2178-2185.
126. D. E. Waddington, M. Sarracanie, H. Zhang, N. Salameh, D. R. Glenn, E. Rej, T. Gaebel, T. Boele, R. L. Walsworth and D. J. Reilly, *Nat. Commun.*, 2017, 8, 1-8.
127. A. Ajoy, K. Liu, R. Nazaryan, X. Lv, P. R. Zangara, B. Safvati, G. Wang, D. Arnold, G. Li and A. Lin, *Sci. Adv.*, 2018, 4, eaar5492.
128. J.-P. Tetienne, T. Hingant, L. Rondin, A. Cavaillès, L. Mayer, G. Dantelle, T. Gacoin, J. Wrachtrup, J.-F. Roch and V. Jacques, *Phys. Rev. B: Condens. Matter Mater. Phys.*, 2013, 87, 235436.
129. A. Ermakova, G. Pramanik, J.-M. Cai, G. Algara-Siller, U. Kaiser, T. Weil, Y.-K. Tzeng, H.-C. Chang, L. McGuinness and M. B. Plenio, *Nano Lett.*, 2013, 13, 3305-3309.
130. S. Kaufmann, D. A. Simpson, L. T. Hall, V. Perunicic, P. Senn, S. Steinert, L. P. McGuinness, B. C. Johnson, T. Ohshima and F. Caruso, *Proc. Nat. Acad. Sci. U.S.A.*, 2013, 110, 10894-10898.
131. Y.-K. Tzeng, P.-C. Tsai, H.-Y. Liu, O. Y. Chen, H. Hsu, F.-G. Yee, M.-S. Chang and H.-C. Chang, *Nano Lett.*, 2015, 15, 3945-3952.
132. Y. Kamei, M. Suzuki, K. Watanabe, K. Fujimori, T. Kawasaki, T. Deguchi, Y. Yoneda, T. Todo, S. Takagi and T. Funatsu, *Nat. Methods*, 2009, 6, 79-81.
133. T. D. Vreugdenburg, C. D. Willis, L. Mundy and J. E. Hiller, *Breast Cancer Res. Treat.*, 2013, 137, 665-676.
134. A. Schroeder, D. A. Heller, M. M. Winslow, J. E. Dahlman, G. W. Pratt, R. Langer, T. Jacks and D. G. Anderson, *Nat. Rev. Cancer*, 2012, 12, 39-50.
135. P.-C. Tsai, O. Y. Chen, Y.-K. Tzeng, Y. Y. Hui, J. Y. Guo, C.-C. Wu, M.-S. Chang and H.-C. Chang, *EPJ Quantum Technol.*, 2015, 2, 1-12.
136. D. A. Simpson, E. Morrisroe, J. M. McCoey, A. H. Lombard, D. C. Mendis, F. Treussart, L. T. Hall, S. Petrou and L. C. Hollenberg, *ACS Nano*, 2017, 11, 12077-12086.
137. V. Petrakova, I. Rehor, J. Stursa, M. Ledvina, M. Nesladek and P. Cigler, *Nanoscale*, 2015, 7, 12307-12311.
138. T. Fujisaku, R. Tanabe, S. Onoda, R. Kubota, T. F. Segawa, F. T.-K. So, T. Ohshima, I. Hamachi, M.

- Shirakawa and R. Igarashi, *ACS Nano*, 2019, 13, 11726-11732.
139. R. Schirhagl, K. Chang, M. Loretz and C. L. Degen, *Annu. Rev. Phys. Chem.*, 2014, 65, 83-105.
 140. Y.-R. Chang, H.-Y. Lee, K. Chen, C.-C. Chang, D.-S. Tsai, C.-C. Fu, T.-S. Lim, Y.-K. Tzeng, C.-Y. Fang and C.-C. Han, *Nat. Nanotechnol.*, 2008, 3, 284-288.
 141. O. Shenderova, A. Koscheev, N. Zaripov, I. Petrov, Y. Skryabin, P. Detkov, S. Turner and G. Van Tendeloo, *J. Phys. Chem. C*, 2011, 115, 9827-9837.
 142. L.-C. L. Huang and H.-C. Chang, *Langmuir*, 2004, 20, 5879-5884.
 143. J.-I. Chao, E. Perevedentseva, P.-H. Chung, K.-K. Liu, C.-Y. Cheng, C.-C. Chang and C.-L. Cheng, *Biophys. J.*, 2007, 93, 2199-2208.
 144. T.-T.-B. Nguyen, H.-C. Chang and V. W.-K. Wu, *Diamond Relat. Mater.*, 2007, 16, 872-876.
 145. I. Pozdnyakova, *Phys. Solid State*, 2004, 46, 758-760.
 146. T. Skaltsas, S. Pispas and N. Tagmatarchis, *Mater. Res. Express*, 2015, 2, 115005.
 147. H.-D. Wang, C. H. Niu, Q. Yang and I. Badea, *Nanotechnology*, 2011, 22, 145703.
 148. X. Kong, L. Huang, C.-M. Hsu, W.-H. Chen, C.-C. Han and H.-C. Chang, *Anal. Chem.*, 2005, 77, 259-265.
 149. B. M. Chang, H. H. Lin, L. J. Su, W. D. Lin, R. J. Lin, Y. K. Tzeng, R. T. Lee, Y. C. Lee, A. L. Yu and H. C. Chang, *Adv. Funct. Mater.*, 2013, 23, 5737-5745.
 150. I. Kovalenko, D. G. Bucknall and G. Yushin, *Adv. Funct. Mater.*, 2010, 20, 3979-3986.
 151. X.-Q. Zhang, M. Chen, R. Lam, X. Xu, E. Osawa and D. Ho, *ACS Nano*, 2009, 3, 2609-2616.
 152. Q. Zhang, V. N. Mochalin, I. Neitzel, I. Y. Knoke, J. Han, C. A. Klug, J. G. Zhou, P. I. Lelkes and Y. Gogotsi, *Biomaterials*, 2011, 32, 87-94.
 153. Y. Wu, A. Ermakova, W. Liu, G. Pramanik, T. M. Vu, A. Kurz, L. McGuinness, B. Naydenov, S. Hafner and R. Reuter, *Adv. Funct. Mater.*, 2015, 25, 6576-6585.
 154. X. Zhang, C. Fu, L. Feng, Y. Ji, L. Tao, Q. Huang, S. Li and Y. Wei, *Polymer*, 2012, 53, 3178-3184.
 155. L. Zhao, T. Takimoto, M. Ito, N. Kitagawa, T. Kimura and N. Komatsu, *Angew. Chem. Int. Ed.*, 2011, 50, 1388-1392.
 156. L. Zhao, Y. Nakae, H. Qin, T. Ito, T. Kimura, H. Kojima, L. Chan and N. Komatsu, *Beilstein J. Org. Chem.*, 2014, 10, 707-713.
 157. L. Zhao, Y.-H. Xu, T. Akasaka, S. Abe, N. Komatsu, F. Watari and X. Chen, *Biomaterials*, 2014, 35, 5393-5406.
 158. L. Zhao, Y. H. Xu, H. Qin, S. Abe, T. Akasaka, T. Chano, F. Watari, T. Kimura, N. Komatsu and X. Chen, *Adv. Funct. Mater.*, 2014, 24, 5348-5357.
 159. L. Zhao, A. Shiino, H. Qin, T. Kimura and N. Komatsu, *J. Nanosci. Nanotechnol.*, 2015, 15, 1076-1082.
 160. A. Krueger and D. Lang, *Adv. Funct. Mater.*, 2012, 22, 890-906.
 161. C. Presti, J. G. Alauzun, D. Laurencin and P. H. Mutin, *Langmuir*, 2014, 30, 9239-9245.
 162. W. S. Yeap, S. Chen and K. P. Loh, *Langmuir*, 2009, 25, 185-191.
 163. H. Girard, J.-C. Arnault, S. Perruchas, S. Saada, T. Gacoin, J.-P. Boilot and P. Bergonzo, *Diamond Relat. Mater.*, 2010, 19, 1117-1123.
 164. P. Betz and A. Krueger, *ChemPhysChem*, 2012, 13, 2578-2584.
 165. A. Krueger, in *Nanodiamonds*, Elsevier, 2017, pp. 183-242.
 166. A. Krüger, Y. Liang, G. Jarre and J. Stegk, *J. Mater. Chem.*, 2006, 16, 2322-2328.
 167. I. Rehor, J. Slegerova, J. Kucka, V. Proks, V. Petrakova, M. P. Adam, F. Treussart, S. Turner, S. Bals and P. Sacha, *Small*, 2014, 10, 1106-1115.

168. N. Prabhakar, T. Näreoja, E. von Haartman, D. Ş. Karaman, H. Jiang, S. Koho, T. A. Dolenko, P. E. Hänninen, D. I. Vlasov and V. G. Ralchenko, *Nanoscale*, 2013, 5, 3713-3722.
169. A. Bumb, S. K. Sarkar, N. Billington, M. W. Brechbiel and K. C. Neuman, *J. Am. Chem. Soc.*, 2013, 135, 7815-7818.
170. D.-M. Liu and I. Chen, *Acta Mater.*, 1999, 47, 4535-4544.
171. J. Slegerova, M. Hajek, I. Rehor, F. Sedlak, J. Stursa, M. Hruby and P. Cigler, *Nanoscale*, 2015, 7, 415-420.
172. P. M. Dove, N. Han, A. F. Wallace and J. J. De Yoreo, *Proc. Nat. Acad. Sci. U.S.A.*, 2008, 105, 9903-9908.
173. J. P. Icenhower and P. M. Dove, *Geochim. Cosmochim. Acta*, 2000, 64, 4193-4203.

2. Motivation and conceptual design

The physical nature of NDs makes them a versatile tool for a number of applications in the biological field, as discussed in introduction part. However, there are still challenges existing. Working as drug delivery platform, the stability, loading capacity, and controllable releasing is often limited by the surface property of NDs. because the drugs are usually adsorbed to the surface of NDs due to the inert surface of raw NDs. In the field of bioimaging, it is necessary to have the specifically targeting ability and the bioimaging agent can be deliver to aimed sites, so it is essential to introduce the targeting moieties to the surface of NDs and stabilize the bioimaging agent in physiological condition. In the application of quantum sensing, ideally, NDs need be monodispersed and the thickness of the coating should be very thin, the different NDs weak the sensing ability each other. And the strength of magnetic signal decrease as the cube of the shell thickness, to achieve good sensitivity, it is essential to stabilize the NDs and have the coating as thin as possible. As mentioned in introduction part, carboxylated NDs are the most common products, after preparation, the oxidation treatments are used to remove the metal impurities and the graphite layers. The carboxylates can stabilize the NDs in water but the NDs will aggregate once the ions strength and/or pH of the solution changes, or the carboxylates on the surface of NDs are covalently binding to functional moieties. In addition, to endow the NDs multi-functionality such as targeting, therapeutic, sensing abilities will be a favor. Therefore, it is crucially to modify the surface properties of NDs. To date, various methods for the production of functional NDs have been reported and the availability of surface groups for all kinds of subsequent functionalization has significantly improved. However, most of the approaches can only be used in limited areas and not appropriate for different fields.

In this dissertation, we are aiming to create thin coatings which can not only stabilize NDs but also enable NDs the potential of multi-functionality by covalent and/or non-covalent post-functionalization. Two nature-inspired coatings from mussel foot proteins and virus were used and one facile adsorption-crosslinking strategy was developed (Figure 2).

In the first approach, inspired from “protein glue” of mussel foot proteins, the dopamine can sticky and polymerize on various surfaces easily and provide many functional groups including amines, alcohols, and conjugated Michael acceptors for post-functionalization. To further increase the hydrophilicity and functional groups, neurotransmitter L-3,4-dihydroxyphenylalanine (L-DOPA), the derivative of dopamine, are firstly used to modified the surface of NDs. Furthermore, the self-polymerization of L-DOPA is relatively easily to control and obtain appropriate coating thickness. The polydopamine is reported as photothermal agent, the poly(L-DOPA) coated NDs may allow us to combine the photothermal with bioimaging simultaneously. Moreover, attaching transferrin and the small molecular dye ICG, will enhance the cell uptake and amplify the photothermal effect. The potential concerns for the poly(L-DOPA) maybe balance the coating thickness, stability, and optical properties. The poly(L-DOPA) have a lot of aromatic structures which may quench the fluorescence of NDs and weak the sensing ability. The coating thickness may affect the stability of NDs.

In the second approach, capsid proteins from cowpea chlorotic mottle virus (CCMV) have been applied to encapsulate NDs within a thin shell of adsorbed CCMV capsid proteins (CPs). Viruses are evolutionary optimized carrier systems, which is stable in physiological condition and can efficiently enter cells. Moreover, the capsid of virus is very thin, the thickness of CCMV capsid is 4 nm, and the residue groups of amino acids from capsid proteins provide large amount of post-functional groups. The CPs coated NDs (ND-CP) can stable NDs and boost the cell uptake and later work for bioimaging and understand the long-term intracellular trafficking study. The potential concerns are whether the CPs will assemble in the surface of NDs, form thin coating and stabilize NDs in buffer condition for a long time, and whether the ND-CP still keep the advantages of the CCMV.

In the third approach, we would like to create a universal method which can stabilize NDs, endow the multi-functionality, and keep the physical properties of NDs for quantum sensing. In the above two coating processes, the small molecules or protein was absorbed to the surface of NDs and then the adsorbed coating was “crosslinked”

either by polymerization or protein-protein interaction. The NDs was enclosed in the polymer or protein cage. So the shell stabilize and endow the post-functional ability. The hyperbranched polyethyleneimine (PEI), a highly branched, cationic polymer with multiple primary/secondary amino groups, was selected as precoating molecules considering it will easily adsorb on the negatively charged surface of NDs. Then the 4-armed polyethyleneglycol based cross-linkers, was used to crosslink the precoated PEI and form nanogel shell to stabilize the NDs. Because the polyethyleneglycol has excellent biocompatibility and solubility. The amine residues from PEI in the nanogel coated NDs (ND-NG) can be used for multi-functionality. This strategy will give the community ideas how to design appropriate coatings for their special applications. The researchers can choose different procoating molecules which have aimed functional groups in addition, the crosslinking agents can be also designed and support functional groups for further use. All of the agents in this approach can be replaced according to their own requirements. Then ND-NG were further modified with paramagnetic ion, Gd^{3+} , and ferritin non-covalently to test the nanoscale sensing ability, modified with photodynamic agent (Ruthenium complex) covalently to show the combination of bioimaging and photodynamic therapy. Moreover, the ND-NG were modified with photothermal agent (ICG) to prove the nanoscale temperature-sensing ability in living cells which will pave the understanding of the role of intracellular temperature in thermal biology.

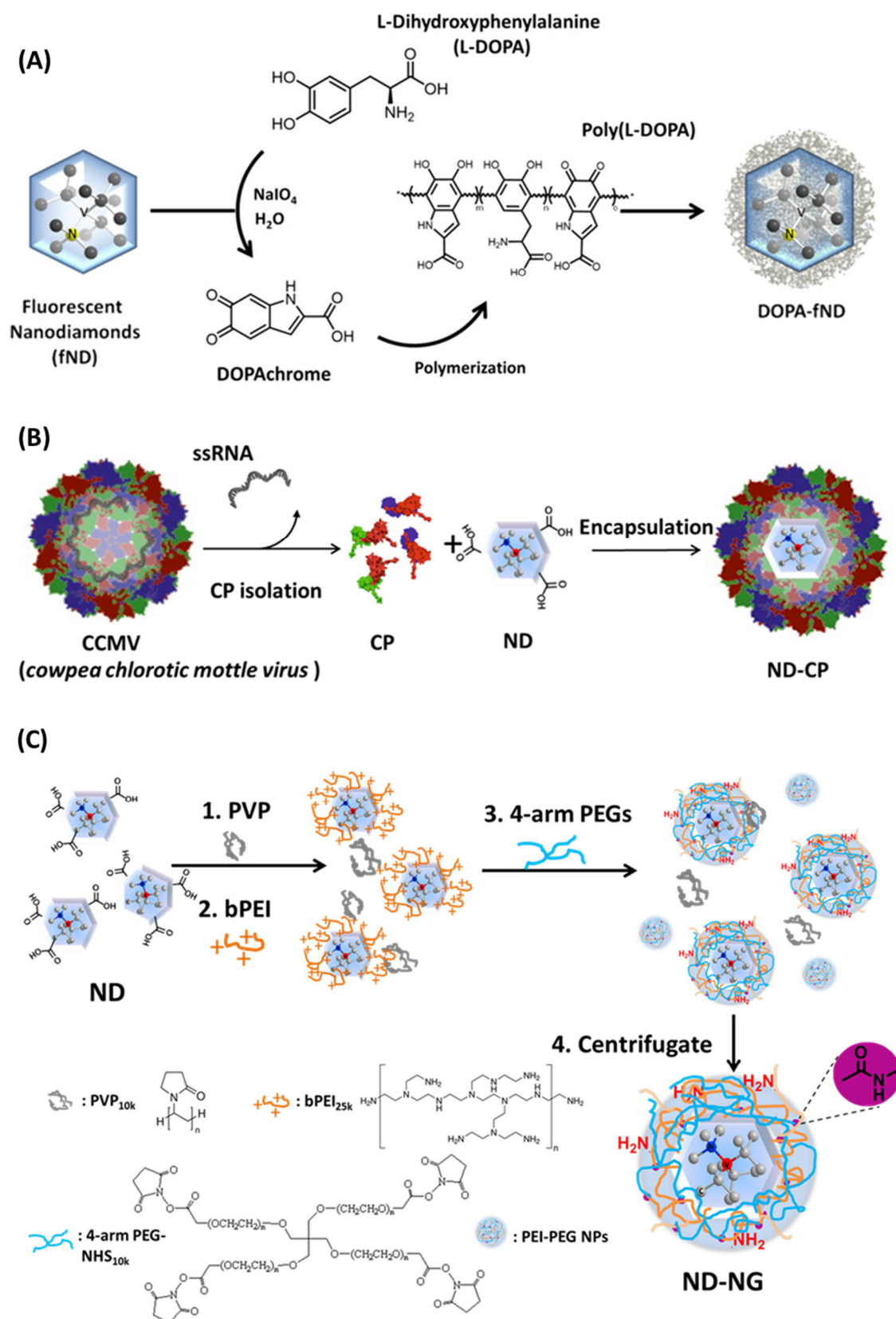


Figure 2. (A) Poly(L-DOPA) coated nanodiamonds system. (B) *Cowpea chlorotic mottle virus* capsid protein encapsulated fluorescent nanodiamonds system. (C) Nanodiamond-nanogel system prepared by adsorption-crosslinking strategy.

3. Transferrin-Coated Nanodiamond–Drug Conjugates for Milliwatt Photothermal Applications

Authors

Sean Harvey, ⁺ Marco Raabe, ⁺ Anna Ermakova, **Yingke Wu**, Todd Zapata, Chaojian Chen, Hao Lu, Fedor Jelezko, David YW Ng, Tanja Weil*

S.Harvey and M.Raabe are shared first author, *corresponding author

Copyright:

Published in Adv. Ther. 2.11 (2019): 1900067.

The following is reproduced with the permission from Copyright (2019) WILEY-VCH Verlag GmbH & Co. KGaA, Weinheim, This work is licensed under a Creative Commons Attribution 4.0 International License.

Author Contributions

S. Harvey: Conducting polymerization of L-DOPA on fND. Conduction and study of poly(L-DOPA) formation by absorbance spectroscopy, FTIR and RAMAN spectroscopy. Analysis of XPS measurements. Integration of transferrin and ICG with poly(L-DOPA) coated fNDs. Conduction of photothermal measurements. Writing of the manuscript.

M. Raabe: DLS studies and analysis, interpretation and discussion of the results. Culturing, preparation and sample testing in cells. Conduction and interpretation of confocal microscopy. Conduction of photothermal measurements. Writing of the manuscript.

A. Ermakova: Conduction of fluorescence and ODMR measurements, interpretation and discussion on the results.

Y. Wu: Reproduced the poly(L-DOPA) coated NDs, performed the TEM measurement, writing and correcting the manuscript.

T. Zapata: Conduction of ODMR measurements.

C. Chen: TEM measurement.

H. Lu: Conduction of XPS measurements.

F. Jelezko: Acquiring funding for the project. Discussion of ODMR measurements.

D. Y. W. Ng: Discussion on the concept and results, writing and correcting the manuscript.

T. Weil: Acquiring funding for the project, design and discussion of the concept and results, writing and correcting the manuscript.

Abstract

Fluorescent nanodiamonds (fNDs) are unique carbon-based nanomaterials due to their outstanding optical and magnetic properties. However, realization of the full potential of fNDs is often limited by their processability because fNDs aggregate strongly in both organic and aqueous solutions. Therefore, robust and potentially universal coating strategies are urgently needed to address these limitations. Derived from mussel foot proteins, the polymerization of L-3,4-dihydroxyphenylalanine (L-DOPA) provides important surface functional groups including amines, carboxylic acid, alcohols, conjugated Michael acceptors. Herein, L-DOPA is polymerized on fNDs with a high control over the shell thickness. Photoluminescence and optically detected magnetic resonance (ODMR) studies reveal that the unique photophysical properties of fNDs are preserved after thin poly(L-DOPA) film coating. Subsequently, conjugation of transferrin, a heme protein that provides efficient receptor specific cellular transport, improves the colloidal stability and cellular uptake of the poly(L-DOPA) coated fNDs. The loading of FDA-approved indocyanine green (ICG) as a photothermal agent yields an integrated biohybrid material exhibiting an amplified photothermal effect in cells at very low energy intake (~ 90 mW/cm²).

3.1 Introduction

Among carbon based materials, fluorescent nanodiamonds (fNDs) are unique as they do not only possess excellent photoluminescence properties, but they are also very precise local sensors of magnetic and electric fields, temperature or mechanical forces.^{1,}

² These characteristics are predominantly derived from the defect centers in nanodiamonds where impurity atoms such as nitrogen³, silicon^{4,5}, germanium⁶ etc. are localized alongside lattice vacancies. Consequently, the type of such crystallographic defects defines its unique optical spectrum as well as spin properties. Hence, the optical behavior of fNDs is independent of its size, in contrast to other classes of nano-emitters such as quantum/carbon dots and gold nanoparticles.⁷ The best studied color center is the nitrogen-vacancy (NV) center.^{2,3,8-11} The remarkable properties of this atom-like defect in the diamond lattice allow application for high resolution magnetic (bio)sensing¹², energy transfer¹³, bioimaging¹² and even quantum computing technologies¹⁴. Due to this, in the presented work, nanodiamonds with NV centers were selected as base material for designing a potent theranostic system.

In order to achieve these aims, the processability of nanodiamonds (NDs) is a recurring challenge. The colloidal stability of NDs in solution, both organic and aqueous, is extremely poor and is further aggravated with the reduction in the size of the diamond particle.^{9,15} Hence, the capability to chemically introduce novel functions tends to be severely hampered by the aggregation of the NDs. To alleviate this primary issue, nanodiamond coating technologies have been developed, using adsorption mechanisms deriving from weak attractive forces (electrostatic, van der Waals, hydrogen bonding) and/or strong covalent interactions.^[8] However, these coating technologies have persistent difficulties due to batch to batch production variability impacting the surface composition of NDs. In addition, it is crucial to understand that the coating material has to fulfil many important criteria including 1) chemical multifunctionality, 2) reproducibility of the coating strategy on NDs from different sources and sizes, 3) colloidal stability of the fND conjugate in biological media and inside cells, 4) minimally affecting the photoluminescence and magnetic sensing capabilities.

While it is synthetically challenging for a coating methodology that performs consistently well regardless of surface properties, Nature has aptly demonstrated otherwise. Derived from mussel foot proteins, the polymerization of catechol pendant groups is the key for the attachment of mussel bivalves onto virtually any surface. Messersmith et al. first showed that polymers of catecholamines, in particular dopamine, can replicate the adhesiveness of the mussel foot¹⁶. The significance of polydopamine was quickly realized resting on its capability to adapt to various surface functions. This behavior was also observed for other catecholamines, such as L-3,4-dihydroxyphenylalanine (L-DOPA)¹⁷⁻²⁰ and norepinephrine²¹⁻²³. Chemically, polycatecholamine films possess important functional groups including amines, alcohols and conjugated Michael acceptors leading to a massive variety of post-functionalized surfaces^{16, 24, 25}. In this context, polydopamine has been demonstrated recently as a proof of concept to functionalize NDs^{26, 27}. Polydopamine-ND systems represent an attractive platform. However post-functionalization with e.g. polyethyleneglycol has been crucial due to the high adhesiveness of polydopamine that potentially contributes to the aggregation of the coated nanodiamonds, especially under physiological buffer conditions.^{28[28]} In comparison, L-DOPA contains an additional carboxylic group giving poly(L-DOPA) coatings a higher hydrophilicity compared to polydopamine^{18, 19}.

Herein, we show that poly(L-DOPA) does not only act as a polar and versatile bridging entity to conjugate multiple functional entities onto fNDs but also enhances its photothermal capability to develop a complex fND therapeutic platform. Herein, we establish the strategy of polymerization of L-DOPA on fNDs from different sources (FND Biotech, Microdiamant) by monitoring the kinetics of polymerization, the control over thickness and colloidal stability under physiological conditions. The effect of the poly(L-DOPA) coating on the photoluminescence and optically detected magnetic resonance (ODMR) were studied and these unique photophysical properties were preserved for fNDs with thin surface coating. Subsequently, the coated fNDs were further decorated by transferrin, a heme cell membrane protein involved in receptor-

specific cellular uptake that stabilizes the biohybrid in cellular media and the FDA-approved indocyanine green (ICG) as a photothermal agent. By localizing a high concentration of ICG in cellular vesicle nanoenvironments, we envision that the integrated material will provide high photothermal toxicity even at very low energy intake (Figure 3.1).

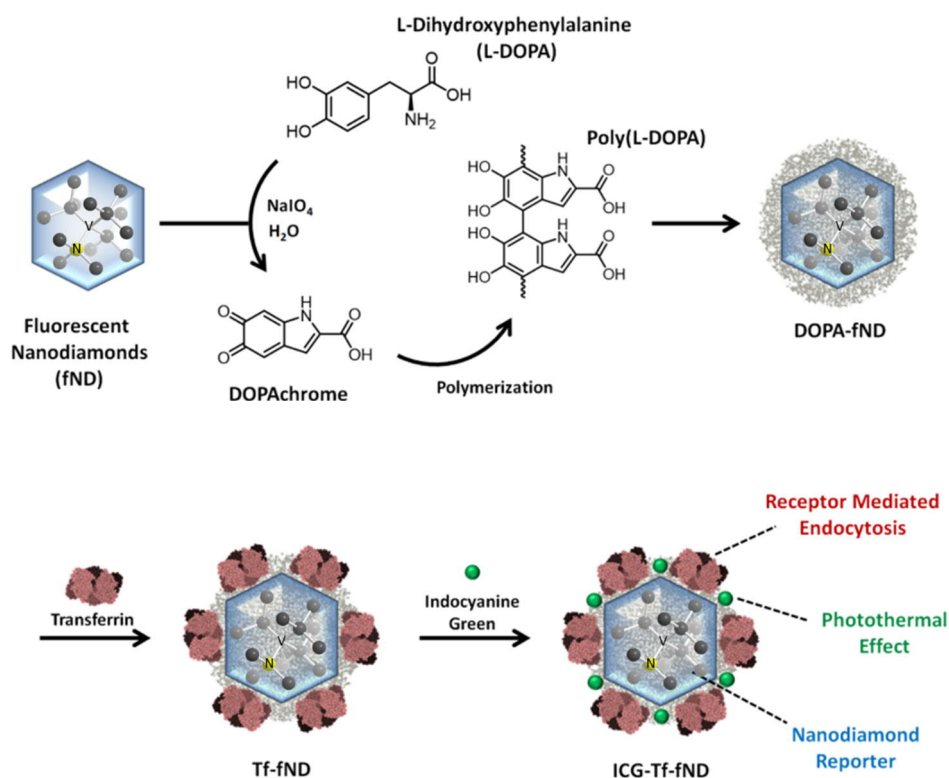


Figure 3.1 Schematic illustration of fND nanosystem preparation.

3.2 Results and Discussion

3.2.1. Preparation and characterization of L-DOPA coated nanodiamonds

Nanodiamonds with 35 nm average diameter were purchased from FND Biotech (Taiwan) and used without further surface treatment. Sodium periodate initiated polymerization of dopamine and L-DOPA in pure MilliQ water was used to avoid buffer salts, which are known to destabilize colloidal NDs.¹⁵ In addition, this method provides faster deposition times compared to polymerization in alkaline buffers²⁹⁻³¹ further reducing ND aggregation. In contrast to the well-established dopamine surface polymerization, L-DOPA provides an additional carboxylic group and poly(L-DOPA) coatings exhibit higher hydrophilicity compared to polydopamine^{18, 19}. We anticipate

that poly(L-DOPA) would show a greater potential in enhancing the aqueous stability of fNDs. In our experimental setup, 100 μg fNDs were dispersed in MilliQ water under sonication. To this solution was added a volume of freshly prepared L-DOPA or dopamine (2.5 mg/ml) solution in MilliQ to bring the final catecholamine concentration to 1-10mM. This mixture was heated to 55°C and sonicated for 5 min to ensure thorough mixing. Finally a volume of freshly prepared sodium periodate solution (10.84 mg/ml) was added to give 0.5 molar equivalents (sodium periodate to catecholamine) and bring the final volume to 1 ml. The solution was sonicated for a further 5 min at 55°C. The reaction was continued on a shaker at 500 rpm for an additional 15 min. The coated fNDs were purified by ultrafiltration (100 kDa). While fNDs coated in the L-DOPA were colloiddally stable, fNDs coated with polydopamine exhibited a high degree of aggregation, lower polymerization efficiency and poorer aqueous stability (Figure S3.1 and S3.12) were observed. The applicability of the L-DOPA coating methodology was evaluated under transmission electron microscopy with three different batches and two different sources of fNDs (FND Biotech, Microdiamant) yielding the DOPA-fNDs (Figure 3.2A, Figure S3.2). The poly(L-DOPA) coating can be clearly seen on each fND, which are well dispersed across the TEM grid with small aggregates attributed to drying effects (Figure 3.2A and 3.2B, Figure S3.2). The poly(L-DOPA) coating was further confirmed by dynamic light scattering (DLS), X-ray photoelectron spectroscopy (XPS), Raman and Fourier transform Infrared (FT-IR) spectroscopy demonstrating a positive outlook towards its applicability across different ND sources (Figure 3.2D, Figure S3.3-S3.5). In addition, the polymerization method allows controlling the thickness of poly(L-DOPA) by simply varying the concentration of the monomer. Between 1 – 10 mM of L-DOPA, the thickness varies linearly from 3 – 15 nm, suggesting that the synthesis is robust and predictable. The aforementioned thicknesses were simultaneously characterized by the absorbance of poly(L-DOPA), DLS and TEM (Figure 3.2). DOPA15nm-fND with 15 nm shell thickness were obtained using 10 mM L-DOPA and XPS was used to elucidate molecular information and ascertain the bonds formed during polymerization. Against

pure fND, L-DOPA and poly(L-DOPA) as controls, the characteristic signals from the C–N–C, C=N–C bonds clearly demonstrate the cyclization of L-DOPA as an intermediate into its polymeric form (Figure S3.3). Moreover, the relative photoelectron count of the C–O, C=O, C–Csp³ and C–Csp² signals indicate contributions from both the fND surface as well as from poly(L-DOPA). As the polymerization of L-DOPA proceeds via a radical mechanism^{24, 32}, it is essential to characterize the influence of the coating towards the magnetic properties of the fND.

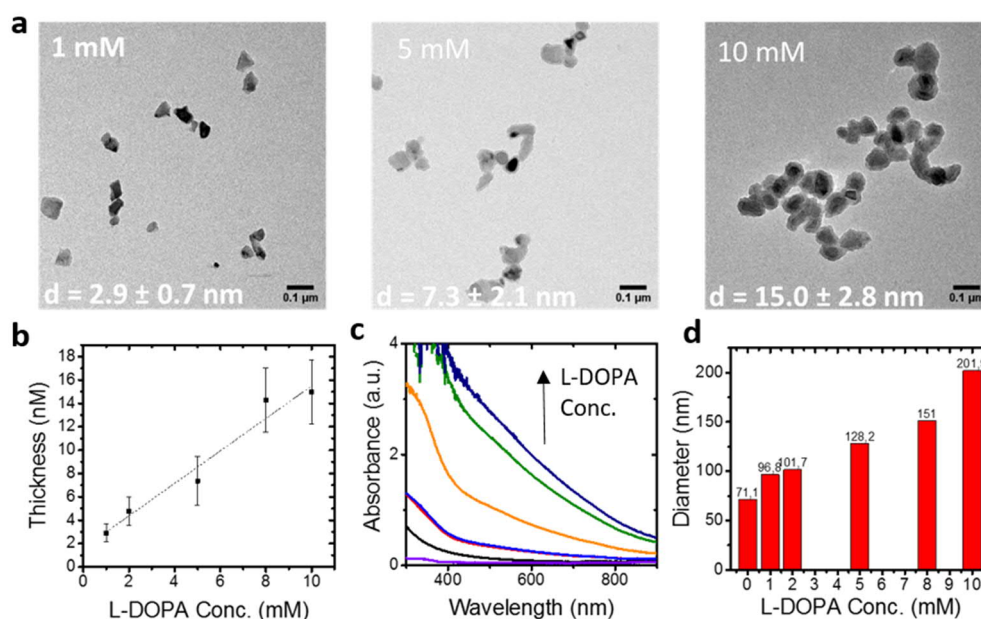


Figure 3.2 (a) Transmission electron microscope images of DOPA-fND prepared with different concentrations of L-DOPA. (b) Poly(L-DOPA) shell thickness increases linearly with L-DOPA concentration. (c) UV-vis absorption spectra of aqueous solutions of DOPA-fND (100 μ g/ml) showing broadband absorbance into the NIR. (d) Dynamic light scattering data. Hydrodynamic diameter of DOPA-fND increases with increasing L-DOPA concentrations.

3.2.2 Physical properties of L-DOPA coated nanodiamonds

In this respect, the effect of poly(L-DOPA) with two different thicknesses (3 nm and 15 nm) to the NV's properties in fNDs was investigated. Spectra measurements were performed on a custom-built confocal microscope with the excitation laser light at 515 and 532 nm. The spectra of coated fNDs reveal that the poly(L-DOPA) layer adds an unique background signal (Figure 3.3A). The intensity of the background signal

depends on the thickness of the layer but the zero phonon lines (ZPL) of NV^- and $NV0$ centers are well visible in each sample. A decrease in the initial fluorescence intensity proportional to the coating thickness was observed for DOPA-fND (Figure S3.6) attributed to the broadband absorbance of polycatecholamines. Unexpectedly, independent of the wavelength of the laser light, the detected fluorescence increased over 60% from the initial excitation and reached saturation level within a few minutes (Figure 3.3C) as measured for twenty DOPA15nm-fND. The high level of fluorescence is stable in time after cessation of laser excitation and remains even after 4 hours in darkness (Figure S3.7, S3.8), which enables more advanced imaging with tracking of nanodiamonds without double counting of the same particle.

To study the charge properties of NV centers in fNDs, optically detected magnetic resonance (ODMR) was observed. Resolved ODMR lines (Figure 3.3B) prove the presence of NV^- centers in NDs after poly(L-DOPA) coating, indicating its suitability for sensing applications. The decrease of ODMR contrast is attributed to background light from the poly(L-DOPA) layer. However, deeper investigations of the spin properties of NV center in poly(L-DOPA) coated NDs are currently ongoing..

Due to the presence of oligomeric and polymeric components of various order within the structure, polycatecholamines are good energy absorbers from UV to NIR^{24, 33-35}. Furthermore, absorbed light is converted to heat with high efficiency allowing their application as photothermal agents³⁶. Photothermal agents that are active in the NIR range are of greater interest due to the reduced absorbance by the body in this region^{37, 38}. We demonstrated that all poly(L-DOPA) coated fNDs exhibited an enhanced photothermal effect over pure fNDs when irradiated at 810 nm, and achieving greater than 10-fold increase ($\Delta T=11.1^\circ C$ vs $0.8^\circ C$) in temperature change for DOPA15nm-fND (Figure 3.3D). Although, a higher photothermal effect was observed for DOPA15nm-fND, we chose to continue our experiments with DOPA7nm-fND ($\Delta T=6.4^\circ C$) providing an appropriate balance between fluorescence intensity and photothermal effects.

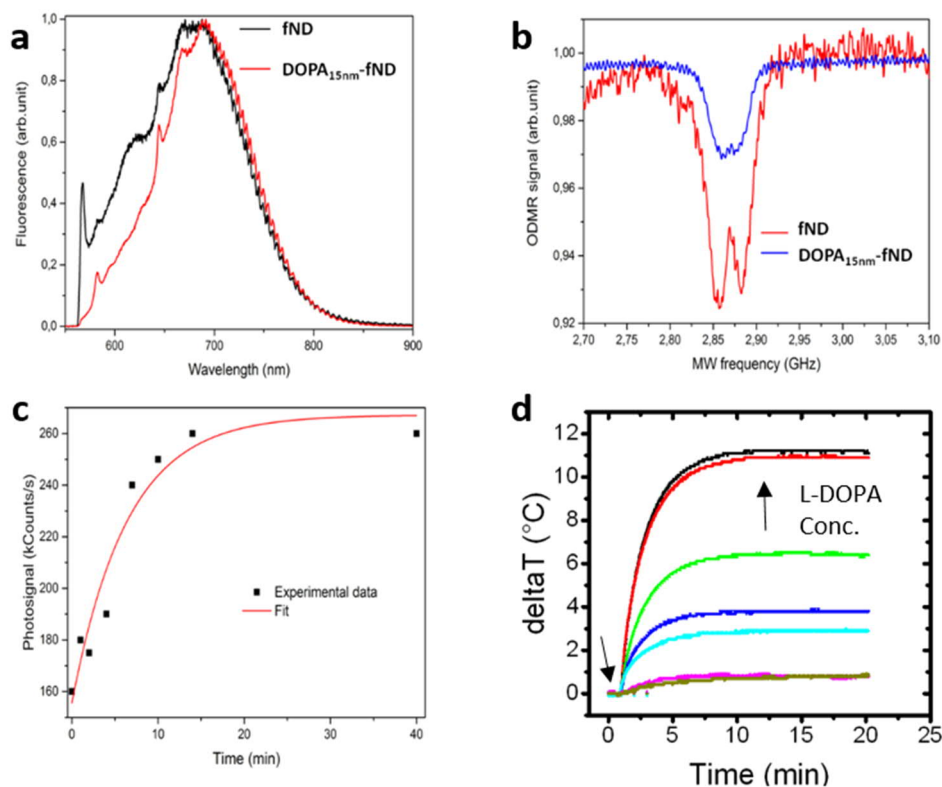


Figure 3.3 (a) Normalized emission spectra (ex. 532 nm) for fND and DOPA15nm-fND. NV0 and NV⁻ zero phonon lines are visible in both spectra. Fluorescence of poly(L-DOPA) coating evident between 570 and 700 nm. (b) Nanodiamonds with PDA layer (15 nm) demonstrate stable ODMR lines, however, the presence of PDA layer decrease the contrast of ODMR. It can be related to background fluorescence from PDA. (c) The fluorescence of DOPA-fND increases with time of laser illumination. Fluorescence increase is stable in time. (d) Temperature increase of aqueous solutions of various concentrations of DOPA-fND (100 $\mu\text{g/ml}$) after near-infrared (NIR) irradiation (810 nm lamp; 1 W/cm²). Arrow indicates when lamp was turned on.

3.2.3 Post-modification of DOPA-fND for uptake studies in vitro

To investigate the poly(L-DOPA) coating as a homogenized platform for the post-functionalization of fNDs, we examined the conjugation of proteins as stabilizing and biologically active functional entities.³⁹⁻⁴¹ As a conserved 3-D structure of the adsorbed protein is essential for its activity, the impact of its conjugation onto the poly(L-DOPA) coating can be directly assessed in a biological assay system.

Human transferrin (Tf, 79.5 kDa), a heme containing protein that binds and transports iron through transferrin receptors expressed at the membrane of many cells and has been used to enhance the uptake of nanoparticles^{42, 43}, was loaded directly onto DOPA-fND by exploiting the amine-reactive Michael acceptors of the quinone moieties formed during the polymerization of L-DOPA. Unbound protein was removed from the reaction mixture by ultrafiltration (molecular weight cut off = 100 kDa) to afford Tf-fND. Upon loading, the hydrodynamic radius increased from 125 nm for DOPA-fND, to ~155 nm for Tf-fND indicating the successful formation of a protein corona around the fND (Figure 3.4B). Successful conjugation was also confirmed by FTIR (Figure S3.9). Transferrins The capability of transferrin to initiate receptor-mediated endocytosis of Tf-fND was evaluated using A549 lung adenocarcinoma cell line. In contrast to fND alone or the precursor DOPA-fND, efficient receptor mediated uptake of Tf-fND was observed through confocal laser scanning microscopy (Figure 3.4A). Next, we attached indocyanine green (ICG), a small molecule dye with innate photothermal properties, onto Tf-fND. The loading of ICG onto Tf-fND was accomplished by overnight incubation of Tf-fND and ICG in the dark with subsequent removal of excess ICG through extensive ultrafiltration to afford ICG-Tf-fND. The amount of ICG loaded was determined through its characteristic absorbance at 400 nm and found to be >180% by mass compared to the fND (1.89 mg/mg fND). In this way, a high local concentration of ICG was obtained, which could enhance the photothermal effect of poly(L-DOPA) coated fNDs. Subsequently, we quantify the photothermal effect of ICG-Tf-fND by observing the differential temperature increase in water upon irradiation at 810 nm. In comparison to DOPA7nm-fND ($\Delta T=6.4^{\circ}\text{C}$) and ICG ($\Delta T=12.4^{\circ}\text{C}$) separately, ICG-Tf-fND ($\Delta T=13.9^{\circ}\text{C}$) showed a 120% and 12% improvement, respectively, in terms of temperature increase attained after 20 min of irradiation (Figure 3.4C). Comparing absolute ICG concentrations, the magnitude difference in temperature profile produced by ICG-Tf-fND suggests that there is an enhancement for the loaded ICG over that of molecularly free ICG. This amplified photothermal effect by confinement was also characteristically observed in hollow

inorganic nanoparticles and plasmonic nanoparticle clusters.^{44, 45} The strong interaction of ICG with Tf-fND was demonstrated by the negligible release of ICG (<5%) from ICG-Tf-fND when incubated in cell media for 24 hours (Figure S3.10).

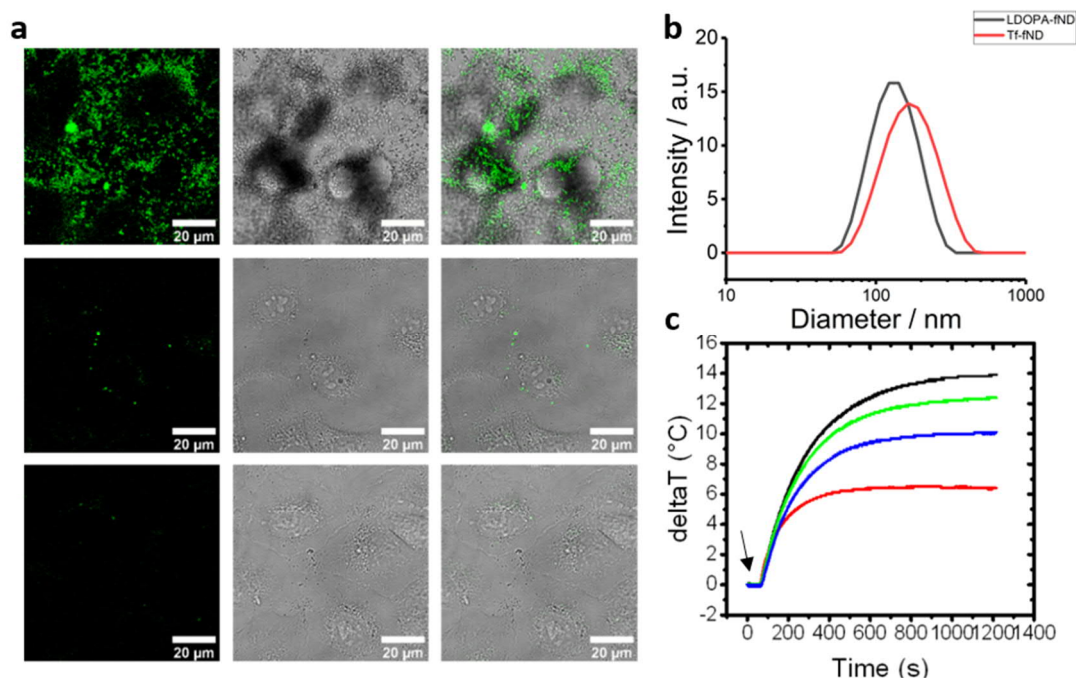


Figure 3.4 (a) Confocal microscopy images of uptake of DOPA7nm-fND (Top row) and Tf-fND (middle) in A549 cells (250 µg/ml). Significant aggregation and sedimentation of DOPA7nm-fND visible. Tf-fND uptaken without sedimentation. Bottom row is blank sample. (b) Dynamic light scattering data for DOPA7nm-fND and Tf-fND. (c) Temperature increase of aqueous solutions of DOPA7nm-fND (100 µg/ml), free ICG (100 and 200 µg/ml) and ICG-Tf-fND (100 µg/ml) after near-infrared (NIR) irradiation (810 nm lamp; 1 W/cm²). Arrow indicates when lamp was turned on.

3.2.4 Photothermal applications in vitro

We subsequently evaluated ICG-Tf-fND in HeLa and A549 cells. The internalization pathway of ICG-Tf-fND was elucidated by confocal microscopy. The fluorescence signal from ICG (ex. 561 nm, em. 750-800 nm) was imaged. It is interesting to note that the transport of ICG-Tf-fND is represented in a receptor mediated manner by formation of endosomal vesicles where the fluorescence signals are highly localized (Figure S3.11) and no freely diffusing ICG are obtained. Molecularly free ICG

rampantly diffuses throughout the cell (Figure S3.11), clearly different to ICG-Tf-fND, which also indicates the strong interaction between ICG and Tf-fND.

Upon internalization, the photothermal effect was initiated using a 810 nm lamp (200 mW) concentrated through the objective onto the sample area. Light densities (W/cm^2) were varied by the magnification of the objective (10x, 20x, 40x) and supplied current. Simultaneously, time-lapsed optical images were recorded in 20 s intervals to visualize the morphological changes due to the localized heating effect by ICG-Tf-fND. First, various light densities (0.09 W/cm^2 , 0.4 W/cm^2 , 4.0 W/cm^2) for the irradiation process were conducted to identify the optimum power for photothermal induced cytotoxicity within 15 min. Efficient and immediate cell rounding (under 5 min) was visually observed at light densities of 0.4 W/cm^2 and 4.0 W/cm^2 (Figure 3.5A). Even very low light densities down to 0.09 W/cm^2 induced cell rounding visually detected within 10 min with cell death thereafter (Figure 3.5B,). A remarkably low power density compared to the previously reported ICG-polydopamine-ND conjugate which required an order of magnitude higher power (2 W/cm^2)²⁷. Live/dead staining of the cells using calcein/propidium iodide combination further demonstrates the characteristic spatial control of the light induced cell death (Figure 3.5C and 3.5D). In comparison, no morphological changes upon irradiation were observed for Tf-fND or fND + ICG mixture at any power density (Figure 3.5A).

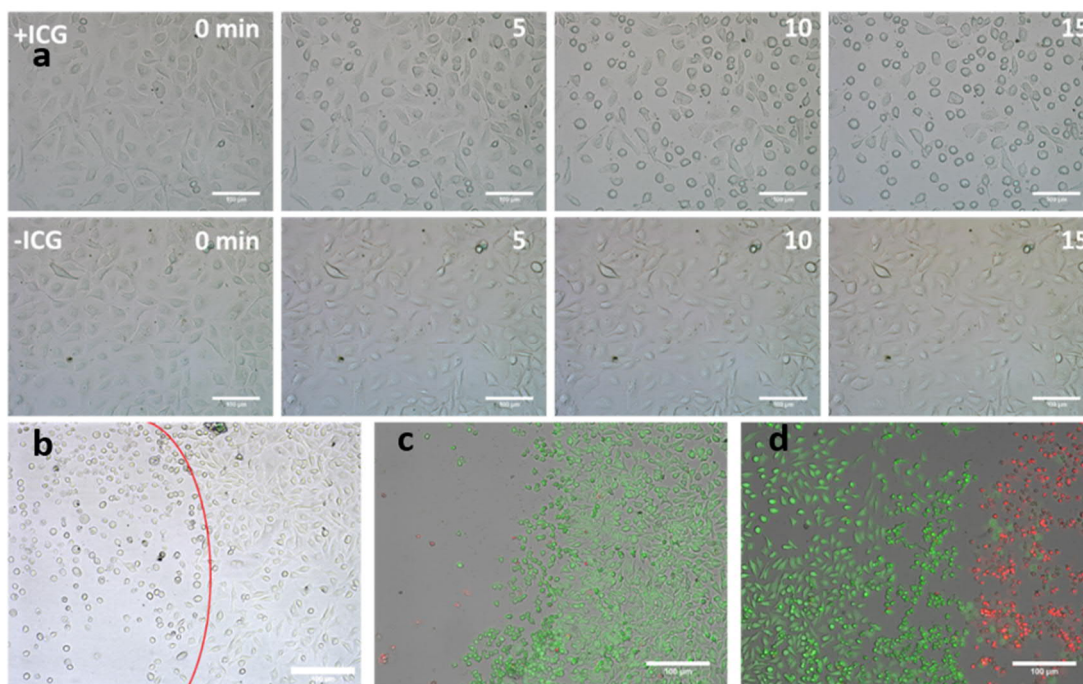


Figure 3.5 (a) Optical images (20x) of HeLa cells incubated overnight with ICG-Tf-fND and Tf-fND at 0, 5, 10 and 15 mins after irradiation with 810 nm lamp, 430 mW/cm². Cell rounding is evident within 5 minutes in ICG-Tf-fND sample. No morphological changes observed with Tf-fND after 15 min. Scale bar = 100 μ m. (b) Brightfield image (10x) of A549 cells incubated overnight with ICG-Tf-fND imaged 4 hours after 15 min irradiation with 810 nm lamp, 90 mW/cm². Border (marked with red line) between irradiated area and non-irradiated area clearly visible. Scale bar = 100 μ m. (c) Live and dead staining (10x) of HeLa cells incubated overnight with ICG-Tf-fND imaged 4 hours after 15 min irradiation with 810 nm lamp, 430 mW/cm². Dead cells were washed away during preparation leaving an empty region bordered by healthy cells. Scale bar = 100 μ m. (d) Live and dead staining (10x) of HeLa cells incubated overnight with ICG-Tf-fND imaged 4 hours after 15 min irradiation with 810 nm lamp, 4 W/cm². Sharp border clearly observed between live (green) and dead (red) cells. Scale bar = 100 μ m.

3.3 Conclusion

In summary, we have described a hierarchical construction of a nanodiamonds-based theranostic system through a poly(L-DOPA) coating that serves as a central focus for

chemical functionalization. By selecting the protein transferrin and the small molecule dye ICG as two vastly different molecular components, we demonstrate that the poly(L-DOPA) is an excellent avenue for post modification with both small molecules and large macromolecules. As an integrated construct, ICG-Tf-fND retains the optical and magnetic sensing capabilities of fNDs, while also exhibiting improved colloidal stability, cellular uptake and an enhanced photothermal effect.

Critical for effective dosing of deep-seated tumors due to the exponential attenuation of light, the activation threshold for the photothermal effect was at least ten times lower, in the milliwatt regime (~90 mW), compared to other nanodiamond based systems.^{27, 46-48}. The endocytic transport behavior and the immediate cellular response towards localized heating, observed in confocal and time-lapsed microscopy, clearly demonstrate the efficiency of the system.

However, there are two main drawbacks. First, the thickness of poly(L-DOPA) has a strong influence on the fluorescence of NDs. Fluorescence of NDs decreases with increasing thickness of poly(L-DOPA) shell dramatically, even with a few nm thickness (Figure S3.6). The reason is the large conjugating structure of poly(L-DOPA), which has strong absorption at the excitation light. Second, it is problematic to covalently modify the poly(L-DOPA) coating, we find the poly(L-DOPA) coating decomposes in the process of covalent functionalization. Like the polydopamine, poly(L-DOPA) is a complex structure composed of oligomers that are connected by covalent and non-covalent interactions. These systems are valuable for cellular experiments, however, in vivo experiments and long-term investigations in biological media are limited by incomplete shielding due to the possible decomposition of the shell.

3.4 Acknowledgements

S.H. and M.R. contributed equally to this work. This project was funded by the ERC Synergy grant 319130 - BioQ, the European Union's Horizon 2020 project "Hyperdiamond" under the grant agreement No 667192, the Collaborative Research Center (CRC) Transregio 234 (project B4), and the Deutsche Forschungsgemeinschaft

(DFG, German Research Foundation) under project number 316249678 (SFB 1279, project C1, C4). Y.W. thanks the China Scholarship Council (CSC) for funding and C.C. is grateful for a doctoral fellowship from Promotionskolleg Pharmaceutical Biotechnology of Ulm University funded by the state of Baden - Württemberg.

3.5 Supporting information

Materials and Methods

Fluorescent nanodiamonds were bought from FND Biotech or provided from Microdiamond. Dulbecco's Modified Eagle's Medium (DMEM, 1x), Dulbecco's Phosphate-Buffered Saline (DPBS, 1x), Fetal Bovine Serum (FBS), MEM Non-Essential Amino Acids Solution (MEM NEAA, 100x) and Penicillin Streptomycin (Pen Strep) were purchased from gibco.

Preparation of DOPA-fND

Fluorescent nanodiamonds (fNDs) were dispersed in MilliQ water using an ultrasonic bath for 30 min. For a typical 500 μ l batch of DOPA-fND 5mM, 50 μ g of fNDs and 197.2 μ l of L-dopa (2.5 mg/ml) were mixed in MilliQ water and sonicated in a water bath at 55°C for 5 min. To the fND L-dopa solution was added 24.7 μ l of sodium periodate solution in water (10.84 mg/ml). The final concentrations of fND, L-dopa and sodium periodate were 100 μ g/ml, 5 mM, and 2.5 mM, respectively. The mixture was sonicated in a water bath at 55°C for 5 min and shaken at room temperature at 500 rpm for 15 min. The coated fNDs (DOPA-fND) were purified by ultrafiltration (100 kDa cutoff, 4000 xg, 5 min); washing 5 times.

Preparation of Tf-fND

DOPA-fND was re-dispersed using an ultrasonic bath for 90 min. For a typical 500 μ l batch of DOPA-fND 5 mM transferrin, DOPA-fND (50 μ g fND) was added to a 500 μ l of transferrin (1 mg/ml) in phosphate buffer (10 mM, pH 8.5) under sonication for 5 min. The mixture was shaken overnight at room temperature at 500 rpm. The DOPA-fND transferrin (Tf-fND) was purified by ultrafiltration (100 kDa cutoff, 4000 xg, 5 min); washing 5 times.

Preparation of ICG-Tf-fND

Tf-fND was re-dispersed using an ultrasonic bath for 90 min. For a typical 500 μ l batch of ICG-Tf-fND, Tf-fND (50 μ g fND) added to 500 μ l of Indocyanine green (ICG, 1 mg/ml) in MilliQ water under sonication for 5 min in the dark. The mixture was shaken overnight at room temperature at 500 rpm in the dark. The Tf-fND loaded with ICG (ICG-Tf-fND) was purified by ultrafiltration (100 kDa cutoff, 4000 \times g, 5 min); washing 5 times.

Transmission Electron Microscopy

One drop of a 0.1 mg/ml solution of DOPA-fND (different concentration of L-dopa) in MilliQ was placed onto an oxygen treated copper grid. A Jeol 1400 transmission electron microscope was used to obtain bright field images. See Figure S3.1.

UV-Vis Absorbance

Ten microliters of fND, DOPA-fND, Tf-fND, or ICG-Tf-fND solutions in MilliQ water (100 μ g/ml) were prepared in separate wells of 384 well low volume well plate. Absorbance scans from 200 to 1000 nm were obtained using a Tecan Spark20M.

Dynamic Light Scattering

200 μ l of 0.2 mg/ml solutions of fND, DOPA-fND and ICG-Tf-fND in Milli-Q were transferred into a borosilicate glass cuvette. The size was measured at 20°C with a 90° angle using a Malvern Zetasizer Nano-S90 (Nano series). The hydrodynamic diameter distribution was presented as intensity.

Fluorescence

Ten microliters of fND, DOPA-fND, Tf-fND, or ICG-Tf-fND solutions in MilliQ water (100 μ g/ml) were prepared in separate wells of 384 well low volume well plate. Fluorescence Intensity scans were obtained using a Tecan Spark20M. An excitation wavelength of 520 nm was used for emission scans. An emission wavelength of 700 nm was monitored for excitation scans

Optically Detected Magnetic Resonance

To investigate the effect from polydopamine coating to spin properties of Nitrogen-Vacancy (NV) centers in fNDs Optically Detected Magnetic Resonance (ODMR)

measurements were performed. It was done at the home build confocal microscope. FNDs were dropped on a glass substrate. Next to fNDs a wire was placed, which was used to apply microwave (MW) field to manipulate spin state of NV^- centers. FNDs were constantly illuminated by laser light (532 nm), MW was tuned from 2.7 to 3.1 GHz. Fluorescence was detected by avalanche photodiode for better sensitivity

Confocal Microscopy

To study the cellular uptake mechanism, A549 cells were plated onto a Greiner Bio-One™ CELLview™ Cell Culture Slides 10-well plate at a density of 75 000 cells/ml in 100 μ l cell medium (Dulbecco's Modified Eagle's Medium + 10% FBS, 1% MEM NEAA, 1% PenStrep). The cells were incubated overnight for attachment at 37°C in 5% CO₂. The next day, the cell medium was removed and replaced by DOPA-fND (250 μ g/ml) and Tf-fND (250 μ g/ml) or free ICG (0.4 mg/ml) and ICG-Tf-fND (250 μ g/ml) each in 100 μ l cell medium. The cells were incubated at 37°C in 5% CO₂ for overnight or 2 h. For imaging, the cells were washed once with Dulbecco's Phosphate-Buffered Saline (DPBS) and 100 μ l of fresh cell media was added. Imaging was then performed using a Leica TCS SP5 scanning confocal microscope system coupled to a 63 \times water immersion objective. The emission of DOPA-fND, Tf-fND, free ICG and ICG-Tf-fND was recorded using a 561 nm laser for excitation and 660-700 nm filter for emission.

X-ray Photoelectron Spectroscopy

Three microliters of fND or DOPA-fND solutions in MilliQ water (1 mg/ml) were deposited on a gold substrate and dried at 40°C. XPS was conducted using a Kratos Axis UltraDLA spectrometer (Kratos, Manchester, England) using an Al K α excitation source with a photon energy of 1487 eV. The data was acquired in the hybrid mode using a 0° take-off angle, defined as the angle between the surface normal and the axis of the analyzer lens. Detailed region XP spectra were collected with setting analyzer pass energy at 80 eV, and a linear background was subtracted for all peak quantifications. The peak areas were normalized by the manufacturer supplied sensitivity factors and surface concentrations were calculated using CasaXPS software.

N 1s, C 1s and O 1s high-resolution spectra were collected with analyzer pass energy of 20 eV. Neutralizer was always used during spectra collection.

RAMAN Spectroscopy

Three microliters of fND or DOPA-fND solutions in MilliQ water (1 mg/ml) were deposited on a gold substrate and dried at 40°C. RAMAN spectroscopy was conducted a Bruker Senterra instrument. A 785 nm laser (20 mW) focused through a 20x objective was used with an acquisition time of 25 seconds.

Fourier Transform Infrared Spectroscopy

Three microliters of fND or DOPA-fND solutions in MilliQ water (1 mg/ml) were deposited on a gold substrate and dried at 40°C. FT-IR spectra were obtained by a Nicolet 730 FT-IR spectrometer in ATR mode using 32 scans.

***In vitro* Photothermal**

Two hundred microliters of fND, DOPA-fND, Tf-fND, and ICG-Tf-fND solutions in MilliQ water (100 µg/ml) were prepared in separate wells of a 96 well plate. The wells were covered with parafilm and a thin thermocouple lead was inserted into liquid. Each sample was irradiated with a 810 nm lamp (Thorlabs M810L3-C1) focused through the 10x objective of a Leica DMI8 microscope. The temperature was recorded over a 20 min period. The power density was calculated to be 1 W/cm².

A549 or HeLa cells were plated onto µ-Dish ibidi (35 mm, low) at a density of 75 000 cells/ml in 500 µl cell medium (Dulbecco's Modified Eagle's Medium + 10% FBS, 1% MEM NEAA, 1% PenStrep). The cells were incubated overnight for attachment at 37°C in 5% CO₂. The next day, the medium was removed and replaced by Tf-fND (100 µg/ml) and ICG-Tf-fND (100 µg/ml) each in 500 µl cell medium. The cells were incubated at 37°C in 5% CO₂ for overnight. For photothermal experiments, the cells were washed once with Dulbecco's Phosphate-Buffered Saline (DPBS) and 500 µl of fresh cell media was added.

The culture dishes were placed in an incubator to maintain the temperature at 37°C. Each sample was irradiated with a 810 nm lamp (Thorlabs M810L3-C1) focused through the 20x objective of a Leica DMI8 microscope for a period of 15 min. Every

twenty seconds images were taken on a full color CCD camera (Leica MC170) attached to the microscope. The images were combined into a time-lapse video with a framerate of 8 images per second. An adjustable power source (Thorlabs LEDD1B) was used to change the light power delivered to the samples.

Dead/Life Staining

After photothermal experiments, cells were incubated 1 h at 37 °C in 5% CO₂. Dead/life staining solution was prepared accordingly to the protocol of ibidi. In summary, 8 µl fluorescein diacetate (5 mg/ml) and 100 µl propidium iodide (1 mg/ml) were added to 5 ml DPBS. Cell medium was removed and 500 µl of the staining solution was added. After 5 min, the cells were washed three times with DPBS.

Imaging was performed using a Leica DMI8 microscope equipped with a Leica MC170 ND camera, DFC9000GT and a sola light engine lumencor®.

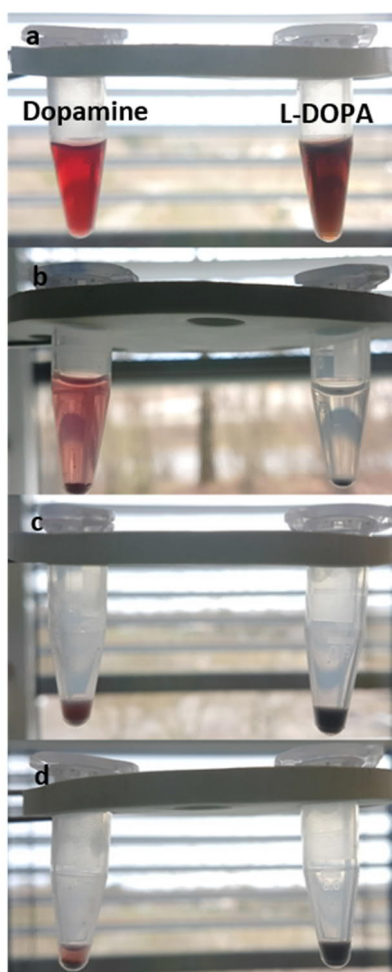


Figure S3.1. Images of nanodiamonds coated in dopamine (*left*) or L-DOPA (*right*) solutions at various stages. (a) 20 min after NaIO₄ addition. L-DOPA shows brown coloration indicative of polycatecholamines. (b) After 2 centrifugation and washing cycles. Red color remains in supernatant of dopamine sample suggesting incomplete polymerization (c) resuspension of nanodiamond pellet. (d) 15 min after resuspension. Sedimentation is visible in dopamine sample.

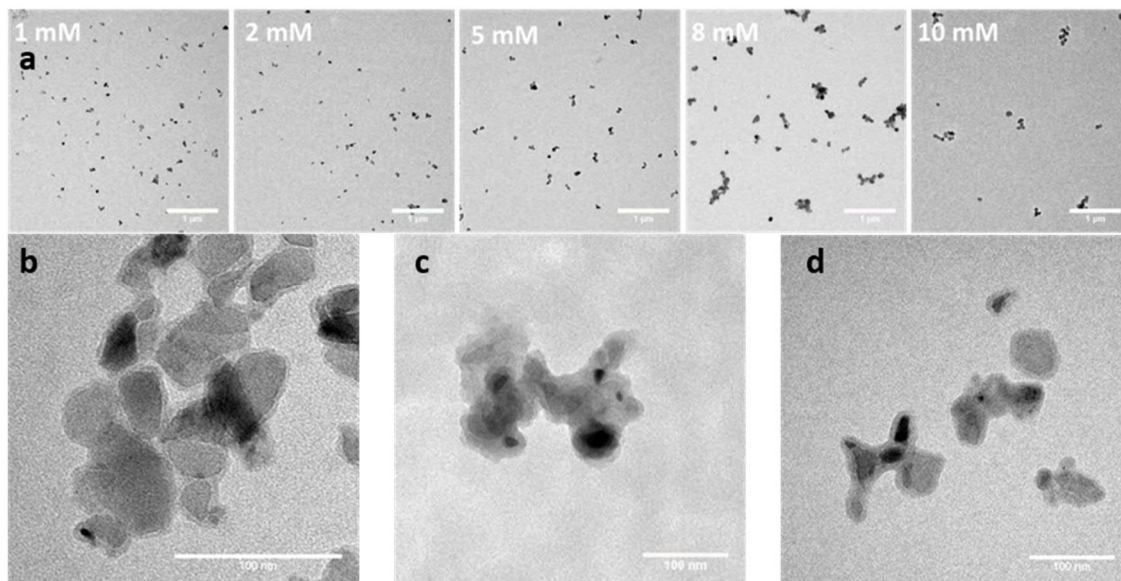


Figure S3.2. (a) Transmission electron microscope images of DOPA-fND prepared with different concentrations of L-DOPA showing lack of agglomeration. (b) Poly(L-DOPA) coating is universal for various batches and sources of nanodiamonds. Microdiamont Leipzig II L-DOPA 1 mM. (c) Microdiamont Leipzig II L- DOPA 10 mM. (d) Microdiamont MD 05 L- DOPA 1 mM.

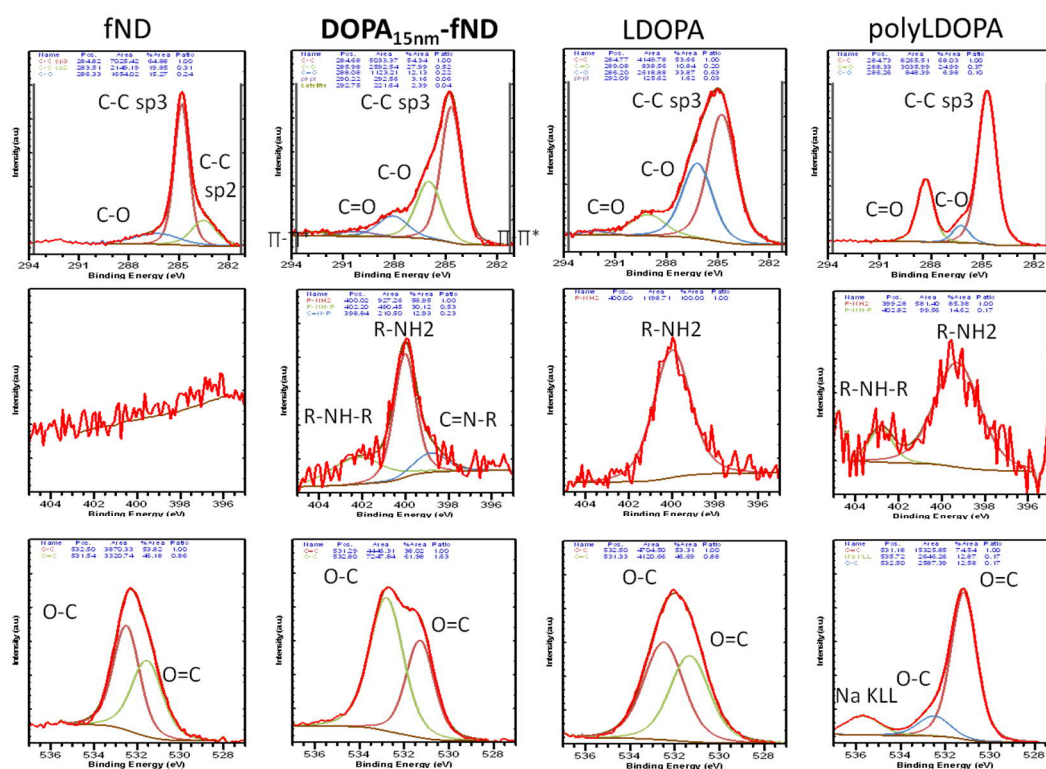


Figure S3.3. X-ray photoelectron spectrographs for raw nanodiamonds (fND), DOPA_{15nm}-fND, L-DOPA, and poly(L-DOPA) nanoparticles. Appearance of Carbonyl/Carboxyl groups and secondary amines indicative of poly(L-DOPA) coating on nanodiamonds. Higher ratio of Carbonyl/Carboxyl to hydroxyl groups in poly(L-DOPA) attributed to longer incubation of reaction mixture. Top row C1s. Middle row N1s. Bottom O1s.

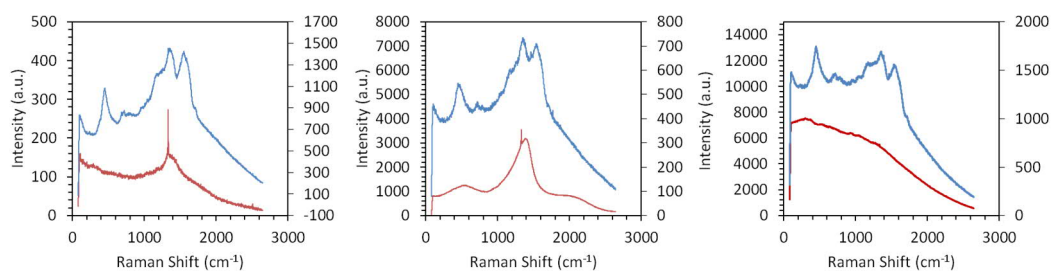


Figure S3.4. Raman spectra for different batches of nanodiamonds with poly(L-DOPA) coating. Spectra of raw nanodiamonds in red and coated nanodiamonds (1 mM L-DOPA concentration) in blue. Although spectra of raw nanodiamonds are significantly different, indicating different levels of impurities and surface compositions, the spectra of the coated nanodiamonds are strikingly similar. Verifying

the universality of the coating. Left fND BIOTECH. Center Microdiamont Leipzig II. Right Microdiamont MD 05. Peak Assignments (a) Diamond ($\sim 1336\text{ cm}^{-1}$) (b) catechol deformation (1385 cm^{-1}) (c) catechol deformation (1557 cm^{-1}).

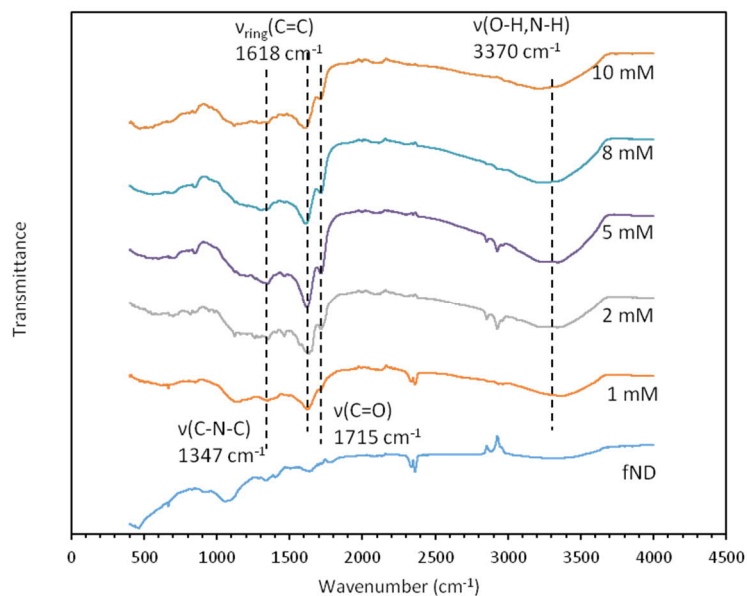


Figure S3.5. Fourier Transmission Infrared (FTIR) spectra of DOPA-fND (fND BIOTECH) prepared with different concentrations of L-DOPA. Peak assignments for poly(L-DOPA) given.

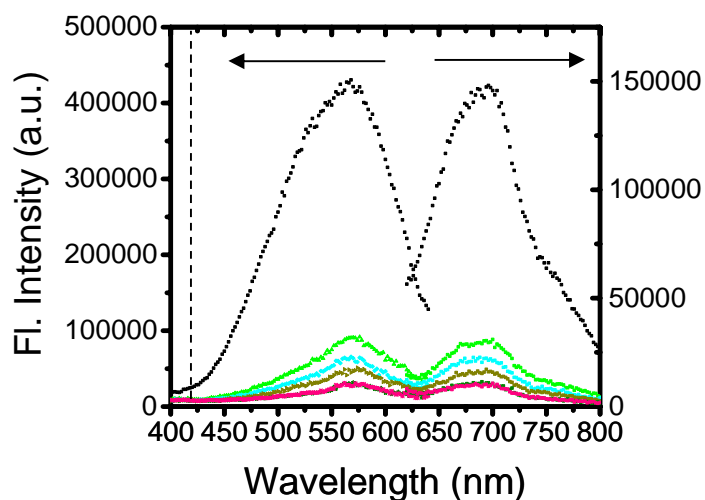


Figure S3.6. Fluorescence excitation and emission spectra of fND (black) and DOPA-fND (colored). Fluorescence decreases with increasing thickness of poly(L-DOPA) shell.

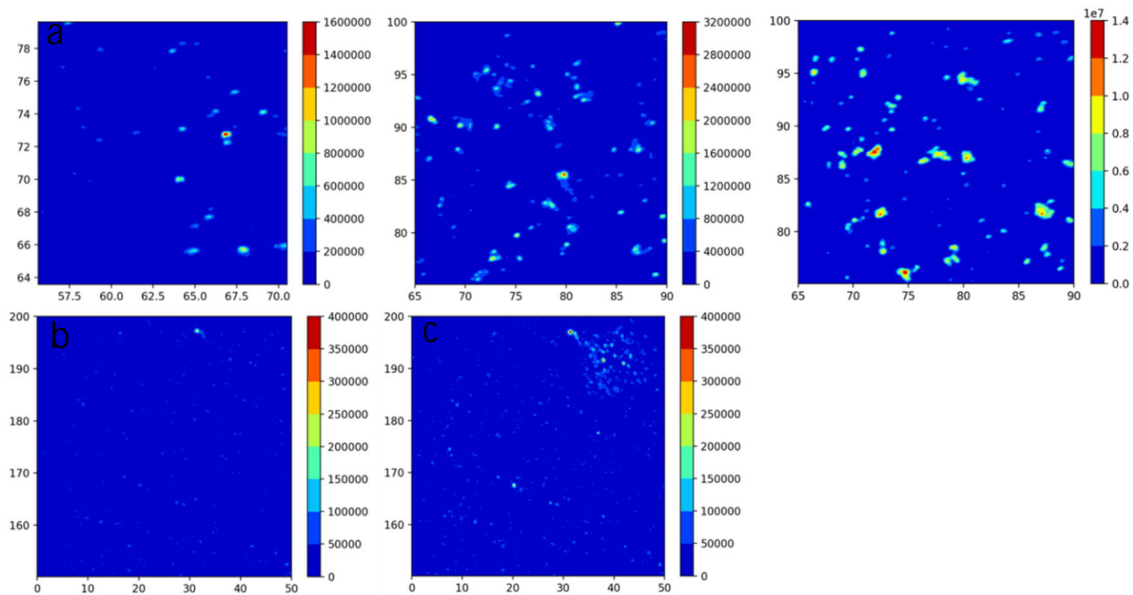


Figure S3.7. (a) Confocal imaging of coated fNDs. Left DOPA_{3nm}-fND. Center DOPA_{15nm}-fND. Right raw nanodiamonds. Same area of NDs sample before (b) and after (c) local laser illumination. Increasing of fluorescence is stable in time (checked after 4 hours).

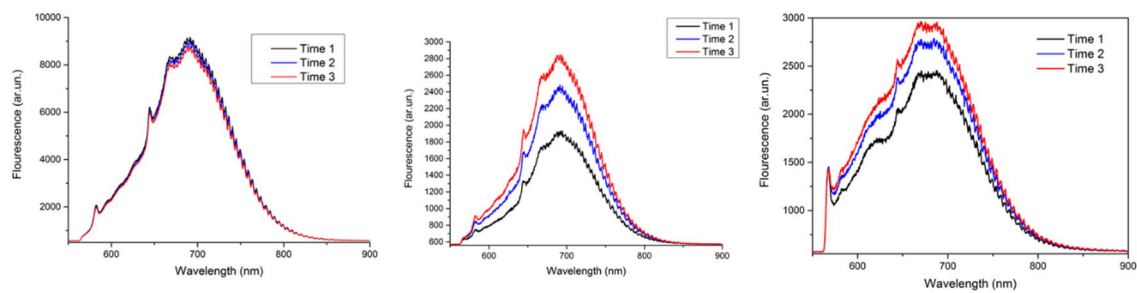


Figure S3.8. Increase in fluorescence after laser irradiation for DOPA-fND (a) *Left* raw nanodiamonds. *Center* DOPA_{3nm}-fND. *Right* r DOPA_{15nm}-fND. No increase in fluorescence observed for raw nanodiamonds.

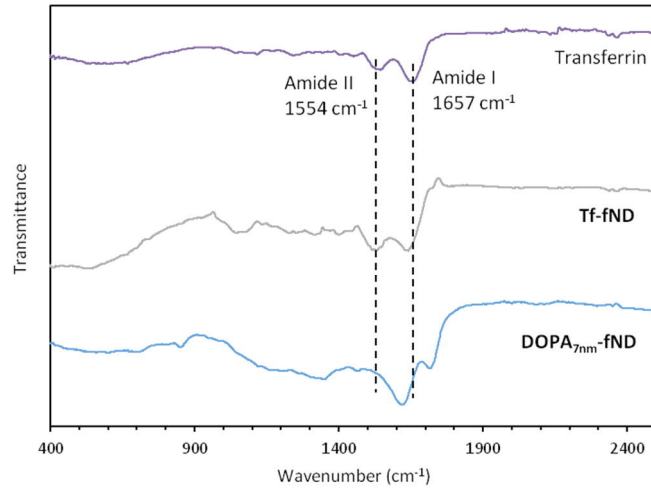


Figure S3.9. FTIR spectra of human Transferrin, Tf-fND, and DOPA_{7nm}-fND. Amide bands observed in Tf-fND spectra indicating successful conjugation of transferrin to surface.

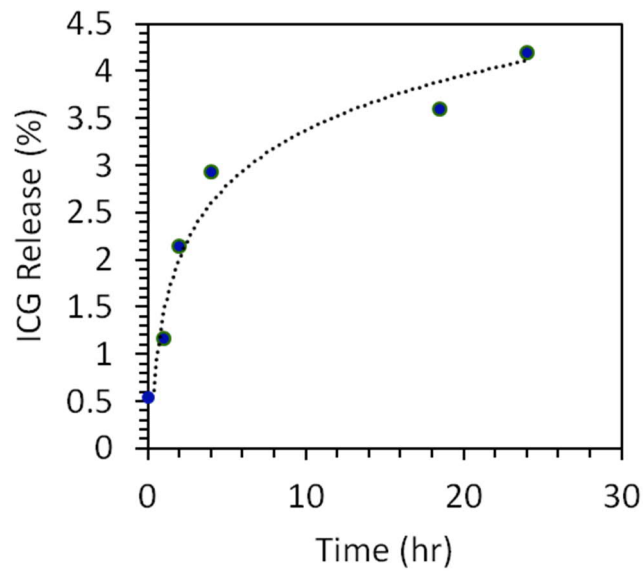


Figure S3.10. Indocyanine green (ICG) release profile *in vitro*. Negligible loss of ICG after 24 hours.

a

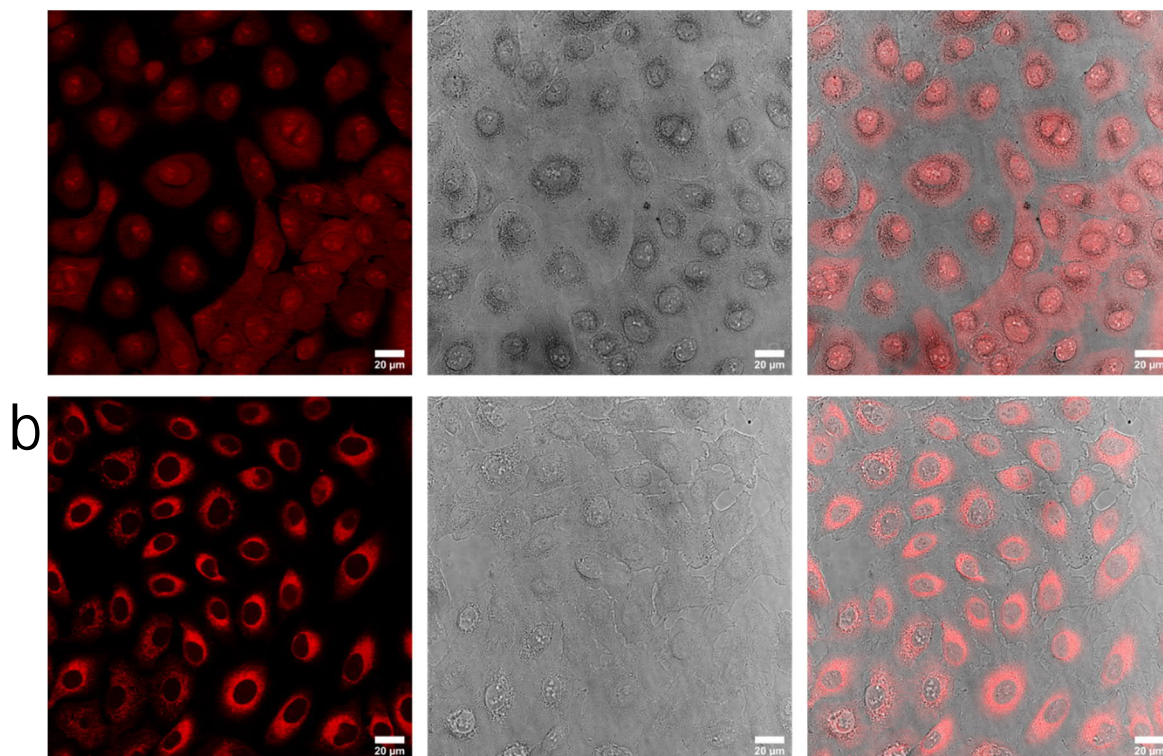


Figure S3.11. (a) Free indocyanine green (ICG, 0.4 mg/ml) was incubated with A549 cells for 2 h at 37°C in 5% CO₂. (b) ICG-Tf-ND (250 μg/ml) was incubated with A549 cells for 2 h at 37°C in 5% CO₂.

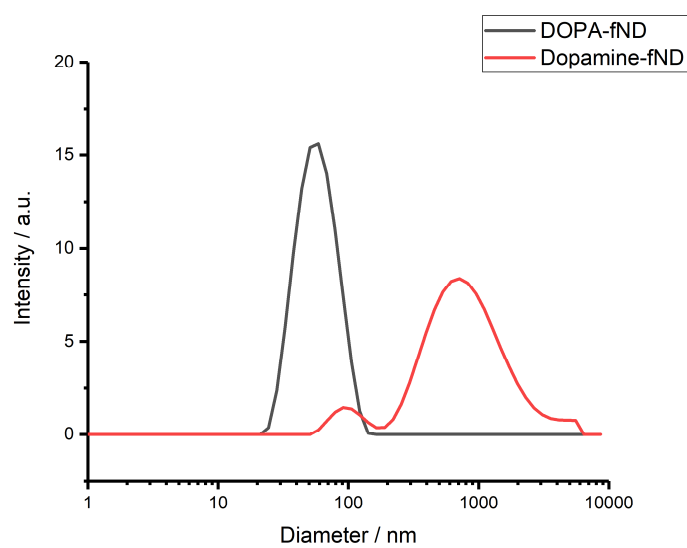


Figure S3.12. DLS spectra of fND coated with either L-DOPA or dopamine.

3.6 References

Uncategorized References

1. V. N. Mochalin, O. Shenderova, D. Ho and Y. Gogotsi, *Nat. Nanotechnol.*, 2012, 7, 11-23.
2. Y. Wu, F. Jelezko, M. B. Plenio and T. Weil, *Angew. Chem. Int. Ed.*, 2016, 55, 6586-6598.
3. R. Schirhagl, K. Chang, M. Loretz and C. L. Degen, *Annu. Rev. Phys. Chem.*, 2014, 65, 83-105.
4. H. Zhang, I. Aharonovich, D. R. Glenn, R. Schalek, A. P. Magyar, J. W. Lichtman, E. L. Hu and R. L. Walsworth, *Small*, 2014, 10, 1908-1913.
5. S. Choi, V. Leong, V. A. Davydov, V. N. Agafonov, M. W. Cheong, D. A. Kalashnikov and L. A. Krivitsky, *Sci. Rep.*, 2018, 8, 1-7.
6. T. Iwasaki, F. Ishibashi, Y. Miyamoto, Y. Doi, S. Kobayashi, T. Miyazaki, K. Tahara, K. D. Jahnke, L. J. Rogers and B. Naydenov, *Sci. Rep.*, 2015, 5, 12882.
7. M. H. Alkahtani, F. Alghannam, L. Jiang, A. Almethen, A. A. Rampersaud, R. Brick, C. L. Gomes, M. O. Scully and P. R. Hemmer, *Nanophotonics*, 2018, 7, 1423-1453.
8. M. Chipaux, K. J. van der Laan, S. R. Hemelaar, M. Hasani, T. Zheng and R. Schirhagl, *Small*, 2018, 14, 1704263.
9. K. van der Laan, M. Hasani, T. Zheng and R. Schirhagl, *Small*, 2018, 14, 1703838.
10. S. Claveau, J.-R. Bertrand and F. Treussart, *Micromachines*, 2018, 9, 247.
11. D. Ho, C.-H. K. Wang and E. K.-H. Chow, *Sci. Adv.*, 2015, 1, e1500439.
12. W. W.-W. Hsiao, Y. Y. Hui, P.-C. Tsai and H.-C. Chang, *Acc. Chem. Res.*, 2016, 49, 400-407.
13. A. Nagl, S. R. Hemelaar and R. Schirhagl, *Anal. Bioanal. Chem.*, 2015, 407, 7521-7536.
14. N. H. Wan, B. J. Shields, D. Kim, S. Mouradian, B. Lienhard, M. Walsh, H. Bakhru, T. Schröder and D. Englund, *Nano Lett.*, 2018, 18, 2787-2793.
15. S. R. Hemelaar, A. Nagl, F. Bigot, M. M. Rodríguez-García, M. P. de Vries, M. Chipaux and R. Schirhagl, *Microchimica Acta*, 2017, 184, 1001-1009.
16. H. Lee, S. M. Dellatore, W. M. Miller and P. B. Messersmith, *Science*, 2007, 318, 426-430.
17. S. Azari and L. Zou, *J. Membr. Sci.*, 2012, 401, 68-75.
18. J. Kuang, J. L. Guo and P. B. Messersmith, *Adv. Mater. Interfaces*, 2014, 1, 1400145.
19. L. Yu, X. Liu, W. Yuan, L. J. Brown and D. Wang, *Langmuir*, 2015, 31, 6351-6366.
20. H. Guo, Y. Sun, X. Niu, N. Wei, C. Pan, G. Wang, H. Zhang, H. Chen, T. Yi and X. Chen, *J. Chromatogr. A*, 2018, 1578, 91-98.
21. S. M. Kang, J. Rho, I. S. Choi, P. B. Messersmith and H. Lee, *J. Am. Chem. Soc.*, 2009, 131, 13224-13225.
22. Y. Liu, G. Zhou, Z. Liu, M. Guo, X. Jiang, M. B. Taskin, Z. Zhang, J. Liu, J. Tang and R. Bai, *Sci. Rep.*, 2017, 7, 1-10.
23. S. Hong, J. Kim, Y. S. Na, J. Park, S. Kim, K. Singha, G. I. Im, D. K. Han, W. J. Kim and H. Lee, *Angew. Chem. Int. Ed.*, 2013, 52, 9187-9191.
24. J. Yang, M. A. C. Stuart and M. Kamperman, *Chem. Soc. Rev.*, 2014, 43, 8271-8298.
25. J. H. Ryu, P. B. Messersmith and H. Lee, *ACS Appl. Mater. Interfaces*, 2018, 10, 7523-7540.
26. Y. Zeng, W. Liu, Z. Wang, S. Singamaneni and R. Wang, *Langmuir*, 2018, 34, 4036-4042.
27. D. Maziukiewicz, B. F. Grześkowiak, E. Coy, S. Jurga and R. Mrówczyński, *Biomimetics*, 2019, 4, 3.
28. H. S. Jung, K. J. Cho, Y. Seol, Y. Takagi, A. Dittmore, P. A. Roche and K. C. Neuman, *Adv. Funct. Mater.*, 2018, 28, 1801252.

29. F. Ponzio, J. Barthès, J. Bour, M. Michel, P. Bertani, J. Hemmerlé, M. d'Ischia and V. Ball, *Chem. Mater.*, 2016, 28, 4697-4705.
30. M. Salomäki, L. Marttila, H. Kivelä, T. Ouvinen and J. Lukkari, *J. Phys. Chem. B*, 2018, 122, 6314-6327.
31. D. K. Yeon, S. Ko, S. Jeong, S.-P. Hong, S. M. Kang and W. K. Cho, *Langmuir*, 2018, 35, 1227-1234.
32. N. ul Huda, S. Islam, M. Zia, K. William, F. i Abbas, M. I. Umar, M. A. Iqbal and A. Mannan, *Z Naturforsch C J Biosci*, 2018, 74, 17-23.
33. J. r. Liebscher, R. Mrówczyński, H. A. Scheidt, C. Filip, N. D. Hädade, R. Turcu, A. Bende and S. Beck, *Langmuir*, 2013, 29, 10539-10548.
34. E. Kaxiras, A. Tsolakidis, G. Zonios and S. Meng, *Phys. Rev. Lett.*, 2006, 97, 218102.
35. M. L. Tran, B. J. Powell and P. Meredith, *Biophys. J.*, 2006, 90, 743-752.
36. Y. Liu, K. Ai, J. Liu, M. Deng, Y. He and L. Lu, *Adv. Mater.*, 2013, 25, 1353-1359.
37. E. Pastrana, *Nat. Methods*, 2013, 10, 36-36.
38. L. Zou, H. Wang, B. He, L. Zeng, T. Tan, H. Cao, X. He, Z. Zhang, S. Guo and Y. Li, *Theranostics*, 2016, 6, 762.
39. C. D. Spicer, C. Jumeaux, B. Gupta and M. M. Stevens, *Chem. Soc. Rev.*, 2018, 47, 3574-3620.
40. A. Beck, L. Goetsch, C. Dumontet and N. Corvaia, *Nat. Rev. Drug Discovery*, 2017, 16, 315-337.
41. C. L. Ventola, *Pharm. Ther.*, 2017, 42, 742.
42. J. Y. Yhee, S. J. Lee, S. Lee, S. Song, H. S. Min, S.-W. Kang, S. Son, S. Y. Jeong, I. C. Kwon and S. H. Kim, *Bioconjugate Chem.*, 2013, 24, 1850-1860.
43. D. Hauser, M. Estermann, A. Milosevic, L. Steinmetz, D. Vanhecke, D. Septiadi, B. Drasler, A. Petri-Fink, V. Ball and B. Rothen-Rutishauser, *Nanomaterials*, 2018, 8, 1065.
44. D. Lapotko, *Nanomed.*, 2009, 4, 813-845.
45. B. n. Vaz, V. n. Salgueiriño, M. s. Pérez-Lorenzo and M. A. Correa-Duarte, *Langmuir*, 2015, 31, 8745-8755.
46. L.-C. Cheng, H. M. Chen, T.-C. Lai, Y.-C. Chan, R.-S. Liu, J. C. Sung, M. Hsiao, C.-H. Chen, L.-J. Her and D. P. Tsai, *Nanoscale*, 2013, 5, 3931-3940.
47. T. K. Ryu, S. W. Baek, R. H. Kang and S. W. Choi, *Adv. Funct. Mater.*, 2016, 26, 6428-6436.
48. T.-K. Ryu, S.-W. Baek, R.-H. Kang, K.-Y. Jeong, D.-R. Jun and S.-W. Choi, *J. Controlled Release*, 2018, 270, 237-245.

4. Highly Stable Fluorescent Nanodiamond Encapsulated by Virus Capsid Protein for Intracellular 3D-Trajectory Analysis

Authors

Yingke Wu[†], Shuqin Cao[†], Md Noor A Alam, Marco Raabe, Sandra Michel-Souzy, Zuyuan Wang, Manfred Wagner, Jeroen J.L.M. Cornelissen*, Tanja Weil*

Y. Wu and S. Cao are shared first author, *corresponding author

Submitted to Journal of Materials Chemistry B, 2021 (*in revision*)

Copyright

The following part is reproduced with permission from the Royal Society of Chemistry (2021).

Author Contributions

Y. Wu: Initiated this project, stabilized the ND in buffer solution, performed the TEM, performed the emission spectrum on ND-CP, analysed the AFM data and CD data, performed the 3D tracking measurement, drafted the manuscript, prepared the final manuscript based on discussions with all authors measurement.

S. Cao: Initiated this project, obtained the CCMV from plants, prepared the CCMV protein, prepared and purified the ND-CP materials with FPLC, characterized the ND-CP by SDS-PAGE, DLS and zeta potential.

M. Alam: Performed the cell viability of ND-CP, prepared the cells for 3D tracking, performed the HET-CAM experiments.

M. Raabe: Performed the HET-CAM experiments.

S. Michel-Souzy: Prepared the ND-CP materials for 3D tracking.

Z. Wang: Analysed the 3D tracking data, performed the theoretical calculation of diffusion coefficient and intracellular viscosity, simulated the the mean square displacement with different models.

M. Wagner: Discussed the concept and results in the projects.

J. Cornelussen: Supervised the project.

T. Weil: Acquiring funding for the project, design and discussion of the concept and results, writing and correcting the manuscript.

Abstract:

Long-term tracking of nanoparticles and intracellular motion is essential to further understand sophisticated transport process and fundamental parameters in living cells. Recently, fluorescent nanodiamonds (NDs) have emerged as a promising tool due to their good biocompatibility and photostability. However, a high dispersity and stability of these fluorescent nanodiamonds under physiological conditions are required before intracellular measurements. Herein, highly stable ND encapsulated with virus capsid proteins (ND-CP) are prepared. A thin protein layer is obtained surrounding the NDs that imparts reactive groups as well as high colloidal stability. The optically physical properties of the coated NDs and the secondary structure of CPs on the surface of NDs are retained. Meanwhile, the ND-CP shows excellent biocompatibility both in vitro and in vivo. Later Long-term 3D trajectories of the ND-CPs were recorded with fine spatiotemporal resolutions, and their intracellular motions were analyzed by different models, the diffusion coefficient and intracellular dynamic viscosity were calculated. The ND-CP with brilliant optical properties and stability under physiological conditions, provides us a new tool to advance the understanding of cell biology, e.g. endocytosis, exocytosis and active transport processes in living cell and the intracellular dynamic parameters.

4.1 Introduction

Among carbon based nanoscale materials, fluorescent nanodiamonds (NDs) emerged in the field of biomedicine, because of its unique optical and magnetic properties as well as excellent biocompatibility. The elemental defects in the lattice of NDs, such as nitrogen vacancy (NV) centers, give stable fluorescence without bleaching or blinking even after irradiation for several months continuously.¹ In addition, the emission wavelength of NDs is size-independent and tunable from visible to the near infrared region based on different elemental defects (i.e. Si, Ge etc.). Furthermore, NDs containing negatively charged NV centers can serve as single-spin sensors to detect many valuable physical properties in the biological microenvironment, such as temperature²⁻⁴, magnetic fields^{5, 6}, electron spins^{7, 8}, and strain⁹. Moreover, it is also widely applied in bioimaging¹⁰⁻¹² and therapy¹³⁻¹⁷ due to its low toxicity in vivo.

For most of these applications, an appropriate surface functionalization of the nanodiamonds (NDs) is required, the colloidal stability of unmodified NDs is extremely poor in solution, the aggregation of NDs becomes dramatically amplified when the size of diamond decreases to the nanoscale¹⁸. Besides, surface functionalization improves the surface flatness, which is often the starting point to further attach other motifs such as drug molecules, dyes, targeting groups or antibodies. Importantly, having a uniformed particle surface increases the amount of binding sites and reproducibility. Furthermore, surface coating is very valuable in vivo to avoid foreign body interactions toward the particles¹⁹ and help the nanoparticles to accumulate and remain in the target sites for a longer period. In order to achieve these aims, different surface coatings have been developed, silica²⁰, hyperbranched polyglycerol (HPG)²¹, poly(L-DOPA)¹⁴, insulin²², human serum albumin (HSA) with polymers¹³ etc. Besides synthetic coatings and common proteins coatings, virus protein cages hybrid bioassemblies have recently gained attention because of their straightforward preparation and biocompatibility.

Plant viruses are nanosized entities composed of coat proteins and genome, which infect plants in order to replicate and form new virus particles. Taking *Cowpea Chlorotic Mottle Virus* (CCMV) as an example, it has been attracted great interest in recent years

due to its intrinsic properties such as perfectly defined structure, stability, biocompatibility, homogeneity, self-assembly, and low toxicity for application purposes. The size of native CCMV is around 30 nm in diameter, which can be disassembled into capsid proteins (CP) and its genome in high salt concentration at neutral pH, the genome could be removed thereafter by centrifugation. The obtained CP could be reassembled into either empty capsids at lower pH or virus-like Particles (VLPs) at neutral pH by using negative templates such as negatively charged inorganic nanoparticles^{23, 24}, negatively charged polymer²⁵, enzymes²⁶, organic aggregates²⁷, etc. What's more, CCMV can be assembled at will into a wide variety of geometries such as tubes, multilayered structures, or dumbbells by controlling the pH and ionic strength of the assembly buffer²⁸⁻³¹.

Here, we report the preparation, characterization, and applications of *cowpea chlorotic mottle virus* capsid protein encapsulated fluorescent nanodiamonds (ND-CP). A schematic outline of the preparation of ND-CP is displayed in Figure 4.1, CP was isolated from the CCMV firstly and stored at capsid storage buffer according to our previous work²⁴, before encapsulation of NDs, the CP was dispersed at the coat protein buffer, then the NDs at PVP solution were added and stirred at 4 °C overnight, later, the resulting ND-CP was obtained.

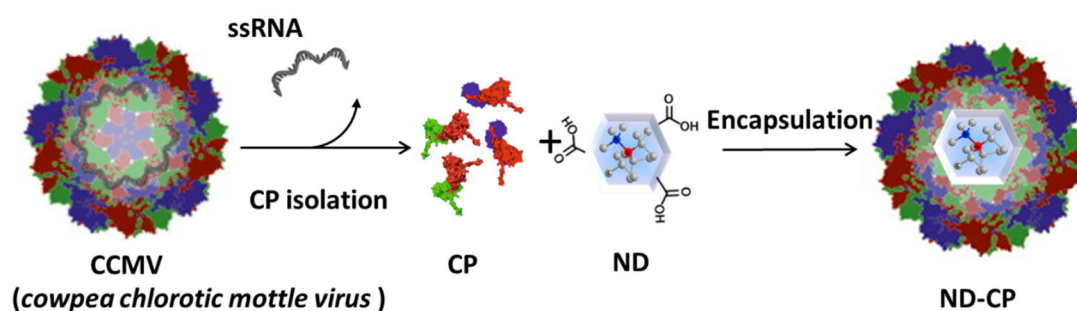


Figure 4.1. Schematic illustration of the preparation of *cowpea chlorotic mottle virus* capsid protein encapsulated fluorescent nanodiamonds (ND-CP).

4.2 Results and Discussion

The resulting ND-CP was purified and analyzed by fast protein liquid chromatography (FPLC) with a UV-vis detector. As it was shown in Figure 4.1A, briefly, free CP eluted out around 18 mL was removed from mixture, Instead of eluting at $V \approx 9.5$ mL (characteristic for native CCMV virus), the NDs coated with CP both in PBS buffer and Tris buffer eluted at a lower volume ($V \approx 8$ mL), suggesting that NDs were successfully coated. The coating of CP on the surface of NDs was further proved by sodium dodecyl sulfate-polyacrylamide gel electrophoresis (SDS-PAGE) since the band of species eluted at $V \approx 8$ mL showed up at the same position as native CCMV (Figure 4.2B). Later the hydrodynamic size and zeta potential of ND-CP was characterized by dynamical light scattering (DLS) (Figure 4.2C and 4.2D). The average hydrodynamic diameters changed from 35 ± 2 nm before coating to 46 ± 3 nm for NDs (PVP) and 52 ± 5 nm for ND-CP respectively. What's more, ND-CP showed good distribution. In addition, the zeta potential changed from -50 mV (the uncoated NDs) to -15 mV (ND-CP).

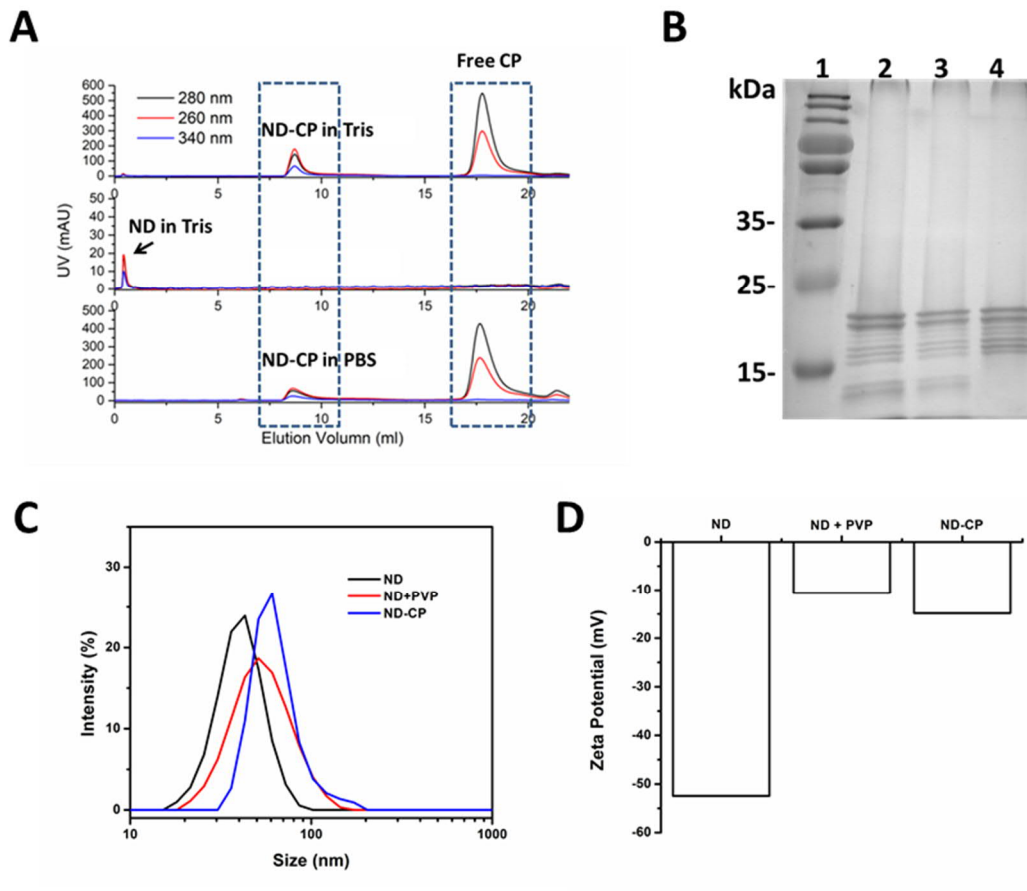


Figure 4.2. (A) FPLC of ND and ND-CP in Tris buffer (50 mM Tris, 50 mM NaCl, 10 mM KCl, pH 7.2), ND-CP in PBS buffer (PBS, 150 mM NaCl, pH 7.2), (B) SDS-PAGE images of ND-CP, 1-standard protein ladder, 2-ND-CP in Tris buffer, 3-ND-CP in PBS buffer, 4-CP in Tris buffer, (C) DLS diagram of uncoated ND, ND+PVP and ND-CP, (D) Zeta potential measurement of uncoated ND, ND+PVP and ND-CP.

The ND and ND-CP were characterized with regards to their distribution, shape, and morphology by transmission electron microscopy (TEM; Figure 4.3A-C). As shown in Figure 4.3A, TEM images revealed that bare NDs were prone to significant aggregation and displayed a heterogeneous distribution whereas non-aggregating, homogeneous single particles could be observed for ND-CP (Figure 4.3B). The histogram analysis of TEM images of ND and ND-CP showed the diameter increased from 15.9 ± 10.6 nm to 23.2 ± 11.2 nm. At high resolution (Figure 4.3C), we could see 3.02 ± 0.96 nm ($n=46$) thickness of the shell of ND-CP, which is comparable to the thickness of the *CCMV* capsid wall. To further assess the structure of the ND-CP, the liquid mode atomic force microscopy (AFM; Figure 4.3D and 4.3E), In Figure 4.3D, the topographic image of ND-CPs showed a good distribution with no significant aggregation. The height-sensor images recorded by AFM were converted into deformation images (Figure 4.3E) using NanoScope Analysis 1.8 software to visualize the nanogel coating. Apart from the height profile images, further nanomechanical properties were simultaneously recorded. In particular, the deformation of the sample caused by the probe was analyzed to receive in-depth information on the structure of the coated NDs. As the ND core is much harder than the CP shell, the deformation of the CP shell could be detected with greater intensity under the same stress conditions. The deformation image revealed clearly that all the ND-CP are core-shell structure.

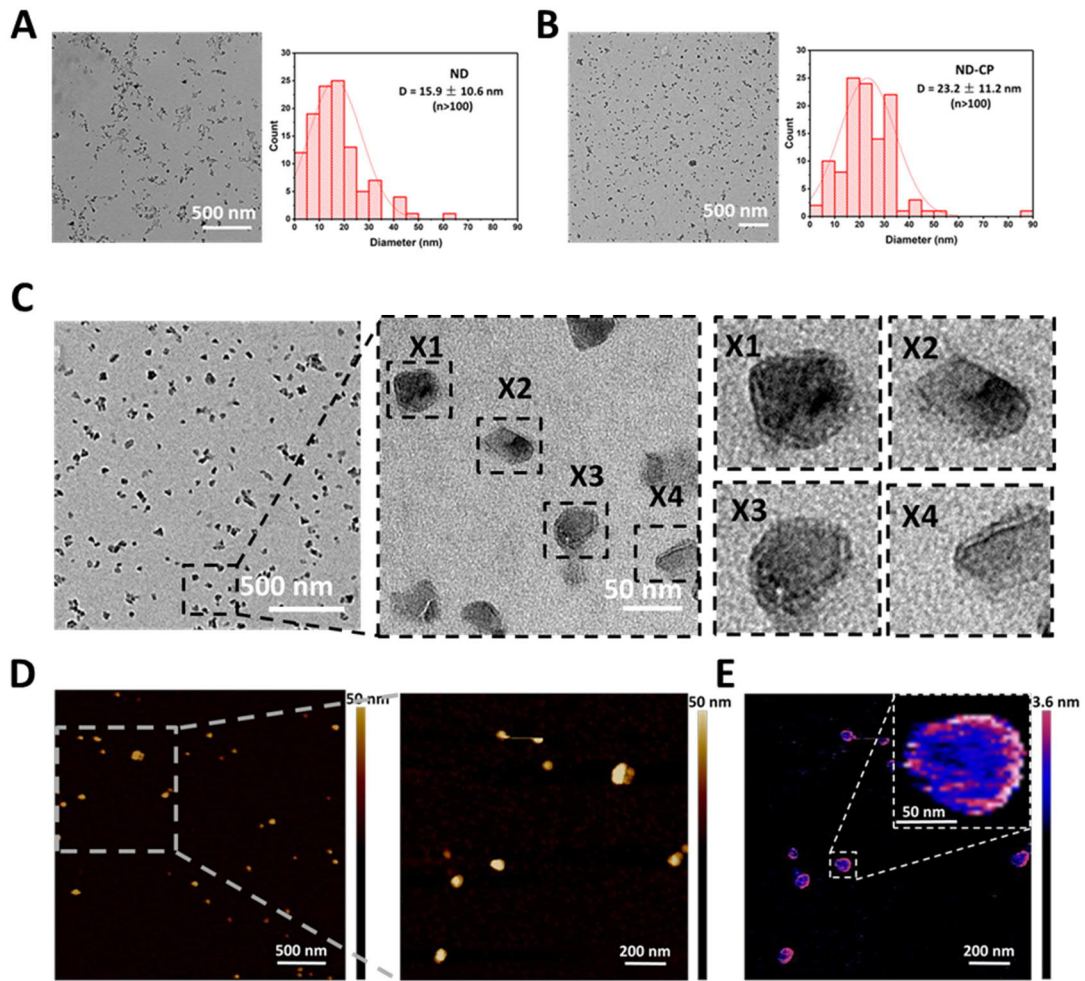


Figure 4.3. (A) TEM image (scale bar: 500 nm) and Size distribution of NDs, (scale bar: 500 nm), (B) TEM image (scale bar: 500 nm) and Size distribution of ND-CPs, (scale bar: 500 nm), (C) TEM images of ND-CP at different magnifications, (D) AFM images of ND-CP at liquid state in high sensor, (E) AFM images of ND-CP in deformation sensor.

To prove the optical physical properties of ND was still kept for potential application, the effect of the CP shell on the charge state of NV centers in NDs was investigated (Figure 4.4A). Spectra measurements were performed on a custom-built confocal microscope with an excitation laser at 532 nm and 100 μ W power in front of the objective (oil, NA=1.35). The spectra of ND-CP revealed that the nanogel shell on the surface of NDs did not affect the fluorescence, and the zero phonon lines of NV^- centers are still well visible without any shift and background noise. NV centers in NDs are

very sensitive to the surface states and at some conditions can switch to the dark state (positively charged NV center; NV^+). These results demonstrate that CP coating did not affect the charge properties of NV centers, which remained in the optically active states (NV^-). This is especially important for the future application of ND-CP in bioimaging and nanoscale sensing. To test whether the CP protein still active and keep the original structure after attached to ND, the circular dichroism (CD) spectroscopy was used to study their secondary structure. As shown in Figure 4.4B, ND didn't have any significant signal, the native CP and ND-CP show similar spectra. It indicated that the CP remained its own structure and can be used for further applications.

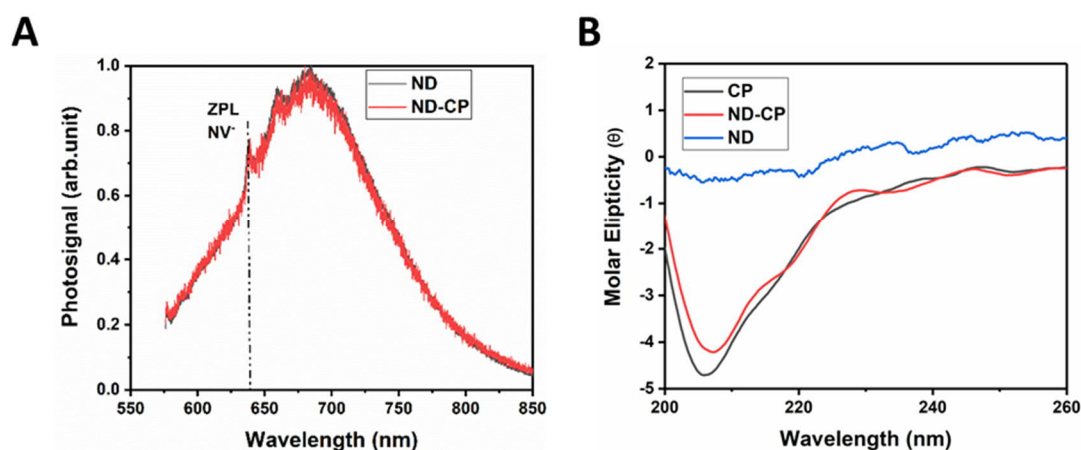


Figure 4.4. (A) Normalized emission spectra (ex. 532 nm) of ND and ND-CP. NV^- zero phonon lines are visible in both spectra. (B) CD spectra of ND, CP and ND-CP

Next, the biocompatibility of ND-CP was investigated using HeLa cell line. As depicted in Figure 4.5A, the cell could proliferate well and low cytotoxicity of ND-CP was observed after the treatment of the cells with a concentration up to 200 $\mu\text{g/mL}$. To further convince the biocompatibility of ND-CP, Hen's Egg Test on the Chorioallantoic Membrane (HET-CAM) method³² is using. It is a potential alternative of animal experiment. The wide availability of fertile eggs and easily achievable hatching temperature (37-38 $^{\circ}\text{C}$) made the HET-CAM a desirable experiment platform. The chorioallantoic membrane (CAM) has an ample vascular network which is suitable for studying tissue xenograft, tumor growth, drugs delivery, wound healing, and

toxicologic study.³³ The CAM is not innervated, and the chick embryo develops a functional brain only on the day 13 of incubation. Therefore HET-CAM model can be considered as an animal friendly and humane alternative of in vivo testing. The following three type of reactions were observed on the CAM: hemorrhage, vascular lysis, and coagulation. The time (in seconds) needed to reach each type of irritational reaction after applying the sample can be used to calculate the irritation score (IS) using following equation³⁴.

$$\text{Irritation score (IS)} = [5 \times (301 - \text{mth})/300] + [7 \times (301 - \text{mtl})/300] + [9 \times (301 - \text{mtc})/300]$$

Here, mth = mean time to hemorrhage, mtl = mean time to vascular lysis, mtc = mean time to coagulation. When no hemorrhage, lysis, or coagulation was recorded within first 5 minutes of sample application, the contribution of respective irritation component was considered null.

Table 4.1. Classification of irritant based on the irritation score (IS)

Classification	Irritation Score (IS)
Maximum	21
Severe irritant	> 9
Non-to-moderate irritant	0 - 9

In our HET-CAM test, we observed hemorrhage from blood vassals started within 2 - 4 seconds after applying the positive control 1% sodium dodecyl sulfate (SDS). Lysis occurred after 25 - 27 seconds, and we observed coagulation within 24 hours. For the negative control (phosphate buffered saline) and various concentrations of NG-CP (50 µg/mL, 100 µg/mL) no instance of irritation was detected within 5 minutes to 24 hours of application (Figure 4.5B). A summary of the results is shown in Table 2. This in ovo results strengthens the superior biocompatibility of ND-CP.

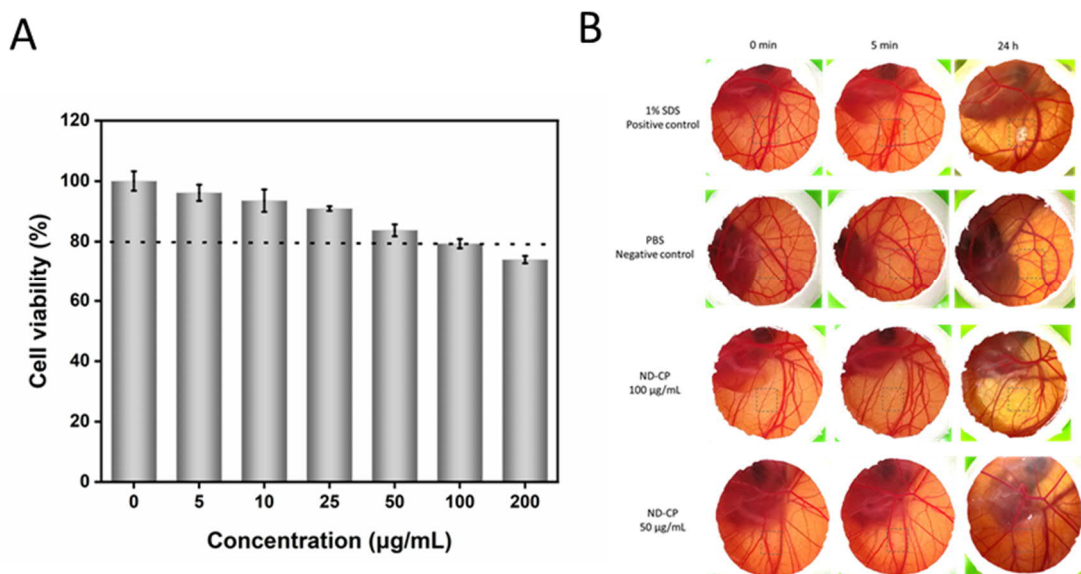


Figure 4.5. (A) Cell viability of ND-CP in HeLa cells. (B) Photographs of HET-CAM test results for 1% SDS (positive control), PBS (negative control) and ND-CP at 50 µg/mL and 100 µg/mL.

Table 4.2 Irritation Score (IS) for different concentrations of ND-CP, compared with 1% SDS (positive control) and PBS (negative control)

Eggs with sample (n=3)	Classification	Irritation score (IS)
1% SDS	Severe irritant	11.40 ± 0.05
PBS	No irritation	0.00
ND-CP (100 µg/mL)	No irritation	0.00
ND-CP (50 µg/mL)	No irritation	0.00

The cell uptaken experiments in Hela cell was carried out to illustrate the internalization behave of ND-CP, the measurements were performed on a custom-built confocal microscope with an excitation laser at 532 nm. As depicted in Figure 4.6A and 4.5B, ND-CP could be taken up into Hela cells at the concentration of 20 µg/mL. As an excellent photostable biomarker, ND-CP was further investigated for cellular tracking on the scanning confocal microscope (see SI for the detailed set-up for 3D-tracking).

During a total measurement time of 60 min. a representative trajectory of single particles are shown in Figure 4.6C. The fluorescence intensities of ND-CP during the tracking experiments are given in Figure 4.6D. The fluorescence intensities of tracked ND-CP remained relatively stable without significant fluctuations. In general, we did not observe significant decrease in the fluorescence intensities indicating that ND-CP allows long-term cellular tracking studies.

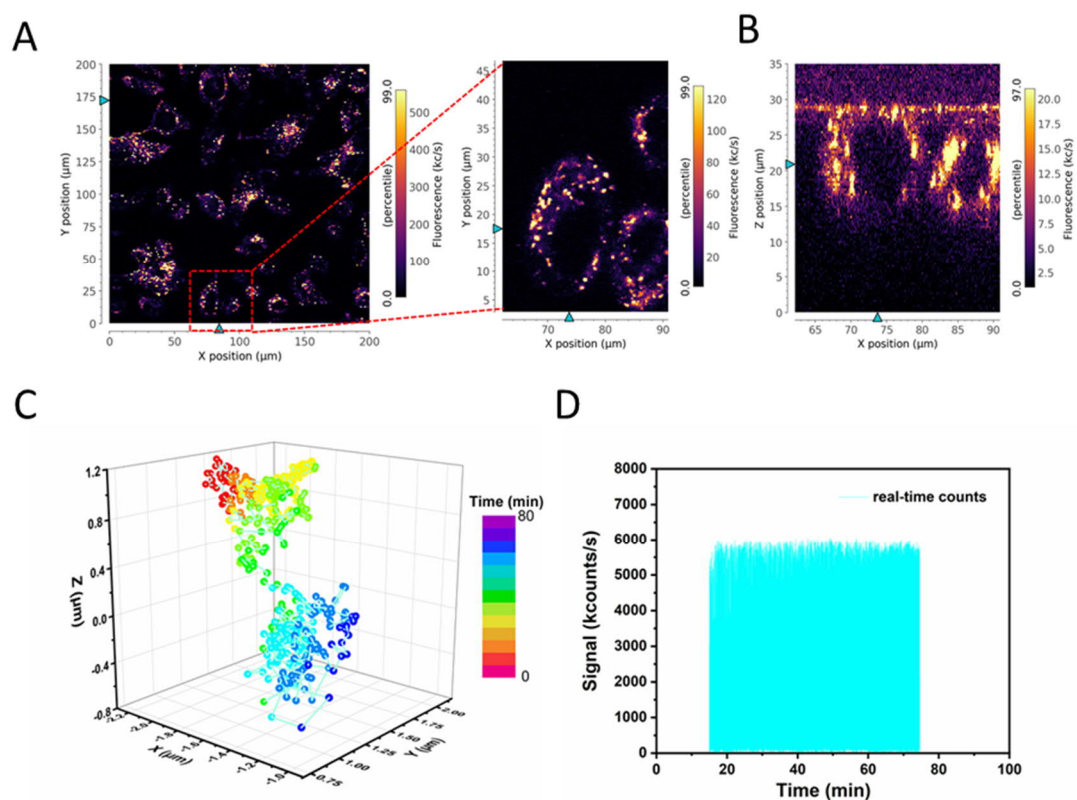


Figure 4.6. (A) X-Y axis confocal microscopy images of ND-CP taken up into HeLa cells at 20 $\mu\text{g}/\text{mL}$ for 4 h. (B) X-Z axis confocal microscopy images of ND-CP taken up into HeLa cells at 20 $\mu\text{g}/\text{mL}$ for 4 h. (C)) The trajectory of tracked ND-CP spots in intracellular space. (D) Real-time fluorescence intensity of the tracked ND-CP spots.

It is essential to quantitatively understand the behavior of ND-CP in 3D space and obtain intracellular dynamic parameters in living cell, the trajectories of ND-CP were analyzed here. The mean square displacement (MSD) data of an intracellular trajectory allow identification of the diffusion behavior of the tracked object and calculation of

the diffusion coefficient. In this work, we recorded three trajectories, labeled as “Trajectory 1”, “Trajectory 2”, and “Trajectory 3”, which contain 520, 88, and 81 position vectors, respectively. The MSDs of the trajectories were calculated as

$$\text{MSD}(t_{\text{lag}}) = \text{MSD}(n\Delta t) = \frac{1}{N-n} \sum_{j=1}^{N-n} |\mathbf{r}((n+j)\Delta t) - \mathbf{r}(j\Delta t)|^2, \quad (1)$$

where t_{lag} is the lag time, Δt is the measurement interval (5 s) of the trajectories, n is the number of intervals contained in the lag time, N is the total number of position vectors in the trajectory, and $\mathbf{r} = [x, y, z]$ is the position vector of the tracked particle. As shown in Figure 4.7A, the MSDs of the three trajectories show different magnitudes and lag time dependencies. To identify the diffusion behavior of the ND-CP, we fitted the MSD data with a power-law as

$$\text{MSD}(t_{\text{lag}}) = At_{\text{lag}}^\alpha, \quad (2)$$

where A and α are fitting parameters. In particular the power index α reflects the diffusion behavior of the tracked object, with $\alpha < 1$, $\alpha = 1$, and $\alpha > 1$ indicating subdiffusion, normal diffusion, and superdiffusion, respectively.^{35, 36} In accordance with the suggestion by Saxton³⁷, we focused on the data with $t_{\text{lag}} < t_{\text{total}} / 4$, where t_{total} is the total time of the trajectory. Furthermore, we divided the MSD data into two regions, corresponding to short and intermediate lag times, respectively. Through segmental fitting with Eq. (2), we obtained the characteristic power indices of the three trajectories, as indicated in Figure 4.7A. The power indices are smaller than one at short lag times and become close to one at intermediate lag times, suggesting different diffusion behaviors of the ND-CP at different lag time scales. Similar MSD results have been reported for tracking of single-walled-carbon-nanotube (SWNT)-labeled kinesins in COS-7 cells³⁸ and the subdiffusion behavior at short lag times could be explained by the existence of mechanical obstacles in the cell^{38, 39}.

Another way to distinguish normal and anomalous (either subdiffusion or superdiffusion) diffusion is by calculating the cumulative distribution function (CDF)

of the square displacements (Δr^2) at a particular t_{lag} .^{35,40} Here we focused on “Trajectory 1”, the longest trajectory recorded in this work, and $t_{\text{lag}} = 2\Delta t = 10$ s. The probability distribution function (PDF) of the square displacements were first calculated (Figure 4.7B, top panel), based on which the CDF was computed (Figure 4.7B, bottom panel). We further fitted the CDF data with single and double exponential functions as follows,

$$\text{CDF}(r^2, t_{\text{lag}}) = 1 - \exp(-r^2/r_0^2), \quad (3)$$

where r_0^2 is the MSD at t_{lag} , and

$$\text{CDF}(r^2, t_{\text{lag}}) = 1 - \left[w \exp(-r^2/r_1^2) + (1-w) \exp(-r^2/r_2^2) \right], \quad (4)$$

where r_1^2 and r_2^2 are the MSDs at t_{lag} , corresponding to the fast and slow mobility components, respectively. The contributions of these two components to the CDF are weighted with factors w and $(1-w)$ respectively. Whereas Equation (3) implies normal diffusion, Equation (4) covers both normal ($w = 0$ or 1) and anomalous ($w \rightarrow 0.5$) diffusion. The r_i^2 ($i = 0, 1, 2$) are related to the diffusion coefficient D_i as $r_i^2 = 6D_i t_{\text{lag}}$. From the fitting, we obtained $r_0^2 = 1.2540 \times 10^{-2} \mu\text{m}^2$, $r_1^2 = 1.7715 \times 10^{-3} \mu\text{m}^2$, $r_2^2 = 1.7590 \times 10^{-2} \mu\text{m}^2$, and $w = 0.2616$. As a result we obtained the following diffusion coefficients (at $t_{\text{lag}} = 10$ s): $D_0 = 2.09 \times 10^{-4} \mu\text{m}^2/\text{s}$, $D_1 = 2.95 \times 10^{-5} \mu\text{m}^2/\text{s}$, and $D_2 = 2.93 \times 10^{-4} \mu\text{m}^2/\text{s}$. A w value of 0.2616 and the much smaller residual of the double exponential fit than that of the single exponential fit (Fig. 4b, top of the bottom panel) confirm that the diffusion behavior of the ND-CP in the HeLa cell is indeed a combination of normal and anomalous diffusion.

We also calculated the lag-time-dependent diffusion coefficient of the ND-CP in HeLa cell according to

$$D(t_{\text{lag}}) = \frac{\text{MSD}(t_{\text{lag}})}{6t_{\text{lag}}}, \quad (5)$$

Applying Eq. (5) to the three trajectories at intermediate lag times, where the power indices are close to one (Figure 4.7A), we obtained the following three diffusion

coefficients, 1.25×10^{-4} , 3.07×10^{-4} , and $1.39 \times 10^{-3} \mu\text{m}^2/\text{s}$ (Figure 4.7C), which are comparable to the values obtained from the single and double exponential fits to the CDF data at $t_{\text{lag}} = 10$ s. The nominal diffusion coefficient of the ND-CP in the HeLa cell was then determined to be the average of these three values, that is, $6.07 \times 10^{-4} \mu\text{m}^2/\text{s}$.

Finally, we estimated the intracellular dynamic viscosity (η) of the HeLa cell according to the Stokes-Einstein-Sutherland relation³⁶,

$$\eta = \frac{k_B T}{6\pi D R_p}, \quad (6)$$

where k_B is the Boltzmann constant ($= 1.38 \times 10^{-23}$ J/K), T is temperature, and R_p is the radius of the particle. Here we assumed the ND-CP particle to be spherical and considered R_p as half of the hydrodynamic diameter. Using $T = 293$ K, $R_p = 26$ nm, and the three D values in Figure 4.7C, we obtained $5.9 \text{ Pa}\cdot\text{s} < \eta < 66.0 \text{ Pa}\cdot\text{s}$. This estimated range of viscosities is expectedly much larger than that of water ($\eta = 1.0 \text{ Pa}\cdot\text{s}$ at 293 K), and it is compatible with the viscosities of many organic solvents at room temperature.⁴¹

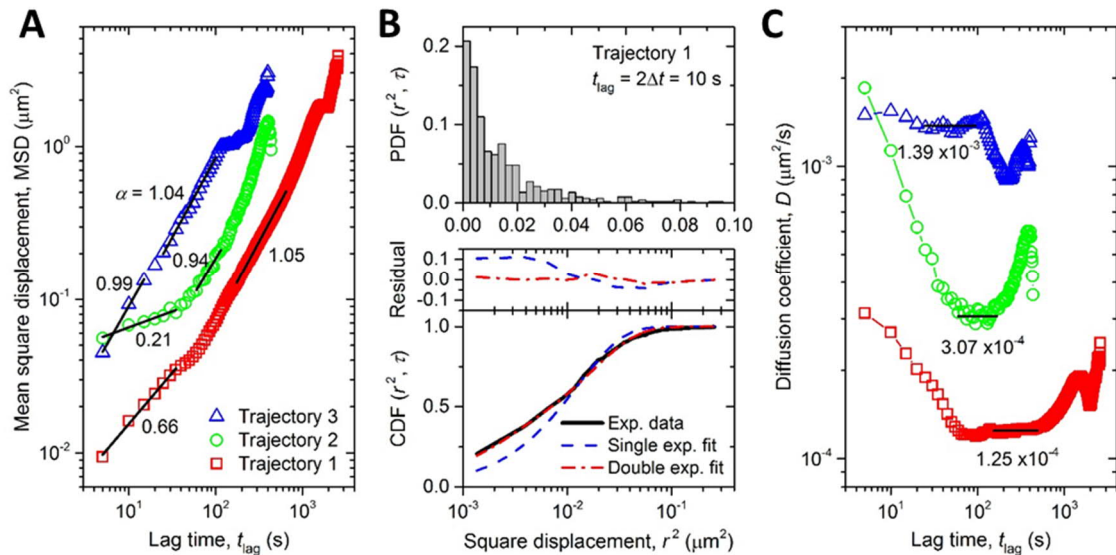


Figure 4.7. (A) Mean square displacement (MSD, Eq. (1)) vs. lag time (t_{lag}) for three independent trajectories. The segments of the MSD profiles at short and intermediate

lag times are analyzed using a power law relation (Eq. (2)). The power indices are indicated. (B) Probability density function (PDF, upper panel, note the linear scale of the x axis) and cumulative density function (CDF, lower panel) distributions of the square displacements at $t_{\text{lag}} = 2\Delta t = 10$ s. The CDF distribution is fitted with single and double exponential functions (Eqs. (3) and (4)). The residuals of the fitting are shown on the top of the lower panel. (C) Time-dependent diffusion coefficient (D , Eq. (5)) of the three trajectories (see (A) for the legends). The nominal D values are calculated as the average values at intermediate lag times, as indicated by the black horizontal lines. In these ranges of the lag times, the power indices in (A) are close to one, implying normal diffusion.

4.3 conclusion

In conclusion, we have developed a novel surface coating and ND-CP showed excellent stability in PBS and Tris buffer. The two components of ND-CP kept their original photophysical properties and structures. Furthermore, they showed good biocompatibility up to 100 $\mu\text{g/mL}$ *in vitro* and *in vivo*, which is fair enough for bioapplications, e.g. bioimaging and intracellular trajectory. The analysis of intracellular motions of ND-CPs revealed it underwent sub-diffusion at the beginning and then changed to normal diffusion. The intracellular dynamic viscosity is significantly higher than that of water. The ND-CP provides us a useful tool to understand the intracellular motions with spatiotemporal details in living cell. In addition, combined with the optically detected magnetic resonance technique⁴², it is possible to get the intercellular magneto-, electro-, and temperature-informations at the nanoscale simultaneously. That will pave a way to understand the cell biology. The ND-CP displays excellent behavior in intracellular tracking experiments, which indicates a

great potential for bioapplication in life science.

4.4 Acknowledgements

We thank Prof. Dr. Theo Lasser for fruitful scientific discussions, Dr. Siyuan Xiang for the measurement of circular dichroism spectroscopy and Pia Winterwerber for the atomic force microscopy measurement. Y.Wu thanks the China Scholarship Council (CSC) for offering a PhD scholarship. We are grateful for financial support from the Deutsche Forschungsgemeinschaft (DFG, German Research Foundation) – Project number 316249678 – SFB 1279 (C04) and ERC Consolidator Grant (Protocage #616907).

4.5 Supporting information

Materials and method

Materials: Nanodiamonds with 35 nm average diameter were purchased from FND Biotech (Taiwan), polyvinylpyrrolidone (MW: 10 kDa) was purchased from Sigma-Aldrich, Quartz glass cuvette were purchased from Hellma-analytics, Quartz SUPRASIL (QS). Amicon Ultra centrifuge filter with 10K MWCO from Pall Microsep™ Advance Centrifuge Device with Omega Membrane were used for particle preparation.

Dulbecco's Modified Eagle's Medium (DMEM, 1x), Dulbecco's phosphate-buffered saline (DPBS, 1x), fetal bovine serum (FBS), Penicillin Streptomycin (Pen Strep) were purchased from gibco. All solvents and chemicals were purchased from commercial sources and were used without further purification

Preparation of CCMV

Pots are filled with soil and the Cowpea beans are planted in the soil. The plants are allowed to grow for ten days and watered regularly. At this point primary leaves are present. The leaves are dusted with carborundum. The inoculation solution is prepared with a purified virus. In both cases a mixture of sap from ground leaves, water and purified virus solution (0.5 mg virus) is prepared. The leaves are inoculated by smoothly

rubbing. By using a household sprayer, the plants are immediately sprayed with water after inoculation to prevent leaf dehydration⁴³. Seven days after inoculation, the leaves are harvested by cutting them from the stem. The plant material is cut into pieces and blended in cold homogenization buffer (0.2 M NaAc, 0.01 M ascorbic acid, 0.01 M Na₂EDTA)⁴⁴. Two layers of cheesecloth are boiled in water containing EDTA and rinsed with MilliQ water. The homogenate is filtrated to remove the larger plant debris. The homogenate is kept at T=4 °C for an hour to allow the proteins to precipitate.⁴⁵ The homogenate is subjected to low-speed centrifugation to precipitate the leaf tissue. The pellet is discarded and the supernatant is added to 10 % (w/v) solid PEG (MW=6000 g/mol). The mixture is stirred for 1 h at T=4 °C. The precipitate is pelleted by low-speed centrifugation. The supernatant is discarded and the bottles are drip-dried thoroughly to remove the PEG solution (Hebert, T. T., Precipitation of plant viruses by polyethylene glycol. *Phytopathology* 1963, 53, 362.) The pellet is suspended in cold virus buffer (0.1 M NaAc, 1 mM Na₂EDTA, 1 mM NaN₃) with the help of a glass stick or a pipette. The resuspension is cleared of undissolved material by low-speed centrifugation. The pellet is discarded and the supernatant is mixed with cesium chloride. Once completely dissolved, the mixture is subjected to a density gradient centrifugation. The obtained solution is dialyzed against virus buffer at T= 4°C, and then stored at T=4 °C. The presence and purity is checked by SDS-PAGE and FPLC. Typical yields of CCMV are 200–300 mg per kg of cowpea tissue. During the whole process, the virus solution is kept cold either in an ice bath or in the cold room (T= 4°C).

Preparation of CP

RNA in a suspension of CCMV (1 mL 10 mg/mL) is precipitated by dialysis against RNA buffer (0.05 M Tris-HCl, 0.5 M CaCl₂, 1 mM DTT) at 4 °C. The white precipitate containing RNA is centrifuged down. The supernatant is removed and the pellet discarded. The supernatant is afterwards dialyzed against cleaning buffer (0.05 M Tris-HCl, 0.5 NaCl, 1 mM DTT). The dissociated protein without RNA is obtained and associated into spherical particles by dialysis against capsid storage buffer (0.05 M NaAc, 1 M NaCl, 1mM NaN₃).⁴⁶

Preparation of ND-CP

In a typical experiment, NDs solution (400 μ L, 0.2 mg/mL; H₂O) is added to a solution of CCMV coat protein (100 μ L, 15 mg/mL; pH 7.2; 250 mM Tris, 500 mM NaCl) and allowed to incubate overnight at 4 °C. The reaction mixture is subsequently resulting CP-NDs are purified using preparative FPLC.

Purification of ND-CP by fast protein liquid chromatography (FPLC)

FPLC analysis were performed on a GE Healthcare ÄKTApurifier™ system equipped with a Superose 610/300 GL column from GE Healthcare and a fractionating device. Injection of 500 μ L pre-filtered samples which are injected on a 24 mL superpose-6 column. Compound elution is monitored using a UV-vis spectrometer at 260 nm, 280 nm. Fractionation are collected separately

SDS-PAGE

Dynamical light scattering (DLS)

DLS analysis was performed using a Nanotracs (Anaspec) instrument. Microtrac FLEX Operating software was used at 25°C with laser wavelength of 780 nm and a scattering angle of 90°. The observed size and standard deviation of the nanoparticles were calculated by taking an average of 5 measurements.

Zeta potential

The ζ -potential of the NDs was characterized by a Zetasizer Nano ZS ZEN3600 instrument (Malvern Instruments) at 25 °C with 633 nm laser.

Transmission Electron Microscopy (TEM)

4 μ L 0.1 mg/mL solution of ND-NGs in MilliQ was placed onto an oxygen treated carbon coated copper grid. After 10 min the solution was removed using a filter paper and grids were stained with uranyl acetate 4% for 1.5 min. The grids were washed three times with MilliQ water and dried before measuring. A Jeol 1400 transmissions electron microscope was used to obtain bright field images. And Image J software was used to process the data.

Atomic Force Microscopy (AFM)

Atomic force microscopy was conducted in liquid state with a Bruker Dimension FastScan Bio™ atomic force microscope, which was operated in PeakForce mode. AFM probes with a nominal spring constant of 0.25 N m⁻¹ (FastScan-D, Bruker) were used. The samples were diluted with MilliQ water to a concentration of 0.05 mg mL⁻¹. Sample solution (30 µL) was added onto a freshly cleaved mica substrate (circular, 15 mm) and incubated for at least 10 min to allow deposition of the structures. Remaining solution was removed and 300 µL MilliQ water was applied onto the mica surface, forming a droplet for measuring in liquid. Samples were scanned with scan rates between 1 and 2 Hz and scan sizes between 0.5 and 2 µm. Images were processed with NanoScope Analysis 1.8.

Cytotoxicity measurements

HeLa cells were seeded on a 96 well half-area flat bottom microplate (6,000 cells/well) at 37 °C, 5% CO₂ in DMEM (with 10% FBS, 1% MEM NEAA, and 1% PenStrep) overnight. Different concentrations of ND-NG, as well as doxorubicin as control were added to the cells and incubated overnight. After removing the medium and washing each well 3 times with DPBS, CellTiter-Glo luminescent cell viability assay was added as instructed by the manufacturer's protocol. A Promega GloMax multi detection plate reader was utilized to measure the luminescence.

Hen's Egg Test on the Chorioallantoic Membrane (HET-CAM)

Fertile chicken eggs were purchased from commercial supplier (supplier name here). The eggs were wipe-cleaned and incubated at 37 °C for 3 days with the pointy end of the eggs downward. Embryo development day (EDD) was counted from the first day of incubation. On the EDD 3, about 6 mL of albumin was removed from each egg by employing a syringe and needle. Later a small area of eggshell was carefully removed from the large end of the eggs and sealed again with thin parafilm tape. The eggs were again incubated until EDD 10. They were inspected once every 24 h to discard any nonviable eggs.

On the EDD 10, the eggs with healthy embryo were selected to treat with experimental materials. The eggs were placed in vicinity of a light bulb to maintain the temperature

while adding the materials. 10 μ L of each sample were dropped directly on the chorioallantoic membrane of three eggs, high resolution photographs were taken before and 5 minutes after application of the samples. Additionally, video was recorded continuously for 5 minutes during the application of samples on CAM of each eggs to observe any manifestation of hemorrhage, vascular lysis, or coagulation. After the video recording- the eggs were incubated again. After 24 h, high resolution photograph of the application site was recorded.

Customer-built confocal microscopy for bioimaging and Intracellular tracking

The confocal setup is a conventional customer-built setup, driven by the software Qudi, which could perform a variety of basic measurement functionalities.

The key hardware of the setup consists of an oil-immersion (Olympus, 1.35, 60 \times), a 532 nm continuous-wave laser, a spectrometer (Princeton Instruments, Acton SP 300i), an avalanche photo-diode (APD, Excelitas, SPCM-AQRH), optical filter for confocal imaging is a bandpass of 709 ± 83.5 nm. For compatibility with the Ibidi cell-chamber, the recommended Ibidi immersion oil by Ibidi was used for the objective of the confocal microscope.

On the detection arm, a motorized flip-mirror was used to conduct fluorescence to the APD or the spectrometer, for confocal imaging and tracking, or for spectral measurements respectively. Fast tracking by CCD camera was applied in some of the literatures, which can reveal real-time marker positions on the focal plane in milliseconds. However, there is a sacrifice of losing the position information on the Z-axis. With the positioning excellence of the 3-D piezo scanners on the scanning confocal microscope, as in our case, it takes a few seconds to perform a tracking action but with the advantage that high precision of 3-D trajectories of the cellular marker can be achieved.

Within the fluorescence image, a measurement loop was carried out repeatedly on single bright and photo-stable ND-CP particles. Firstly, a fluorescence scan was performed in a small-range of $100 \mu\text{m} \times 100 \mu\text{m}$ on the X-Y plane, and then zoom in to one single cell and find out the ND-CP fluorescence and measurement the spectrum to

prove it is NV center. A $600\text{ nm} \times 600\text{ nm} \times 2\text{ }\mu\text{m}$ cube was taken as an optimiser to catch the tracking ND-CP particles. Every 5 second the optimiser was use to find out the the best focal point to collect maximum fluorecence counts in the well-aligned scanning confocal setup in the $600 \times 600 \times 2\text{ }\mu\text{m}^3$. The real-time fluorecence intensity was recorded and the maximum intensity should be kept similar in the whole process. Otherwise the process was given up and to look for other points.

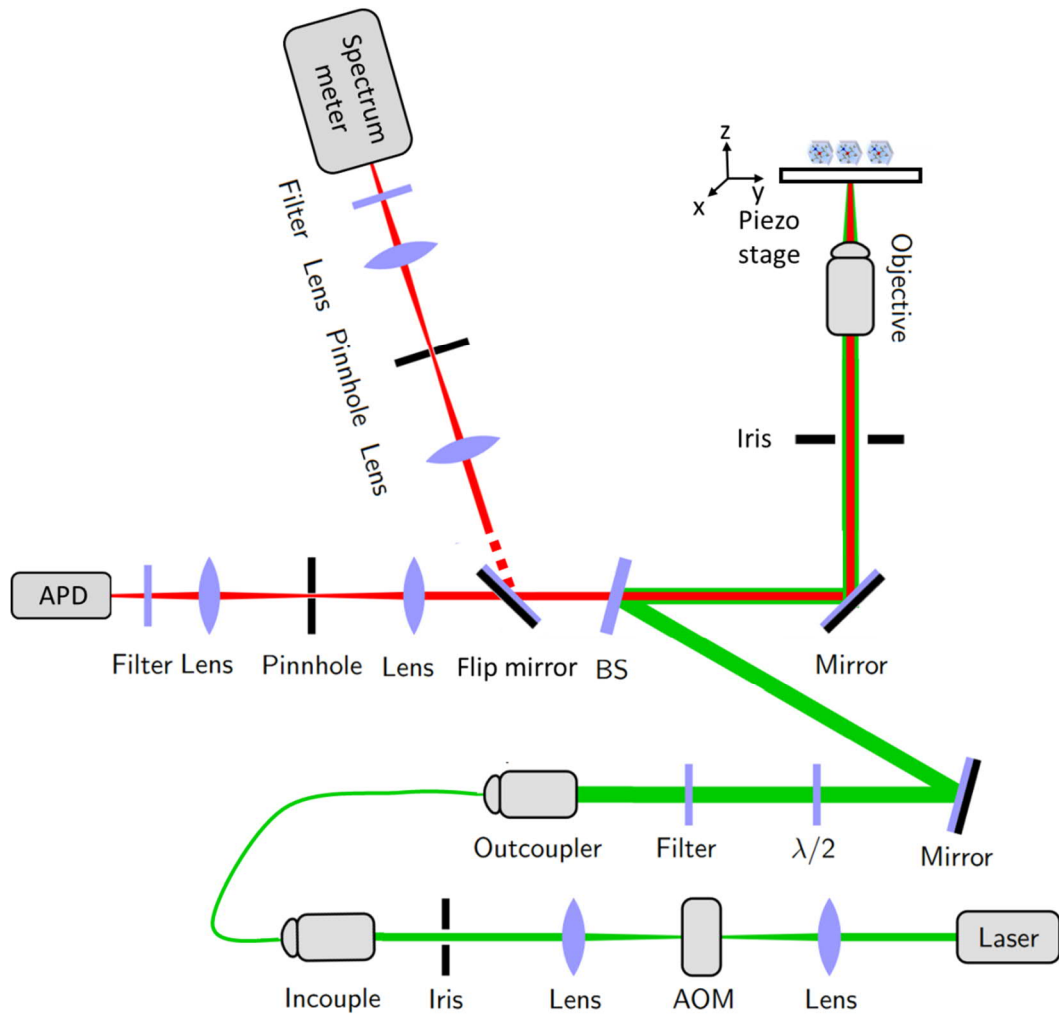


Figure S4.1. Schematic of the customer-built confocal microscopy

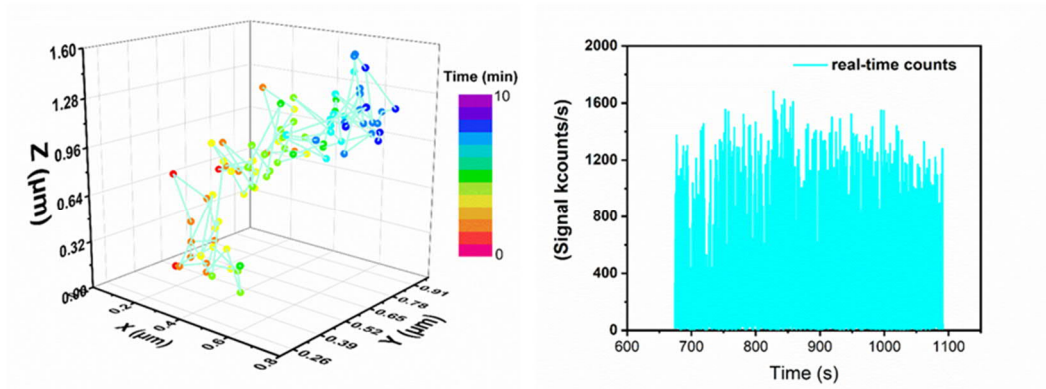
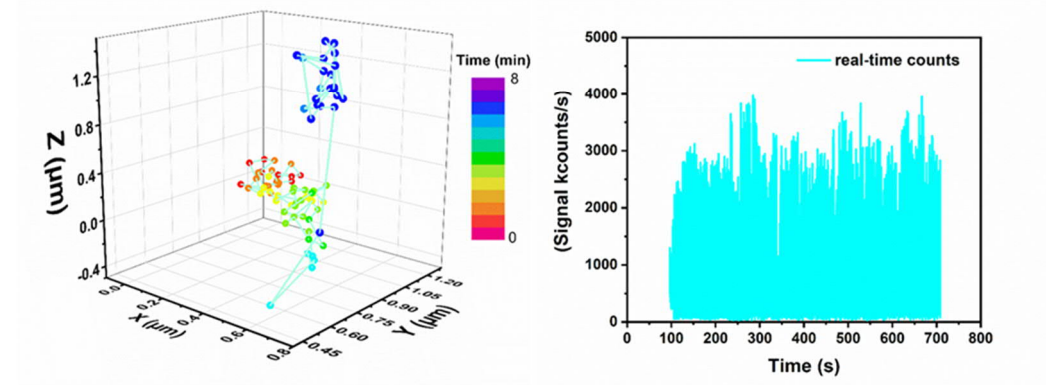
A**B**

Figure S4.2. (A) The trajectory of tracked ND-CP spot 2 in intracellular space of HeLa cell and Real-time counts of fluorescence of the tracked ND-CP spot 2; (B) The trajectory of tracked ND-CP spot 3 in intracellular space of HeLa cell and Real-time counts of fluorescence of the tracked ND-CP spot 3.

4.6 References

1. G. Balasubramanian, I. Chan, R. Kolesov, M. Al-Hmoud, J. Tisler, C. Shin, C. Kim, A. Wojcik, P. R. Hemmer and A. Krueger, *Nature*, 2008, 455, 648-651.
2. P. Neumann, I. Jakobi, F. Dolde, C. Burk, R. Reuter, G. Waldherr, J. Honert, T. Wolf, A. Brunner and J. H. Shim, *Nano Lett.*, 2013, 13, 2738-2742.
3. D. A. Simpson, E. Morrisroe, J. M. McCoey, A. H. Lombard, D. C. Mendis, F. Treussart, L. T. Hall, S. Petrou and L. C. Hollenberg, *ACS Nano*, 2017, 11, 12077-12086.
4. T. Sekiguchi, S. Sotoma and Y. Harada, *Biophys. Physicobiol.*, 2018, 15, 229-234.
5. A. Ermakova, G. Pramanik, J.-M. Cai, G. Algara-Siller, U. Kaiser, T. Weil, Y.-K. Tzeng, H.-C. Chang, L. McGuinness and M. B. Plenio, *Nano Lett.*, 2013, 13, 3305-3309.
6. T. Zhang, G.-Q. Liu, W.-H. Leong, C.-F. Liu, M.-H. Kwok, T. Ngai, R.-B. Liu and Q. Li, *Nat. Commun.*, 2018, 9, 1-8.
7. V. R. Horowitz, B. J. Alemán, D. J. Christle, A. N. Cleland and D. D. Awschalom, *Proc. Nat. Acad. Sci. U.S.A.*, 2012, 109, 13493-13497.
8. R. D. Akiel, X. Zhang, C. Abeywardana, V. Stepanov, P. Z. Qin and S. Takahashi, *J. Phys. Chem. B*, 2016, 120, 4003-4008.
9. K. Xia, C.-F. Liu, W.-H. Leong, M.-H. Kwok, Z.-Y. Yang, X. Feng, R.-B. Liu and Q. Li, *Nat. Commun.*, 2019, 10, 1-9.
10. S. Han, M. Raabe, L. Hodgson, J. Mantell, P. Verkade, T. Lasser, K. Landfester, T. Weil and I. Lieberwirth, *Nano Lett.*, 2019, 19, 2178-2185.
11. M. D. Torelli, N. A. Nunn and O. A. Shenderova, *Small*, 2019, 15, 1902151.
12. H. S. Jung, K. J. Cho, Y. Seol, Y. Takagi, A. Dittmore, P. A. Roche and K. C. Neuman, *Adv. Funct. Mater.*, 2018, 28, 1801252.
13. Y. Wu, A. Ermakova, W. Liu, G. Pramanik, T. M. Vu, A. Kurz, L. McGuinness, B. Naydenov, S. Hafner and R. Reuter, *Adv. Funct. Mater.*, 2015, 25, 6576-6585.
14. S. Harvey, M. Raabe, A. Ermakova, Y. Wu, T. Zapata, C. Chen, H. Lu, F. Jelezko, D. Y. Ng and T. Weil, *Adv. Ther.*, 2019, 2, 1900067.
15. Y. Zhang, Z. Cui, H. Kong, K. Xia, L. Pan, J. Li, Y. Sun, J. Shi, L. Wang and Y. Zhu, *Adv. Mater.*, 2016, 28, 2699-2708.
16. Z. Cui, Y. Zhang, K. Xia, Q. Yan, H. Kong, J. Zhang, X. Zuo, J. Shi, L. Wang and Y. Zhu, *Nat. Commun.*, 2018, 9, 1-11.
17. T. K. Ryu, S. W. Baek, R. H. Kang and S. W. Choi, *Adv. Funct. Mater.*, 2016, 26, 6428-6436.
18. K. van der Laan, M. Hasani, T. Zheng and R. Schirhagl, *Small*, 2018, 14, 1703838.
19. L. Zhao, Y.-H. Xu, T. Akasaka, S. Abe, N. Komatsu, F. Watari and X. Chen, *Biomaterials*, 2014, 35, 5393-5406.
20. A. Bumb, S. K. Sarkar, N. Billington, M. W. Brechbiel and K. C. Neuman, *J. Am. Chem. Soc.*, 2013, 135, 7815-7818.
21. L. Zhao, T. Takimoto, M. Ito, N. Kitagawa, T. Kimura and N. Komatsu, *Angew. Chem. Int. Ed.*, 2011, 50, 1388-1392.
22. R. A. Shimkunas, E. Robinson, R. Lam, S. Lu, X. Xu, X.-Q. Zhang, H. Huang, E. Osawa and D. Ho, *Biomaterials*, 2009, 30, 5720-5728.
23. A. Liu, M. V. de Ruiter, W. Zhu, S. J. Maassen, L. Yang and J. J. Cornelissen, *Adv. Funct. Mater.*,

- 2018, 28, 1801574.
24. A. Liu, M. Verwegen, M. V. de Ruiter, S. J. Maassen, C. H.-H. Traulsen and J. J. Cornelissen, *J. Phys. Chem. B*, 2016, 120, 6352-6357.
 25. I. J. Minten, Y. Ma, M. A. Hempenius, G. J. Vancso, R. J. Nolte and J. J. Cornelissen, *Org. Biomol. Chem.*, 2009, 7, 4685-4688.
 26. L. Schoonen, R. J. Nolte and J. C. van Hest, *Nanoscale*, 2016, 8, 14467-14472.
 27. S. Sinn, L. Yang, F. Biedermann, D. Wang, C. Kübel, J. J. Cornelissen and L. De Cola, *J. Am. Chem. Soc.*, 2018, 140, 2355-2362.
 28. J. Bancroft, E. Hiebert and C. Bracker, *Virology*, 1969, 39, 924-930.
 29. L. Lavelle, M. Gingery, M. Phillips, W. Gelbart, C. Knobler, R. Cadena-Nava, J. Vega-Acosta, L. Pinedo-Torres and J. Ruiz-Garcia, *J. Phys. Chem. B*, 2009, 113, 3813-3819.
 30. J. A. Speir, S. Munshi, G. Wang, T. S. Baker and J. E. Johnson, *Structure*, 1995, 3, 63-78.
 31. T. Douglas, E. Strable, D. Willits, A. Aitouchen, M. Libera and M. Young, *Adv. Mater.*, 2002, 14, 415-418.
 32. G. Winter, A. B. Koch, J. Löffler, M. Lindén, C. Solbach, A. Abaei, H. Li, G. Glatting, A. J. Beer and V. Rasche, *Cancers*, 2020, 12, 1248.
 33. A. Vargas, M. Zeisser-Labouèbe, N. Lange, R. Gurny and F. Delie, *Adv. Drug Deliv. Rev.*, 2007, 59, 1162-1176.
 34. A. Schrage, A. O. Gamer, B. van Ravenzwaay and R. Landsiedel, *Altern. Lab. Anim.*, 2010, 38, 39-52.
 35. A. V. Weigel, B. Simon, M. M. Tamkun and D. Krapf, *Proc. Nat. Acad. Sci. U.S.A.*, 2011, 108, 6438-6443.
 36. N. Gal, D. Lechtman-Goldstein and D. Weihs, *Rheol. Acta*, 2013, 52, 425-443.
 37. M. J. Saxton, *Biophys. J.*, 1997, 72, 1744-1753.
 38. N. Fakhri, A. D. Wessel, C. Willms, M. Pasquali, D. R. Klopfenstein, F. C. MacKintosh and C. F. Schmidt, *Science*, 2014, 344, 1031-1035.
 39. Š. Bálint, I. V. Vilanova, Á. S. Álvarez and M. Lakadamyali, *Proc. Nat. Acad. Sci. U.S.A.*, 2013, 110, 3375-3380.
 40. G. J. Schütz, H. Schindler and T. Schmidt, *Biophys. J.*, 1997, 73, 1073-1080.
 41. D. S. Viswanath, T. K. Ghosh, D. H. Prasad, N. V. Dutt and K. Y. Rani, *Viscosity of liquids: theory, estimation, experiment, and data*, Springer Science & Business Media, 2007.
 42. R. Schirhagl, K. Chang, M. Loretz and C. L. Degen, *Annu. Rev. Phys. Chem.*, 2014, 65, 83-105.
 43. J. J. Bujarski, in *Plant Virology Protocols*, Springer, 1998, pp. 183-188.
 44. B. Verduin, *J. Gen. Virol.*, 1978, 39, 131-147.
 45. R. Hamilton, J. Edwardson, R. Francki, H. Hsu, R. Hull, R. Koenig and R. Milne, *J. Gen. Virol.*, 1981, 54, 223-241.
 46. M. Comellas-Aragonès, H. Engelkamp, V. I. Claessen, N. A. Sommerdijk, A. E. Rowan, P. C. Christianen, J. C. Maan, B. J. Verduin, J. J. Cornelissen and R. J. Nolte, *Nat. Nanotechnol.*, 2007, 2, 635-639.

5. Fluorescent Nanodiamond–Nanogels for Nanoscale Sensing and Photodynamic Applications

Authors

Yingke Wu,[†] Md Noor A Alam,[†] Priyadharshini Balasubramanian, Pia Winterwerber, Anna Ermakova, Michael Müller, Manfred Wagner, Fedor Jelezko, Marco Raabe*, and Tanja Weil*

Y. Wu and M. Alam are shared first author, *corresponding author

Copyright

Published in Adv. NanoBiomed Res. 2021, 2000101.

The following is reproduced with the permission from Copyright (2019) WILEY-VCH Verlag GmbH & Co. KGaA, Weinheim, This work is licensed under a Creative Commons Attribution 4.0 International License.

Author contributions

Y. Wu: Initiated this project, prepared all of the ND-NGs, performed material characterizations(DLS, TEM, emission spectrum, FTIR), prepared and characterized (TEM) the ND-NG-Gd, ND-NG-Ferritin for ODMR measurement, prepared and characterized the ND-NG-Ru by TEM, DLS FTIR, quantified the Ru content in ND-NG-Ru, prepared the draft of the manuscript, prepared the final manuscript based on discussions with all authors.

M. Alam: Initiated this project, performed photodynamic profile study. prepared cells for confocal measurement, performed the cell viability of ND-NG-Ru, performed the HET-CAM measurement, performed live/dead and Annexin-V staining of the cells, prepared the final manuscript based on discussions with all authors

P. Balasubramanian: Performed ODMR measurements and analysed the data, prepared the final manuscript based on discussions with all authors.

P. Winterwerber: Performed the AFM measurement

A. Ermakova: Performed and analyzed the spectrum of ND and ND-NG.

M. Müller: Prepare and characterized the Ru complex

M. Wagner: Discussed the concept and results in the projects

F. Jelezko: Discussed the ODMR measurement and supervised the project.

M. Raabe: Initiated this project, performed the cell viability of ND-NG, performed the confocal microscopy of ND-NG and ND-NG-Ru, performed the HET-CAM measurement, prepared the final manuscript based on discussions with all authors, supervised the project.

T. Weil: Acquiring funding for the project, design and discussion of the concept and results, writing and correcting the manuscript.

Abstract

Fluorescent nanodiamonds (NDs) are carbon-based nanoparticles with various outstanding magneto-optical properties. After preparation, NDs have a variety of different surface groups that determine their physicochemical properties. For biological applications, surface modifications are crucial to impart a new interphase for controlled interactions with biomolecules or cells. Herein, a straight-forward synthesis concept denoted “adsorption-crosslinking” is applied for the efficient modification of ND surfaces, which sequentially combines fast non-covalent adsorption based on electrostatic interactions and subsequent covalent cross-linking. As a result, a very thin and uniform nanogel coating surrounding the NDs is obtained, which imparts reactive groups as well as high colloidal stability. The influence of the reaction time, concentration, molecular weight, and structure of the cross-linker has been analyzed and the impact of these parameters on the nanogel shell, the availability of reactive chemical surface functions and the quantum sensing properties of the coated NDs will be demonstrated. Post-modification of nanogel-coated NDs with phototoxic ruthenium complexes afford ND-based photodynamic therapeutic agent. The adsorption-crosslinking method for surface modification of NDs reported herein provides new avenues towards functional probes and traceable nanocarriers for high resolution bioimaging, diagnosis, nanoscale sensing and precise photodynamic therapy.

5.1 Introduction

Among many carbon-based nanoscale materials, fluorescent nanodiamonds (NDs) have emerged for various applications in nanomedicine and bioimaging, because of their unique magneto-optical properties as well as their excellent biocompatibility.¹⁻³ The optically active atom defects in the lattice of NDs, such as the nitrogen vacancy (NV) center, provide stable fluorescence without photobleaching or photoblinking.⁴ Due to their stable fluorescence, NDs with NV centers have been applied widely in bioimaging⁵⁻⁷ as well as real-time reporters for drug delivery.⁸⁻¹² In addition, the emission wavelength of NDs is size-independent but tunable from the visible to the near infrared region based on the color center (e.g., Si, Ge, etc.).¹³ Furthermore, NDs containing negatively charged NV (NV⁻) centers can serve as single-spin sensors to detect many valuable physical parameters in a biological microenvironment, such as temperature,¹⁴⁻¹⁶ magnetic fields,^{17, 18} electron spins,^{19, 20} and mechanical strain.²¹

However, for most of these applications, an appropriate surface functionalization of the NDs is essential, because the colloidal stability of unmodified nanosized NDs in physiological buffer systems is extremely poor due to aggregation.²² Moreover, the shell provides further reactive groups to attach the desired functionalities, such as drug molecules, dyes, cell or tissue targeting groups or various proteins like antibodies.²³ The surface coating shields the inner ND surface and creates a new interface, which is particularly attractive for *in vitro* or *in vivo* applications, i.e. to prevent foreign body interactions,²⁴ to increase their circulation times²² or their accumulation at the target site²⁵. In the past, various different ND surface coating materials and strategies have been reported. The covalent attachment of functionalities such as a silica shell,²⁶ hyperbranched polyglycerols (HPG),²⁷ poly(1-DOPA),⁹ and antibodies²⁸ has been explored as well as non-covalent adsorption of biomolecules or polymers like polyethyleneimine,²⁹ insulin,³⁰ and albumin-based copolymers.⁸ Nevertheless, uncontrolled aggregation as well as precipitation still represents a challenge and each reported functionalization strategy has its benefits but also inherent limitations. Covalent conjugation approaches are typically challenged by the low number of

functionalities intrinsically present at the ND surface.³¹ Therefore, often only few surface groups could be attached and batch-to-batch variations of the NDs can cause reproducibility problems. ND coating by physical adsorption is a straight forward procedure, which is less influenced by changes of the ND surface groups. However, ligand loss often occurs in biological media thus limiting the stability of the nanoparticle i.e. during cell studies.³² It is our understanding that the combination of both covalent and non-covalent coating approaches would offer several invaluable benefits of both methods.

Herein, we report a straight forward procedure based on the non-covalent adsorption and covalent crosslinking method that imparts a nanogel shell at the ND surface. First, the adsorption of multifunctional and positively charged ligands pre-coats the NDs based on electrostatic interactions followed by a cross-linking step to afford a stable and soft nanogel shell. Hyperbranched polyethyleneimine (PEI) is a highly branched, cationic polymer with multiple primary amino groups that has been widely used in biomedical applications, such as cell transfection^{33, 34} and therapy³⁵⁻³⁷. In addition, to avoid aggregation of NDs during the adsorption of PEI, polyvinylpyrrolidone (PVP) has been applied as a commonly used stabilizer³⁸⁻⁴⁰ with proven biocompatibility as demonstrated in biomedical applications such as in tissue engineering.⁴¹⁻⁴³ PEI has been crosslinked with polyethyleneglycol to generate the soft and homogeneous ND-nanogel shell providing high colloidal stability, reactive primary amino groups for post modifications and low cellular toxicity. We have accomplished a ND-nanogel platform for the design of ND-based photosensitizers for photodynamic applications (PDT). Photodynamic therapy is widely applied in skin cancer and here, light energy is converted locally at the tumor site into reactive oxygen species that affect cancer cell viability.⁴⁴ In addition, the ions level and proteins species in tumor cells are changing simultaneously in the process of therapy. The realtime monitoring of the process is ideally helpful to understand the therapeutic process. In this way, a ND-based photodynamic therapeutic agent with ions and proteins sensing function has been realized and their potential for different biological applications has been demonstrated.

5.2 Results and Discussion

The adsorption and crosslinking procedure to generate a nanogel shell around NDs is depicted in Figure 5.1A. First, the NDs are mixed with hyperbranched polyethyleneimine (PEI, MW: 25 kDa) in the presence of polyvinylpyrrolidone (PVP, MW: 10 kDa) in Milli-Q water. At slightly alkaline (pH7.4) in the presence of phosphate-buffered saline PBS, the 4-arm PEG-NHS ester was applied to cross-link the surface adsorbed PEI for about 90 min. Purification was accomplished by several washing steps to remove unreacted precursors and smaller nanogels without the embedded ND in order to obtain the pure ND-nanogels (ND-NGs) the ND-NGs is listed in Table S5.1.

The ND and ND-NGs were characterized with regards to their distribution, shape, and morphology by transmission electron microscopy (TEM; Figure 5.1B and 5.1C). As shown in Figure 5.1B, TEM images revealed that bare NDs were prone to significant aggregation and displayed a heterogeneous distribution whereas non-aggregating, homogeneous single particles could be observed for ND-NGs (Figure 5.1C). High-resolution transmission electron microscopy (HRTEM) imaging revealed a uniform ring of 2 nm surrounding the NDs indicating the presence of a dry nanogel coating (Figure S5.1). Because the shell was low in contrast and measured under dry condition by TEM, we further assessed the core-shell structure of the ND-NGs by liquid mode atomic force microscopy (AFM; Figure 5.1D and 5.1E), in which the nanogel could swell compared to the dry TEM conditions. In Figure 1D, the topographic image of ND-NGs showed a good distribution with no obvious aggregation. The height-sensor images recorded by AFM were converted into deformation images using NanoScope Analysis 1.8 software to visualize the nanogel coating. Apart from the height profile images, further nanomechanical properties were simultaneously recorded. In particular, the deformation of the sample caused by the probe was analyzed to receive in-depth information on the structure of the coated NDs. As the ND core is much harder than the nanogel shell, the deformation of the nanogel shell could be detected with greater

intensity under the same stress conditions. The deformation image revealed clearly that all NDs were uniformly surrounded by a soft shell (Figure 5.1D, right). Furthermore, the deformation image was studied at higher magnification (Figure 5.1E) and approximately 10 nm thickness of the nanogel was determined in liquid, which is sufficiently thin for nanoscale sensing applications.

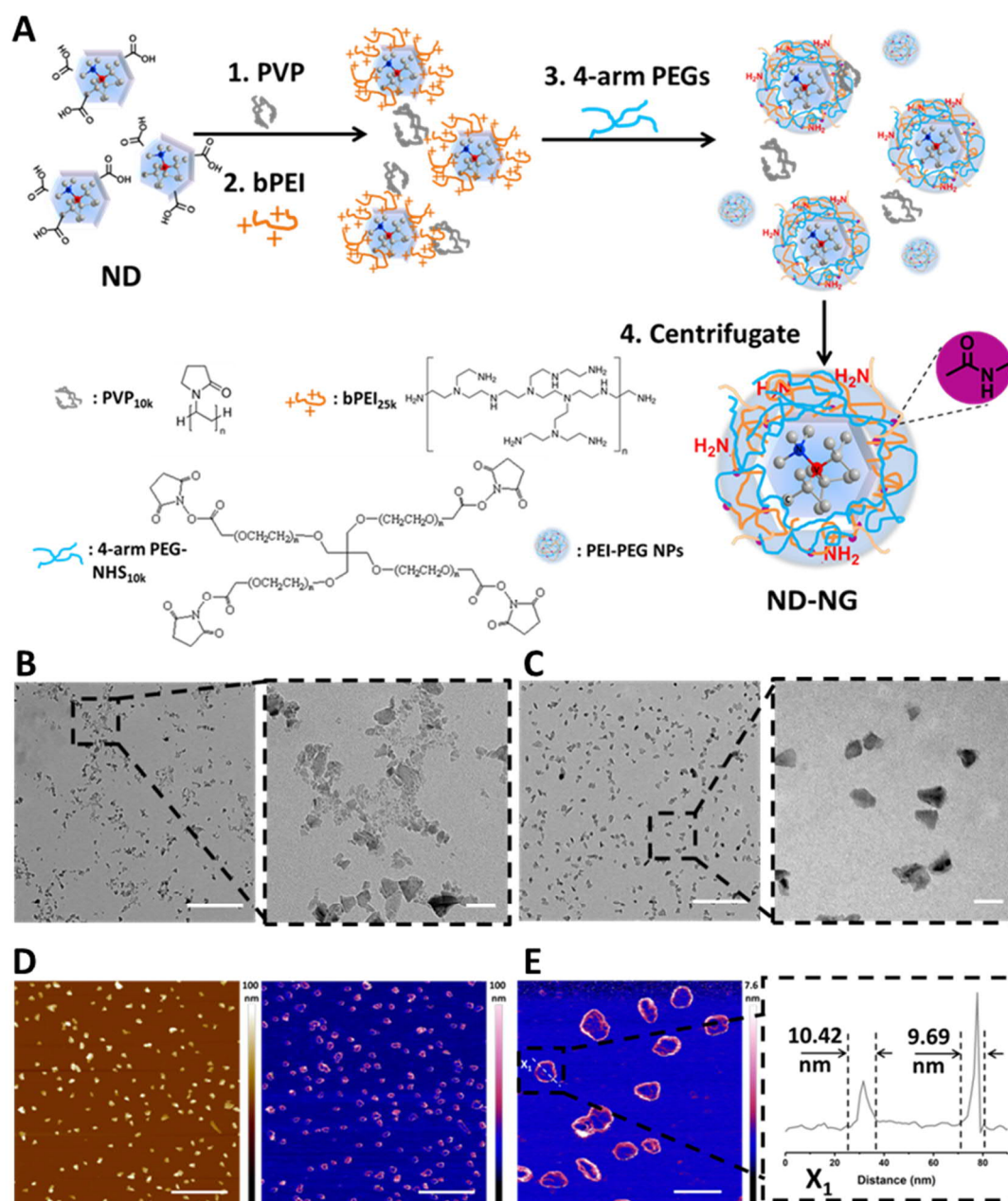


Figure 5.1. (A) Schematic illustration of the preparation of ND-NGs. (B) TEM images of NDs (left: scale bar = 500 nm; right: scale bar = 50 nm). (C) TEM images of ND-

NGs (left: scale bar = 500 nm; right: scale bar = 50 nm). (D) AFM images of ND-NGs at liquid state (left: height sensor; right: deformation; scale bar = 500 nm). (E) AFM images of ND-NGs (left: scale bar=100 nm; right: deformation distance curve of ND-NGs).

The samples were characterized by dynamic light scattering (DLS) to measure the shell thickness of dispersed ND-NGs in aqueous solution. The hydrodynamic diameter of NDs was 36.2 ± 2.4 nm and the hydrodynamic diameter of ND-NGs was 57.0 ± 1.2 nm in Milli-Q water (Figure 5.2A) resulting in a shell thickness of 10.4 ± 3.6 nm of the ND-NGs. The ND-NG samples were also characterized by multi-angle light scattering, which is more sensitive to detect aggregation. No aggregate formation was observed and a shell thickness of about 9 nm (Figure S5.2) was measured. These findings are in agreement with the results from the AFM measurements (10 nm). Variation of the reaction conditions on the size of ND-NGs was investigated by DLS. The size of ND-NGs increased with the reaction time from 45.7 ± 5.6 nm to 52.2 ± 4.0 nm. However, the increments slowed down gradually and stabilized after 90 min suggesting that the reaction reached saturation or completion approximately after this reaction time. When the concentration of the cross-linker was increased from 0.125 to 8 mg mL⁻¹, ND-NGs of 57.0 ± 1.2 nm were obtained with 2 mg mL⁻¹ but the sizes subsequently increased to 74.9 ± 9.9 nm for 8 mg mL⁻¹ cross-linker (Figure S5.4A). In addition, the PEI concentrations were also varied from 0.01 to 10 mg mL⁻¹ to assess the influence of its concentration on the resulting colloidal stability (Figure 5.2B). Aggregation was detected at a concentration of ND-NGs of 0.01 mg mL⁻¹, because the low amount of PEI around single ND was insufficient for colloidal stability. At 1 mg mL⁻¹, the size was 50.2 ± 6.0 nm indicating that a sufficient amount of PEI covered the surface of the NDs thus forming a thin shell. Further increase in PEI to 10 mg mL⁻¹ resulted in a significantly thicker shell (160.9 ± 22.6 nm). The influence of the molecular weight (MW) of PEI and a regularly branched polyamidoamine (PAMAM) dendrimer with a globular sphere-like structure (PAMAM-G3) as well as the buffer which was used to

prepare ND-NGs were investigated (Figure S5.3). NDs aggregated and precipitated when PEIs with lower MW were used (PEI 600 Da and PEI 2000 Da). Alternatives, such as the positive charged dendrimer PAMAM-G3, did not improve colloidal stability and precipitation was likewise observed, implying that only the positive charged branched polymer with appropriate MW (PEI 25,000 Da) and molecular structure allowed the preparation of stable ND-NGs. The ionic constituents of the buffer affected the preparation of ND-NGs as well (Figure 5.2A, Table S5.2), yielding ND-NGs with various sizes in Milli-Q water (83.3 ± 11.0 nm), PBS (57.0 ± 1.2 nm) and HEPES (59.6 ± 6.7 nm).

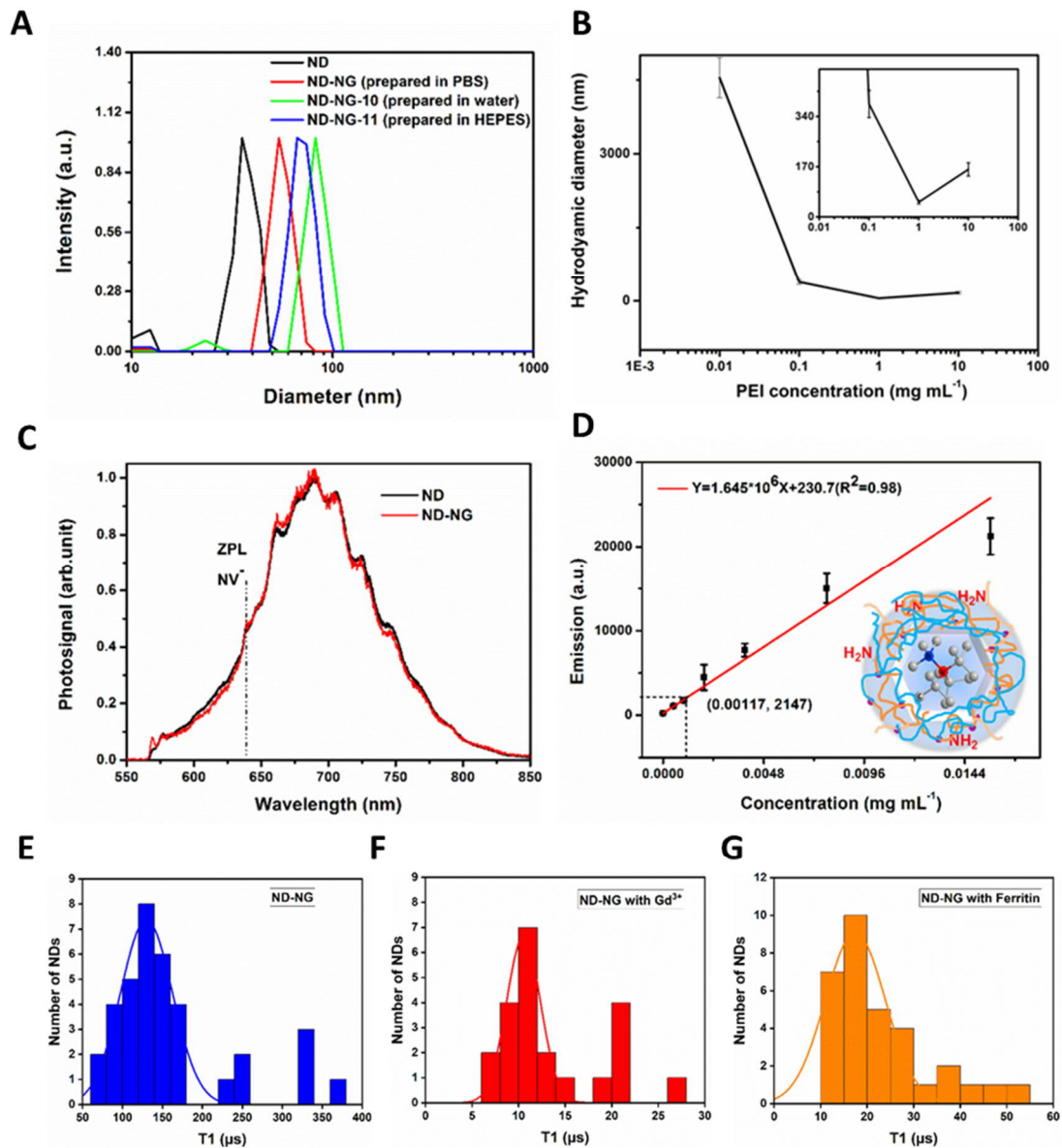


Figure 5.2. (A) Hydrodynamic diameter of NDs and ND-NGs measured by DLS. (B) Influence of the PEI concentration on the size of ND-NGs. (C) Normalized emission spectra (ex. 532 nm) of NDs and ND-NGs. NV^- zero phonon lines are visible in both spectra. (D) Standard curve of fluorescence intensity using ethylenediamine concentration. (E) T_1 time of ND-NG. (F) T_1 time of ND-NG with Gd^{3+} . (G) T_1 time of ND-NG with ferritin.

The effect of the nanogel shell on the photophysical properties of NDs containing NV centers was investigated (Figure 5.2C and Figure S5.4B). For optical measurements, ND-NGs with a diameter of 57.0 ± 1.2 nm were used representatively. Furthermore, the effect of the nanogel shell on the charge state of NV centers in NDs was investigated at the single nanoparticle level (Figure 5.2C). Spectra measurements were performed on a custom-built confocal microscope with an excitation laser at 532 nm and 100 μ W power in front of the objective (oil, NA=1.35). The spectra of ND-NGs revealed that the nanogel shell on the surface of NDs did not affect the fluorescence, and the zero phonon lines of NV^- centers are still well visible without any shift and background noise. NV centers in NDs are very sensitive to the surface states and at some conditions can switch to the dark state (positively charged NV center; NV^+). These results demonstrate that nanogel coating did not affect the charge properties of NV centers, which remained in the optically active states (NV^-). This is especially important for the future application of ND-NGs in bioimaging and nanoscale sensing. To prove the nanoscale sensing ability of ND-NG, Gd^{3+} and ferritin were selected as representatives for paramagnetic ions and proteins. To evaluate the influence of the Gd^{3+} and ferritin attached to ND-NG on the NV spin longitudinal T_1 relaxation time, we used a confocal microscope equipped to perform T_1 spin relaxometry. A pulsed T_1 sequence was chosen, consisting of repetitive laser pulses in absence of a microwave. The spin relaxation from the $m_s = 0$ spin state to the thermally mixed state was probed. We did the relaxometry measurements on randomly selected single particles and averaged the resulting T_1

constants for each sample. The T_1 time decreased from $129.47 \pm 32.5 \mu\text{s}$ of ND-NG to $10.53 \pm 1.82 \mu\text{s}$ of ND-NG attached with Gd^{3+} and $17.43 \pm 6.45 \mu\text{s}$ of ND-NG attached with ferritin. (Figure 5.2E, F, and G)

Post-functionalization allows controlling the chemical, physical, and physiological properties of ND essential for further applications.²² PEI possesses many amine groups, which are positively charged at physiological pH. Bare NDs have a zeta potential of $-37.2 \pm 0.6 \text{ mV}$, which increased to about $18.8 \pm 0.78 \text{ mV}$ (Table S1) after coating, due to many free primary amino groups located at the ND-NG surface. Fluorescamine is a commonly used fluorogenic reagent for the detection and quantification of amino groups. An excess of fluorescamine was added to the ND-NGs solution and the fluorescence intensity was measured using an excitation and emission wavelength of 365 nm and 470 nm (Figure S5.5), respectively. In comparison to the control samples, ND-NG, fluorescamine, and water, only the ND-NGs incubated with fluorescamine showed significant fluorescence proving the accessibility of amino groups present on the surface of ND-NGs. Using ethylenediamine to achieve a calibration plot (Figure 5.2D), the content of the amine groups on ND-NGs was calculated to be $3.90 \times 10^{-5} \text{ mol } -\text{NH}_2 \text{ per gram ND-NGs}$. Assuming that ND consists only of C atoms and all of the ND-NGs particles have a spherical shape of about 40 nm diameter,²⁷ this results in an estimated number of about 2,769 amino groups per ND-NG.

Next, the biocompatibility of ND-NGs was investigated using A549 human lung adenocarcinoma cell line (Figure 5.3). As depicted in Figure 5.3B and 5.3C, ND-NGs were efficiently taken up into A549 cells. We found many homogeneously distributed spherical structures and assume that ND-NGs were located in intracellular vesicles. The uptake was dependent on concentration of ND-NGs and incubation time. When we increased the incubation time from 6 h to 24 h and the concentration of ND-NGs from $100 \mu\text{g mL}^{-1}$ to $200 \mu\text{g mL}^{-1}$, the uptake became even more prominent. In addition, the cell could proliferate well and the cell morphology was not altered. Low cytotoxicity of ND-NGs was observed after the treatment of the cells with a concentration up to 800

$\mu\text{g mL}^{-1}$ (Figure 5.3A).

To further evaluate the biocompatibility of ND-NG, the Hen's Egg Test on the Chorioallantoic Membrane (HET-CAM) method⁴⁵ was chosen, a potential alternative of animal experiments. The wide availability of fertile eggs and easily achievable hatching temperature (37-38 °C) made the HET-CAM a desirable experiment platform. The chorioallantoic membrane (CAM) has an ample vascular network which is suitable for studying tissue xenograft, tumor growth, drug delivery, wound healing, and toxicologic study.⁴⁶ The CAM is not innervated, and the chick embryo develops a functional brain only on the day 13 of incubation⁴⁷. Therefore HET-CAM model can be considered as an animal friendly and humane alternative of *in vivo* testing. In our HET-CAM test, we observed hemorrhage from blood vessels started within 2 - 4 seconds after applying the positive control (1% sodium dodecyl sulfate; SDS). Lysis occurred after 25 - 27 seconds, and we observed coagulation within 24 hours. For the negative control (phosphate buffered saline) and various concentrations of ND-NG ($100 \mu\text{g mL}^{-1}$, $400 \mu\text{g mL}^{-1}$, $800 \mu\text{g mL}^{-1}$) no instance of irritation was detected within 5 minutes to 24 hours of application (Figure 5.3D and Figure S5.6). A summary of the results is shown in Table S3. These *in ovo* results strengthen the superior biocompatibility of ND-NG.

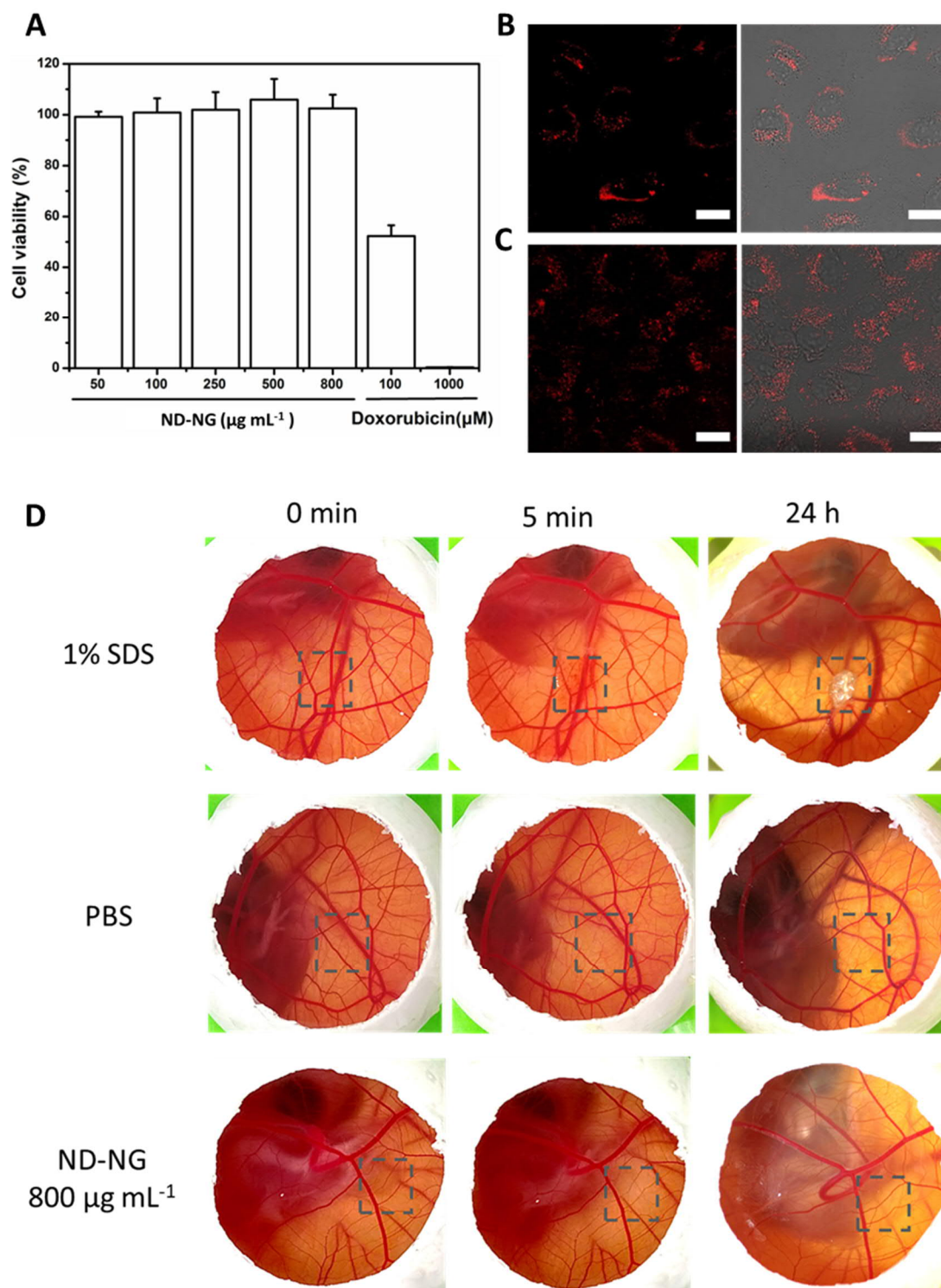


Figure 5.3. (A) Cell viability of ND-NGs in A549 cells. (B, C) Confocal microscopy images of ND-NGs taken up into A549 cells (scale bar = 20 µm). (B) at 100 µg mL⁻¹ for 6 h, (C) at 200 µg mL⁻¹ for 24 h. (D) Photographs of HET-CAM test results for 1% SDS (positive control), PBS (negative control) and ND-NG at 800 µg mL⁻¹.

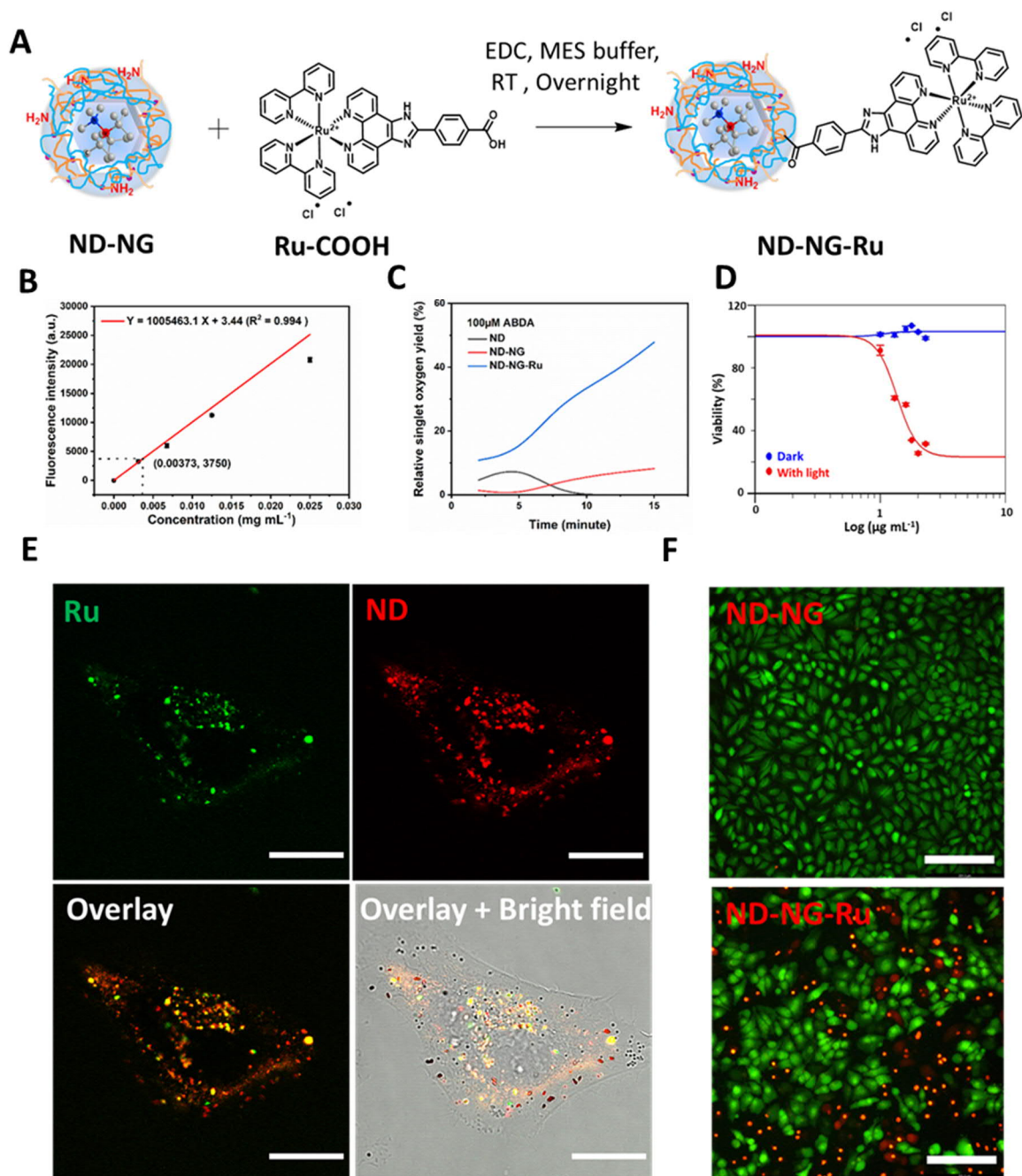


Figure 5.4. (A) Schematic illustration of the preparation of ND-NG-Ru. (B) Standard curve of fluorescence intensity using different concentration of Ru-COOH. (C) Singlet oxygen yield of ND-NG-Ru. (D) Logarithmic fitting curve for cell viability of ND-NG-Ru. (E) Confocal microscopy images in HeLa cells after 4 h incubation with $100 \mu\text{g mL}^{-1}$ ND-NG-Ru (scale bar = $20 \mu\text{m}$). (F) Live/dead staining of HeLa cells incubated with ND-NG or ND-NG-Ru after 15 min of irradiation (scale bar = $200 \mu\text{m}$).

To underline the potential of ND-NGs as a theranostic platform, a photodynamic therapy (PDT) agent, [4-(1*H*-imidazo[4,5-*f*][1,10]phenanthrolin-2-yl- κ N7, κ N8)benzoato]-bis(2,2'-bipyridine- κ N1, κ N1')ruthenium(1+)chloride (Ru-COOH) was conjugated to the ND-NGs by the reaction of its carboxylic acid with amine groups of ND-NGs in the presence of EDC to afford ND-NG-Ru (Figure 5.4A). PDT is a treatment using photosensitizing agents, whose bioactivity is activated by light.⁴⁸ The photosensitizer produce reactive oxygen species i.e. singlet oxygen ($^1\text{O}_2$) for therapeutic purposes. Singlet oxygen is cytotoxic, which strongly decreases i.e. viability of tumor cells.⁴⁹ PDT is minimally invasive compared to other treatment procedures (e.g., surgery), and can be used together with other therapeutic techniques. Due to the low invasiveness of this approach, small or no scarring at the application site after healing represents an additional benefit for the patient's quality of life. However, there are some drawbacks including low tumor specificity, inefficient cellular uptake, and higher activation energies (if required) leading to prolonged illumination times. To overcome these challenges, ND-NG was used as a carrier system. After modification with Ru-COOH, the attenuated total reflection Fourier transform infrared (ATR-FTIR) spectrum of ND-NG-Ru was measured (Figure S5.8) and showed that the peak intensity of the stretching vibration of N-H decreased dramatically as the amine group reacted with the carboxylic acid groups of Ru-COOH. To quantify the number of Ru complexes on ND-NG-Ru, the fluorescence intensity was measured using an excitation and emission wavelength of 460 nm and 610 nm, respectively. In comparison to the control samples (ND-NG), only ND-NG-Ru showed emission properties in the characteristic range (Figure S5.9). Using a series of Ru-COOH solutions, a calibration plot was generated (Figure 5.4B) and the content of the Ru complexes on the ND-NG-Ru was calculated to be 3.78 μg per mg of ND-NGs. The DLS and TEM measurements of ND-NG-Ru revealed a high colloidal stability with good dispersion and stability in aqueous media (Figure S5.10 and S5.11). Compared to the hydrodynamic size of ND-NG, the dimension of ND-NG-Ru increased from 57.0 ± 1.2 nm to 73.7 ± 4.9 nm, respectively.

Besides, no significant aggregation was observed in TEM images. PDT relies on the efficient production of singlet oxygen in cellular environments. To monitor the generation of $^1\text{O}_2$ in a quantitative fashion, we performed $^1\text{O}_2$ production efficiency tests as reported previously.⁵⁰ The singlet oxygen sensor 9,10-anthracenediyl-bi(methylene)dimalonic acid (ABDA) was used, which forms an endoperoxide of ABDA in the presence of $^1\text{O}_2$ that alters its absorbance spectrum. Therefore, the production of $^1\text{O}_2$ was monitored by measuring this particular change in absorbance of ABDA (Figure 5.4C). ND-NG-Ru, ND-NGs, and bare NDs as control were mixed with 100 μM of ABDA and were irradiated with a 470 nm LED array (20 mW cm^{-2}) for 15 min. Relative changes in absorbance confirmed the successful generation of $^1\text{O}_2$. We also examined the intracellular localization of ND-NG-Ru in a human cervical cancer cell line (HeLa cells) by laser scanning confocal microscopy. These cells were incubated with ND-NG-Ru (100 $\mu\text{g mL}^{-1}$) for about 4 h before images were recorded (Figure 5.4E). ND-NG-Ru were efficiently taken up and many homogeneously distributed spherical structures were observed suggesting that ND-NGs were mainly located in intracellular vesicles. To evaluate light induced cellular toxicity, HeLa cells were incubated with 0 - 200 $\mu\text{g mL}^{-1}$ ND-NG-Ru for 4h before irradiation with 470 nm LED light for 15 min (50 mW cm^{-2}). The applied power is comparable to reported photosensitizing drugs.⁵¹ We found a very low IC_{50} of around 23 $\mu\text{g mL}^{-1}$ for the ND-NG-Ru (Figure 5.4D), which is similar to the reported IC_{50} of 15 $\mu\text{g mL}^{-1}$ of the Ru-tetrazole coordinated nanoparticles.⁵² Live/dead staining of the cells using fluorescein diacetate/propidium iodide further demonstrated that ND-NG-Ru induced cell death upon irradiation could be spatially controlled (Figure 5.4F).

5.3 Conclusion

In summary, we have developed the adsorption-crosslinking method as a novel synthesis concept for surface modification of NDs. The approach combines both non-covalent adsorption and covalent stabilization thus integrating the advantages of both coating strategies within one system while overcoming their respective drawbacks.

Using this method, we successfully prepared ND-NG samples with a thin and uniform nanogel shell as well as a homogenous size distribution while elucidating the chemical tools to control its formation. Critically, the photophysical properties of the NV centers of ND were not affected by surface modification. Especially the nanoscale sensing possibility. Quantification of the number of amine groups, which are presented on the surface of ND-NGs was achieved. Furthermore, the ND-NG were well tolerated at cell experiments and *in vivo* testing. Introduction of a photodynamic therapy agent Ru-COOH was achieved in a post-modification approach. ND-NG-Ru showed successful photodynamic activity *in vitro*. By demonstrating the capability to combine multiple functions i.e. the nanoscale sensing and photodynamic ability, the versatility of the platform was proven. Importantly, the adsorption-crosslinking method can be expanded to other chemical motifs, as reactive groups are still available within the nanogels for further modification. We believe that our studies pave the way to customized ND-based nanotheranostics for precise diagnosis and therapy at the subcellular level.

5.4 Acknowledgements

The authors thank the Polymer Analytics for multiangle DLS measurements, Dr. David Yuen Wah Ng for the fruitful discussion and suggestions, Dr. Gönül Kizilsavas for her support, and Adriana Sobota for her suggestions regarding the HET-CAM assay. The authors are grateful for the financial support from the European Union's Horizon 2020 Research and Innovation Program under FETOPEN grant agreement no. 858149 (AlternativeToGd) and from the Deutsche Forschungsgemeinschaft (DFG, German Research Foundation) – Project number 316249678 – SFB 1279 (C04). Y. Wu thanks the China Scholarship Council for a fellowship.

5.5 Supporting information

Materials and Methods

Materials: Nanodiamonds with 35 nm average diameter were purchased from FND Biotech (Taiwan), 4-arm PEG-SCM (MW: 10 kDa, Creative PEGWorks), branched

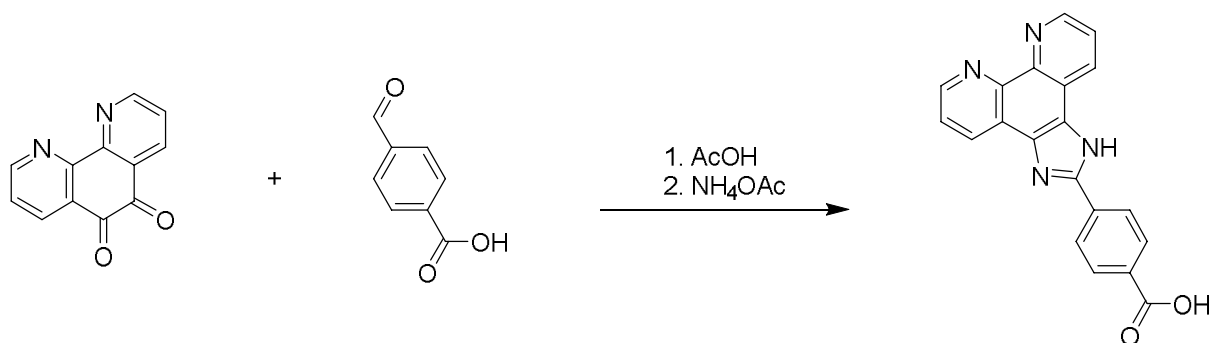
polyethylenimine (MW: 25 kDa by LS), polyvinylpyrrolidone (MW: 10 kDa), (3-carboxypropyl)triphenylphosphonium bromide, *N*-hydroxy-succinimide (NHS), 9,10-anthracenediyl-bi(methylene)dimalonic acid, fluorescamine and ethylenediamine were purchased from Sigma-Aldrich, Dulbecco's Modified Eagle's Medium (DMEM, 1x), Dulbecco's phosphate-buffered saline (DPBS, 1x), fetal bovine serum (FBS), Penicillin Streptomycin (Pen Strep) were purchased from gibco, MitoLite™ Blue FX490 were purchased from AAT Bioquest. All solvents and chemicals were purchased from commercial sources and were used without further purification

Preparation of ND-NGs

Firstly, 100 μL ND (2 mg mL^{-1}) stock solution was dispersed in 300 μL water. Afterwards, 100 μL PVP (20 mg mL^{-1}), 200 μL PEI (5 mg mL^{-1}), and 300 μL PBS buffer (10 mM, pH 7.4) were added. After 5 min sonication, 2 mg of 4-arm PEG-SCM was added to cross-link the PEI on the surface of ND. The final volume was adjusted to 1 mL with MilliQ water. After sonication for 30 min and reaction of 90 min on a shaker at 800 rpm, the obtained ND-NGs were washed 3 times by centrifugation at 12,000 g for 20 min.

Preparation of 4-(1*H*-imidazo[4,5-*f*][1,10]phenanthroline-2-yl)-benzoic acid

4-(1*H*-imidazo[4,5-*f*][1,10]phenanthroline-2-yl)-benzoic acid was synthesized according to literature.⁵³ 150 mg (0.7 mmol, 1 eq.) 1,10-phenanthroline-5,6-dione, 136 mg (0.9 mmol, 1.3 eq.) 4 formylbenzoic acid and 1347 mg (17.5 mmol, 25 eq.) ammonium acetate were dissolved in 15 mL glacial acetic acid in a 50 mL round bottom flask and refluxed at 150 °C for 3 h. After 3 h a yellow precipitate was formed, and the reaction mixture was cooled down to room temperature. 30 mL of cold deionized water was added and the precipitate was vacuum filtrated. The precipitate was washed three times with 30 mL of cold deionized water and dried overnight. The product was used without further purification since the purity was high enough, which was confirmed via ¹H-NMR and LC-MS.

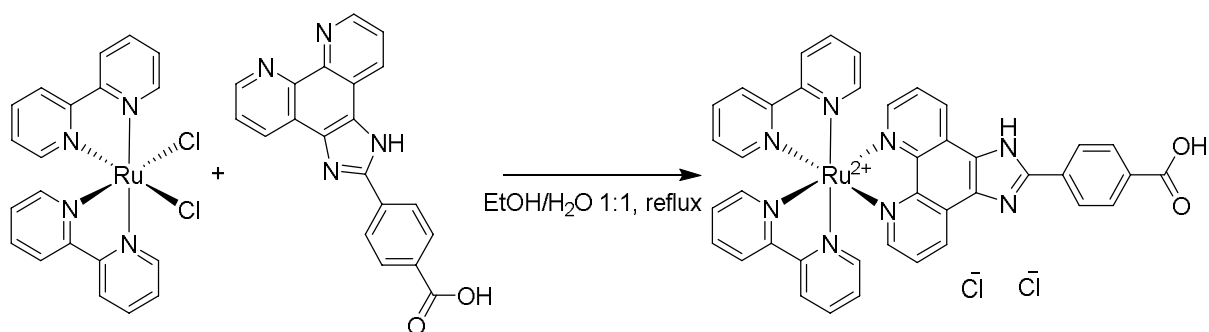


Name	M / g/mol	m / mg	n / mmol	V / mL	Eq.
1,10-phenanthroline-5,6-dione	210.19	150	0.7		1
4-formylbenzoic acid	150.13	136	0.9		1.3
acetic acid	60.05			15	
ammonium acetate	77.08	1347	17.5		25

Preparation of Ru-COOH ([4-(1*H*-imidazo[4,5-*f*][1,10]phenanthroline-2-yl-κN7, κN8)benzoato]-bis(2,2'-bipyridine-κN1,κN1')ruthenium(1+)chloride)

Ru(bpy)₂Cl₂ (100 mg, 206 μmol, 1 eq.) and 4-(1*H*-imidazo[4,5-*f*][1,10]phenanthroline-2-yl)-benzoic acid (77 mg, 227 μmol, 1.1 eq.) were dissolved in 10 mL ethanol/water (3/1) and refluxed under inert gas atmosphere for 8 h. Afterwards, the solvent was removed under vacuum and the crude product was dissolved in methanol and then precipitated in diethyl ether (−20 °C). The precipitate was filtered off and washed three times with cold diethyl ether. The pure product was dissolved in water and lyophilized. The yield was 121 mg (77%).

RP-LCMS *m/z* calcd. [M]⁺ = 753.77 obs. 754



Name	M g/mol	m mg	n mmol	V mL	Eq.
cis-dichlorobis(bipyridine)ruthenium(II)	484.35	100	0.20		1
4-(1H-imidazo[4,5-f][1,10]phenanthrolin-2-yl)benzoic acid	340.34	77	0.23		1.1
ethanol	46.07			5	
water	18.01			5	

Preparation of ND-NG-Ru

100 μL ND-NG (2 mg mL⁻¹) was mixed with 500 μL Ru complex (4 mg mL⁻¹) and 100 μL EDC (20 mg mL⁻¹). Afterwards, MES buffer (1 M, pH 4.7) was added to bring the volume to 1 mL and reacted at room temperature overnight. Next, ND-NG-Ru were washed three times by centrifugation at 12,000 g for 20 min to obtain 100 μL ND-NG-Ru (2 mg mL⁻¹) for further use.

UV-Vis Absorbance and Fluorescence

20 μL of water, ND, ND-NGs solutions in MilliQ water (2 mg mL⁻¹) were prepared in separate wells of a 384-well low volume microplate. Absorbance scans from 200 to 1000 nm were obtained using a Tecan Spark 20M microplate reader. Fluorescence intensity scans were obtained using a Tecan Spark 20M device as well. An excitation wavelength of 560 nm was used for emission scans. An emission wavelength of 680 nm was monitored for excitation scans.

Quantitative analysis of the surface group of ND-NGs

A standard curve of fluorescamine-ethylenediamine was prepared to calculate the amine groups in ND-NG as followed: 10 μL ethylenediamine solution with concentration of 25 $\mu\text{g mL}^{-1}$, 12.5 $\mu\text{g mL}^{-1}$, 6.25 $\mu\text{g mL}^{-1}$, 3.125 $\mu\text{g mL}^{-1}$, 1.5625 $\mu\text{g mL}^{-1}$, 0.78125 $\mu\text{g mL}^{-1}$, water, and 2 mg mL^{-1} ND-NGs were added in separate wells of 384-well low volume well plate, and then 10 μL fluorescamine (6 mg mL^{-1}) was added. After 15 min incubation at room temperature, fluorescence intensity were obtained by a Tecan Spark 20M. The fluorescence intensity–concentration curve was drawn and the amine group content in ND-NGs was calculated.

Transmission Electron Microscopy (TEM)

One drop of a 0.1 mg mL^{-1} solution of ND-NGs in MilliQ was placed onto an oxygen treated copper grid. A Jeol 1400 transmissions electron microscope was used to obtain bright field images.

Dynamic Light Scattering (DLS)

500 μL of 0.1 mg mL^{-1} solutions of ND, ND-NGs in MilliQ were transferred into a borosilicate glass cuvette. The size was measured at 20 $^{\circ}\text{C}$ with a 90 $^{\circ}$ angle using a particle sizer (Zeta Potential/Particle Sizer, NicompTM 380 ZLS, PSS, Santa Barbara, CA, USA). The hydrodynamic diameter distribution was presented as intensity. Zeta potential was measured at 25 $^{\circ}\text{C}$ with a Malvern Zetasizer Nano-S90 (Nano series).

Atomic Force Microscopy (AFM)

Atomic force microscopy was conducted in liquid state with a Bruker Dimension FastScan BioTM atomic force microscope, which was operated in PeakForce mode. AFM probes with a nominal spring constant of 0.25 N m^{-1} (FastScan-D, Bruker) were used. The samples were diluted with MilliQ water to a concentration of 0.05 mg mL^{-1} . Sample solution (30 μL) was added onto a freshly cleaved mica substrate (circular, 15 mm) and incubated for at least 10 min to allow deposition of the structures. Remaining solution was removed and 300 μL MilliQ water was applied onto the mica surface, forming a droplet for measuring in liquid. Samples were scanned with scan rates between 1 and 2 Hz and scan sizes between 0.5 and 2 μm . Images were processed with NanoScope Analysis 1.8.

Confocal Microscopy

To study the cellular uptake mechanism, A549 cells were seeded in ibidi 8 well μ -slide and incubated overnight. The ND samples were added and incubated for 4 h at 37 °C. Afterward, MitoLite™ Blue FX490 dye was added according to the manufacturer's instruction to stain the mitochondria. A Leica TCS SP5 confocal system was used to acquire the images and they were analyzed by ImageJ software.

Cytotoxicity measurements

A549 cells were seeded on a 96 well half-area flat bottom microplate (6,000 cells/well) at 37 °C, 5% CO₂ in DMEM (with 10% FBS, 1% MEM NEAA, and 1% PenStrep) overnight. Different concentrations of ND-NG, as well as doxorubicin as control were added to the cells and incubated overnight. After removing the medium and washing each well 3 times with DPBS, CellTiter-Glo luminescent cell viability assay was added as instructed by the manufacturer's protocol. A Promega GloMax multi detection plate reader was utilized to measure the luminescence.

Singlet oxygen sensing using ABDA absorption peak at 380 nm

400 $\mu\text{g mL}^{-1}$ of ND, ND-NG, and ND-NG-Ru samples were prepared by diluting to 100 μM 9,10-anthracenediyl-bis(methylene)dimalonic acid (ABDA). Simultaneously another three samples were prepared by diluting in pure water (400 $\mu\text{g mL}^{-1}$) for background subtraction. All the samples were irradiated with a 470 nm LED light source for 15 min, the light source power density was 20 mW cm^{-2} . A Tecan Spark 20M microplate reader was employed to measure the absorbance at 380 nm excitation wavelength for different time points. A gradual decline of absorbance was observed for samples diluted in ABDA due to conversion of ABDA to endoperoxide in presence of singlet oxygen, which indicates efficient formation of singlet oxygen by ND-NG-Ru upon irradiation.

Phototoxicity experiment

HeLa cells were plated in two 96 well half-area flat bottom microplate (130,000 cells per mL, 50 μl each well). After 36 h of incubation in 37 °C and 5% CO₂, different concentrations of ND-NG-Ru diluted in cell medium (DMEM with 10% FBS, 1%

MEM NEAA, and 1% PenStrep) were added to the cells and left in the incubator for cellular uptake. After 4 h of incubation, cells were washed using DPBS. One of the microplates was irradiated by a 470 nm blue LED light source for 15 min (power density 50 mW cm⁻²). Both plates were kept in the incubator for four hours, afterwards CellTiter-Glo luminescent cell viability assay was employed as instructed by the manufacturer's protocol. A Promega GloMax multi detection plate reader was employed to determine the luminescence.

For IC₅₀ calculation, Quest Graph™ IC50 Calculator by AAT Bioquest, Inc. was used.^[2] Calculated IC₅₀ value was 23.07 µg mL⁻¹.

Live/dead staining of HeLa cell

HeLa cells were plated in a 24-well microplate (400 µL each well, 75,000 cells per ml). Cells were incubated overnight. Next day, old medium was removed and 300 µL of 50 µg mL⁻¹ ND-NG and ND-NG-Ru (in cell medium) were added to the cells. After additional 4 h of incubation, cells were washed using DPBS, then fresh cell medium was added. Some wells were irradiated for 15 min by a 470 nm LED (power density 50 mW cm⁻²), other wells were protected from irradiation. After photo-treatment, the cells were kept in incubation for additional 2 h. Later the cells were treated with live/dead staining solution. The solution was prepared by following the ibidi protocol, 8 µL fluorescein diacetate (5 mg mL⁻¹) and 100 µL propidium iodide (1 mg mL⁻¹) were mixed to 5 mL of DPBS. After 5 minutes of live/dead staining solution treatment, the cells were washed three times with DPBS. Imaging was performed immediately using a Leica DMI8 microscope with a Leica MC170 HD camera system.

Hen's Egg Test on the Chorioallantoic Membrane (HET-CAM)

Fertile chicken eggs were purchased from commercial supplier (LSL Rhein-Main Geflügelvermehrungsbetriebe GmbH & Co.KG). The eggs were wipe-cleaned and incubated at 37 °C for 3 days with the pointy end of the eggs downward. Embryo development day (EDD) was counted from the first day of incubation. On the EDD 3, about 6 mL of albumin was removed from each egg by employing a syringe and needle. Later a small area of eggshell was carefully removed from the large end of the eggs and

sealed again with thin parafilm tape. The eggs were again incubated until EDD 10. They were inspected once every 24 h to discard any nonviable eggs.

On the EDD 10, the eggs with healthy embryo were selected to treat with experimental materials. The eggs were placed in vicinity of a light bulb to maintain the temperature while adding the materials. 10 µL of each sample were dropped directly on the chorioallantoic membrane of three eggs, high resolution photographs were taken before and 5 minutes after application of the samples. Additionally, video was recorded continuously for 5 minutes during the application of samples on CAM of each eggs to observe any manifestation of hemorrhage, vascular lysis, or coagulation. After the video recording- the eggs were incubated again. After 24 h, high resolution photograph of the application site was recorded.

The following three type of reactions were observed on the CAM: hemorrhage, vascular lysis, and coagulation. The time (in seconds) needed to reach each type of irritational reaction after applying the sample can be used to calculate the irritation score (IS) using following equation⁵⁴:

$$\text{Irritation score (IS)} = [5 \times (301 - \text{mth})/300] + [7 \times (301 - \text{mtl})/300] + [9 \times (301 - \text{mtc})/300]$$

Here, mth = mean time to hemorrhage, mtl = mean time to vascular lysis, mtc = mean time to coagulation. When no hemorrhage, lysis, or coagulation was recorded within first 5 minutes of sample application, the contribution of respective irritation component was considered null.

Classification Irritation Score (IS).

Classification of irritant based on the irritation score (IS)

Classification	Irritation Score (IS)
Maximum	21
Severe irritant	> 9
Non-to-moderate irritant	0 - 9

Results and Discussion

Table S5.1. Formula of ND-NG series

Samples	ND (mg mL ⁻¹) 1)	PVP _{10k} (mg mL ⁻¹)	bPEI _{25k} (mg mL ⁻¹)	Buffer	4-arm- PEG NHS _{10k} (mg mL ⁻¹)	Size by DLS (nm)
ND-NG-1	0.2	2	10	PBS(PH 7.4, 3mM)	2	160.9 ± 22.6
ND-NG*	0.2	2	1	PBS(PH 7.4, 3mM)	2	57.0 ± 1.2
ND-NG-2	0.2	2	0.1	PBS(PH 7.4, 3mM)	2	382.4 ± 46.3
ND-NG-3	0.2	2	0.01	PBS(PH 7.4, 3mM)	2	4544.1 ± 407.1
ND-NG-4	0.2	2	1	PBS(PH 7.4, 3mM)	8	74.9 ± 9.9
ND-NG-5	0.2	2	1	PBS(PH 7.4, 3mM)	4	69.1 ± 8.4
ND-NG-6	0.2	2	1	PBS(PH 7.4, 3mM)	1	55.4 ± 6.9
ND-NG-7	0.2	2	1	PBS(PH 7.4, 3mM)	0.5	59.9 ± 6.6
ND-NG-8	0.2	2	1	PBS(PH 7.4, 3mM)	0.25	63.5 ± 7.1
ND-NG-9	0.2	2	1	PBS(PH 7.4, 3mM)	0.125	55.6 ± 6.9
ND-NG-10	0.2	2	1	Milli-Q water	2	83.3 ± 11.0
ND-NG-11	0.2	2	1	HEPES (PH 7.4, 3mM)		59.6 ± 6.7

	0.2	2	1(bPEI ₆₀₀)	PBS(PH 7.4, 3mM)	2	precipitate
	0.2	2	1(bPEI ₂₀₀₀)	PBS(PH 7.4, 3mM)	2	precipitate
	0.2	2	1(PAMAM-G3)	PBS(PH 7.4, 3mM)	2	precipitate

*the sample is selected as representative for all of the research without special statement.

Table S5.2. Size and zeta potential of ND-NGs

Samples	Hydrodynamic diameter (nm)	Zeta potential (mV)
ND	36.2 ± 2.4	-37.2 ± 0.6
ND-NG (prepared in PBS)	57.0 ± 1.2	18.8 ± 0.78
ND-NG-10 (prepared in water)	83.3 ± 11.0	18.1 ± 6.63
ND-NG-11 (prepared in HEPES)	59.6 ± 6.7	22.0 ± 5.97

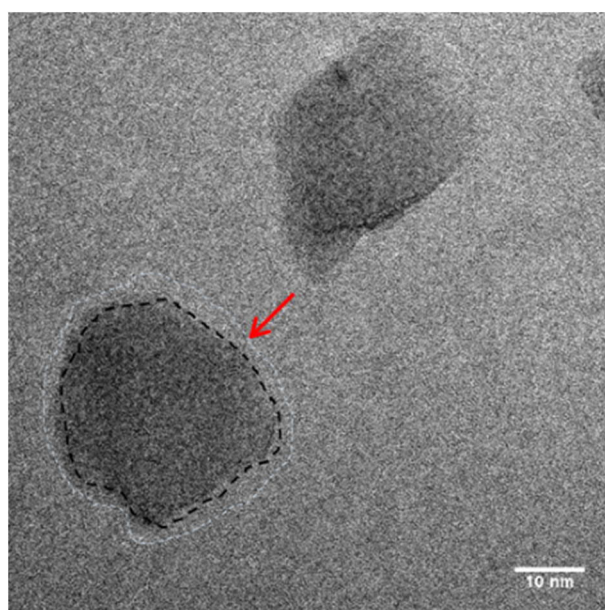


Figure S5.1. High-resolution TEM image of ND-NG.

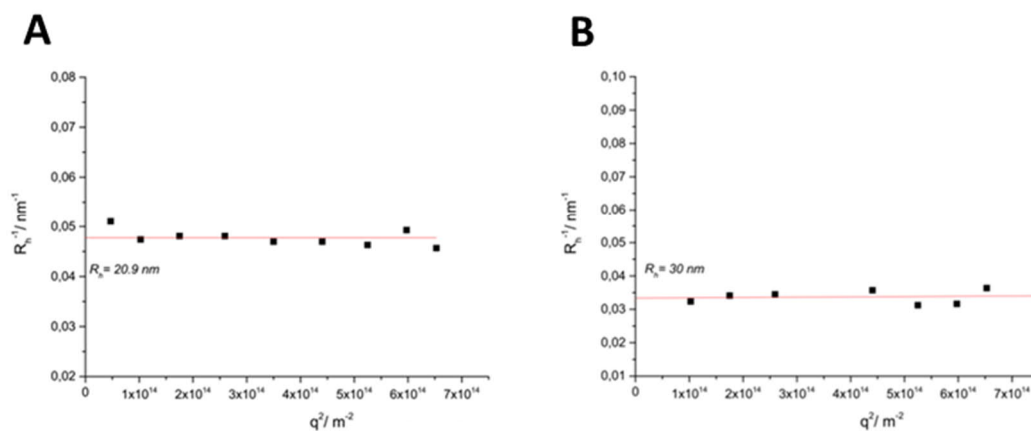


Figure S5.2. Hydrodynamic radius (R_h) measured by a multi-angle light scattering systems. (A) NDs, (B) ND-NGs.

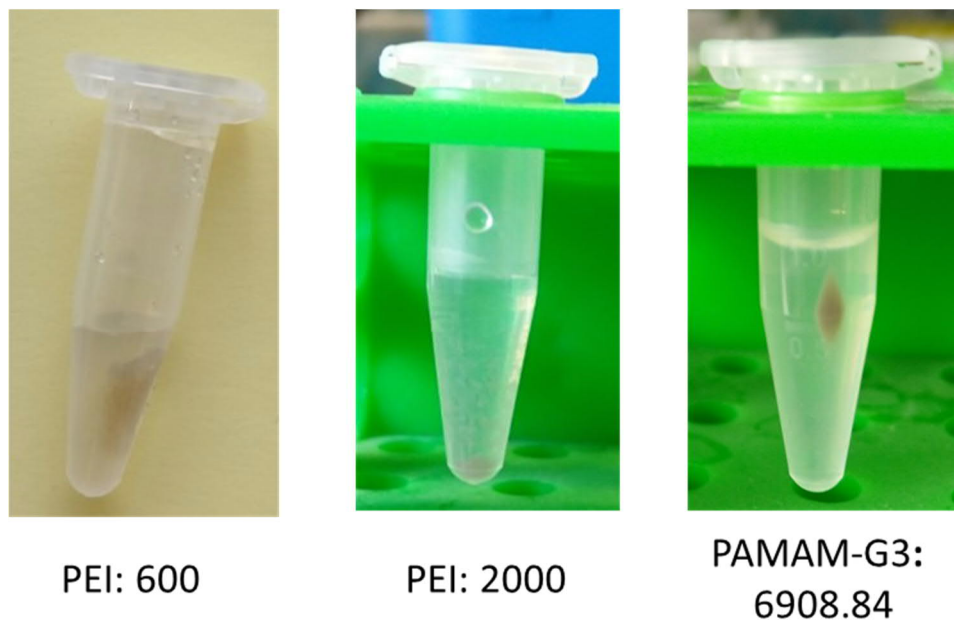


Figure S5.3. ND-NGs prepared with PEI 600, PEI 2000 and PAMAM-G3.

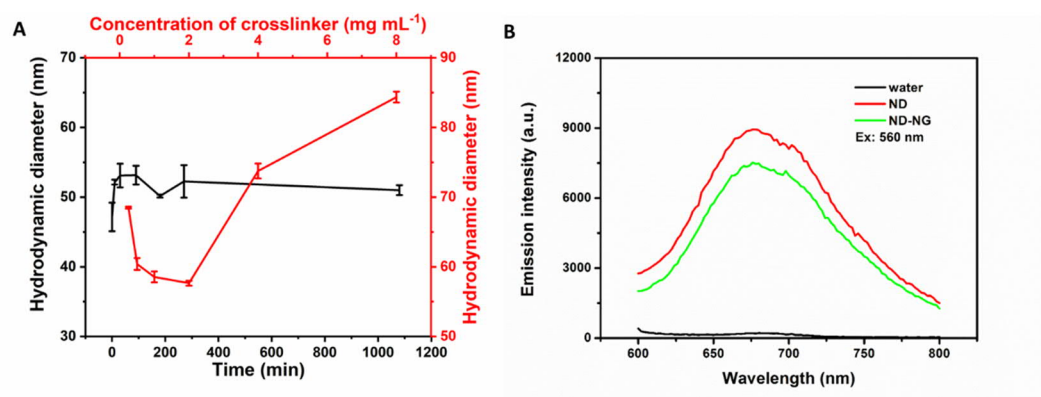


Figure S5.4. (A) Influence of reaction time and the concentration of the cross-linker on the size of ND-NGs. (B) Emission spectra of ND and ND-NG (ex. 560 nm).

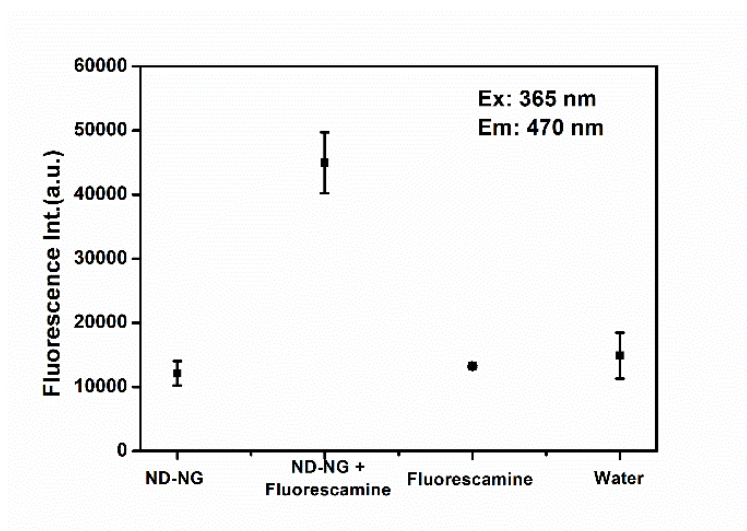


Figure S5.5. Fluorescence intensity of ND-NG, ND-NG with fluorescamine, fluorescamine and water.

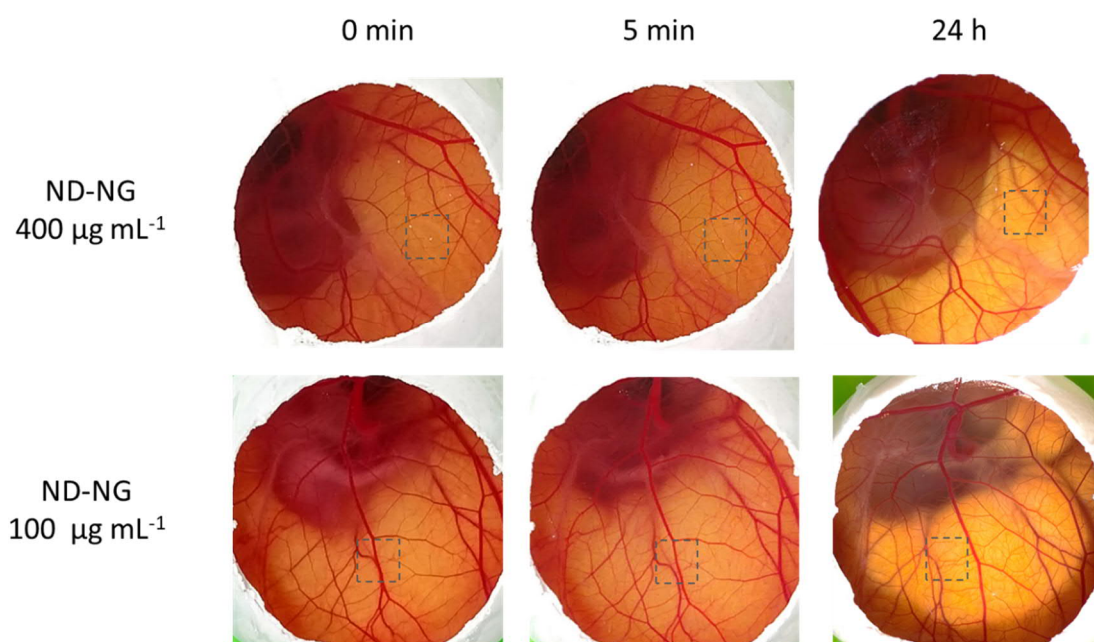


Figure S5.6. Photographs of HET-CAM test results for ND-NG at $400 \mu\text{g mL}^{-1}$ and $100 \mu\text{g mL}^{-1}$.

Table S3: Irritation Score (IS) for different concentrations of ND-NG, compared with 1% SDS (positive control) and PBS (negative control)

Eggs with sample (n=3)	Classification	Irritation score (IS)
1% SDS	Severe irritant	11.40 ± 0.05
PBS	No irritation	0.00
ND-NG (100 $\mu\text{g/mL}$)	No irritation	0.00
ND-NG (400 $\mu\text{g/mL}$)	No irritation	0.00
ND-NG (800 $\mu\text{g/mL}$)	No irritation	0.00

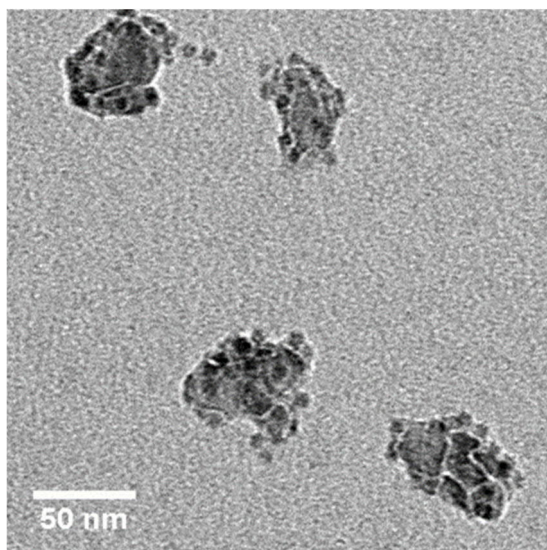


Figure S5.7. TEM image of ND-NG with Ferritin.

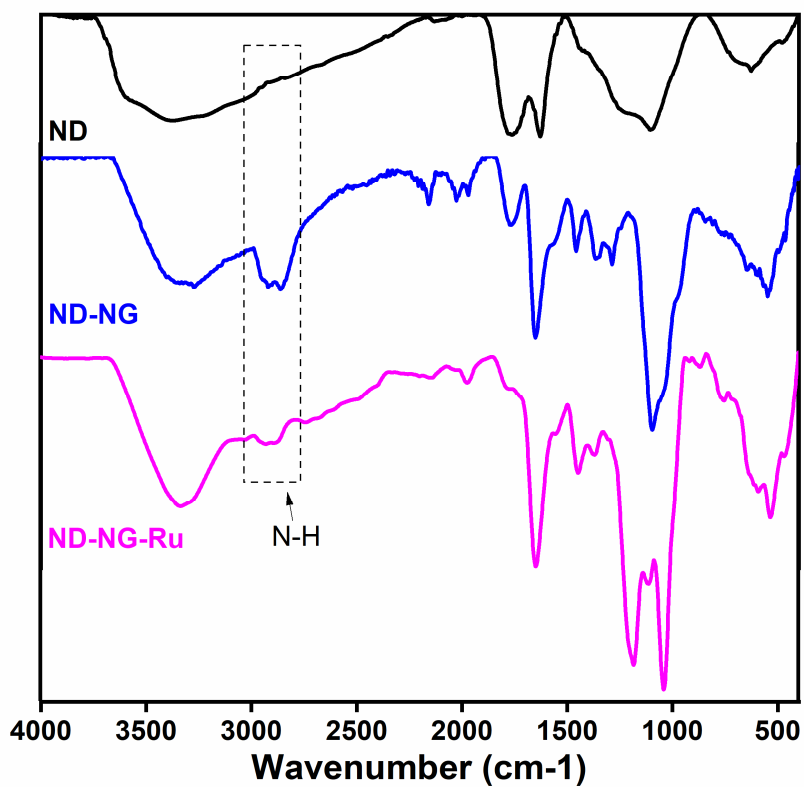


Figure S5.8. Attenuated total reflection-fourier transform infrared spectroscopy (ATR-FTIR) spectrum of ND-NG-Ru.

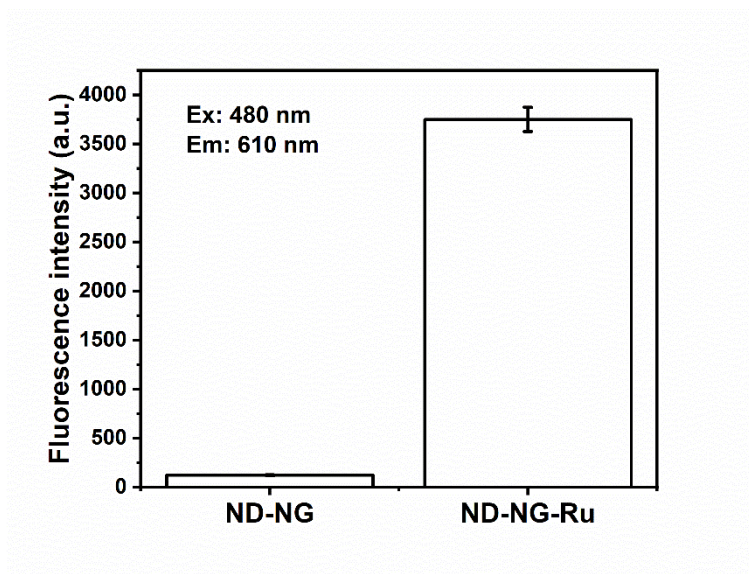


Figure S5.9. Fluorescence intensity of ND-NG, ND-NG-Ru.

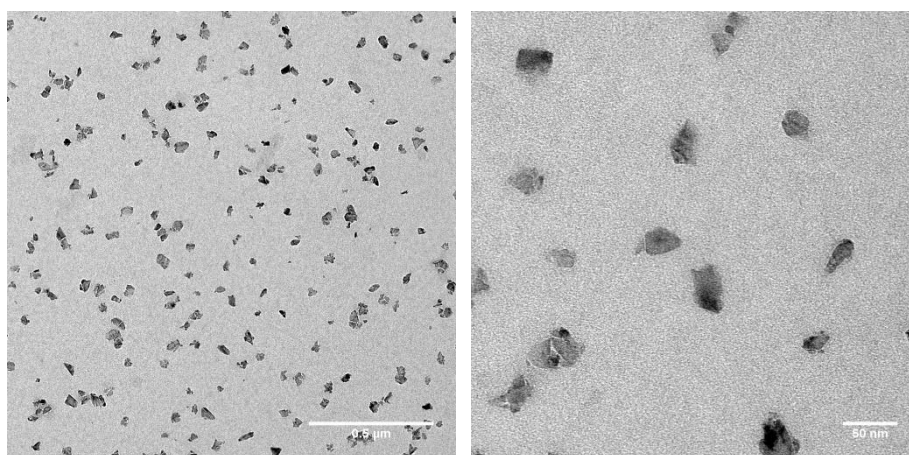


Figure S5.10. TEM image of ND-NG-Ru (left: scale bar = 500 nm; right: scale bar = 50 nm)

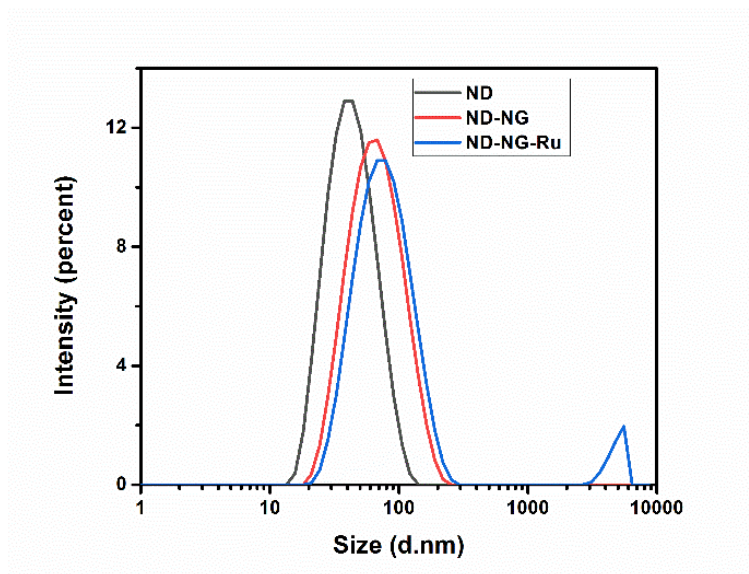


Figure S5.11. DLS spectra of uncoated ND, ND-NG, and ND-NG-Ru.

5.6 References

1. M. Ibrahim, Y. Xue, M. Ostermann, A. Sauter, D. Steinmueller - Nethl, S. Schweeberg, A. Krueger, M. R. Cimpan and K. Mustafa, *J. Biomed. Mater. Res. A*, 2018, 106, 1697-1707.
2. K. Adach, M. Fijalkowski, G. Gajek, J. Skolimowski, R. Kontek and A. Blaszczyk, *Chem.-Biol. Interact.*, 2016, 254, 156-166.
3. V. Vijayanthimala, P.-Y. Cheng, S.-H. Yeh, K.-K. Liu, C.-H. Hsiao, J.-I. Chao and H.-C. Chang, *Biomaterials*, 2012, 33, 7794-7802.
4. G. Balasubramanian, I. Chan, R. Kolesov, M. Al-Hmoud, J. Tisler, C. Shin, C. Kim, A. Wojcik, P. R. Hemmer and A. Krueger, *Nature*, 2008, 455, 648-651.
5. S. Han, M. Raabe, L. Hodgson, J. Mantell, P. Verkade, T. Lasser, K. Landfester, T. Weil and I. Lieberwirth, *Nano Lett.*, 2019, 19, 2178-2185.
6. M. D. Torelli, N. A. Nunn and O. A. Shenderova, *Small*, 2019, 15, 1902151.
7. H. S. Jung, K. J. Cho, Y. Seol, Y. Takagi, A. Dittmore, P. A. Roche and K. C. Neuman, *Adv. Funct. Mater.*, 2018, 28, 1801252.
8. Y. Wu, A. Ermakova, W. Liu, G. Pramanik, T. M. Vu, A. Kurz, L. McGuinness, B. Naydenov, S. Hafner and R. Reuter, *Adv. Funct. Mater.*, 2015, 25, 6576-6585.
9. S. Harvey, M. Raabe, A. Ermakova, Y. Wu, T. Zapata, C. Chen, H. Lu, F. Jelezko, D. Y. Ng and T. Weil, *Adv. Ther.*, 2019, 2, 1900067.
10. Y. Zhang, Z. Cui, H. Kong, K. Xia, L. Pan, J. Li, Y. Sun, J. Shi, L. Wang and Y. Zhu, *Adv. Mater.*, 2016, 28, 2699-2708.
11. Z. Cui, Y. Zhang, K. Xia, Q. Yan, H. Kong, J. Zhang, X. Zuo, J. Shi, L. Wang and Y. Zhu, *Nat. Commun.*, 2018, 9, 1-11.
12. T. K. Ryu, S. W. Baek, R. H. Kang and S. W. Choi, *Adv. Funct. Mater.*, 2016, 26, 6428-6436.
13. M. H. Alkahtani, F. Alghannam, L. Jiang, A. Almethen, A. A. Rampersaud, R. Brick, C. L. Gomes, M. O. Scully and P. R. Hemmer, *Nanophotonics*, 2018, 7, 1423-1453.
14. P. Neumann, I. Jakobi, F. Dolde, C. Burk, R. Reuter, G. Waldherr, J. Honert, T. Wolf, A. Brunner and J. H. Shim, *Nano Lett.*, 2013, 13, 2738-2742.
15. D. A. Simpson, E. Morrisroe, J. M. McCoey, A. H. Lombard, D. C. Mendis, F. Treussart, L. T. Hall, S. Petrou and L. C. Hollenberg, *ACS Nano*, 2017, 11, 12077-12086.
16. T. Sekiguchi, S. Sotoma and Y. Harada, *Biophys. Physicobiol.*, 2018, 15, 229-234.
17. A. Ermakova, G. Pramanik, J.-M. Cai, G. Algara-Siller, U. Kaiser, T. Weil, Y.-K. Tzeng, H.-C. Chang, L. McGuinness and M. B. Plenio, *Nano Lett.*, 2013, 13, 3305-3309.
18. T. Zhang, G.-Q. Liu, W.-H. Leong, C.-F. Liu, M.-H. Kwok, T. Ngai, R.-B. Liu and Q. Li, *Nat. Commun.*, 2018, 9, 1-8.
19. V. R. Horowitz, B. J. Alemán, D. J. Christle, A. N. Cleland and D. D. Awschalom, *Proc. Nat. Acad. Sci. U.S.A.*, 2012, 109, 13493-13497.
20. R. D. Akiel, X. Zhang, C. Abeywardana, V. Stepanov, P. Z. Qin and S. Takahashi, *J. Phys. Chem. B*, 2016, 120, 4003-4008.
21. K. Xia, C.-F. Liu, W.-H. Leong, M.-H. Kwok, Z.-Y. Yang, X. Feng, R.-B. Liu and Q. Li, *Nat. Commun.*, 2019, 10, 1-9.

22. K. van der Laan, M. Hasani, T. Zheng and R. Schirhagl, *Small*, 2018, 14, 1703838.
23. J. J. Virgen-Ortíz, J. C. dos Santos, Á. Berenguer-Murcia, O. Barbosa, R. C. Rodrigues and R. Fernandez-Lafuente, *J. Mater. Chem. B*, 2017, 5, 7461-7490.
24. L. Zhao, Y.-H. Xu, T. Akasaka, S. Abe, N. Komatsu, F. Watari and X. Chen, *Biomaterials*, 2014, 35, 5393-5406.
25. L.-W. Tsai, Y.-C. Lin, E. Perevedentseva, A. Lugovtsov, A. Priezhev and C.-L. Cheng, *Int. J. Mol. Sci.*, 2016, 17, 1111.
26. A. Bumb, S. K. Sarkar, N. Billington, M. W. Brechbiel and K. C. Neuman, *J. Am. Chem. Soc.*, 2013, 135, 7815-7818.
27. L. Zhao, T. Takimoto, M. Ito, N. Kitagawa, T. Kimura and N. Komatsu, *Angew. Chem. Int. Ed.*, 2011, 50, 1388-1392.
28. X. Q. Zhang, R. Lam, X. Xu, E. K. Chow, H. J. Kim and D. Ho, *Adv. Mater.*, 2011, 23, 4770-4775.
29. X.-Q. Zhang, M. Chen, R. Lam, X. Xu, E. Osawa and D. Ho, *ACS Nano*, 2009, 3, 2609-2616.
30. R. A. Shimkunas, E. Robinson, R. Lam, S. Lu, X. Xu, X.-Q. Zhang, H. Huang, E. Osawa and D. Ho, *Biomaterials*, 2009, 30, 5720-5728.
31. J. Ackermann and A. Krueger, *Carbon*, 2020.
32. S. R. Hemelaar, A. Nagl, F. Bigot, M. M. Rodríguez-García, M. P. de Vries, M. Chipaux and R. Schirhagl, *Microchimica Acta*, 2017, 184, 1001-1009.
33. P. A. Longo, J. M. Kavran, M.-S. Kim and D. J. Leahy, in *Methods in enzymology*, Elsevier, 2013, vol. 529, pp. 227-240.
34. H. Wang, Q. Li, J. Yang, J. Guo, X. Ren, Y. Feng and W. Zhang, *J. Mater. Chem. B*, 2017, 5, 1408-1422.
35. Y. H. Kim, J. H. Park, M. Lee, Y.-H. Kim, T. G. Park and S. W. Kim, *J. Controlled Release*, 2005, 103, 209-219.
36. L. Kong, J. Qiu, W. Sun, J. Yang, M. Shen, L. Wang and X. Shi, *Biomater. Sci.*, 2017, 5, 258-266.
37. W. Sun, Y. Wang, M. Cai, L. Lin, X. Chen, Z. Cao, K. Zhu and X. Shuai, *Biomater. Sci.*, 2017, 5, 2468-2479.
38. C. Graf, D. L. Vossen, A. Imhof and A. van Blaaderen, *Langmuir*, 2003, 19, 6693-6700.
39. K. M. Koczur, S. Mourdikoudis, L. Polavarapu and S. E. Skrabalak, *Dalton Trans.*, 2015, 44, 17883-17905.
40. M. Farahmandjou, S. Honarbakhsh and S. Behrouzina, *Phys. Chem. Res.*, 2016, 4, 655-662.
41. R. Mishra, R. Varshney, N. Das, D. Sircar and P. Roy, *Eur. Polym. J.*, 2019, 119, 155-168.
42. E. Doğan, P. Tokcan, M. Diken, B. Yilmaz, B. Kizilduman and P. Sabaz, *Adv. Mater. Sci.*, 2019, 19, 32-45.
43. Y. Guo, Z. Hao and C. Wan, *Tribol. Int.*, 2016, 93, 214-219.
44. F. Heinemann, J. Karges and G. Gasser, *Acc. Chem. Res.*, 2017, 50, 2727-2736.
45. G. Winter, A. B. Koch, J. Löffler, M. Lindén, C. Solbach, A. Abaei, H. Li, G. Glatting, A. J. Beer and V. Rasche, *Cancers*, 2020, 12, 1248.
46. A. Vargas, M. Zeisser-Labouèbe, N. Lange, R. Gurny and F. Delie, *Adv. Drug Deliv. Rev.*, 2007, 59, 1162-1176.
47. E. Aleksandrowicz and I. Herr, *ALTEX-ALTERN ANIM EX*, 2015, 32, 143-147.
48. M. C. DeRosa and R. J. Crutchley, *Coord. Chem. Rev.*, 2002, 233, 351-371.
49. T. J. Dougherty, C. J. Gomer, B. W. Henderson, G. Jori, D. Kessel, M. Korbelik, J. Moan and Q. Peng, *JNCI: J. Natl. Cancer Inst.*, 1998, 90, 889-905.

50. T. Wang, N. Zabarska, Y. Wu, M. Lamla, S. Fischer, K. Monczak, D. Y. Ng, S. Rau and T. Weil, *Chem. Commun.*, 2015, 51, 12552-12555.
51. S. Chakraborty, B. K. Agrawalla, A. Stumper, N. M. Vegi, S. Fischer, C. Reichardt, M. Kögler, B. Dietzek, M. Feuring-Buske and C. Buske, *J. Am. Chem. Soc.*, 2017, 139, 2512-2519.
52. B. Wei, M. Y. Guo, Y. M. Lu, P. P. Sun, G. W. Yang and Q. Y. Li, *Z. Anorg. Allg. Chem.*, 2018, 644, 6-11.
53. A. J. Simaan, Y. Mekmouche, C. Herrero, P. Moreno, A. Aukauloo, J. A. Delaire, M. Réglie and T. Tron, *Chem. Eur. J.*, 2011, 17, 11743-11746.
54. A. Schrage, A. O. Gamer, B. van Ravenzwaay and R. Landsiedel, *Altern. Lab. Anim.*, 2010, 38, 39-52.

6. A Nanodiamond-Based Theranostic Agent for Light-Controlled Intracellular Heating and Nanoscale Temperature Sensing

Authors

Yingke Wu,[†] Md Noor A Alam,[†] Priyadharshini Balasubramanian, Anna Ermakova, Stephan Fischer, Holger Barth, Manfred Wagner, Marco Raabe,* Fedor Jelezko,* and Tanja Weil*

Y. Wu and M. Alam are shared first author, *corresponding author

Copyright

Published in Nano Lett. 2021, 21, 9, 3780–3788.
<https://pubs.acs.org/doi/10.1021/acs.nanolett.1c00043>.

The following is reproduced with the permission from Copyright (2021) American Chemical Society, This work is licensed under a Creative Commons Attribution 4.0 International License. Further permissions related to the material excerpted should be directed to the ACS.

Author contributions

Y. Wu: initiated this project, prepared the materials, performed material characterizations(DLS, TEM, absorbance curve, emission spectrum), performed the TEM measurement of nanodiamond in cells, and partially performed ODMR measurements, prepared the draft of the manuscript, prepared the final manuscript based on discussions with all authors.

M. Alam: initiated this project, performed photothermal profile study, prepared cells for confocal microscopy and intracellular temperature measurement, cytotoxicity study, live/dead and Annexin-V staining of the cells, prepared the final manuscript based on discussions with all authors.

P. Balasubramanian: performed ODMR measurements and analyzed the data. prepared the final manuscript based on discussions with all authors.

A. Ermakova: performed some of the initial ODMR measurements.

S. Fischer: designed, supplied and cultured the cells for ODMR measurements

H. Barth: designed, supplied and cultured the cells for ODMR measurements

M. Wagner: discussed the concept and results in the projects.

M. Raabe: initiated this project, performed confocal microscopy and prepared cells for TEM. prepared the final manuscript based on discussions with all authors, supervised the project.

F. Jelezko: supervised the project.

T. Weil: Acquiring funding for the project, design and discussion of the concept and results, writing and correcting the manuscript.

Abstract

Temperature is essential in all biological process and almost all of the biological activities are temperature-related but it is bare known about the temperature in living cells. Especially in photothermal therapy (PTT), which is gaining interest in cancer treatment because this method is non-invasive in combination with a high spatial control. Huge amount of high efficiently photothermal agent are developed in past decades, however, almost none of them investigate the intracellular temperature in PTT. Because highly sensitive and sophistic nanothermometers is required and it should be not affected by intracellular factors including pH, ions. Fluorescent nanodiamonds (ND) are a unique carbon material possessing optical defects inside the carbon lattice which enable sensing of temperature on nanoscale completely independent of external conditions. Herein, we coat ND with polymers to form a nanogel shell around NDs that can absorb indocyanine green, a common photothermal agent finally get nanodiamond-nanogel- indocyanine green (ND-NG-ICG) materials. Upon irradiation with light, we show not only successful killing of cancer cells with a high control in space but also we are able to sense the increase of temperature using single NDs as nanothermometers in cells. It pushes the PTT research to an intracellular level. Also it opens a door for us to explore the intracellular temperature influence on living cell biological process.

6.1 Introduction

Temperature plays a fundamental role in every biological process in a living organisms and almost all of the biological activities are temperature-controlled or temperature-related, for instance cell differentiation, proliferation, and death¹ protein function^{2, 3} as well as gene expression⁴. All these biological actions take place or are controlled at specific intracellular locations. Hence, probing or even manipulating the local intracellular temperature is important to understand the fundamental relationship between biological activities and their temperature such as the precise monitoring of temperature during hyperthermia.

For example, several research groups have reported that tumor cells could be effectively killed if the temperature in cells reached above 42 °C^{5,6}. To effectively ablate the tumors, often much higher temperatures (above 50 °C) are present in the tumor core to make sure that the edge of the tumors will also reach the required therapeutic temperature⁷⁻⁹. Counterintuitively, mitochondria are maintaining a physiological temperature of close to 50 °C without harming the cell¹⁰. Therefore, it is essential to gain a deeper understanding of the local intracellular temperature change and its effect on tumor cells in more detail.

This information would be very beneficial to optimize existing techniques such as photothermal therapy (PTT). PTT is routinely applied to induce temperature increase in diseased cells or tissues and is showing a high potential in the field of cancer treatment.^{5, 11} During PTT, a photothermal agent (PA) is delivered into tumor cells or tissue and upon illumination by light, the PA converts absorbed light energy into heat. Over time, this process leads to either partial or complete ablation of the tumor cells or tissue.¹² PTT is non-invasive, has a strong promise to improve the recovery time, and provides a better output as a cancer treatment¹³. PAs are extremely important for the efficiency of PTT because it depends on the accumulation of light-responsive PA in the target region and its light-to-heat conversion efficiency. Well-designed PAs should generate certain amount of heat after the absorption of non-toxic light, which is usually in the near-infrared range (NIR, 650–900 nm) for a better penetration depth^{14, 15}. During

the past years, various PA have been designed mostly in form of nanomaterials which benefit from the enhanced permeability and retention (EPR) effect after intravenous injection^{16, 17}. These nanomaterials include metal-based nanomaterials¹⁸⁻²², carbon-based nanomaterials²³⁻²⁸, and organic molecules-based nanomaterials^{29, 30}. However, these PAs lack the function to sense the temperature and therefore, it was not possible to correlate between the local temperature and the effect on the cell.

To directly measure the intracellular temperature on nanoscale, different kinds of fluorescence-based nanothermometers, including quantum dots³¹, rare-earth metal complexes, polymers³², and genetically encoded proteins³³, have been developed. However, biological factors, such as pH, ion concentration, and/or microviscosity, could affect these fluorescence-based thermometers, resulting in inaccurate reading of the temperature. Nanodiamonds (NDs), containing nitrogen-vacancy (NV⁻) centers, are well known to be highly bio-compatible and physicochemically inert, providing a fluorescence that shows neither photoblinking nor photobleaching. Furthermore their fluorescence are hardly influenced by pH, ion concentration, viscosity, molecular interaction, and organic solvent³⁴. This is the case because the temperature response from NDs differs strongly from most fluorescence probes. Upon a change in temperature, the ground state spin levels of NV⁻ centers in NDs are shifted.³⁵ Additionally, NV⁻ centers have been demonstrated to be useful as highly sensitive nanoscale thermometers based on the thermal shifts of the resonant frequencies of the spin transitions at 2.87 GHz ($m_s = 0$ to $m_s = \pm 1$)³⁶⁻³⁸ or the zero-phonon line (ZPL) at 637 nm^{39, 40}. Therefore, NDs are an ideal material for designing an intracellular self-reporting photothermal system to probe the local temperature change in a PTT process. Herein, we report the preparation of a self-reporting photothermal system, called nanodiamond-nanogel-indocyanine green (ND-NG-ICG). A schematic outline of the preparation of ND-NG-ICG is displayed in Figure 6.1A. The nanodiamond-nanogel (ND-NG) was prepared according to our previous work (Chapter 5). Explicitly, hyperbranched polyethyleneimine (PEI) was used to precoat NDs in the presence of polyvinylpyrrolidone (PVP) as stabilizer, and subsequently, a 4-arm polyethyleneglycol

NHS ester was added to crosslink the precoated PEI on the surface of NDs in phosphate-buffered saline (PBS) buffer to form the nanogel shell. After purification, the positively charged ND-NG was obtained. Finally, anionic indocyanine green (ICG) was mixed with ND-NG solution to form ND-NG-ICG involving strong electrostatic interaction. Furthermore, the photothermal effect and the temperature sensing were proven in vitro.

6.2 Results and Discussion

ND-NG was prepared as reported in chapter 5, previously and was mixed with ICG. Afterwards, free ICG was removed by centrifugation to obtain pure ND-NG-ICG. The amount of ICG loaded on ND-NG by electrostatic interactions is essential for the efficiency of PTT and was determined by the characteristic absorbance of ICG at 789 nm. Firstly, we prepared a calibration curve of the absorbance of ICG over its concentration (Figure S6.1). Because NDs could interfere during the absorbance measurement, we determined the concentration of free ICG which remained in the supernatant after centrifugation. We found that 64.5 μg ICG was loaded on 200 μg ND-NG-ICG which is equal to a loading efficiency of 24.4%. Since ICG was loaded by non-covalent adsorption, which could cause unwanted leakage, we investigated the release of ICG over time. The ICG was release dramatically at first 10 min and reached the equilibrium. Only about 10% ICG was released over 20 days due to the strong interaction between ICG and ND-NG (Figure S6.2). ND-NG-ICG was characterized by dynamic light scattering (DLS; Figure 6.1B) and transmission electron microscopy (TEM; Figure 6.1C and 6.1D) to investigate its size distribution, shape, and morphology. ND-NG-ICG showed a monomodal size distribution in DLS (Figure 6.1B) with polydispersity index (PDI) of 0.243 and the hydrodynamic diameter increased from 37.7 ± 0.23 nm of ND to 56.9 ± 0.27 nm of ND-NG and finally, to 99.6 ± 0.53 nm of ND-NG-ICG in Milli-Q water (Figure S6.3). These findings were supported by TEM images of ND-NG-ICG which did not show obvious aggregation as well (Figure 6.1C). The photophysical properties of NDs containing NV^- centers are important for the further application of ND-NG-ICG in intracellular temperature sensing. The emission

spectra of ND and ICG as well as the absorption spectra of ICG were measured firstly (Figure S6.3). We found that the emission spectra of ND and the absorption spectra of ICG were overlapping, which could induce an energy transfer upon irradiation of ND-NG-ICG at 532 nm. To further check the influence of the coating on the NV^- centers in NDs, ND-NG-ICG was dropped on a glass coverslip. Spectra measurements were performed on a custom-built confocal microscope using a 532 nm excitation with a power of 110 μ W in front of the objective (oil, NA = 1.35). The spectra of ND-NG-ICG revealed that the intensity of the peak at 680 nm slightly decreased due to a low energy transfer to ICG. The zero phonon line of NV^- at 637 nm was clearly visible without any background noise (Figure 6.1E). NV^- centers in NDs are very sensitive to the surface charge and at some conditions can switch to the dark state (positively charged NV center; NV^+). These results demonstrated that the NV^- centers in ND-NG-ICG remained in the optically active state which was necessary for the intracellular temperature sensing.

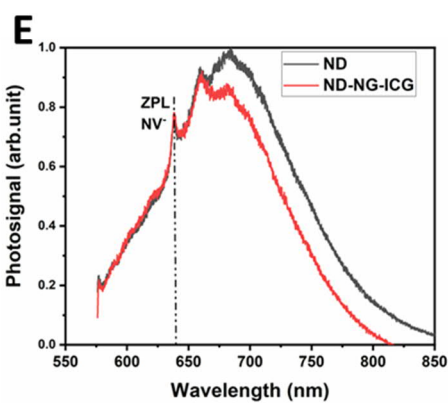
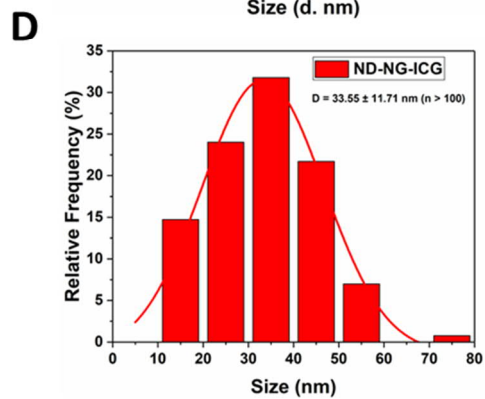
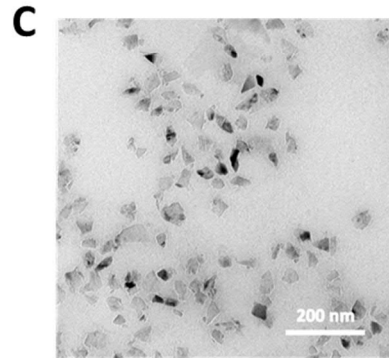
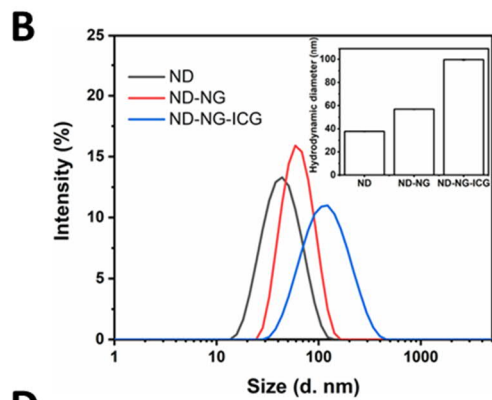
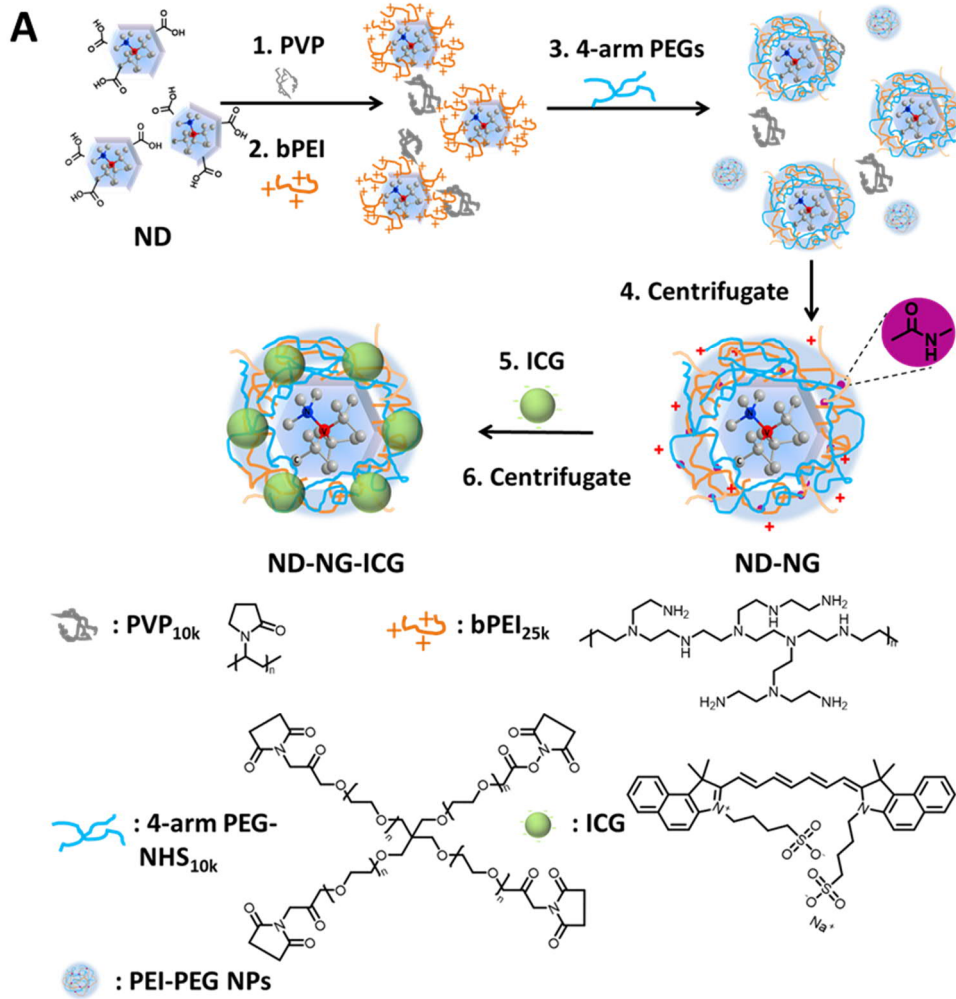


Figure 6.1. (A) Schematic illustration of the synthesis route of ND-NG-ICG. (B) The hydrodynamic diameter of ND, ND-NG, and ND-NG-ICG measured by DLS. (C) TEM images of ND-NG-ICG (scale bar = 200 nm). (D) Histogram analysis of ND-NG-ICG. (E) Normalized emission spectra (ex. 532 nm) of ND and ND-NG-ICG. The zero-phonon line (ZPL) of NV^- is visible in both spectra.

To understand the influence of ND-NG-ICG on cells, firstly, the biocompatibility of ND-NG-ICG was investigated in a human cervical carcinoma cell line (HeLa). As displayed in Figure 2A, ND-NG-ICG showed good cell viability after the treatment of the cells with a concentration up to 400 $\mu\text{g/ml}$. In addition, as depicted in Figure 2B, ND-NG-ICG were efficiently taken up into HeLa cells, and the cell could grow well and the cell morphology was not altered. Moreover, to further investigate the location of ND-NG-ICG in cells, the 10 $\mu\text{g/ml}$ and 100 $\mu\text{g/ml}$ ND-NG-ICG were incubated with HeLa cell and then embedded in resin after stain, and cut to 100nm section for TEM measurement (Figure 2C and 2D). It found that the ND-NG-ICGs can be internalized, encapsulated in a vesicle and take in. And the behavior was concentration-independent. There is no significant difference of cell uptake between 10 $\mu\text{g/ml}$ and 100 $\mu\text{g/ml}$ ND-NG-ICG. Only difference was that there were much less ND-NG-ICG were found in the cells for the 10 $\mu\text{g/ml}$ ND-NG-ICG.

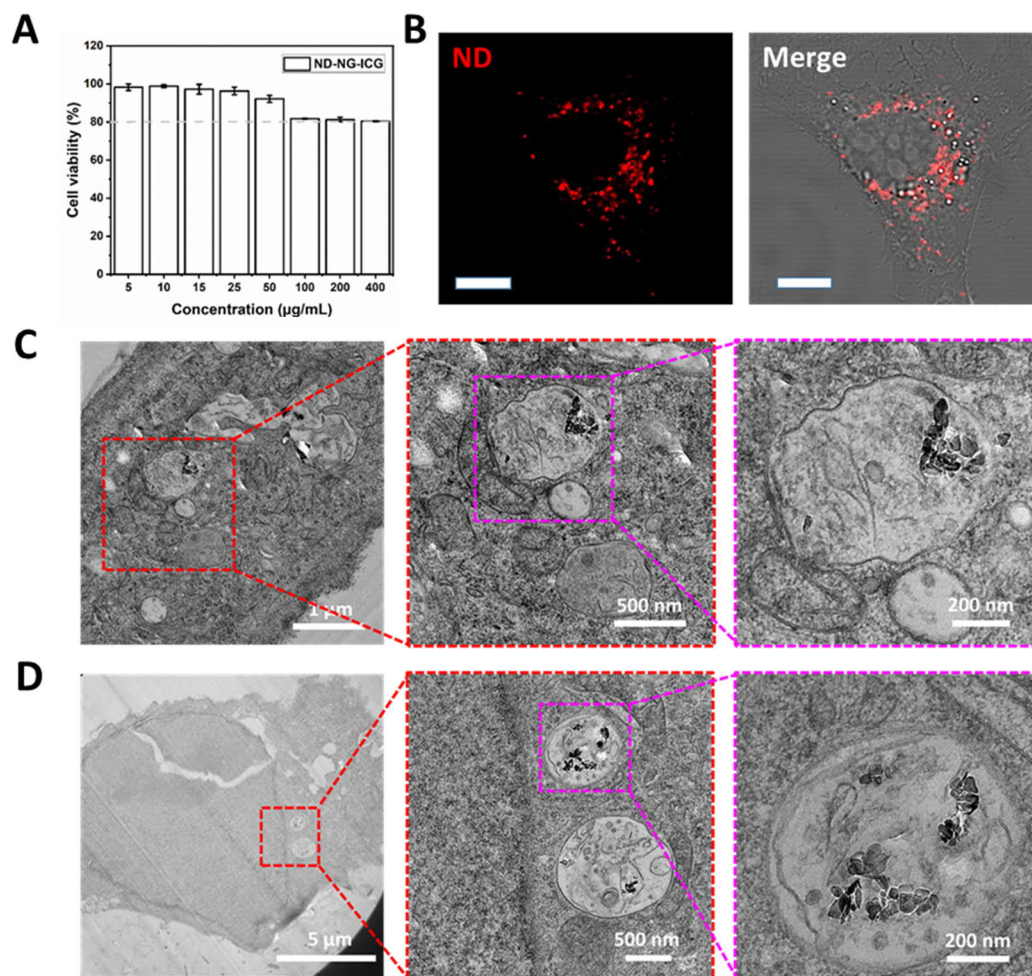


Figure 6.2. (A) Cell viability of HeLa cells after 4h incubation with ND-NG-ICG. (B) Confocal microscopy images of ND-NG-ICG which were taken up into HeLa cells with a concentration of 100 $\mu\text{g/mL}$ after 4 hours (scale bar = 10 μm). (C) TEM images of ND-NG-ICG which were taken up into HeLa cells with a concentration of 10 $\mu\text{g/mL}$ after 4 hours. (D) TEM images of ND-NG-ICG which were taken up into HeLa cells with a concentration of 100 $\mu\text{g/mL}$ after 4 hours.

Later, to measure the nanoscale local temperature change in cells under irradiation, a home-built wide-field fluorescence microscope combined with optically detected magnetic resonance (ODMR) spectroscopy was developed (Figure 6.3A, Figure S6.5 and S6.6). Based on the physical property of NV^- centers in ND, the ground state spin levels are shifted in response to a change in temperature which provides a robust readout of temperature. As shown in Figure 6.3C, the ODMR spectra of ND-NG-ICG under NIR irradiation were recorded and fitted with a sum of two Lorentzians, we can

found after 3 min irradiation, the ODMR spectrum shifted to the low frequency. But for the ND-NG samples (Figure S6.7), there is no significant shift of the ODMR spectra after NIR irradiation. To readout the intracellular temperature change, the ODMR spectra was recorded up to 7 minutes continuously and then the ODMR spectra were extracted every 60 seconds and fitted with a sum of two Lorentzians and the temperature change were calculated out by the equation:

$$D(T) \approx D_0 + \frac{dD}{dT}T$$

Where $dD/dT = 74$ kHz/K.

And the temperature change (ΔT) – time curve was obtained and fitted (Figure 6.3E), it was found that the temperature increased sharply by more than 30 °C and saturated after 250 seconds of irradiation for the ND-NG-ICG samples, but there is no significant temperature change for the ND-NG samples under irradiation.

Moreover, we also investigated the photothermal effect of ND-NG-ICG by thermocouple in solution. We quantified the photothermal effect of ND-NG-ICG measuring the change in temperature of water upon irradiation of 810 nm with the power of 0.35 W/cm². Firstly, we evaluated the change in temperature of ND-NG in absence of the ICG dye at different concentrations (Figure 6.3D). We found a concentration-independent temperature increase of less than 4 °C which reached a saturation after 5 minutes of irradiation. In contrast, ND-NG-ICG revealed a concentration-dependent increase of temperature of 4 °C to 17 °C for concentrations starting from 10 µg/mL to 200 µg/mL after 5 minutes of irradiation. Free ICG, using a concentration ranging from 10 µg/mL to 200 µg/mL of ICG (which equals a concentration ranging from 31 µg/mL to 620 µg/ml of ND-NG-ICG), it showed an increase in temperature of 9 °C to 24 °C after 3 minutes of irradiation (Figure S6.4). Comparing free ICG, and ND-NG-ICG still showed excellent photothermal effect. These results indicated that the nanoscale local temperature in cells compared with the materials in solution.

The operational principle of NV-based thermometry relies upon the accurate measurement of the transition frequency, which can be optically detected with high

spatial resolution. For a sensor containing NV color centers, the temperature sensitivity is given by the equation:

$$\eta_{ESR} \approx \frac{4}{3\sqrt{3}} \frac{1}{dD/dT} \frac{\Delta f}{C\sqrt{R}}$$

where dT is ***, Δf is***, C is ***,... Here $dD/dT = 74$ kHz/K, $C \approx 0.05$, $\Delta f = 5$ MHz and $R = 3$ M cts/s, then the calculated sensitivity $\eta = 600$ mK/ $\sqrt{\text{Hz}}$ here. But theoretically a single NV can potentially exhibit a sensitivity better than 1 mK/ $\sqrt{\text{Hz}}$.

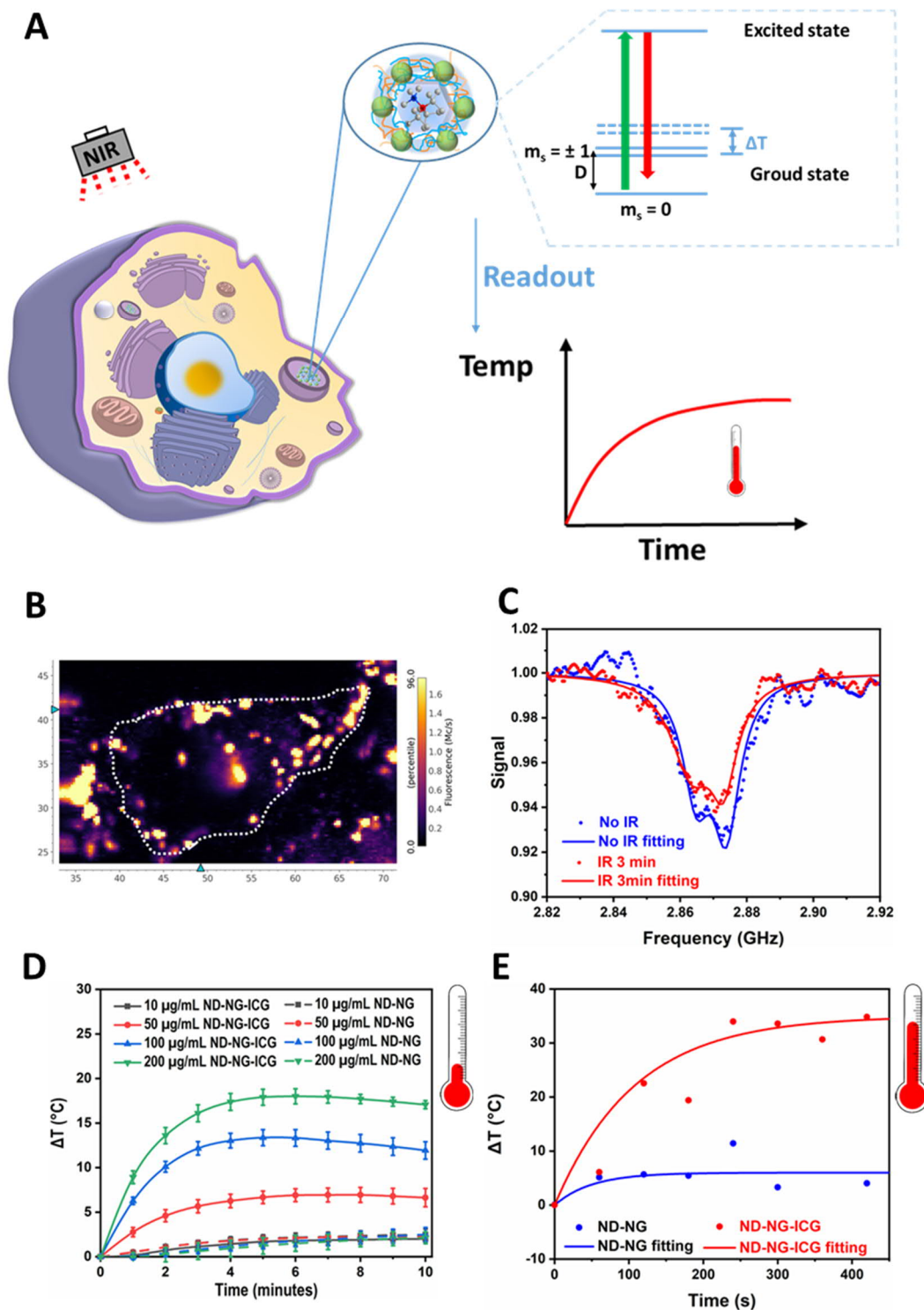


Figure 6.3. (A) Illustration of the temperature measurement in living cells. And simplified energy levels of the NV^- center in diamond showing a ground state spin triplet and an excited state. At zero magnetic field, the $m_s = \pm 1$ sub-levels are split from the $m_s = 0$ state by a temperature-dependent zero field splitting D_0 . By monitoring the temperature-dependent shift D_0 of zero field splitting using the optically detected

magnetic resonance (ODMR) technique, at room temperature, $D_0 \approx 2.87$ GHz. It varies depending on temperature T , $D(T) = D_0 + \alpha T$, where $\alpha = 74$ kHz/K. (B) fluorescence image of ND-NG-ICG in a living cell. (C) Representative ODMR spectra of ND-NG-ICG which was fitted with a sum of two Lorentzians, under near-infrared (NIR) irradiation (810 nm lamp; 0.35 W/cm^2) at the time of 0 min and 3 min. (D) The thermal profile of ND-NG and ND-NG-ICG with a concentration of $10 \text{ }\mu\text{g/mL}$, $50 \text{ }\mu\text{g/mL}$, $100 \text{ }\mu\text{g/mL}$, and $200 \text{ }\mu\text{g/mL}$ under near-infrared (NIR) irradiation (810 nm lamp; 0.35 W/cm^2). (E) The change of intracellular temperature measured by ODMR for NG-NG-ICG and ND-NG over 600 seconds under near-infrared (NIR) irradiation (810 nm lamp; 0.35 W/cm^2).

To understand the photothermal effect on cells, a LED light with a wavelength of 810 nm was focused onto the sample area through the objective of a microscope for 10 minutes. The light power density was 350 mW cm^{-2} , which is the same value we used in ODMR measurements later on. After 10 minutes of irradiation, the cells were further incubated for 4 h and live/dead staining of PTT treated cells was performed. As shown in Figure 6.4, without irradiation at 810 nm, cells could proliferate well, showed a normal cell morphology, and almost no dead cells were found neither at $10 \text{ }\mu\text{g/mL}$ of ND-NG-ICG nor at $100 \text{ }\mu\text{g/mL}$ of ND-NG-ICG. After irradiation at 810 nm, the cell viability was not impaired at low concentrations of ND-NG-ICG ($10 \text{ }\mu\text{g/mL}$) and ND-NG. However, most of the cells treated with a high concentration of ND-NG-ICG ($100 \text{ }\mu\text{g/mL}$) were dead in the live/dead imaging within the irradiated area.

According to the ODMR measurement, the local temperature close to the surface of ND-NG-ICG is above $50 \text{ }^\circ\text{C}$ after 250 seconds of irradiation and the local temperature is independent of the concentration because both $10 \text{ }\mu\text{g/mL}$ and $100 \text{ }\mu\text{g/mL}$ revealed a similar local temperature increase. This data revealed that cells can compensate a local high temperature ($> 50 \text{ }^\circ\text{C}$) for a low concentration of ND-NG-ICG but a high concentration of ND-ND-ICG resulted in cell death probably due to an accumulative effect of the local temperature spots. Our results also support that small areas in cells can possess different temperatures without effecting the cell viability. For example, it

is reported that in mitochondria the temperature is higher than in the cytosol.¹⁰

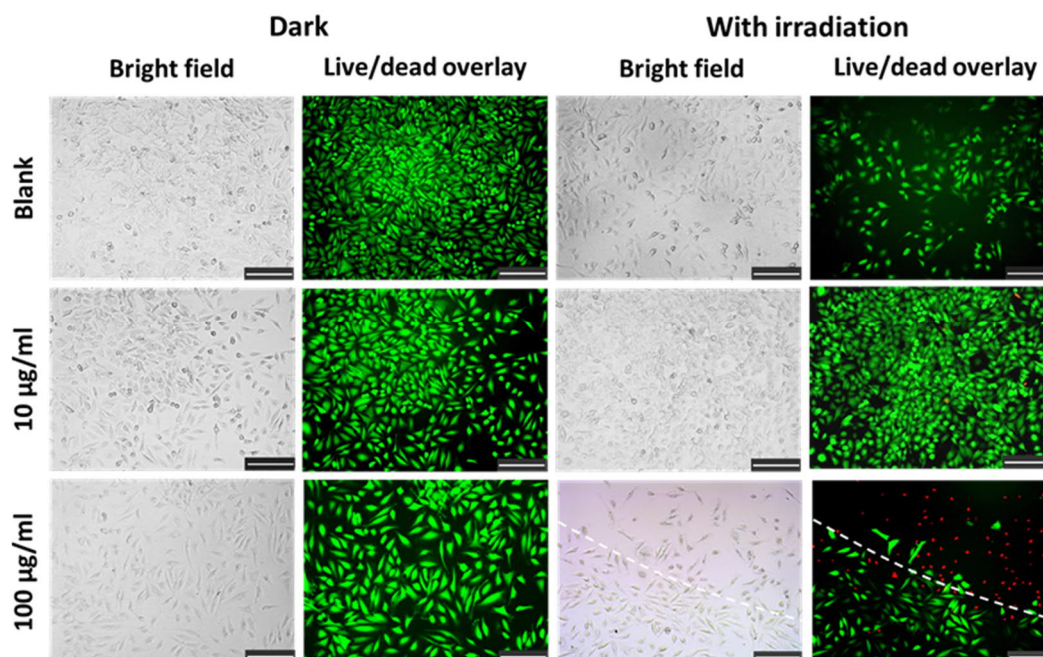


Figure 6.4. Live/dead staining of HeLa cells incubated with different concentration of ND-NG-ICG after 10 min irradiation using a near-infrared (NIR) LED lamp (810 nm lamp; 0.35 W/cm²; scale bar = 200 µm).

6.3 Conclusion

In summary, we successfully prepared a nanoscale photothermal agent equipped with a self-reporting system. This agent monitored the temperature increase due to the photothermal effects in situ and in living cells. The ODMR results showed that the local temperature increased by 30 °C within 250 seconds. Moreover, we found that the cells can tolerate a high local temperature of more than 50 °C if the concentration of the photothermal agent is low. This data support that the intracellular temperature of cells can be inhomogeneous and can even differ by 30 °C without affecting the cell viability. Our present study describes the local temperature increase induced by a photothermal agent and paves the way to a deeper understanding of the influence of the photothermal effect on nanoscale. Combining this agent with subcellular targeting groups enables detailed temperature measurements in different organelles in the future and will help to gain a better understanding of the effect of temperature on cellular organelles.

6.4 Acknowledgements

The authors thank Mr. Kai Philipps for the ICG emission spectrum measurement, Christoph Sieber for the preparation TEM samples of cells, and Dr. David Yuen Wah Ng for fruitful discussions and suggestions. The authors are grateful for the financial support from the Sibylle Kalkhof-Rose-Stiftung, the European Union's Horizon 2020 Research and Innovation Program under FETOPEN grant agreement no. 858149 (AlternativeToGd), the ERC Synergy Grant HyperQ (No. 856432), the VW Foundation as well as from the Deutsche Forschungsgemeinschaft (DFG, German Research Foundation) - Project number 316249678 - SFB 1279 (C01, C02, C04) and Project number 390874152 - EXC 2154 POLiS. Y.W. thanks the China Scholarship Council for a fellowship.

6.5 Supporting information

Materials and method

Materials: Nanodiamonds with 35 nm average diameter were purchased from FND Biotech (Taiwan), 4-arm PEG-SCM (MW: 10 kDa, Creative PEGWorks), branched polyethylenimine (MW: 25 kDa by LS), polyvinylpyrrolidone (MW: 10 kDa), (3-carboxypropyl)triphenylphosphonium bromide, *N*-hydroxy-succinimide (NHS), 9,10-anthracenediyl-bi(methylene)dimalonic acid, fluorescamine and ethylenediamine, indocyanine green were purchased from Sigma-Aldrich, Dulbecco's Modified Eagle's Medium (DMEM, 1x), Dulbecco's phosphate-buffered saline (DPBS, 1x), fetal bovine serum (FBS), Penicillin Streptomycin (Pen Strep) were purchased from gibco, MitoLite™ Blue FX490 were purchased from AAT Bioquest. All solvents and chemicals were purchased from commercial sources and were used without further purification

Preparation of ND-NG

Firstly, 100 μL ND (2 mg mL^{-1}) stock solution was dispersed in 300 μL water. Afterwards, 100 μL PVP (20 mg mL^{-1}), 200 μL PEI (5 mg mL^{-1}), and 300 μL PBS

buffer (10 mM, pH 7.4) were added. After 5 min sonication, 2 mg of 4-arm PEG-SCM was added to cross-link the PEI on the surface of ND. The final volume was adjusted to 1 mL with MilliQ water. After sonication for 30 min and reaction of 90 min on a shaker at 800 rpm, the obtained ND-NGs were washed 3 times by centrifugation at 12,000 g for 20 min.

Preparation of ND-NG-ICG

100 μ L 2 mg/ml ND-NG was mixed with 400 μ L 0.1 mg/ml ICG and was sonicated 30 seconds, then reacted overnight on a shaker at 800 rpm, the ND-NG-ICG were obtained by centrifugation at 12,000 g for 20 min to remove the supernatant.

Loading efficiency

A standard curve of ICG absorbance was prepared to calculate the ICG content in ND-NG-ICG as followed: 20 μ L ICG solution with concentration of 62.5 μ g/ml, 31.25 μ g/ml, 15.63 μ g/ml, 7.81 μ g/ml, 3.91 μ g/ml, 1.95 μ g/ml water, and supernatant of ND-NG-ICG were added in separate wells of 384-well low volume well plate. And then absorbance intensity at 789 nm were obtained by a Tecan Spark 20M. The absorbance intensity–concentration curve was drawn und the ICG content in ND-NG-ICG was calculated.

ICG releasing curve

The 200 μ g ND-NG-ICG was added to 500 ml MilliQ water and put on a shaker at 800 rpm, at the setting time points, one of the ND-NG-ICG aliquots was centrifuged at 12,000 g for 20 min, the absorbance of supernatant at 789nm was measured by a Tecan Spark 20M, and the released ICG content was calculated.

UV-Vis Absorbance and Fluorescence

20 μ L of ICG solution (0.1 mg/mL) were prepared in separate wells of a 384-well low volume microplate. Absorbance scans from 200 to 1000 nm were obtained using a Tecan Spark 20M microplate reader. And the emission spectra of ICG was measured using a 40 μ l micro cuvette at Perkin Elmer Lambda 900 device. It was excited at 600 nm and the emission spectra was collected from 750 nm to 1000nm. Later the spectra were normalised.

Transmission Electron Microscopy (TEM)

One drop of a 0.1 mg mL⁻¹ solution of ND-NGs in MilliQ was placed onto an oxygen treated copper grid. A Jeol 1400 transmission electron microscope was used to obtain bright field images.

Dynamic Light Scattering (DLS)

500 µL of 0.1 mg mL⁻¹ solutions of ND, ND-NG, ND-NG-ICG in MilliQ were transferred into a borosilicate glass cuvette. The size was measured at 25 °C with a 90° angle using a particle sizer (Malvern Zetasizer Nano-S90 (Nano series)). The hydrodynamic diameter distribution was presented as intensity. Zeta potential was measured at 25 °C with a Malvern Zetasizer Nano-S90 (Nano series).

Photothermal profile study for bulk ND-NG, ND-NG-ICG and pure ICG solutions in water

Various concentration of ND-NG, ND-NG-ICG and pure ICG were prepared to measure the photothermal temperature changes. Subsequently, a K-type thermocouple wire and an automated temperature input device (USB-TC01, National Instruments) were employed to record the real-time temperature change of 100 µL of each samples. The process were repeated three times for each concentration. An 810 nm LED lamp (Thor Labs, M810L3) was used to irradiate the samples, light irradiance was 350 mW cm⁻².

Samples preparation of cell with ND-NG-ICG for Transmission Electron Microscopy (TEM)

Cells were seeded in a 24-well plate pre-placed with carbon coated sapphire discs (d:3mm) with a density of 50,000 cells/ml. After co-incubation with nanoparticles (NPs), sapphire discs were placed between two aluminum plates to create a ‘sandwich’ and afterwards were mounted into a holder (Engineering Office, M. Wohlwend) and immediately fixated in a Wohlwend HPF Compact 01 high-pressure freezer (Engineering Office, M. Wohlwend) with a pressure of 2100 bar. The frozen samples were then stored in liquid nitrogen.

Frozen sapphire discs were carefully removed from the aluminum ‘sandwich’ and

transferred into 1 ml pre-cooled freeze substitution medium (0.2% (w/v) osmium tetroxide, 0.1% (w/v) uranyl acetate, 5% (v/v) distilled water in acetone) and kept in a freeze substitution unit (AFS2, Leica). Samples were then slowly warmed up to 0 °C over a period of 20 h in the unit. After being warmed up, the freeze-substituted samples were brought to room temperature, then the substitution medium was removed and the discs were washed 3 times with acetone at half an hour intervals. Then the discs were infiltrated sequentially in gradient epoxy resin-acetone mixture (1;1, 1:2 and 2:1) for 1 h. Samples were then infiltrated in 100% epoxy resin overnight. Finally, each sample was transferred into a new Eppendorf tube containing fresh epoxy resin for polymerization at 60 °C for 24 h.

Following polymerisation, sapphire discs were detached using liquid nitrogen. Resin blocks with the cells imprinted on were trimmed and sectioned into 100nm/80nm sections by a 45° diamond knife (Diatome) in EM UC6 ultramicrotome (Leica).

Confocal Microscopy

Confocal laser scanning microscopy (CLSM) was utilized to observe the cellular uptake of ND-NG-ICG. HeLa cells were seeded in a ibidi 8 well μ -slide (10^5 cells mL^{-1} , 200 μL each well) and incubated overnight. Next morning, cells were washed once with Dulbecco's phosphate-buffered saline (DPBS) and 100 $\mu\text{g mL}^{-1}$ ND-NG-ICG (mixed with cell culture medium) was added to the cells. After four hour incubation at 37 °C, the cells were washed three times with DPBS to remove the particles which were not uptaken, then fresh medium was added. A Leica TCS SP5 confocal microscope system was used to obtain the microscopy images and later they were analyzed with ImageJ software.

Cytotoxicity study

HeLa cells were seeded on a white 96 well half-area flat bottom cell culture microplate (Greiner). Seeded cell concentration was 110,000 cell mL^{-1} , 50 μL each well. After overnight incubation at 37 °C and 5% CO_2 , various concentrations of ND-NG-ICG were added to the cells and incubated again for 24 hours. Next day, the cells were washed three times with DPBS and added fresh cell culture medium (containing

DMEM with 10% FBS, 1% MEM NEAA, and 1% PenStrep). Afterward, freshly prepared CellTiter-Glo luminescent cell viability assay (Promega) was applied as instructed by the manufacturer's protocol. The luminescence signals were recorded with a Promega GloMax multi detection plate reader.

Sample preparation for intracellular temperature measurements

Coverslips of 15 mm diameter were placed in a 12 well cell culture plate to seed HeLa cells. The cell concentration was 10^6 cells/mL, 500 μ L in each well. After overnight incubation, 10 μ g mL⁻¹ and 100 μ g mL⁻¹ of ND-NG and ND-NG-ICG samples in cell culture medium were added to the cells. Subsequently after four hour incubation at 37 °C, the cells were washed 3 times with DPBS to remove the excess nanoparticles which were not uptaken, and fresh clear DMEM (without phenol red) was added to the cells. The ODMR measurements were performed immediately. As depicted in Figure S6.8, the cell attached coverslip was put on ODMR sample holder, a sandwich structure samples was gotten, microwave antenna and cells were in the middle of two coverslips which was full of culture medium.

Live/dead staining of HeLa cell

HeLa cells were seeded on two ibidi 8 well μ -slide with a cell concentration of 160,000 cells mL⁻¹ (300 μ L in each well) and incubated overnight. Subsequently 10 μ g mL⁻¹ and 100 μ g mL⁻¹ ND-NG and ND-NG-ICG samples were prepared by diluting the stock solution with cell culture medium. 200 μ L of each concentration of samples were added to the cells and kept in the incubator for four hours. Then both plates were washed three times with DPBS, and added fresh culture medium. Meanwhile, the 810 nm LED was mounted to a Leica DMI8 microscope using a microscope collimation adapter (Thor Labs) to irradiate one of the treated μ -slides for 20 minutes (350 mW cm²). After photo-treating the cells, both μ -slides were kept in dark for additional four hours. Afterward, cells were treated with freshly prepared live/dead staining solution. The solution was prepared as stated in the ibidi protocol. Briefly 8 μ L fluorescein diacetate (5 mg mL⁻¹) and 100 μ L of propidium iodide (1 mg mL⁻¹) were mixed with DPBS (5 mL). 300 μ L of live/dead staining solution was added to each well of the μ -slide and kept in dark for

5 minutes. Later, the cells were washed with DPBS. Imaging was performed immediately using a Leica DMI8 microscope with a Leica MC170 HD camera system.

Results and Discussion

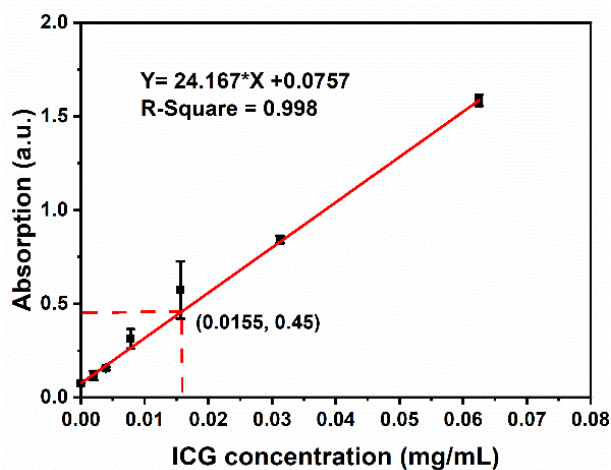


Figure S6.1. The standard curve of absorbance at 789 nm and ICG concentration.

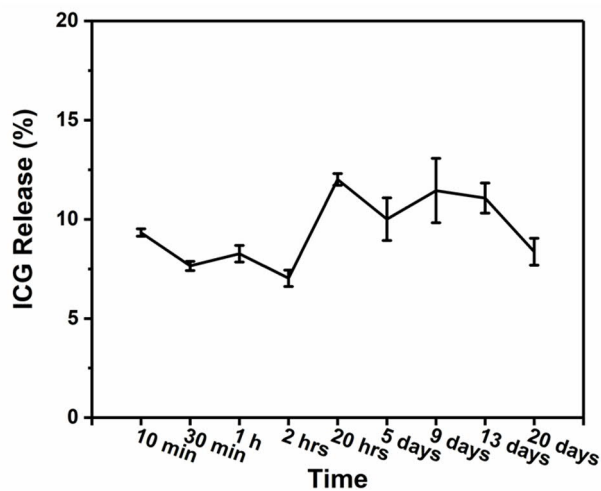


Figure S6.2. ICG release profile in vitro.

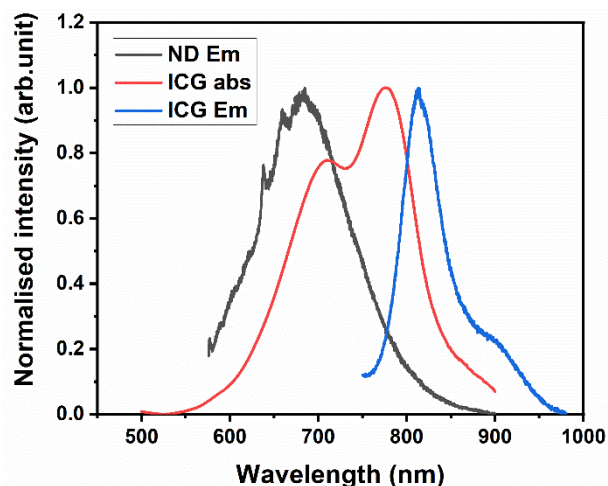


Figure S6.3. Normalized emission spectra (ex. 532 nm) of ND (black), normalized absorption spectra of ICG (red), and normalized emission spectra (ex. 600 nm) of ICG (blue).

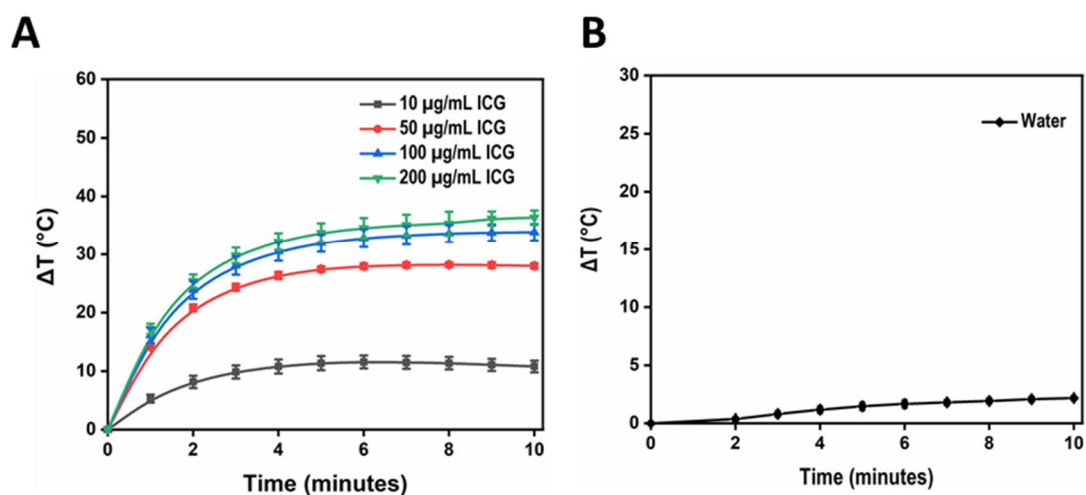


Figure S6.4. (A) Thermal profile of ICG at a concentration of 10 $\mu\text{g/mL}$, 50 $\mu\text{g/mL}$, 100 $\mu\text{g/mL}$, and 200 $\mu\text{g/mL}$ under near-infrared (NIR) irradiation (810 nm lamp; 0.35 W/cm^2). (B) Thermal profile of water under near-infrared (NIR) irradiation (810 nm lamp; 0.35 W/cm^2).

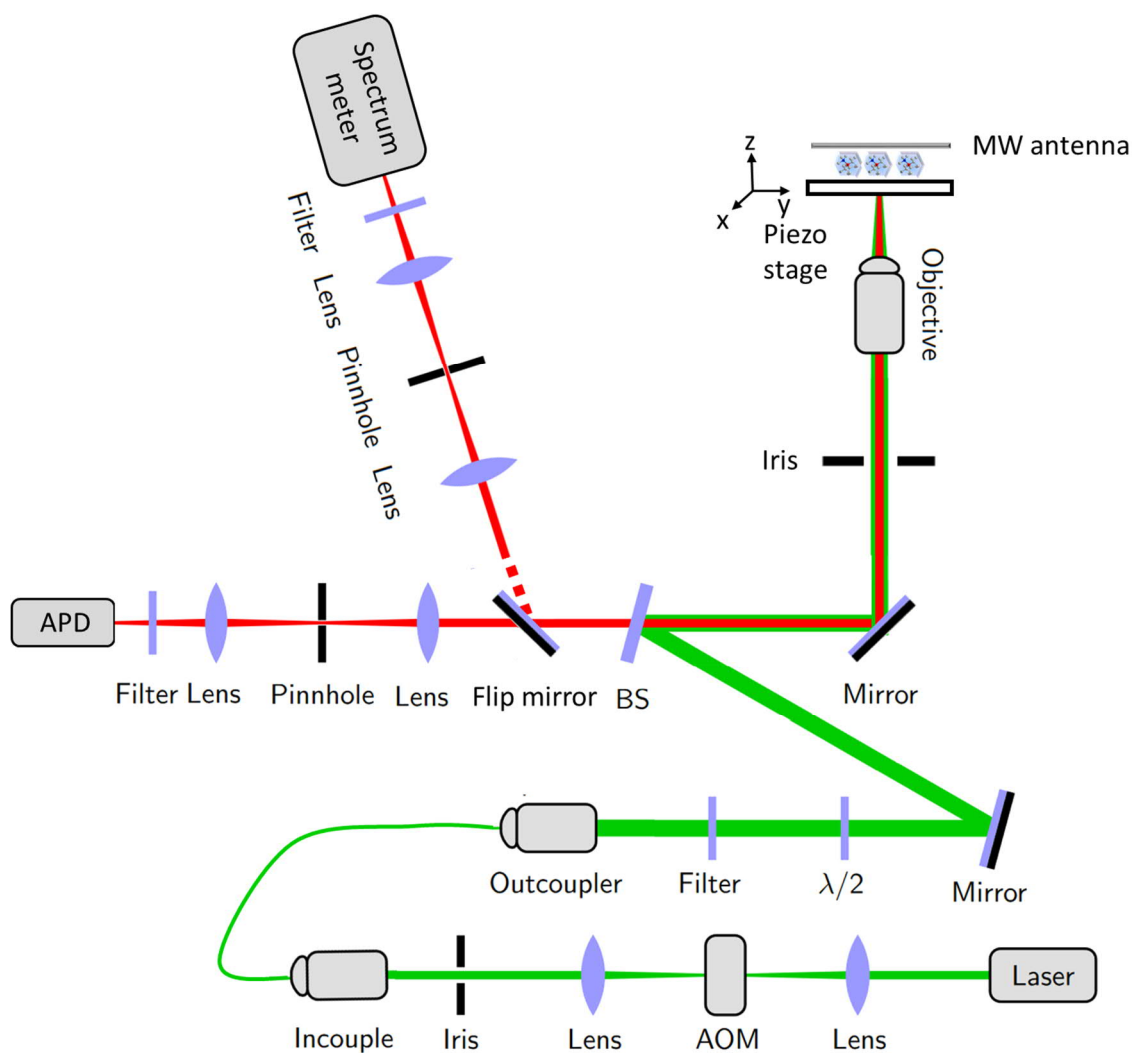


Figure S6.5. Schematic of home-built wide-field fluorescence microscope with optically detected magnetic resonance (ODMR) spectroscopy. Briefly, a 532nm wavelength laser (Laser Quantum gem 532) is used to excite the NV center, A lens focused the beam coming from the laser source onto a TeO₂ acousto-optic modulator (AOM) (Crystal Technology 3200-146), which is used as an optical switch in the pulsed experiments. After the AOM, the laser is coupled into a single-mode fiber, the fiber thereby acted as a mode cleaner, since it couples only the Gaussian TEM₀₀ mode. It was necessary because the clean Gaussian mode produced by the laser can be distorted while passing the AOM. The outcoupled light from the fiber subsequently passed a 530nm notch filter (Chroma Technology HQ530/30M) to filter out potential fluorescence arising from the fiber, and a $\lambda/2$ -plate (Thorlabs WPH10M-532), which enables polarization adjustments. Another mirror then lead the beam to a beam-sampler

(BS) (ThorlabsBSF20-B), which has the property to be mainly transparent for the NV center's fluorescence, but still reflects some parts of the green light towards an immersion oil objective (Olympus UPLSAPO60XO). It was used to focus the green light down to the diamond sample, as well as to collect the fluorescence light and direct it back towards the beam-sampler. By means of a 3D-piezostage with a scan range of $200 \times 200 \times 25 \mu\text{m}$ together with an accuracy of 0.5nm (NPoint NPXY200Z25A), scanning and positioning of the objective and therefore the focal spot was possible. The emission was adjust by flip mirror to either a spectrometry (Princeton Instrument Acton-SpectraPro SP-2500) or an avalanche photodiode (APD) (Excelitas Technologies SPCMAQRH-15) to get spectra or confocal image.

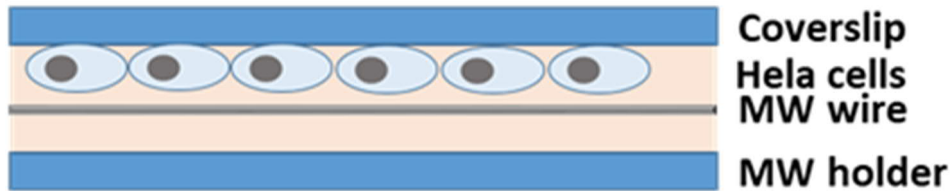


Figure S6.6. Schematic of cell samples for intracellular measurement.

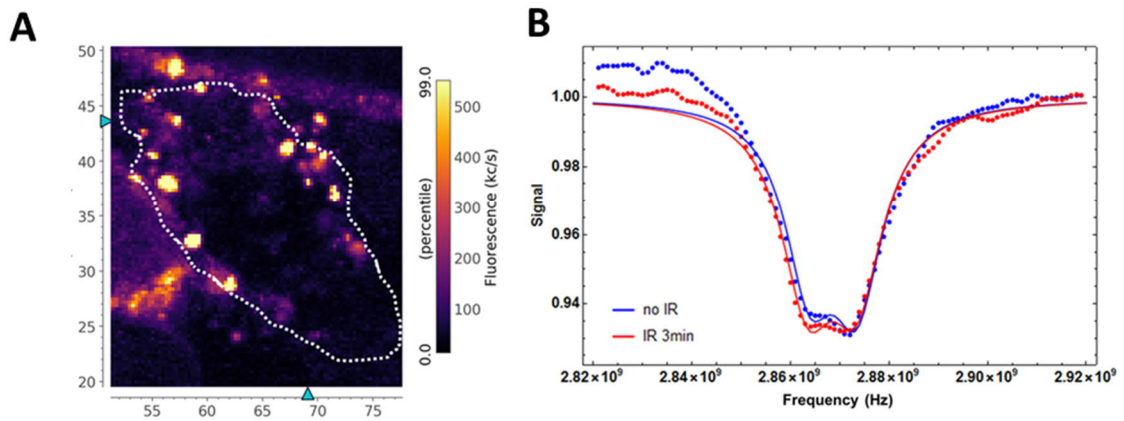


Figure S6.7. (A) fluorescence image of ND-NG in a living cell. (B) Representative ODMR spectra of ND-NG which was fitted with a sum of two Lorentzians, under near-infrared (NIR) irradiation (810 nm lamp; 0.35 W/cm^2) at the time of 0 min and 3

min.

6.6 References

1. C. Franceschi, *Aging Clin. Exp. Res.*, 1989, 1, 3-15.
2. H. Marsden, I. K. Crombie and J. Subak-Sharpe, *J. Gen. Virol.*, 1976, 31, 347-372.
3. J. Martinez, I. Georgoff and A. Levine, *Genes Dev.*, 1991, 5, 151-159.
4. R. S. Seymour, *Biosci. Rep.*, 2001, 21, 223-236.
5. W. Wei, X. Zhang, S. Zhang, G. Wei and Z. Su, *Mater. Sci. Eng. C*, 2019, 104, 109891.
6. A. C. Doughty, A. R. Hoover, E. Layton, C. K. Murray, E. W. Howard and W. R. Chen, *Materials*, 2019, 12, 779.
7. C.-W. Hsiao, E.-Y. Chuang, H.-L. Chen, D. Wan, C. Korupalli, Z.-X. Liao, Y.-L. Chiu, W.-T. Chia, K.-J. Lin and H.-W. Sung, *Biomaterials*, 2015, 56, 26-35.
8. Q. Chen, L. Xu, C. Liang, C. Wang, R. Peng and Z. Liu, *Nat. Commun.*, 2016, 7, 1-13.
9. C. Zhang, W. Bu, D. Ni, C. Zuo, C. Cheng, Q. Li, L. Zhang, Z. Wang and J. Shi, *J. Am. Chem. Soc.*, 2016, 138, 8156-8164.
10. D. Chrétien, P. Bénil, H.-H. Ha, S. Keipert, R. El-Khoury, Y.-T. Chang, M. Jastroch, H. T. Jacobs, P. Rustin and M. Rak, *PLoS Biol.*, 2018, 16, e2003992.
11. F. Chen and W. Cai, *Nanomed.*, 2015, 10, 1-3.
12. H. Norouzi, K. Khoshgard and F. Akbarzadeh, *Lasers Med. Sci.*, 2018, 33, 917-926.
13. A. Espinosa, A. K. Silva, A. Sánchez - Iglesias, M. Grzelczak, C. Péchoux, K. Desboeufs, L. M. Liz - Marzán and C. Wilhelm, *Adv. Healthc. Mater.*, 2016, 5, 1040-1048.
14. X. Huang, I. H. El-Sayed, W. Qian and M. A. El-Sayed, *J. Am. Chem. Soc.*, 2006, 128, 2115-2120.
15. C. Tchounwou, S. S. Sinha, B. P. Viraka Nellore, A. Pramanik, R. Kanchanapally, S. Jones, S. R. Chavva and P. C. Ray, *ACS Appl. Mater. Interfaces*, 2015, 7, 20649-20656.
16. Y. Matsumura and H. Maeda, *Cancer Res.*, 1986, 46, 6387-6392.
17. D. Jaque, L. M. Maestro, B. Del Rosal, P. Haro-Gonzalez, A. Benayas, J. Plaza, E. M. Rodriguez and J. G. Sole, *Nanoscale*, 2014, 6, 9494-9530.
18. M.-F. Tsai, S.-H. G. Chang, F.-Y. Cheng, V. Shanmugam, Y.-S. Cheng, C.-H. Su and C.-S. Yeh, *ACS Nano*, 2013, 7, 5330-5342.
19. C. Loo, A. Lin, L. Hirsch, M.-H. Lee, J. Barton, N. Halas, J. West and R. Drezek, *Technol. Cancer Res. Treat.*, 2004, 3, 33-40.
20. Y. Sun, B. T. Mayers and Y. Xia, *Nano Lett.*, 2002, 2, 481-485.
21. X. Huang, S. Tang, X. Mu, Y. Dai, G. Chen, Z. Zhou, F. Ruan, Z. Yang and N. Zheng, *Nat. Nanotechnol.*, 2011, 6, 28-32.
22. Y. Li, W. Lu, Q. Huang, C. Li and W. Chen, *Nanomed.*, 2010, 5, 1161-1171.
23. B. Geng, D. Yang, D. Pan, L. Wang, F. Zheng, W. Shen, C. Zhang and X. Li, *Carbon*, 2018, 134, 153-162.
24. C. Liang, S. Diao, C. Wang, H. Gong, T. Liu, G. Hong, X. Shi, H. Dai and Z. Liu, *Adv. Mater.*, 2014, 26, 5646-5652.
25. K. Yang, J. Wan, S. Zhang, B. Tian, Y. Zhang and Z. Liu, *Biomaterials*, 2012, 33, 2206-2214.
26. K. Yang, S. Zhang, G. Zhang, X. Sun, S.-T. Lee and Z. Liu, *Nano Lett.*, 2010, 10, 3318-3323.
27. B. Tian, C. Wang, S. Zhang, L. Feng and Z. Liu, *ACS Nano*, 2011, 5, 7000-7009.
28. T. K. Ryu, S. W. Baek, R. H. Kang and S. W. Choi, *Adv. Funct. Mater.*, 2016, 26, 6428-6436.

29. J. Yu, M. A. Yaseen, B. Anvari and M. S. Wong, *Chem. Mater.*, 2007, 19, 1277-1284.
30. Y. Liu, N. Song, Z. Li, L. Chen and Z. Xie, *Dyes Pigm.*, 2019, 160, 71-78.
31. J.-M. Yang, H. Yang and L. Lin, *ACS Nano*, 2011, 5, 5067-5071.
32. K. Okabe, N. Inada, C. Gota, Y. Harada, T. Funatsu and S. Uchiyama, *Nat. Commun.*, 2012, 3, 1-9.
33. S. Kiyonaka, T. Kajimoto, R. Sakaguchi, D. Shinmi, M. Omatsu-Kanbe, H. Matsuura, H. Imamura, T. Yoshizaki, I. Hamachi and T. Morii, *Nat. Methods*, 2013, 10, 1232-1238.
34. T. Sekiguchi, S. Sotoma and Y. Harada, *Biophys. Physicobiol.*, 2018, 15, 229-234.
35. V. M. Acosta, E. Bauch, M. P. Ledbetter, A. Waxman, L.-S. Bouchard and D. Budker, *Phys. Rev. Lett.*, 2010, 104, 070801.
36. P. Neumann, I. Jakobi, F. Dolde, C. Burk, R. Reuter, G. Waldherr, J. Honert, T. Wolf, A. Brunner and J. H. Shim, *Nano Lett.*, 2013, 13, 2738-2742.
37. G. Kucsko, P. C. Maurer, N. Y. Yao, M. Kubo, H. J. Noh, P. K. Lo, H. Park and M. D. Lukin, *Nature*, 2013, 500, 54-58.
38. D. A. Simpson, E. Morrisroe, J. M. McCoey, A. H. Lombard, D. C. Mendis, F. Treussart, L. T. Hall, S. Petrou and L. C. Hollenberg, *ACS Nano*, 2017, 11, 12077-12086.
39. T. Plakhotnik, M. W. Doherty, J. H. Cole, R. Chapman and N. B. Manson, *Nano Lett.*, 2014, 14, 4989-4996.
40. P. C. Tsai, C. P. Epperla, J. S. Huang, O. Y. Chen, C. C. Wu and H. C. Chang, *Angew. Chem. Int. Ed.*, 2017, 56, 3025-3030.

7. Summary and Outlook

This work aims to develop functional ND coatings, which can stabilize NDs and provide rich opportunities for post-functionalization. The surface coating acts as a bridge between the prepared NDs and attractive bioapplications. All of the used approaches are summarized in Figure 7.1 and compared in Table 7.1 based on the important parameters for bioapplication.

In the first approach (chapter 3), inspired from “protein glue” of mussel foot proteins, the dopamine can sticky and polymerize on various surfaces easily and provide many functional groups including amines, alcohols, and conjugated Michael acceptors for post-functionalization. To further increase the hydrophilicity and functional groups, neurotransmitter L-3,4-dihydroxyphenylalanine (L-DOPA), the derivative of dopamine, are firstly used to modified the surface of NDs. Furthermore, the protein transferrin and the small molecule dye ICG are selected as two vastly different molecular components to modified poly(L-DOPA) coated NDs. It shows that poly(L-DOPA) is an excellent option for non-covalent post-modification with both small molecules and large macromolecules. As an integrated construct, ICG-Tf-ND retains the optical and magnetic sensing capabilities of NDs, while also exhibiting improved colloidal stability, cellular uptake, and an enhanced photothermal effect. Poly(L-DOPA) coating stabilizes optical properties of NV centers in nanocrystals and at the same time, no significantly negative effects to charge state of NV^- defects were observed. In addition, a high cytotoxic effect was revealed for HeLa cells even at an ultra-low power intensity of the laser. This could open new avenues to the noninvasive treatment of malignant tumors deep within the body, which could reach tissue in the brain, prostate, colorectal and pancreas. However, there are two main drawbacks. First, the thickness of poly(L-DOPA) has a strong influence on the fluorescence of NDs. Fluorescence of NDs decreases with increasing thickness of poly(L-DOPA) shell dramatically, even with a few nm thickness (Figure S3.6). The reason is the large conjugating structure of poly(L-DOPA), which has strong absorption at the excitation light. Second, it is problematic to covalently modify the poly(L-DOPA) coating, we find the poly(L-DOPA) coating

decomposes in the process of covalent functionalization. Like the polydopamine, poly(L-DOPA) is a complex structure composed of oligomers that are connected by covalent and non-covalent interactions. These systems are valuable for cellular experiments, however, *in vivo* experiments and long-term investigations in biological media are limited by incomplete shielding due to the possible decomposition of the shell.

In order to further boost cellular uptake of the NDs, a virus-inspired protein coating has been developed (chapter 4). Viruses are evolutionary optimized carrier systems, which is stable in physiological condition and can efficiently enter cells. Moreover, the capsid of virus is very thin, the thickness of CCMV capsid is 4 nm, and the residue groups of amino acids from capsid proteins provide large amount of post-functional groups. First, the CP was isolated from the CCMV by decomposing the virus and removing the RNA, then stored in a capsid storage buffer. Before encapsulation of NDs, the CP was dispersed in the coat protein buffer, then the NDs at PVP solution was added to induce the CP self-assembly and obtain CP encapsulated NDs (ND-CP). The CP shell on ND is with around 4 nm extremely thin, which is comparable to the wall thickness of CCMV capsid. The ND-CP showed good colloidal stability in buffers. The NV centers in nanocrystals keep their optical properties at the same time, no significantly negative effects on the charge state of NV⁻ defects is found. In addition, the coating also does not affect the fluorescent properties of NDs. Moreover, the ND-CP shows good biocompatibility in HET-CAM model up to 100 µg/mL *in vitro* and *in ovo*. The analysis of intracellular motions of ND-CP revealed confined diffusion at the beginning, which then changed to normal diffusion (i.e., $MSD \propto t_{lag}$), which has also been observed for adenovirus-like particles. The intracellular tracking ability of ND-CP with detailed time, spatial, and spectral shows a great potential in life science. In addition, the well-established protein modification can be used for the functionalization of ND-CP. The ND-CP can be taken as multifunctional platform for different application, including drug delivery and bioimaging. After combining with the targeting group, it can be used to sense the temperature and/or radicals in special organelles. Nevertheless, there are a

few main concerns about this system: first, only a few amount of the ND-CPs can be taken up by cells and majority of them will just aggregated on the surface of cells; the internalization of ND-CP in cells needs to be further investigated. Moreover, the stability of ND-CP after further modification on the CP protein and the internalization behaviors are very difficult to predict due to the sophisticated structure of the virus protein, small changes may result in big differences, compared to other coatings.

After investigating and analyzing the above two systems, we developed the third approach called adsorption-crosslinking strategy (chapter 5 and chapter 6), we believe it can work as a universal method which can stabilize NDs, endow the multi-functionality, and keep the physical properties of NDs for quantum sensing. In the above two coating processes, the small molecules or protein was absorbed to the surface of NDs and then the adsorbed coating was “crosslinked” either by polymerization or protein-protein interaction. The NDs was enclosed in the polymer or protein cage. So the shell stabilize and endow the post-functional ability. As a proof of concept, hyperbranched polyethyleneimine (PEI), a highly branched, cationic polymers with multiple primary amino groups, was selected to precoat the NDs and then a 4-armed polyethyleneglycol cross-linker reacted with PEI and formed a nanogel shell. The shell thickness of the obtained nanogel coated NDs (ND-NG) can be decreased to 10 nm and also display long-term stability (up to one year in water). Furthermore, ND-NG showed excellent biocompatibility with the concentration up to 800 $\mu\text{g/mL}$ *in vitro* and *in ovo*. To conform the post-functional ability of ND-NG, ND-NG were further modified with paramagnetic ion, Gd^{3+} , ferritin non-covalently and photodynamic agent (Ruthenium complex) covalently successfully, the paramagnetic Gd^{3+} and ferritin on the surface of ND-NG can be sensed out in a nanoscale manner in T_1 relaxation experiments. The Ruthenium complex modified ND-NG (ND-NG-ICG) exhibited combination of bioimaging and photodynamic therapy. Moreover, the ND-NG was combined with indocyanine green (ICG), and the ND-NG-ICG system displayed temperature reporting ability in the photothermal therapeutic process in intracellular level. For all of the photothermal therapeutic process so far, it is barely know how the local temperature

affect the cells. Moreover, it will give us a chance to further investigate how the local temperature in the organelles affect the organelles' behavior after adding the organelle-targeting motifs to the ND-NG-ICG system. However, it is very challenging for the nanoparticle to enter the organelles or nucleus of cells.

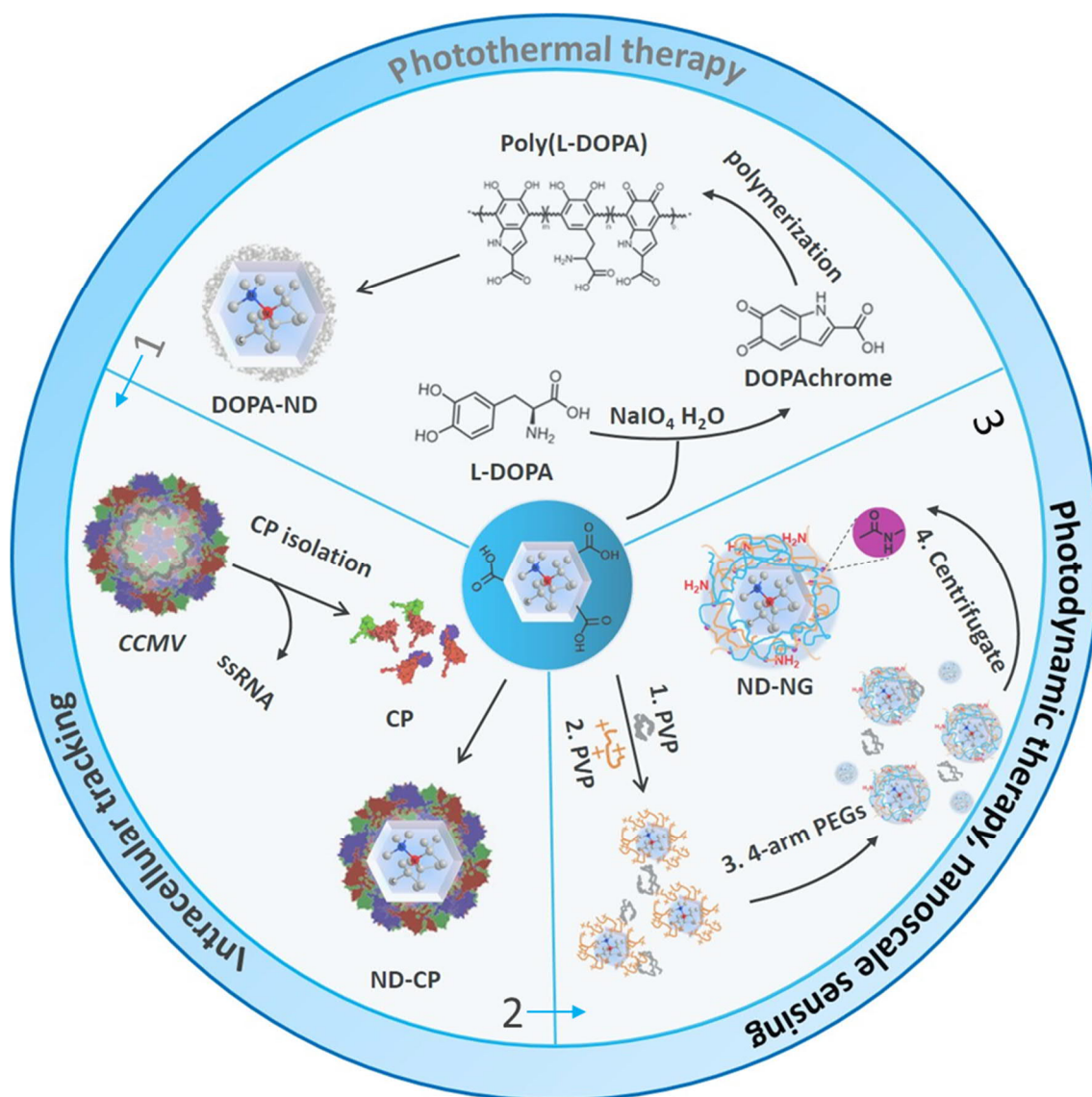


Figure 7.1 Summary of all projects: From Coating Design to Application.

	Poly(L-DOPA) coated NDs	CCMV capsid protein coated NDs	Nanogel coated NDs
Method	Adsorption, crosslinking	Adsorption	Adsorption, crosslinking
Thinnest shell	3 nm	4 nm	10 nm
stability	+	++	+++
Post- functionalization	Non-covalent	No data	Non-covalent, covalent
cellular uptake	++	+	+++
bioapplication	drug delivery, Photothermal therapy	Cell trafficking	Photodynamic therapy, nanoscale sensing, nanothermom eter

Table 7.1 Comparison of all approaches in this thesis.

In the final paragraph, I would like to share some experience and personal ideas. Looking back to the past years I spent on the surface functionalization, the first problem I met it was the quality of NDs, the quality of commercial NDs varies batch-to-batch. There are so many surface modification methods of NDs to get monodispersed NDs in literature, but when we started to reproduce them, most of them are not reproducible at our hands. The content of chemical groups on the surface of NDs can differ, the approach using the functional groups directly to react with other moieties chemically may not be a good choice. It used cause the aggregation in the modification reaction. For most of the commercial NDs, the company usually used TEM, DLS and zeta potential to do the quality control. So it would be great to build a surface modification method which is only related to the size and surface charge of NDs. This is why the silica coating process, protein coating process, and polydopamine process are more reproducible. These coating processes are relatively less dependent on the detailed

content of chemical groups on the surface. The other thing I have to mention is using water-soluble polymer such as polyethylene glycol to modify the surface of NDs, to get stable NDs, the PEG need to be very dense and form 'brush' conformation rather than the 'mushroom' conformation. However, it may be quite challenging considering the limited content of functional groups we can use on the surface of NDs. Even with 'grafting from', we need to think about two cases, first, avoiding the aggregation when you are modify the NDs with functional initiators. And then think about how many initiating points can be formed on the surface, and how many initiating points can form the polymers. The molecule weight of water-soluble polymers should be taken into account, lower molecule weight water-soluble polymers may not form enough thick water layers to stabilize NDs. The polyglycerol coated NDs shows excellent properties such as stability, functionality, and attracts a lot of researchers, it is better to keep in mind when you are trying this method, first of all, the uncontrollable ring-opening polymerization of glycidol and the dispersity of NDs in glycidol results in the aggregation of most of the polyglycerol coated NDs, from our experimental results, the percentage of single polyglycerol coated NDs was less than 10 % or even less. But what we can learn from this is design water-soluble monomer which can controllably polymerize to hyperbranched water-soluble macromolecules, in this case, you do not need to worry too much about the initiating points on the surface of NDs. Some points about the bioapplication of NDs I would like to spot out. Firstly, we need to think about what is exact goals for you, for bioimaging and drug delivery, you do not really need the monodispersed NDs, the targeting and controlled drug releasing are more dominating your research. For the quantum sensing in cell, the monodispersity of NDs are more important, which can let you get better resolution and sensitivity. The cell uptake of NDs normally is via endocytosis, most likely, the NDs are not internalized in endosomes one by one. That means the NDs may not be monodispersed in cells. Furthermore, most of the ODMR setup is based on the normal wide-field optical microscopy. It is not possible to figure out the single ND who owes more than one NV^- , and also it has diffraction limit (more than 200 nm). So if the smaller size NDs are used,

the resolution needs to be paid attention. Moreover, compared to the bulk diamond, each nanodiamond has different shape and noises on the surface, which results the NDs cannot as absolute thermometer and magnetometer. The calibration is necessary. Considering the producing process of HPHT NDs, it is doubting that the absolute thermometer and magnetometer will be achieved by HPHT NDs. The detonation NDs have much similar spherical shapes, the single digital detonation ND and single NV center in detonation NDs has been realized recently, we are looking forward to the single NV in single digital detonation ND, it will be an option as absolute thermometer and magnetometer in cell.

8. List of abbreviations

AFM	atomic force microscopy
APD	avalanche photo-diode
ATR-FTIR	attenuated total reflection Fourier transform infrared
ABDA	9,10-anthracenediyl-bi(methylene)dimalonic acid
BSA	bovine serum albumin
CCMV	<i>Cowpea chlorotic mottle virus</i>
CP	capsid protein
CD	circular dichroism spectroscopy
CDF	cumulative distribution function
CLEM	correlative light-electron microscopy
DNDs	detonation nanodiamonds
DOX	doxorubicin
DCC	<i>N,N'</i> -dicyclohexylcarbodiimide
DIC	<i>N,N'</i> -diisopropylcarbodiimide
DLS	dynamic light scattering
DMEM	Dulbecco's Modified Eagle's Medium
DPBS	Dulbecco's Phosphate-Buffered Saline
EDC	1-ethyl-3-(3-dimethylaminopropyl)carbodiimide
EDD	embryo development day
EPR	enhanced permeability and retention effect
EM	electron microscopy
FLIM	fluorescence lifetime imaging microscopy
FBS	fetal bovine serum
FPLC	fast protein liquid chromatography
FT-IR	Fourier transform infrared
HPHT	high-pressure high-temperature
HCC	horse heart cytochrome c
HPG	hyperbranched polyglycerol

HET-CAM	Hen's Egg Test on the Chorioallantoic Membrane
HRTEM	high-resolution transmission electron microscopy
HSA	human serum albumin
ICG	indocyanine green
IS	irritation score
ISC	intersystem crossing
L-DOPA	L-3,4-dihydroxyphenylalanine
LM	light microscopy
MSD	mean square displacement
MEM NEAAS	MEM Non-Essential Amino Acids Solution
MPS	mononuclear phagocytic system
MRI	magnetic resonance imaging
NDs	nanodiamonds
NV	nitrogen vacancy
NV ⁻	negatively charged NV
ND-CP	virus capsid protein encapsulated NDs
ND-NG	nanodiamond-nanogel
ND-NG-ICG	nanodiamond-nanogel-indocyanine green
NNI	National Nanotechnology Initiative
ND	Nanodiamond
NV ⁰	neutral Nitrogen Vacancy
NDX	nanodiamond-drug complexes
NOE	nuclear Overhauser effect
ND-NG-Ru	nanodiamond-nanogel-Ruthenium complex
NIR	near-infrared
4-OHT	4-hydroxytamoxifen
ODMR	optically detected magnetic resonance
PEI	polyethyleneimine
PEG	Polyethyleneglycol

PECVD	plasma-enhanced chemical vapor deposition
PBS	phosphate buffer saline
PANI	polyaniline
PLAL	pulsed laser ablation in liquids
PLLA	poly(lactic acid)
PTT	photothermal therapy
PDT	photodynamic therapy
PDF	probability distribution function
PVP	polyvinylpyrrolidone
RES	reticuloendothelial system
RDX	hexogen
Ru-COOH	[4-(1 <i>H</i> -imidazo[4,5- <i>f</i>][1,10]phenanthrolin-2-yl- κ N7, κ N8)benzoato]-bis(2,2'-bipyridine- κ N1, κ N1')ruthenium(1+)chloride
SBR	signal-to-background (autofluorescence) ratio
STED	stimulated emission depletion microscopy
SDS-PAGE	sodium dodecyl sulfate-polyacrylamide gel electrophoresis
SDS	sodium dodecyl sulfate
SWNT	single-walled-carbon-nanotube
TAM	tamoxifen
TNT	trinitrotoluene
TEM	transmission electron microscopy
T_1	spin-lattice relaxation
Tf	transferrin
VLPs	virus-like Particles
WHO	world health organization
XPS	X-ray photoelectron spectroscopy
ZPL	zero-phonon line

Acknowledgement

Appendix

List of Publications and Conference

Peer-reviewed papers related to PhD thesis

Transferrin-Coated Nanodiamond–Drug Conjugates for Milliwatt Photothermal Applications.

Sean Harvey, † Marco Raabe, † Anna Ermakova, **Yingke Wu**, Todd Zapata, Chaojian Chen, Hao Lu, Fedor Jelezko, David YW Ng, Tanja Weil*. *Adv. Ther.* 2019, 2(11), 1900067.

Fluorescent Nanodiamond–Nanogels for Nanoscale Sensing and Photodynamic Applications.

Yingke Wu, † Md Noor A Alam, † Priyadharshini Balasubramanian, Pia Winterwerber, Anna Ermakova, Michael Müller, Manfred Wagner, Fedor Jelezko, Marco Raabe*, and Tanja Weil*. *Advanced NanoBiomed Research*. 2021, accepted († shared first)

A Nanodiamond-Based Theranostic Agent for Light-Controlled Intracellular Heating and Nanoscale Temperature Sensing.

Yingke Wu, † Md Noor A Alam, † Priyadharshini Balasubramanian, Anna Ermakova, Stephan Fischer, Holger Barth, Manfred Wagner, Marco Raabe,* Fedor Jelezko,* and Tanja Weil*. *Nano Letters*. 2021, accepted. († shared first, in revision)

Fluorescent Nanodiamond Emitters with Virus Capsid Protein Corona Facilitating Cellular Uptake and Intracellular 3D-Trajectory Analysis.

Yingke Wu†, Shuqin Cao†, Md Noor A Alam, Marco Raabe, Sandra Michel-Souzy, Zuyuan Wang, Manfred Wagner, Jeroen J.L.M. Cornelissen*, Tanja Weil*. *J. Mater. Chem. B*. 2021, *under review*. († shared first)

Conference

Protein coated fluorescent nanodiamonds as multifunctional platforms.

Yingke Wu, Md Noor A Alam, Shuqin. Cao, Jeroen J.L.M. Cornelissen, Manfred Wagner, Tanja Weil.

Hasselt Diamond Workshop 2020 - SBDD XXV, Hasselt, Belgium, March 2020
(Poster)

Curriculum vitae

Personal Details:

Name: Yingke Wu

Date of Birth: 08. September 1991 in Tianmen, P. R. China

Nationality: Chinese

Address: Ricarda-Huch-Str. 9. Apt.11, 55122 Mainz, Germany

Academic Education:

September 2017 – July 2021, PhD student in chemistry at Max Planck Institute for Polymer Research, Germany. Doctoral thesis. " Surface Modification of Nanodiamonds for Bioapplication"

September 2014 – June 2017, Master of Engineering in Chemistry, Sichuan University, P. R. China. Master thesis. " Preparation and characteristic of biodegradable waterborne polyurethane tissue engineering scaffold"

September 2010 – June 2014, Bachelor of Engineering in Chemistry, Hebei University of Technology, P. R. China. Bachelor thesis. "Preparation of porous polymer with hierarchically porous interlocking inverse opal structure"

Honors and Awards:

2017 - 2021 Chinese Government Scholarship

2014 - 2017 The First Prize of Postgraduate Scholarship

2015 The Best Poster Award by Elsevier in Chinese Biomaterials Congress

2013 The First Prize of Tianjin Second Polymer Chemistry and Physics Contest

Languages:

English (Fluent), Chinese (Native), German (Elementary)